Characterisation of cementitious composites with green two-dimensional (2D) nanomaterial produced from sugar industry waste

By

Bo Huang

Department of Engineering
Lancaster University
UK

This thesis is submitted for the degree of Doctor of Philosophy,
August 2021

Declaration

I declare that the research work in this thesis titled 'Characterisation of cementitious composites with green two-dimensional (2D) nanomaterial produced from sugar industry waste' has been original carried out by me in the Engineering department of Lancaster University. The following academic publications and conferences have been published from this thesis.

- **Huang, B**., Piukovics, G., Niloufar, ,Z., Ye, J., Saafi, M. and Ye, J., 2021. Novel hybrid cement composite-based sensor for in-situ chloride monitoring in concrete structures, ***Construction and Building Materials***, (under review)
- **Huang, B.,** Saafi, M., Chi, Y, Ye, J., Zhou, Y. and Ye, J., Cyclic voltammetry and electrochemical impedance spectroscopy (EIS) characterization of cement composites with green two-dimensional (2D) nanomaterial produced from sugar industry waste, ***Composite Structures***, (to be submitted))
- **Huang, B**. Saafi, M. and Ye, J., Mechanical properties of SNS sheet fibre-reinforced cementitious composite: the effect of sonication, fibre content and water ratio, ***Composite Structures***, (to be submitted)
- **Huang, B**, *Development of Bio-Engineered Cementitious Composites for Sustainable Construction,* The 2020 Adam Neville PhD Prize in Cement and Concrete, University of Leeds, UK, 19th November 2020.
- **Huang, B**, Saafi, M* and Ye J. *Carrot-based covalently bonded saccharides as a new 2D material for healing defective calcium-silicate-hydrate in cement: Integrating atomistic computational simulation with experimental studies,* Lancaster University Engineering Department Postgraduate Research Conference, Lancaster University, UK, 1st -2nd July 2020.
- **Huang, B**, Saafi, M*, Chi, Y and Ye J. *Hydration of Bio-Engineered Cementitious Composites (2D Sugar beetroot nanoplatelets),* The 22nd International Conference on Composite Structures (ICCS22) and 1st Chinese conference on composite structures (CCCS1), Wuhan University, China, 31st October – 3rd November 2019.
- **Huang, B**, Saafi, M* and Ye J. *Novel engineered high performance sugar beetroot 2D nanoplatelet- cementitious composites,* Lancaster University Engineering

Department Postgraduate Research Conference, Lancaster University, UK, 3rd -4th July 2019.

- **Huang, B**, Saafi, M* and Ye J. *Investigating the cementitious composites drying behaviour through electrochemical impedance spectroscopy analysis,* 2018 Lancaster University international Postgraduate Research Conference, Lancaster University, UK, 18th May 2019.
- **Huang, B**, Saafi, M* and Ye J. *Waste bioextracts for the development of cement composites,* Lancaster University Engineering Department Postgraduate Research Conference, Lancaster University, UK, 4th – 5th July 2018.
- **Huang, B**, Saafi, M* and Ye J. *The influence of bio-nanoplatelet (SNS) additions on the performance of cement pastes,* 2018 Lancaster University international Postgraduate Research Conference, Lancaster University, UK, 12th May 2018.
- **Huang, B,** Saafi, M* and Ye J. *Development of bio-Engineered cementitious composites for sustainable construction,* Lancaster University Engineering Department Postgraduate Research Conference, Lancaster University, UK, 5th -6th July 2017.

Bo Huang

Lancaster University, UK

Abstract

In recent years, nanomaterials have been used to engineering cementitious composites to have improved performance. In particular, two-dimensional (2D) nanomaterials such as graphene, graphene oxide (GO) and boron nitride (BN) are considered as ideal candidates for cementitious materials admixtures, due to their high surface area and excellent mechanical properties. However, the applications of these 2D nanomaterials in those mixtures have been hindered by several roadblocks including high costs, incompatibility with the cementitious materials, health and environmental issues associated with their processing.

The objective of this thesis is to study the properties of the cementitious composites, incorporating a newly developed 2D bio nanomaterial. The 2D bio nanomaterial is in the form of sugar beet pulp nanosheets (SNSs) synthesised from sugar industry waste. The SNSs incorporation has two functions. One is amplifying the effect of the hydration products and the other is reinforcing the hydration phases of the cementitious composites.

An extensive experimental programme was carried out to characterise the cementitious composites, the hydration mechanism and the mechanical and fracture properties. First, the 2D SNSs were characterised by scanning electron microscopy (SEM), transmission electron microscope (TEM), x-ray energy dispersive x-ray spectrometer (EDS), fourier-transform infrared spectroscopy (FTIR), x-ray diffractometer (XRD), thermogravimetric analysis (TGA), differential scanning calorimetry (DSC), nitrogen adsorption and desorption isotherm. Second, the effect of SNSs on the hydration mechanism of OPC was investigated using electrochemical impedance spectroscopy (EIS), cyclic voltammetry (CV), TGA and DSC. The thermal behaviour of the

cementitious composites was examined, relationship between the degree of hydration (DOH) and the SNS concentration was established and the mechanism of hydration was elucidated using CV and EIS-equivalent circuit. Third, the compressive, flexural and tensile strength, and fracture properties of the cementitious composites was obtained through mechanical testing. Fourth, the influence of SNSs on the microstructure, types of hydration product and porosity were determined using SEM, EDS, BET, XRD and TEM. The development of the hydration phases, pore size and crack propagation in the matrix as a result of SNSs are elucidated. In addition, a hydration mechanism of the cementitious composites is proposed.

The obtained results from the experiments show that the SNS is an excellent nanomaterial to reinforce the cementitious composites. The SNS addition can substantially develop the cementitious composites DOH and promote the microstructure quality. The flexural, tensile and the fracture properties of SNS-cement pastes were significantly improved at different w/c ratios and in different SNS dispersion states. The mechanical performance and the microstructure changes indicates that the SNS can bridge fibre within the cementitious composites, accelerate the hydration and promote the chemical bonding.

Acknowledgements

The PhD journey was a significant chapter in my life. Through this journey, I have received a great deal of guidance and support.

Firstly, I would like to express my sincere gratitude to my supervisor, Professor Mohamed Saafi and his guidance, support and appreciation at all my PhD stages. I have benefited greatly from your patience, vast knowledge and professionalism, and your genius of wisdom and substance is a great asset that I will never be able to learn more from in my lifetime. I also would like to special thanks to Professor Jianqiao Ye for his continuous feedback and encouragement.

I am very grateful to all the academic personnel, colleagues and friends who have helped me in my academic career. Special thanks to Professor Yin Chi and Professor Junjie Ye for their guidance and academic support. Thanks to Malcolm Weightman and the other technical staff in the Engineering Department for their kind support during my PhD experimental stage.

Many thanks to my father, Mr Huang, and my mother, Mrs Feng for their continued unconditional support and encouragement. Life has been challenging, but we have managed to pull through. I would like to sincerely thank my girlfriend Mengyi Xu for her company and love along the way.

Contents

List of Table

List of Figures

List of Abbreviations

2D	Two-dimensional
a-SNS	Adsorbed SNS
ASTM	American society for testing and materials
AC	Alternating current
BET	Brunauer-Emmett-Teller
BN	Boron nitride
BC	Bacterial nanocellulose
BS EN	British Standard European Norm
COOH	Carboxyl group
C_3A	Tricalcium aluminate ($Ca_3Al_2O_6$)
C_4AF	Tetra-calcium aluminoferrite ($4CaO \cdot Al_2O_3Fe_2O_3$)
CO_2	Carbon dioxide
CNF	Cellulose nanofibres
C-S-H	Calcium silicate hydrate
$CaCO_3$	Calcium carbonate
CBW	Chemically bound water
CV	Cyclic voltammetry
CNCs	Cellulose nanocrystals
CMOD	Crack mouth opening displacement
C_2S	Dicalcium silicate (Ca_2SiO_4)
C_3S	Tricalcium silicate ($3CaO.SiO_2$)
CNTs	Carbon nanotubes
CH	Calcium hydroxide

DOH	Degree of hydration
DSC	Differential scanning calorimetry
DTG	Derivative thermogravimetry
DWCNT	Double-walled carbon nanotube
Ettringite	$Ca_6Al_2(SO_4)_3(OH)_{12}\cdot 26H_2O$
EIS	Electrochemical impedance spectroscopy
EDS	Energy-dispersive X-ray spectroscopy
FTIR	Fourier-transform infrared spectroscopy
f-SNS	Free SNS
FAO	Food and agricultural organisation
GNPs	Graphene nanoplatelets
GO	Graphene oxide
GONPs	Graphene oxide nanosheets
G	Graphene
IC	Isothermal calorimetry
IEA	International Energy Agency
ITZ	Interfacial transition zone
MWCNTs	Multi-wall carbon nanotubes
MC	Methylcellulose
NFC	Nano fibrillated cellulose
NCs	Nanocelluloses
NaOH	Sodium hydroxide
NS	Nano-silica
OPC	Ordinary Portland cement
OH	Hydroxy group

PAD	Phase angle threshold
PC	Portland cement
SAAs	Superficial active agents
SBP	Sugar beet pulp
SDBS	Sodium dodecylbenzene sulfonate
SEM	Scanning electron microscopy
SCD	Short-circuit diffusion
SNSs	Sugar beet pulp nanosheets
SP	Superplasticiser
SSA	Specific surface area
STS	Splitting tensile strength
SWCNT	Single-walled carbon nanotubes
TGA	Thermogravimetric analysis
TEM	Transmission electron microscopy
UPV	Ultrasonic pulse velocity
XRD	X-ray diffraction
Uv-Vis	Spectroscopic ultraviolet-visible spectroscopic
w/c ratio	Water - cement ratio

List of Symbols

K_{IC}	Fracture toughness
CI	Crystallinity index
σ_f	Flexural strength (N/mm^2)
σ_{ac}	Cementitious composites ionic ac-conductivity.
σ_c	Compressive strength (N/mm^2)
σ_{ct}	Splitting tensile strength
δ	Deflection
G_F	Fracture energy
L	The length of the specimen (mm)
$m = m_1 + m_2$	m is the mass, m_1 is the mass of the prism between support, m_2 is the loading fixture without attaching to the machine mass
ν	Scan rate
C	Capacitance
I	Current
f	Frequency of the electric field
R	ideal gas constant
T	absolute temperature
n	A number of electrons involved
F	Faraday's constant
A	Surface area of the electrode
ω	Radial frequency
C_O^*	Concentration of oxidant
D_0	Diffusion coefficient of the oxidant

C_R^*	The concentration of the reductant on the electrode surface
D_R	Diffusion coefficient of the reductant.
$\mathrm{R_s}$	Pore solution expresses the resistance of the solution
$\mathrm{C_{dl}}$	The electric double-layer capacitance
$\mathrm{Z_w}$	Diffusion behaviour refer to the ion penetration process in the solution Warburg impedance
$\mathrm{C_e}$	The electrodes capacitance
$\mathrm{R_e}$	The electrodes represent the resistance
ϵ''	The imaginary part of the dielectric constant
Z'	The real part of the impedance
ϵ_0	Distributed capacitance of vacuum
D	Cross-sectional diameter of the specimen (mm)
δ_0	The final failure of the beam displacement
W_0	Area of the load relate to displacement plot
g	Acceleration under gravity
K_{IC}	Fracture toughness of the cement pastes
P_{max}	The maximum applied load
G_F	Fracture energy of the cement pastes
S	Span of the beam
Q	Charge transfer

Chapter 1 Introduction

1.1 Problem statement

Concrete is the most widely used artificial material in the world. Ordinary Portland cement (OPC) is the main ingredient used to make concrete. The production and manufacturing of OPC is one of the main contributors to CO_2 emissions, accounting for 8-9% of global CO_2 emissions (Benhelal *et al.*, 2013; Zhang *et al.*, 2014; Lawrence, 2015; Monteiro, Miller and Horvath, 2017). Because of the rapid growth in world population, the demand for concrete infrastructure is expected to increase at a rapid pace. As a result, the consumption of OPC and its CO_2 emissions will continue to rise over the next 30 years.

As the world is pushing for global green economy to meet its net-zero CO_2 emissions target, reduction of the carbon footprint of concrete is critical to meeting this target. One of the emerging strategies to reduce CO_2 emissions associated with OPC production is to develop new concretes that contains less cement than traditional concretes but still have the same mechanical properties and durability characteristics. One popular approach to this is to improve the nano-micro properties of OPC binders using two-dimensional (2D) reinforcing nanomaterials such as graphene (G), graphene oxide (GO) and boron nitride (BN) by increasing the amount of the hydration products and acting as reinforcing phases in the cement matrix. By improving the nano-micro scale of OPC binders, it may be possible to design smaller size structural members with lower volumes of concrete thereby reducing the consumption of OPC and its CO_2 emissions as a result.

However, the production process of 2D nanomodified cementitious composites has encountered some obstacles. The 2D nanomaterials generally lack dispersibility and

tend to agglomerate in cement pastes. The agglomeration of 2D nanomaterials leads to microstructural defects in the matrix and induces stress concentration (Konsta-Gdoutos, Metaxa and Shah, 2010; Parveen, Rana and Fangueiro, 2013; Onuaguluchi, Panesar and Sain, 2014; Njuguna, Vanli and Liang, 2015; Awan *et al.*, 2017; Zhou *et al.*, 2017). Furthermore, 2D nanomaterials consume high quantities of energy during processing, pose high health, environmental and safety risks and are also expensive to mass-produce.

Therefore, there is a need for new low-cost and environmentally friendly 2D nanomaterials that are compatible with cementitious composites, to engineer concrete infrastructure with a low-carbon footprint.

1.2 Aim and Objectives

This PhD thesis aims to investigate the properties of cementitious composites infused with novel green two-dimensional (2D) nanomaterial produced from sugar industry waste with the objective to develop low-embodied carbon and high-performance construction materials. The 2D nanomaterial serves two essential functions: i) it improves the hydration kinetics of the cementitious composites, thereby improving the growth of the hydration products and ii) it controls microcracks of the cementitious which in return increases their fracture energy and resistance to cracks. These two coupled functions enable the design of cementitious composites with better longevity and a low carbon footprint.

The objectives of this PhD thesis are as follows:

1. To characterise the Sugar beet pulp nanosheets (SNSs) material to understand its properties, chemical composition and morphology.

2. To prepare sonication dispersion SNS aqueous suspensions and characterise the sonicate dispersion time effect of SNS solution agglomerate behaviour and stability.
3. To evaluate the rheology of the interaction between SNS and cement particles and to track the distribution of SNS on the cement hardened matrix.
4. To investigate the effect of SNS on the hydration behaviour of cementitious composites, electrochemical impedance spectroscopy (EIS), cyclic voltammetry (CV) and the equivalent circuit being used to elucidate the interaction mechanism between SNS and cement particles.
5. To investigate the effect of SNS on the mechanical properties of cementitious materials. The effect of different variables such as water-cement ratios, curing ages and SNS concentrations will determine the compressive and flexural strength.
6. To determine the influence of the SNS on the fracture energy, fracture toughness and splitting tensile strength of the cementitious materials. To establish the SNS strength mechanism (fibre crack bridge) of cementitious composites.
7. To explore the microstructural information of SNS in cementitious materials, analyse the effects of the SNS dispersion and content in the microstructure of cementitious materials, and reveal the mechanism of SNS micro-modification cementitious materials.

1.3 Contribution to knowledge

To solve the issue of CO_2 emissions from cement, there has been extensive research conducted previously in this area and technologies developed as a result are not deemed to be sustainable. The expensive and non-environmentally friendly technology

designed to reduce the exhaust methods cannot be widely applied in real construction. This study proposes for the first time the use of a new green SNSs 2D bio-nano material to replace the expensive 2D nanomaterial, manufacturing with OPCs to produce multifunctional cement pastes. The new generation of cement pastes produces better performing cementitious material with lower OPC content, thus reducing CO_2 emissions associated with OPC production. Compared to current cement-reinforced 2D nanomaterials such as graphene, GO and BN, SNSs have the advantage of low cost, sustainability, carbon-neutrality and low environmental, health and safety risks.

To the best of our knowledge, this research is the first to use high-efficiency SNSs alone as additives in the design and development of cementitious composites. The hydration of OPC in the presence of SNS is not thoroughly understood and the interaction mechanisms between the SNSs and the OPC particles during hydration are still not established. The widespread use of SNS will open a future research arena and tremendously benefit the field of civil engineering materials and the construction industry.

1.4 Outline of the thesis

The PhD thesis is divided into the following seven chapters:

Chapter 1 presents the problem statement, research aims and objectives, contributions to knowledge and the thesis organisation.

Chapter 2 presents a literature review on relevant research in the field of nanomaterials reinforced cementitious composites. This chapter covers the mechanical and physical properties of carbon nanotubes (CNTs), nano-silica (NS), graphene, graphene oxide (GO), cellulose nanocrystal (CNC) and cellulose nanofiber (CNF), and discusses their applications in cementitious materials.

Chapter 3 introduces the manufacturing process and characterisation properties of SNS materials and investigates the aqueous colloidal properties and stability of SNS.

Chapter 4 introduces the concept of SNS reinforced cementitious composites hydration and quantifies the influence of the addition of SNS. In this chapter, the cementitious composites hydration effects of SNS are determined by the SNS cement pastes rheology, thermogravimetric analysis (TGA), differential scanning calorimetry (DSC), electrochemical impedance spectroscopy (EIS), cyclic voltammetry (CV) and equivalent circuit. The effect of SNS on the hydration products is quantified, which provides theoretical and technical support for the evolution of the hydration mechanism of SNS-cementitious composites. Three mechanisms of improving hydration are deduced from the experimental results, including three-dimensional steric stabilisation, short-circuit diffusion (SCD) and SNS intercalation and dissolution mechanism.

Chapter 5 presents the design, experimental program and test results of the mechanical experiments of SNS cementitious composite materials. It also discusses different water-cement (w/c) ratios, SNS disperse state, SNS concentration and three different ages (7, 14, and 28 days). The mechanical experiments of SNS-reinforced cementitious composites include compression tests, three-point fracture tests, four-point bending flexural tests and splitting tensile tests. The test results of the mechanical properties of SNSs reinforce cementitious composites, and these are analysed and determined.

Chapter 6 characterises the microstructure and hydration products of SNS-cementitious composites and discusses the modifications mechanism of the microstructure. Experiments include SNS adsorption centrifugation, scanning electron microscopy (SEM), energy-dispersive spectroscopy (EDS), x-ray diffraction (XRD), transmission electron microscopy (TEM), nitrogen adsorption-desorption isotherm experiments, and the test results reveal the evolution of the crystal structure properties and morphology

of different concentrations of SNS at specified ages. The effect of ultrasonic disperse of SNS on the microstructure of cementitious pastes is also investigated.

Chapter 7 summarizes the research findings with the purpose of addressing the research aims and objectives, making practical implications and recommendations for future work.

Chapter 2 Background of nanomaterials reinforced cementitious composites

2.1 Introduction

This chapter presents the literature review of the material properties for cementitious composites, the mechanism of the hydration process and the up-to-date research on different dimensions of nanomaterial additives reinforced cementitious composites. The nanomaterial reinforces cementitious composites introduced through carbon nanotubes (CNTs), nano-silica (NS), graphene (G), graphene oxide (GO), cellulose nanocrystals (CNC) and cellulose nanofibers (CNF). Following that, this chapter also presents the current utilisation of sugar beet waste in the industry, thus providing the fundamental information for the research and application of 2D material SNS-cementitious development.

2.2 Properties of cementitious materials

2.2.1 Portland cement

Portland cement (PC) is the most widely used type of cement, and acts primarily as a hydraulic binder in concrete construction. PC undergoes rapid hydration when in contact with water, generating a series of complex physical and chemical reactions. During the curing process, the hydration reaction consumes the cement enabling it to harden and adhere together. The loss of plasticity during hydration is called ‘setting’. The main cementing part of the concrete is produced by the complex and porous microstructural hydration products during the setting process. The initial pore spaces are gradually filled with the hydration process (EN, 2011).

Concrete is a composite material comprised of water, binder (cement or lime), as well as fine and coarse granular material (aggregate or filler) (Neville, 2013). Since its advent in 1824, concrete has a history of nearly 200 years and has become one of the most important building materials in infrastructure construction. With its significant compression resistance and wide adaptability, concrete is the most widely used and consumed artificial building material in contemporary times. Concrete has the advantage over other building materials of being a widely available raw material due to its simple production process, low cost, fire resistance and durability. Concrete is extensively used to construct and maintain buildings, bridges, roads and marine structures (Neville, 1995). In 2020, the worldwide cement output was raise to 4.1 billion metric tons (Statista, 2021).

Due to the complex nature of concrete properties, the composition and characteristics of cement need to be further understood and developed on multiple scales (Monteiro, 2006). Ordinary Portland cement (OPC) cementitious composites is a multi-phase, non-homogeneous, and brittle material. The cementitious composites are mainly consists of cement particles and hydration products. The size of the hydration product is mainly in the range of 7-200 μm, the C-S-H gel particle size is around 10nm (Taylor, 1993).

In order to further tighten the relationship between cement macroscopic properties and microstructures, a large number of scholars have adopted a bottom-up approach and used nanotechnology to modulate the microstructure of cementitious composites. With the aim of developing a multifunctional concrete with the mechanical properties of durability and porosity (Li *et al.*, 2004; Sanchez and Sobolev, 2010; Alshaghel *et al.*, 2018).

2.2.2 Degree of hydration (DOH)

Cementitious composites are heterogeneous material, the DOH of OPC particles largely determines their properties (Bullard *et al.*, 2011). The DOH of OPC is generally indicated by the quantity of hydrated cement particles versus to the quantity of cement particles utilised (Taylor, 1997). As the DOH of the cement particles increases, the hydration phase content of the hydration products (e.g., C-S-H, CH) will generally become higher. Calcium silicate hydrate (C-S-H) is the most important product of the cement hydration, which is the primary source of the cementitious materials' mechanical strength.

However, under the current production process, the cement particles cannot be completely hydrated. Cement particles will rapidly form hydration products after being in contact with water, adhering to the surface of the other particles. Therefore, A large amount of OPC particles are in an unhydrated or partially hydrated state, because water is not able to physically enter the interior of the unhydrated cement particles (Scrivener *et al.*, 2019). To compensate for the cement particles low DOH and to achieve the high-performance structural requirements of concrete, large amounts of OPC is used in construction

2.2.3 Hydration mechanism of cement

The components of PC clinker are four main compounds: tricalcium silicate (Alite, C_3A, $3CaO \cdot SiO_2$), dicalcium silicate (Belite, C_2S or $2CaO \cdot SiO_2$), tricalcium aluminate (C_3A or $3CaO \cdot Al_2O_3$) and tetra-calcium aluminoferrite (C_4AF or $4CaO \cdot Al_2O_3Fe_2O_3$). During the hydration process, the hydrate reactions proceed simultaneously with different nucleation frameworks, growth reaction rates and dissolution rates, progressing to different hydration products.

Cement matrix composite is a multi-component, structurally inhomogeneous composite consisting of calcium silicate hydrate (C-S-H) gel, calcium hydroxide (CH), unreacted cement phases, pores and their pore solutions in a solid-liquid-gas phase in a non-homogeneous system (Neville, 2013). Studies have shown that concrete is anisotropic under tensile or compressive stresses, due to the random arrangement of particles in the crystal, the asymmetry of the molecules themselves and their specific orientation (Hughes and Ash, 1970). The hydration products are produced at different rates, intermixed with the C-S-H, portlandite, ettringite, alumina, ferric oxide and mono-sulphate (AFm) (Odler, 1998).

2.2.3.1 Alite

Alite (C3S) is an impure form of tricalcium silicate (Ca_3SiO_5 or $3CaO \cdot SiO_2$), the predominant, typical and most abundant phase in PC, accounting for about 50-80% (Taylor, 1997; Scrivener, Juilland and Monteiro, 2015). The hydrate reaction process of C3S is complex and controversial, and has continually developed in the previous research (Bullard *et al.*, 2011; Scrivener and Nonat, 2011; Scrivener, Juilland and Monteiro, 2015). The main hydration products of the C3S hydration reactions are calcium silicate hydrate (C-S-H) gel and calcium hydroxide (portlandite) crystalline, which are generally shown as the following equation:

$$\underset{\text{Alite}}{2(3CaO.SiO_2)} + \underset{\text{Water}}{6H_2O} \rightarrow \underset{\text{C-S-H}}{3CaO.SiO_2.3H_2O} + \underset{\text{CH}}{3Ca(OH)_2} \qquad (2.1)$$

The C-S-H gel is the mainly cementitious compound of silicate cement, responsible for the strength of the cementitious material and presents the amorphous state (Allen, Thomas and Jennings, 2007). The morphology of C-S-H is influenced by the water to cementitious material ratio, the calcium to silicon ratio, the curing conditions, the degree of hydration (DOH) of the cement and the chemical admixtures. Thus, the

morphology of C-S-H under SEM observation, does not show a specific crystalline morphology including needle-like, fibrillar, curly foil, lamellar foil pack and honeycomb (Siddique and Cachim, 2018; Shen *et al.*, 2019).

Portlandite ($Ca(OH)_2$) in cement pastes appears in the form of CH crystals with various shapes, including massive crystals, platelet crystals, hexagonal structure, large elongated crystals and fine dispersed crystals (Richardson, 2000; Siddique and Cachim, 2018). Calcium hydroxide nucleates and grows in the capillaries free space, accounting for approximately 20-25 vol% of the cement pastes. The presence of foreign matter affects the equilibrium of the hydration reaction and the nucleation and growth of cement products (Afridi *et al.*, 1989; Sun *et al.*, 2016).

2.2.3.2 Belite (C_2S)

The primary component of Belite (C_2S) dicalcium silicate (Ca_2SiO_4) is an important industrial mineral in OPC products. Belite crystalline lattice is similar to Alite in that it can accommodate foreign ions (Mg^{2+}, Al^{3+}, Fe^{2+}, K^+, Sulphate and Phosphate) (Lai, Nojiri and Nakano, 1992). The reaction process of Belite hydrate is similar to the C_3S. However, the reaction process rate is much slower than the Alite (Odler, 1998). The Belite hydration reaction produces similar hydration products (C-S-H and $Ca(OH)_2$) with the equation below:

$$2(Ca_2SiO_4) + 4H_2O \rightarrow 3CaO.2SiO_2.3H_2O + Ca(OH)_2 \qquad (2.2)$$

Belite Water C-S-H gel Portlandite

During the reaction process, the reactivity of Belite is affected by the foreign ions types and amounts, and the hydration rate varies with the crystallite size of C3S particles, water/solid ratio and hydration temperature (Kantro and WEISE, 1979).

2.2.3.3 Tricalcium aluminate(C_3A)

The chemical composition of C_3A is calcium aluminate ($Ca_3Al_2O_6$). When C_3A is mixed with foreign elements, changes can occur. For example, sodium can lead to orthorhombic or monoclinic structures (Odler, 1998). Due to the highly alkaline phase, tricalcium aluminate is a highly reactive phase in the OPC. The hydration process of C3A is similar to C3S phase hydration reactivity, which depends on the types and amount of the foreign ions.

The calcium sulphate that exists at the clinker participates in the reaction of C_3A. The sulphate that existed in the initial reaction between C_3A and water prompts the rapid formation of ettringite ($Ca_6Al_2(SO_4)_3(OH)_{12}\cdot 26H_2O$) and releases a large amount of heat, the equation is shown below (Odler, 1998):

$$3(CaO.Al_2O_3) + 3(CaSO_4.2H_2O) + 26H_2O \rightarrow 3CaO.Al_2O_3.3CaSO_4.32H_2O \quad (2.3)$$

C3A Calcium sulphate Water AFt rodlike

During the reaction process, the slowing C_3A reaction rate is similar to the C3S hydration induction period. The hydration rate is affected by the calcium sulphate content (Collepardi *et al.*, 1978; Minard *et al.*, 2007). When the sulphate is exhausted, the initially generated ettringite will continue to react with unreacted C_3A to form monosulfate hydrate ($C_4A\bar{S}H_{12}$), as shown by the following equation (Mindess, Young and Darwin, 1981):

$$2(3CaO.Al_2O_3) + 3CaO.Al_2O_3.3CaSO_4.32H_2O + 4H_2O \rightarrow 3(CaO.Al_2O_3.CaSO_4.12H_2O) \quad (2.4)$$

C3A AFt rod-like monosulphate

As the curing time increases, the unhydrated C3A react with $Ca(OH)_2$ and water to form calcium aluminate hydrates ($4CaO.Al_2O_3.13H_2O$) (St John, Poole and Sims, 1998).

$$3CaO.Al_2O_3 + Ca(OH)_2 + 12H_2O \rightarrow 4CaO.Al_2O_3.13H_2O \quad (2.5)$$

C3A calcium aluminate hydrates

2.2.3.4 Tetra-calcium aluminoferrite (C_4AF)

The chemical composition of the C_4AF is tetra-calcium aluminoferrite ($4CaO{\cdot}Al_2O_3{\cdot}Fe_2O_3$), which is a dark brown crystalline phase, and its structure consists of Ca^{2+} ions bridging octahedral FeO_6 and tetrahedral FeO_4. The reactions of the hydration product of C_4AF with water is similar to the C_3A with a slower hydration rate. The reactivity of C_4AF depends on the iron content (the Al/Fe ratio), also the reactivity increases with the rising temperature and fineness (Fukuhara *et al.*, 1981). The following equation gives the reaction of C_4AF with $Ca(OH)_2$ and water to form C_4FH_{13} and calcium aluminate hydrate.

$$4CaO.Al_2O_3.Fe_2O_3 + 4Ca(OH)_2 + 22H_2O \rightarrow 4CaO.Al_2O_3.13H_2O + 4CaO.Fe_2O_3.13H_2O \quad (2.6)$$

C4AF calcium aluminate hydrated

2.3 Nanomaterials in cementitious composites

The application of nanotechnology in concrete began at the beginning of the last century. Nanomaterials is the term to describe materials whose monomer size (at least in one dimension) ranges from 1 to 100 nm (Buzea, Pacheco and Robbie, 2007). Nano-concrete is concrete manufactured by nanomaterials or has nanomaterials additives, where the size of the nanoparticles is less than 500 nm (Malhotra and Mehta, 1996; Aïtcin, 2000). Nanomaterials fill and bridge the microcrack which affect concrete's macro-mechanical properties due to their unique physicochemical properties (size, shape, surface morphology, compressive strength, tensile strength and solubility). Different nanomaterials have proved to be effective in improving the hydration process and regulating the production of hydration products.

Different carbonaceous nanomaterials or inorganic nano additives have been widely used in research to construct intelligent, multifunctional and sustainable high-

performance cement composites. The development of nanomaterials in high-performance concrete and nanostructures can improve the mechanical properties, durability and functional properties of cement-based materials (Horszczaruk, Łukowski and Seul, 2020). With the development of nanotechnology, the nanoscale study has led to the bottom-up design concept of nanoscale studies on cement-based microstructures. The following section describes the up-to-date research of nanomaterials in 1D, 2D and nano cellulose materials.

2.3.1 Nanomaterials effect on the cementitious composites

2.3.1.1 Carbon nanotubes (CNTs)

CNTs were first discovered by Japanese electron microscopist Iijima (1991). CNTs are nanoscale materials made from single or multi-layered graphite sheets; it is an excellent material due to its novel structure and excellent physical and mechanical properties (Novoselov and Geim, 2007; Manzur, Yazdani and Emon, 2014). As shown in Figure 2.1 diagrammatic, CNTs can be divided into three categories: single-wall carbon nanotubes (SWCNTs), double-walled carbon nanotubes (DWCNTs) and multi-wall carbon nanotubes (MWCNTs) based on concentric tubes (Ajayan, 1999; Ma *et al.*, 2010; Rafique *et al.*, 2016). The CNTs have remarkable chemical stability, mechanical properties, high strength, elastic constants and high aspect ratios (typically in the range of 100 to 1000) (J M Makar, Margeson and Luh, 2005). Due to the structural characteristics of carbon nanotubes, it is widely used to improve the performance of concrete.

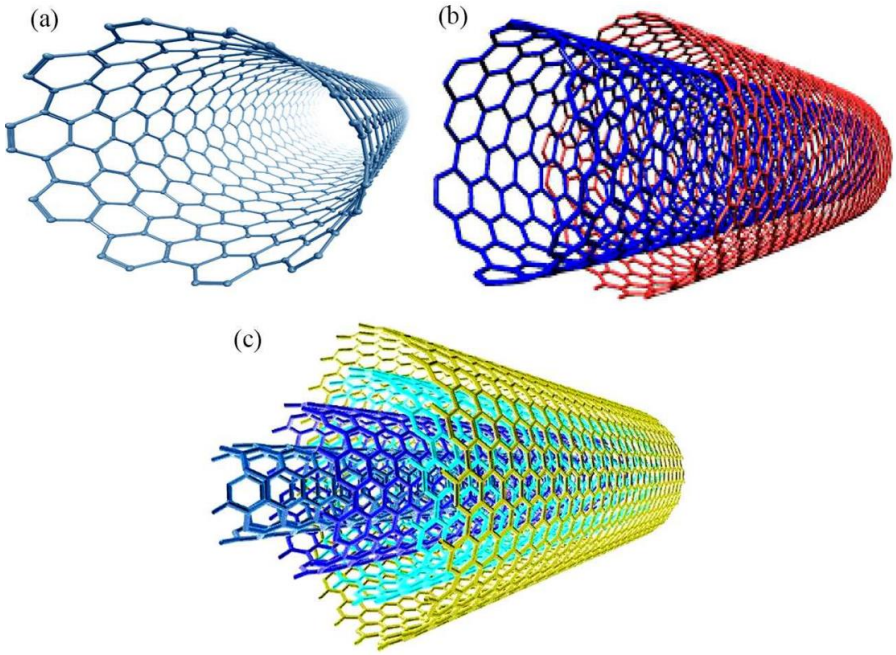

Figure 2.1 Structure of (a) SWCNTs, (b) DWCNTs, and (c) MWCNTs (Rafique *et al.*, 2016)

As shown in Figure 2.1 (a) SWCNTs are composed of a single layer of carbon atoms with good symmetry and homogeneity. The SWCNTs SEM images is shown in Figure 2.2 (Abjameh, Moradi and Amani, 2014). Figure 2.1 (b-c) shows that DWCNTs and MWCNTs are composed of multiple carbon atom layers, usually in the form of coaxial cables. Figure 2.3 shows the SEM of MWCNTs in a cotton-like entangled state (Dassios *et al.*, 2015) and the MWCNTs transmission electron micrographs representative are shown in Figure 2.4 (Hassan, Elkady and Shaaban, 2019). The Young's modulus of typical SWCNTs is around 1.0 TPa, the yield strength is between 20 and 60 GPa, the density is around 1.33 g/m^3, the range of diameter and length are 0.75 to 3 nm and 1 to 50 μm, respectively (Salvetat *et al.*, 1999; J M Makar, Margeson and Luh, 2005).

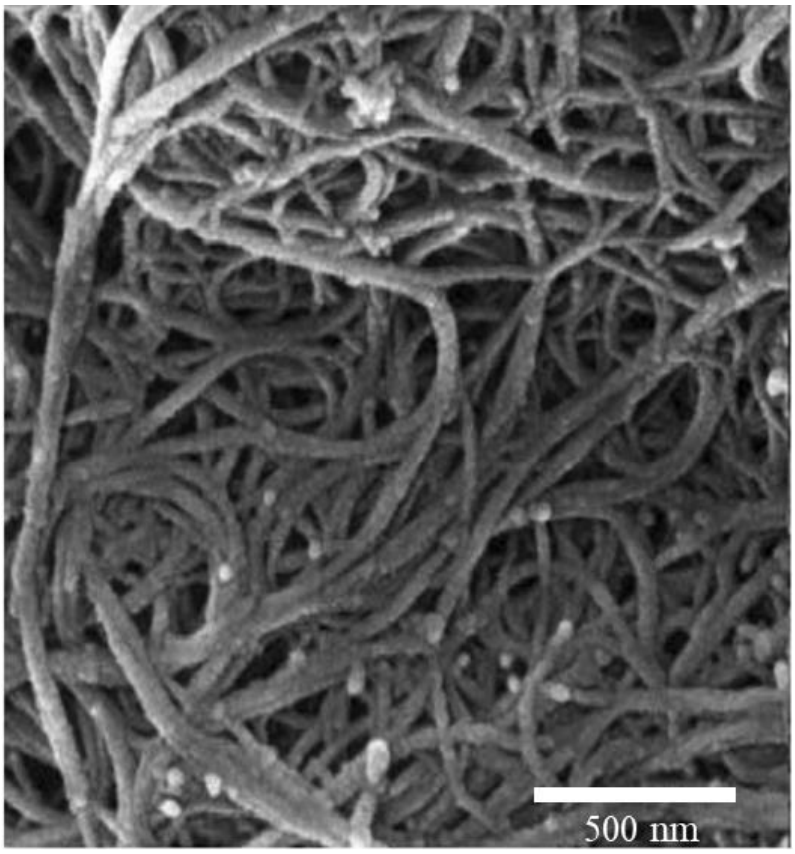

Figure 2.2 SEM images of SWCNTs (Abjameh, Moradi and Amani, 2014)

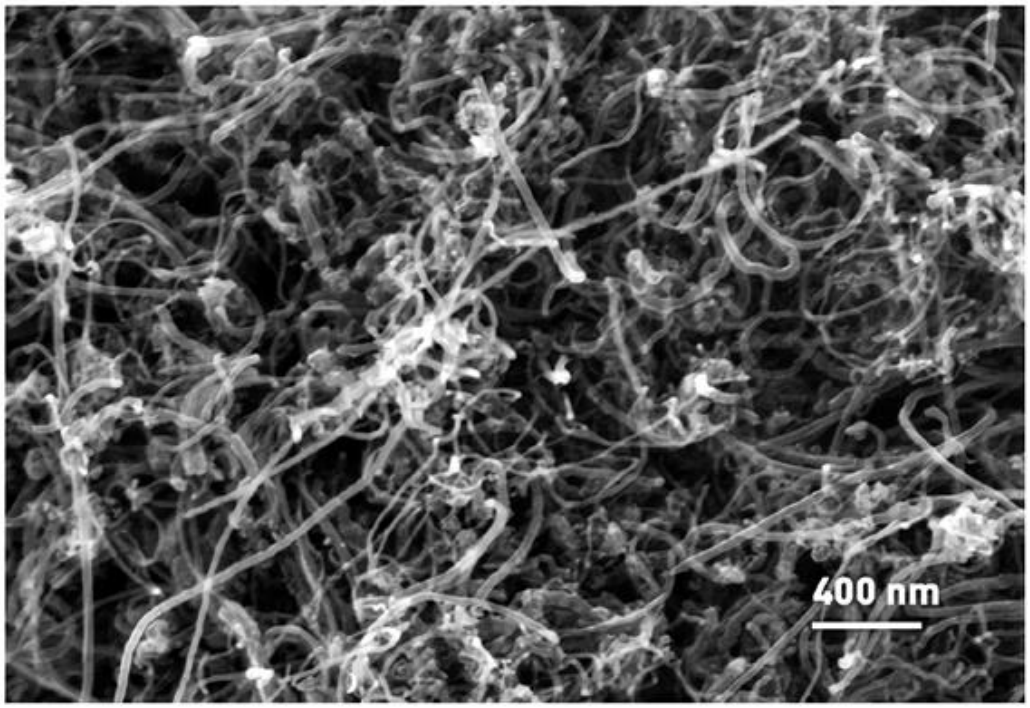

Figure 2.3 SEM of long multi-walled carbon nanotubes (Dassios *et al.*, 2015)

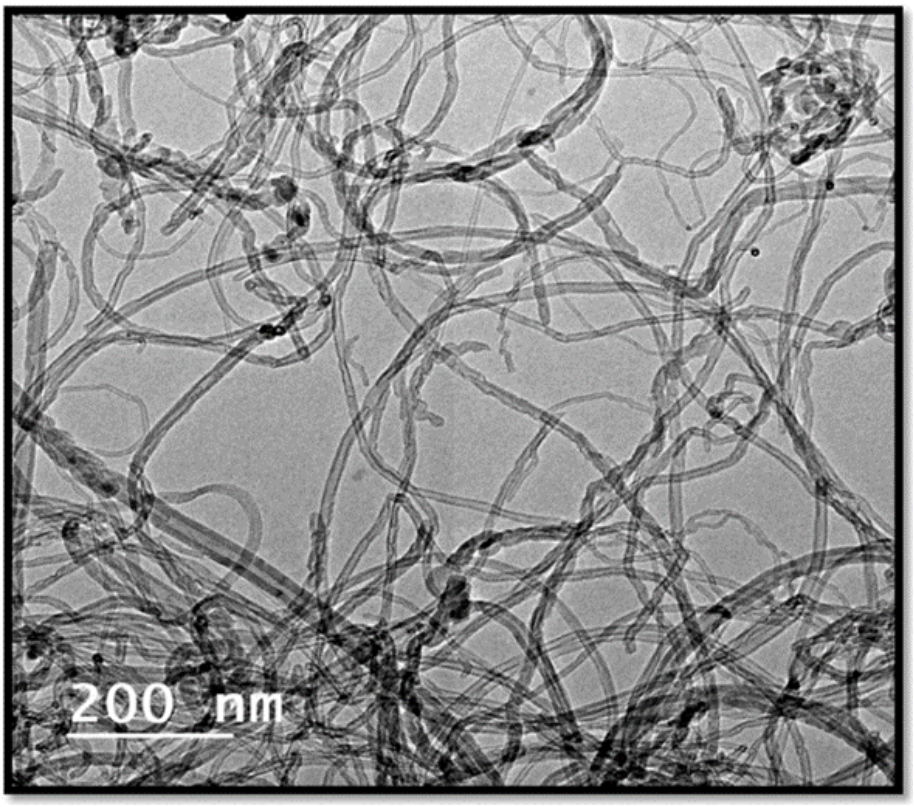

Figure 2.4 TEM of multi-walled carbon nanotubes (Hassan, Elkady and Shaaban, 2019)

2.3.1.1.1 Single-wall carbon nanotubes

Makar, Margeson and Luh (2005) pioneered the study of cementitious materials for SWCNTs. In their study, the SEM results demonstrate the CNT presence between the cement composites cracks, showing the structural features of crack bridging and fibre pull-out (Figure 2.5). Furthermore, the SWCNTs cement-based composite has higher microhardness at the microscopic level compared to the control cement matrix, the hardness testing shows that SWCNT accelerates the early hydration process of cement. These results showed that a strong bond was formed between the cement pastes and CNTs.

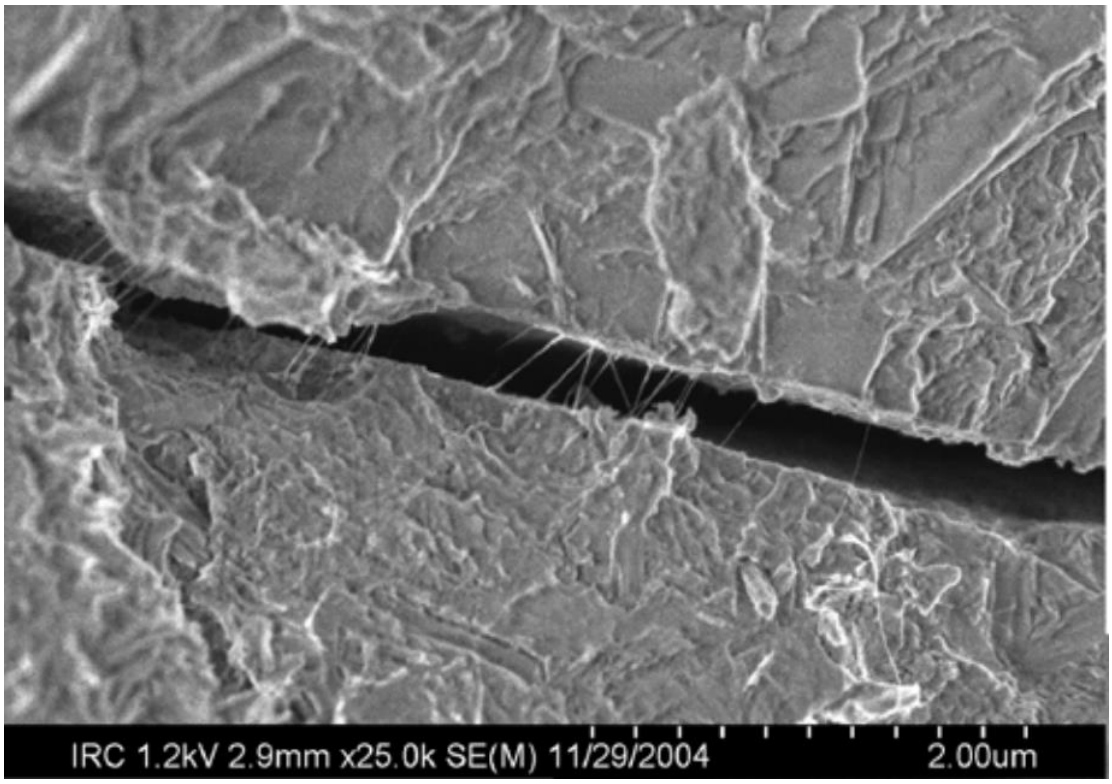

Figure 2.5 CNT bridging across the crack (J M Makar, Margeson and Luh, 2005)

As a material modification, the addition of SWCNTs to the cement matrix can effectively improve their mechanical properties. Compared with SWCNTs, MWCNTs have advantages of mechanical properties, chemically resistance, cheaper and easier to produce in large scale (Saifuddin, Raziah and Junizah, 2013; Eatemadi *et al.*, 2014; Norizan *et al.*, 2020).

2.3.1.1.2 Multi-wall carbon nanotubes

Li, Wang and Zhao (2005) studied the mechanical properties of MWCNT modified cement-based composites treated with H_2SO_4 and HNO_3 solutions. The results showed that the acid and alkaline treated MWCNTs significantly improved the flexural strength, compressive strength and failure strain of the cement matrix composites. Compared with the control group, the material's compressive strength, flexural strength, and failure strain increased by 19%, 25% and 23%, respectively. This phenomenon proves

that the surface-modified nanotubes improve the bond strength of cement hydrate interfacial interactions (e.g. C-S-H and calcium hydroxide).

Luo, Duan and Li (2009) studied that dissolution/dispersion of MWCNTs in aqueous solutions and cement matrix can be enhanced through surface active agents (SAAs) . The SSAs reduces the MWCNTs surface tension and increase its spreading. The results show that by incorporating suitable surfactants and applying ultrasonic dispersion, the uniform and stable distribution of MWCNTs can improve the flexural and compressive strength of the cement matrix by 29.1% and 20.8%, respectively.

Konsta-Gdoutos, Metaxa and Shah (2010) further investigated the dispersibility of the MWCNTs on cementitious materials. Experiments were carried out with commercially available surfactants combined with ultrasonic energy to optimise the dispersion of MWCNTs. The results indicate that proper dispersion of CNT requires ultrasonic energy application. With the optimum weight ratio of surfactant to MWCNTs, short carbon nanotubes show better dispersity than long carbon nanotubes. The highly dispersed MWCNTs cementitious composites generate a higher amount of C-S-H and reduce the nanopores. When short nanotubes are added at 0.08-wt% of cement, the flexural strength of the cementitious composites (w/c=0.5) is increased by 40% and the Young's modulus by 35%.

Chaipanich *et al.* (2010) investigated the impact of adding CNTs at 0.5-wt% and 1.0-wt% of cement, in fly ash cementitious composite. The results show that there was good interaction between the carbon nanotubes and fly ash cement-based composite as shown in the SEM image in Figure 2.6. On the microscopic scale, CNTs fill the pores of the hydration products of calcium alumina and C-S-H gels, increasing the density of the cement-based mixture.

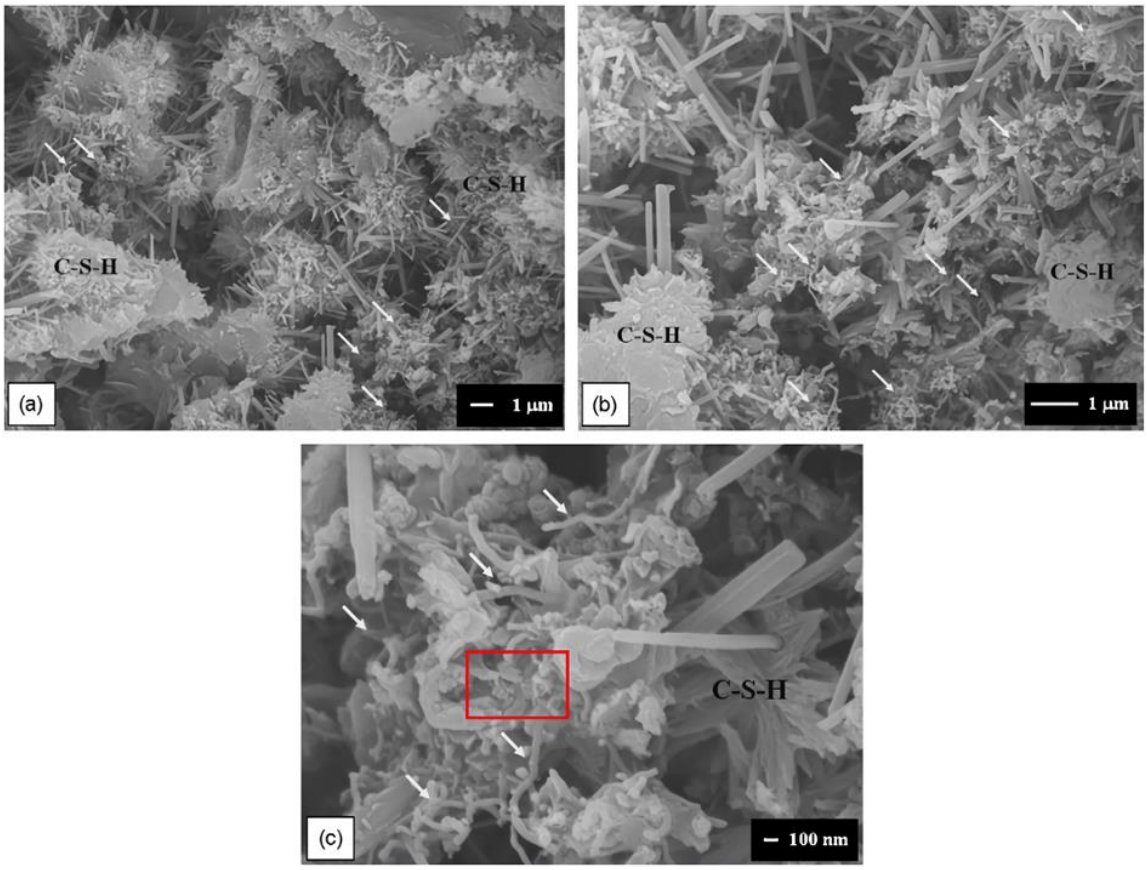

Figure 2.6 SEM images of carbon nanotubes filling with fly ash cementitious hydration products (a) 5000×, (b) 10,000× and (c)30,000× (Chaipanich *et al.*, 2010)

Abu Al-Rub, Ashour and Tyson (2012) studied the effect of the aspect ratio of MWCNTs reinforcements on cementitious nanocomposites at different concentrations. The mechanical properties of MWCNTs were investigated at different ages on cement bases at different concentrations of additions, with length-to-diameter ratios of 1250-3750 and 157. The experimental results show that the dispersity of short MWCNTs is relatively good, with a 269% increase in flexural strength and an 81% increase in ductility for the 0.2-wt% additive cement-based samples at 28 days. When MWCNT is embedded in bridging cement microcracks its pull-out properties limit the propagation of microcracks in the mixtures (Figure 2.7). However, as shown in Figure 2.8, the uniform distribution of MWCNT is not guaranteed. The dispersion technology in the

cement matrix needs to be further improved to more effectively utilise the long microcrystalline nanotubes in the cement composite.

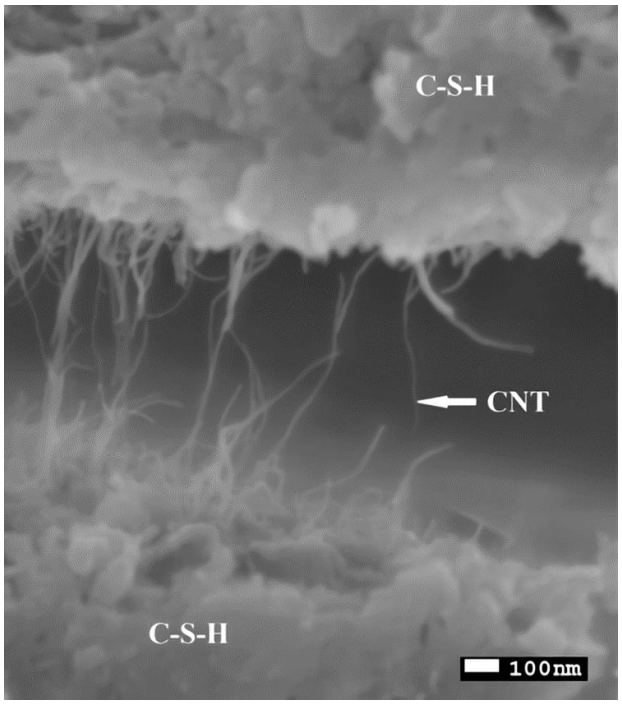

Figure 2.7 SEM showing MWCNTs bridging microcrack within cement pastes composites (Abu Al-Rub, Ashour and Tyson, 2012)

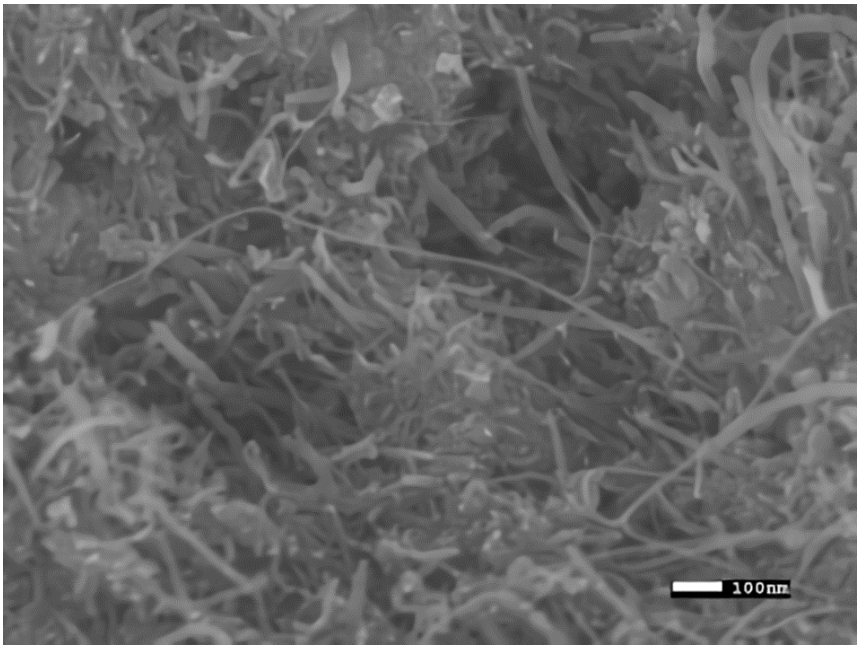

Figure 2.8 SEM showing MWCNT agglomerated within cement pastes (Abu Al-Rub, Ashour and Tyson, 2012)

Isfahani, Li and Redaelli (2016) investigated the dispersion degree of CNTs in aqueous suspensions and mortars, characterised by the different CNT concentrations and sonication time. UV-Vis spectroscopy results show that the dispersion of functionalized-CNT suspensions gradually increases with the increase of sonication time up to 120 min, and the dispersion of pristine-CNT reaches its maximum at 60 min. Furthermore, Balasubramaniam, Mondal, Ramasamy, Gadyam S Palani, *et al.* (2017) investigated the effect of a small amount of MWCNTs additives on the mechanical strength of cement composites. This research examined that the availability of CNTs was significantly reduced from 0.5% to 0.025% based on the weight of cement, while ensuring the cohesion between the optimised cement hydrate matrix and CNTs treated with ultrasonication. The low amount of CNTs effectively strengthened the mortar interface, which results in the compressive and split strength increased by 77% and 17%, respectively.

Recently, Hassan, Elkady and Shaaban (2019) investigated the effect of CNTs reinforced concrete on mechanical strength and corrosion resistance. Research showed that the CNTs added to the concrete mix act as a bridge to the microcracks, improving mechanical properties. However, the CNT additives led to increased corrosion rates of reinforcing steel in the low-risk range, and the CNTs utilisation led to dispersion and health hazards. The better mechanical strength of cementitious can be achieved among other additives, by adding chemical admixtures such as superplasticisers, cement replacement materials (e.g. silica fume) and steel fibres.

In summary, the higher intensity and unique structural characteristics of CNT additives in cementitious materials significantly reinforces their ductility, Young's modulus, and flexural strength. The CNTs accelerate the hydration process through the nucleation effect and significantly improve its durability. However, the application of CNT in

cementitious has several disadvantages, the agglomeration of CNTs adversely affects the flow properties of the fresh pastes, causing stress concentration, and restricting the development of the mechanical strength of cementitious. The inhomogeneous microstructures require more appropriate dispersion methods, the surfactants and sonication are commonly used methods. In addition, the limitation of CNT crack bridging cannot guarantee the stable continuous CNT network to fill the adjacent C-S-H.

2.3.1.2 Nano-silica (NS)

The diameter of NS particles is between 1 nm and 100 nm, SEM and TEM images are shown in Figure 2.9 (B.-W. Jo *et al.*, 2007) and Figure 2.10 (Ma *et al.*, 2019). Due to the NS pozzolanic reaction and pore-filling properties, the NS is a widely used nanomaterial in strengthening the performance of cementitious composites (Han *et al.*, 2017).

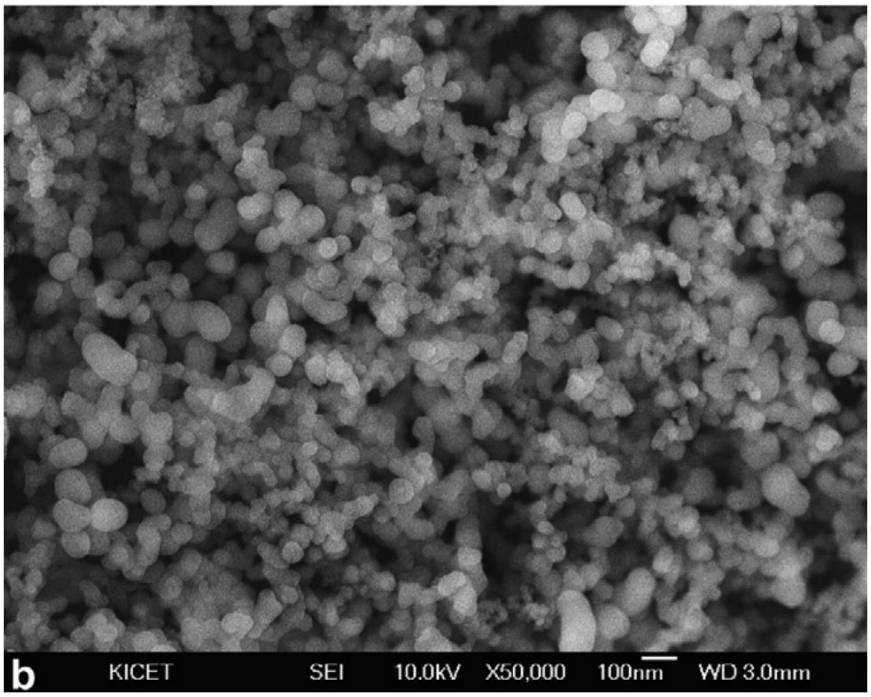

Figure 2.9 The scanning electron microscope image of nano-silica (B.-W. Jo *et al.*, 2007)

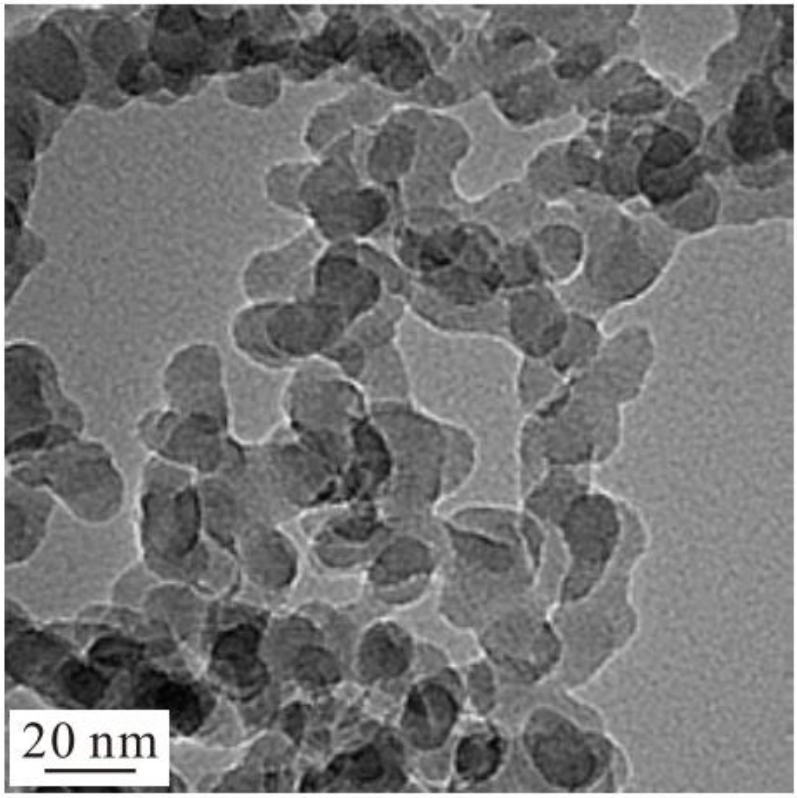

Figure 2.10 TEM image of nano-silica (Ma *et al.*, 2019)

2.3.1.2.1 Ordinary portland cement

Li *et al.* (2004) investigated the mechanical properties and microstructure of nano-SiO_2 cement mortar in the initial research. It was found that after the addition of NS, the compressive and flexural properties of the cement mortar were improved 26% and 27% at 28 days. SEM observed the SiO_2 nanoparticles were homogeneously dispersed in the mortar. NS can not only fill the pores, but also act as an activator to promote hydration. The addition of SiO_2 improves the microstructure of the cement pastes and reduces the $Ca(OH)_2$ compounds hydrate formation. The improvement mechanism of the microstructure explains the increase in the highest mechanical properties of cement mortar (Li *et al.*, 2004).

Jo *et al.* (2007) further investigated the performance of NS mortar, and confirmed that the 7 days and 28 days strength of the mortars were significantly improved after the NS was incorporated. Amorphous or glassy silica is the main component of pozzolan,

which can react with calcium hydroxide formed by the hydration of calcium silicate. The reaction rate of pozzolanic is proportional to the surface area available for reaction.

Haruehansapong, Pulngern and Chucheepsakul (2014) investigated the effect of different particle sizes of NS on the compressive strength of cement mortars. The research approved the particle size of NS does not affect the optimal NS substitution content. However, SiO_2 nanoparticles with a larger diameter (above 40nm) have greater dispersity than 12 and 20 nm, which results in better reinforcement of the compressive strength of the mortar. The ineffective dispersion and agglomeration of extremely small NS particles will affect the mechanical properties of cement mortar.

A study conducted by Ma and Zhu (2017) found that an increase in NS content (range of 0 to 1.8%) leads to a gradual increase in the quality of hydrated calcium silicate gels (C-S-H) and ettringite crystals (alumina, ferric oxide, tri- sulphate (AFt)). As shown in Figure 2.11, the addition of NS is 1.2 -wt% of cement, which results in the well compacted cementitious matrix. The presence of C-S-H gel and AFt crystals shows the optimal amount (1.2 -wt%), which is consistent with the improvement in the compressive strength and splitting tensile strength results by 9.04 and 17.42%, respectively.

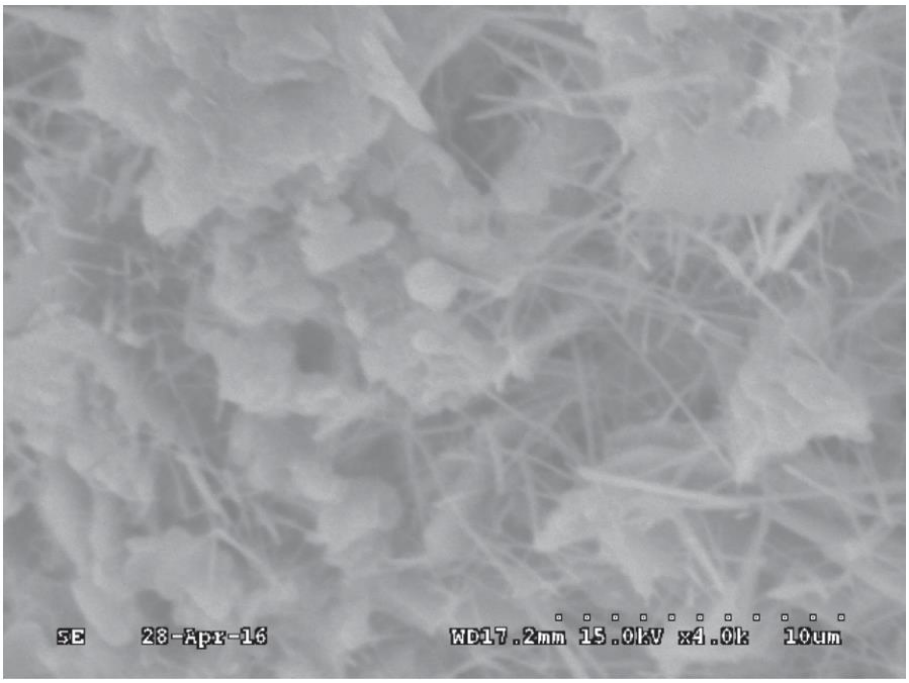

Figure 2.11 SEM images of cementitious matrix with 1.2-wt% Nano-SiO_2 (Ma and Zhu, 2017)

2.3.1.2.2 Ultrafine cement

Kontoleontos *et al.*(2012) studied the influence of colloidal nanosilica on ultrafine cement. The results show that NS lightly increases the strength of ultrafine crystals in the early hydration stages due to the packing effect. In the later stages of hydration, there is a compressive strength increase as the NS evolution promotes the hydration of Portland cement reaction consumption $Ca(OH)_2$. The mercury intrusion porosimetry shows the NS derives from the porosity and pore size distribution of the hardened cement pastes. NS promoting the densification of the internal structure of cement hydration, increased the chain length of silicate and modified the C-S-H gels internal structure. Najigivi, Khaloo and Rashid (2013) also found that nano-SiO_2 as an efficient pozzolanic material can promote concrete hardening and enhance mechanical properties. Studies have found that nano-SiO_2 can reduce the size and quantity of the $Ca(OH)_2$ crystals. The SEM image confirmed that nano-SiO_2 fills the nano-pores in the

C-S-H gel structure, acting as a core to tightly bond with the reinforced gel particles. This process makes the interface transition zone (ITZ) more compact between the aggregate and the bonding pastes matrix.

2.3.1.2.3 Fly ash cement

Ma *et al.* (2019) investigated the response of NS to the high hydration capacity and microstructural development of fly ash cement. Studies have shown that NS in cement systems accelerates the early hydration process and reduces the calcium hydroxide (CH) content from 14.17% to 12.04%. NS also increases the C-S-H polymerization, increasing the early strength of concrete. The addition of NS reduces the Ca/Si ratio and contributes to the enrichment of CH in the interfacial transition zone (ITZ), which is the key to enriching the mortar ITZ (Ma *et al.*, 2019).

In summary, the addition of NS to the cementitious material significantly fills the pores and increases the density of the microstructure, resulting in smaller porosity and higher strength and durability. NS as a nucleation site reacts with cement pastes through volcanic ash, the initial calcium hydroxide formation can effectively accelerate cement hydration. However, NS has a tendency to agglomerate in cementitious composites even if various dispersion agents exist. Also, the cost of NS is relatively high and its use has a serious impact on environmental pollution and the health of operators.

2.3.2 Two-dimensional (2D) graphene nanomaterials

2D materials have reduced the thickness of the materials to a single layer of atoms. Hence, 2D materials are also known as single-layer crystalline materials. The monolayer material has only covalent bonds, but can strongly hold the layers of atoms together in 2D materials. Compared to 1D materials, 2D materials eliminate van der Waals interactions. Simultaneously, the properties of 2D nanosheets are very different

from those of three-dimensional materials, and the fluidity of 2D materials is restricted to two dimensions (Mathesh et al., 2015).

In terms of the 2D nanomaterials structure, 2D nanosheets increase the surface area to volume ratio, resulting in more reactants with the material and usually faster reaction rates in contact. The 2D material atoms are exposed on the surface, resulting in a more reactive material than bulk materials, making 2D materials more sensitive to their surroundings (Mathesh et al., 2015). In the case of graphene manufactured from graphite, the graphene 2D form is light and transparent to prevent the passage of liquids (allow water), vapours and gases (helium atoms) (Nair et al., 2012), and has excellent electrical conductivity (Balandin *et al.*, 2008) and strength higher than steel (Lee *et al.*, 2008). The discovery of 2D material nanosheets provides an additional dimension to the interaction of cement and concrete. This section will focus on the 2D material graphene and graphene oxides, their material properties and the impact on cementitious composites.

2.3.2.1 Graphene (G)

In 2004, British physicists Geim and Novoselov discovered a 2D carbon-based material graphene, which could exist alone and is obtained by mechanical exfoliation from bulk graphite (Novoselov et al., 2004). Graphene is a flat monolayer of carbon atoms connected by sp^2 covalent bonds, Figure 2.12 demonstrate the chemical structure of graphene, the basic structural unit of MWCNT (Pereira, Neto and Peres, 2009; Iwan and Chuchmała, 2012; Vinayan, 2016). The Graphene tensile strength (130 GPa) and Young's modulus (1.0TPa) (Lee *et al.*, 2008), high surface area (2630 m^2/g) (Stoller *et al.*, 2008), superior thermal conductivity (5000 W/mK) (Balandin *et al.*, 2008) and excellent electrical conductor (electron mobility excess of 200,000 $cm^2V^{-1}s^{-1}$) (Bolotin *et al.*, 2008) show the many excellent performances and outstanding properties of

graphene-based materials which have triggered a wave of theoretical and applied research, among which hundreds of related studies have appeared (Zhu *et al.*, 2010; Mounet *et al.*, 2018).

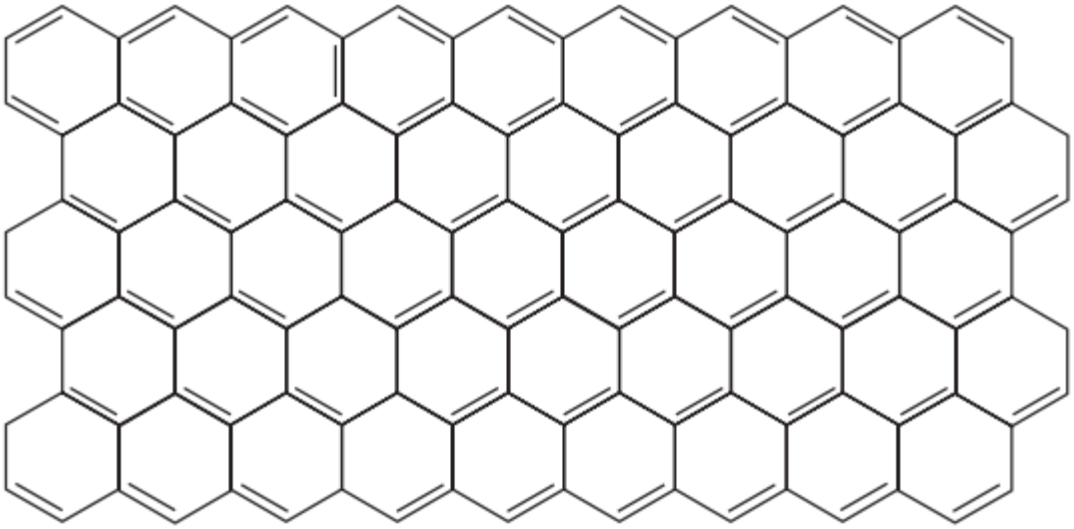

Figure 2.12 A schematic representation of graphene chemical structure (Iwan and Chuchmała, 2012)

Wang, Jiang and Wu (2016) investigated the effect of graphene nanoplatelets (GNPs) on the physical behaviour of cement pastes. The experiment used methylcellulose (MC) as a dispersant to uniformly disperse GNPs in an aqueous solution by ultrasonic method. The results showed that the optimum concentration ratio of GNPs to MC is 1:7. The flexural strength and compressive strength of cement pastes with 0.05-wt% GNPs are increased by 15% to 24% and 3% to 8%. This is because GNPs raise the DOH and promote the hydration products. As shown in Figure 2.13, the zigzag morphology and behaviour of uniformly distributed GNPs hinder fracture development, reduce porosity and maintain the integrity of the matrix.

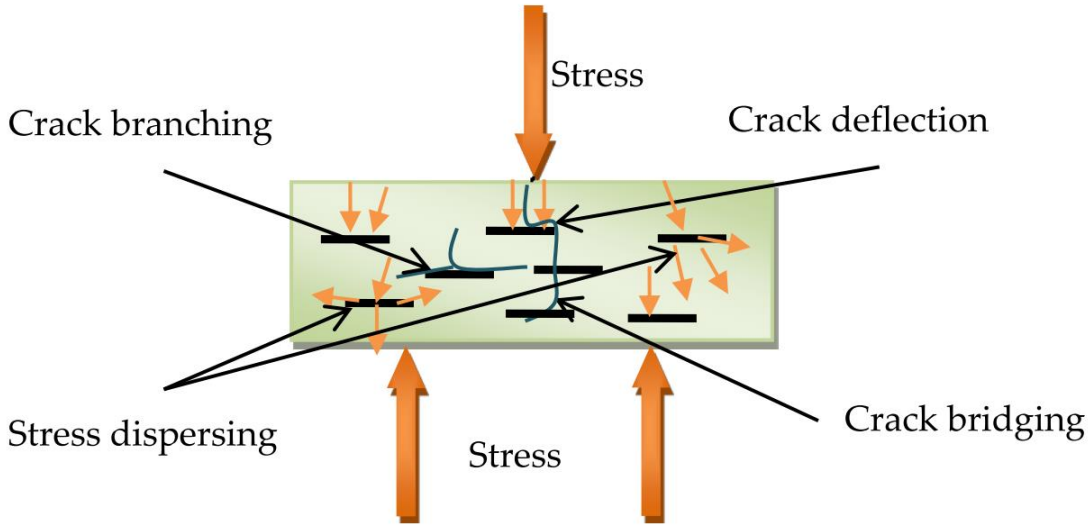

Figure 2.13 Scheme of GNPs-cement composite under bending load (Wang, Jiang and Wu, 2016)

Jing *et al.*(2017) researched the dry mechanical dispersion of graphene effect on the hydration behaviour of cement composites. The dried GNPs were uniformly dispersed, and mixed into dried OPC for 72 h, and the hydration test was performed. The results showed that after cement and graphene were mixed, it was no significant change in the process and DOH reaction, and the content of non-evaporable water and calcium hydroxide did not change significantly. This is because the homogeneous dispersion of dry-dispersed graphene in cement pastes only displays the mechanical effect, which can be corroborated by the effect of high specific surface area (SSA) GNPs on flowability. The agglomerated graphene locks the water within the flocculation and impedes the flow of the cement composite. The flowability of the 0.2 and 0.4-wt% GNPs cement pastes were reduced by 17.4% and 39.1% compared to the control cement.

Du and Dai Pang (2018) investigated the optimal dispersion of GNPs in cement pastes based on the amount of dispersant dosage and sonication time. The experimental results show that sonication and the addition of a polycarboxylate-based superplasticiser can

effectively stabilize the GNPs suspension. The 1% of GNPs suspensions with 15% surfactant are sufficient to maintain stability for 6 hours under one hour of sonication. The stable 1% GNP admixtures double the hardness of the cement pastes. The mercury intrusion testing results reveal that GNPs reduce the cement pastes effective porosity and critical pore diameter by 37% and 30%, respectively.

Baomin and Shuang (2019) conducted experiments on the mechanical properties and hydration reaction of GNPs modified cement composites. The graphene was treated with a dispersant and ultrasonication. The experimental results show that the optimal mechanical properties of the cement composites are at 0.06-wt% addition of GNPs. After curing for 3 days, 7 days and 28 days, the compressive and flexural strengths of 0.06-wt% GNPs samples were amplified by 6.9%, 8.7%, 11.0% and 28.0%, 30.6% and 27.8%, respectively. However, when the graphene concentration exceeds the threshold of 0.06-wt%, there is a low enhancement trend in the graphene cement composite compressive and flexural strength. The phase analysis from the XRD spectrum showed that the mineral constituents C3S and C3A were rapidly consumed in the graphene cement composites. GNPs contribute to more cement hydration production. The hydration reaction of GNP on cement composites schematic is shown in Figure 2.14. Sodium dodecylbenzene sulfonate (SDBS) is an anionic surfactant, and the hydrophilic group of SDBS can be adsorbed on the GNP surface to facilitate the hydration of the cement particles. The strong adsorption capacity and large SSA of GNPs accelerate the migration speed of calcium ions, resulting in an equilibrium concentration gradient of calcium ions. GNPs provide more space for ion transportation on the cement particle surface and promote the early nucleation effect, so that the ion exchange fully accelerates the DOH and promote C-S-H and Aft produces (Baomin and Shuang, 2019).

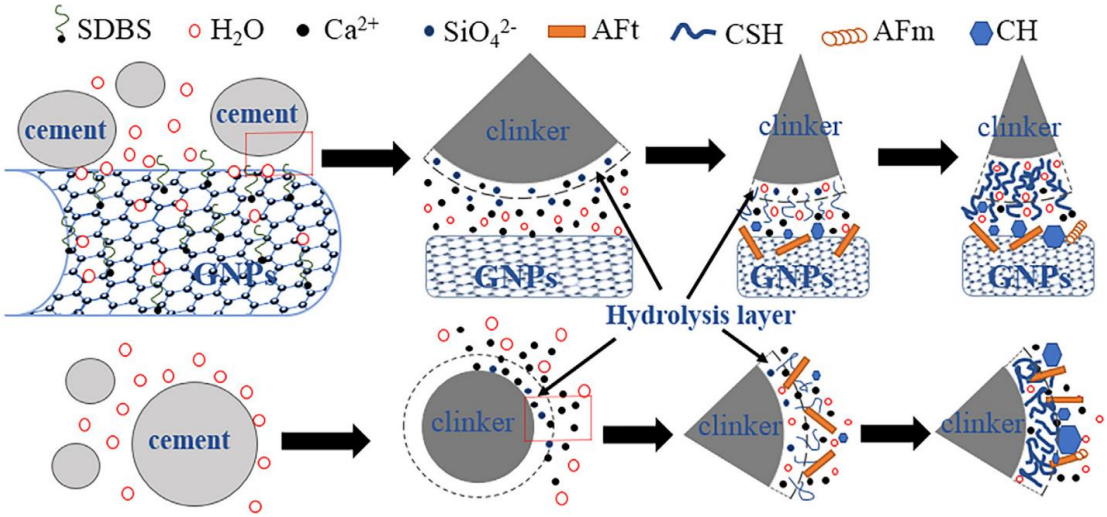

Figure 2.14 The schematic of GNPs influence on hydration reaction in GNPs/cement composites (Baomin and Shuang, 2019)

In summary, graphene makes significant improvements in modifying the mechanical properties and the hydration process of cement composites. The graphene-reinforced cementitious composite mechanism includes the nano-additive effect, which makes the cement matrix more compactable and denser. Graphene, with a large SSA, promotes the cement hydration reaction, the graphene nucleation effect facilitates the C-S-H production. Furthermore, the graphene bridging provides effectively prevents the formation and propagation of micro-cracks in cementitious composites. Despite a combination of surfactants, the combination of mechanical stirring and sonication have been proven to achieve uniform dispersion of graphene in water. However, the graphene sheets have strong van der Waals force and hydrophobicity and that together with the lack of appropriate dispersion techniques in cement pastes. Graphene cementitious composites can lead to poor dispersion and uneven distribution, thereby limiting the degree of reaction, and causing defects in the early stage. The dispersibility and stability of graphene solutions are the main issues limitations for widespread use in the construction industry.

2.3.2.2 Graphene oxide (GO)

GO is one of the most attractive and widely recognized graphene-based nanomaterials in cement composites. Figure 2.15 shows the schematic chemical oxidation from graphene to GO (S. Lv *et al.*, 2013). GO is composed of a single bonded layer of carbon atoms in the honeycomb lattice. The chemical structure of GO is shown in Figure 2.16 (Iwan and Chuchmała, 2012). The GO lattice structure is based on graphene, with the introduction of the chemicals oxygen-containing epoxy group (C-O-C), hydroxyl group (-OH) and carboxyl group (-COOH) at the edges. The presence of hydrophilic groups allow the surface of GO to have high dispersion in water, and further provides a large number of active sites for linking other functional groups and organic molecules. Different types of graphene derivatives are developed as nano-additives in cementitious materials. As shown in Figure 2.17 (M M Mokhtar *et al.*, 2017), the TEM of GO with ultra-high strength and high SSA can be used to bridge cementitious surfaces (Rafiee *et al.*, 2013).

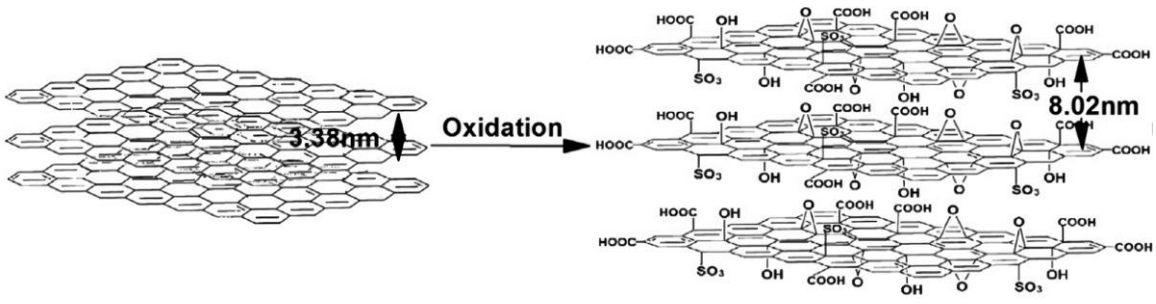

Figure 2.15 Sketch map of GO nanosheets preparation (S. Lv *et al.*, 2013)

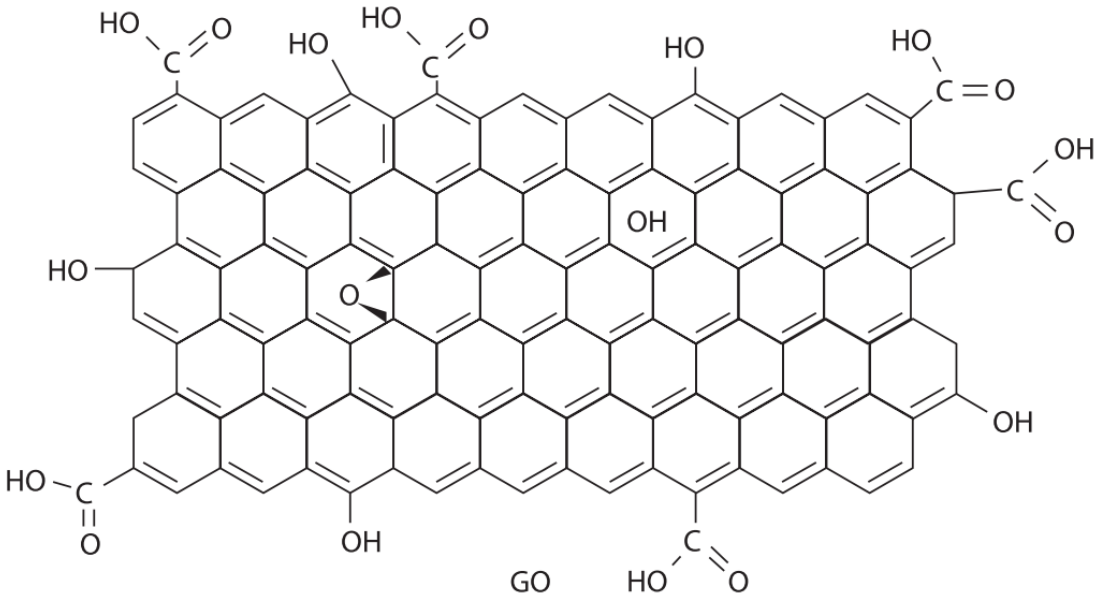

Figure 2.16 The schematic representation of graphene oxide (Iwan and Chuchmała, 2012)

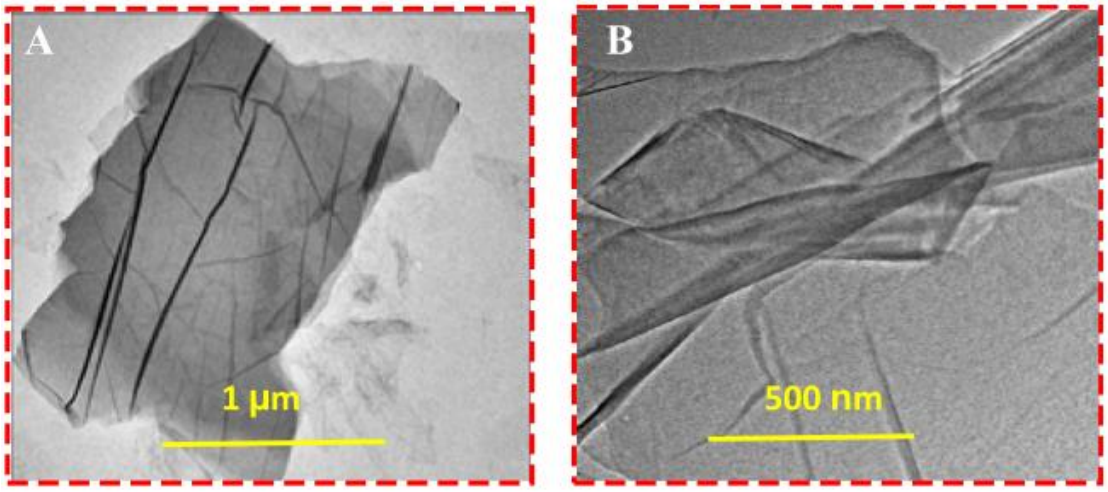

Figure 2.17 The TEM of GO (M M Mokhtar *et al.*, 2017)

Lv *et al.*(2013) investigated the GO nanosheets effect of microstructure and mechanical properties in cementitious pastes. The results show that GO significantly improves the mechanical properties of cementitious materials. Compared to the control group the tensile strength of cement composites with 0.03% GO increased by 78.6%, flexural strength increased by 60.7% and compressive strength increased by 38.9%. SEM observations revealed that GO was effective in modulating the microstructure of the

hydration products, thereby reducing the brittleness of the cement. GO contributes to controlling the growth points and growth patterns through template effect, forming flower-like crystals. The regulation mechanism of GO on cementitious hydration products is shown in Figure 2.18, the functional groups on the GO surface promote the hydration crystals form.

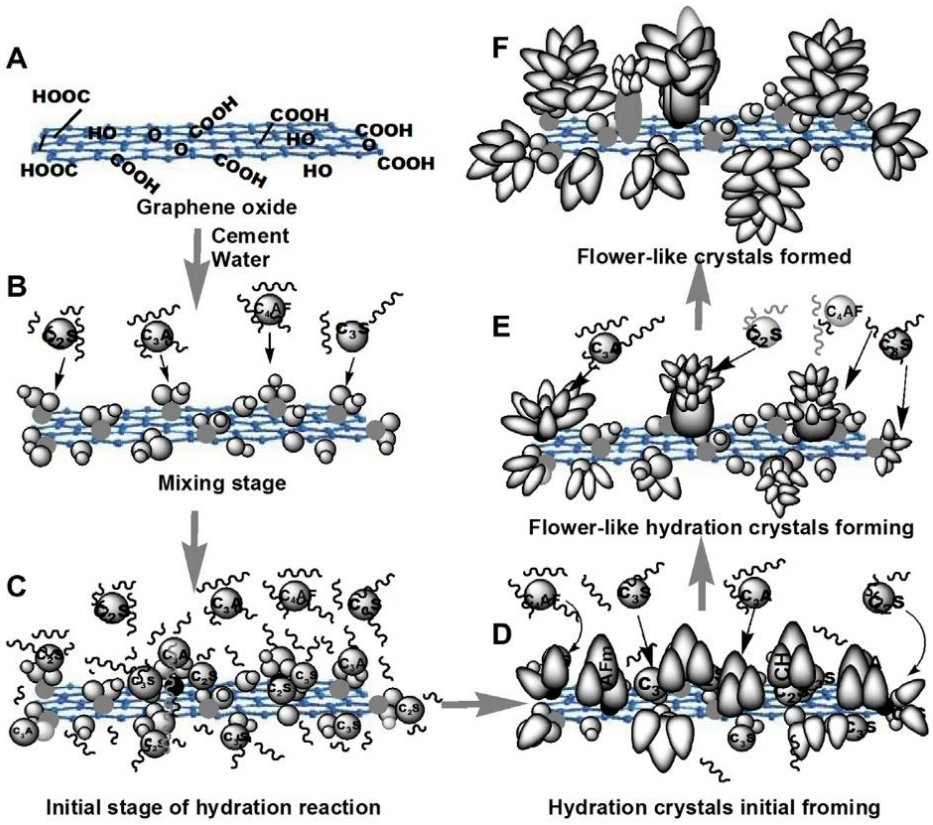

Figure 2.18 Schematic diagram of GO regulation mechanism on cement hydration crystals (S. Lv *et al.*, 2013)

Pan *et al.*(2015)'s research examines how the mechanical properties of graphene oxide reinforce OPC. Results show that the addition of 0.05-wt% GO increased the compressive strength and flexural strength of cement-based composites by 15-33% and 41%-59%, respectively. GO cement composites show a broader stress-strain curve in the post-peak region, which reduces the suddenness of failure. Due to the high surface area of GO in the cement matrix, the production of calcium silicate hydrate is increased,

effectively impeding crack propagation. However, the GO mixed with cement pastes leads to a significant reduction in workability. In the case of poor dispersion, it can seriously affect the performance improvement of the cementitious composites.

The oxidation of graphene produces the 2D material graphene oxide nanosheets (GONPs). Mokhtar et al. (2017) investigated the application of GONPs in cement-based nanocomposites. The results show that the cement matrix addition of 0.02% GONPs increased 13% compressive strength, and the addition of 0.03% GONPs resulted in a 41% increase in indirect tensile strength. The small proportion of GONPs additives significantly reduced the pore size of the cement matrix and improved its microstructure, thus strengthen the mechanical properties of these cementitious composites.

Chen *et al.* (2018) investigated the mechanical properties of multilayer GO carbon fibre-cement composites. The experimental results showed that the compressive strength of the composite material with 1% GO cement is increased by 46.90%, while the flexural tensile strength of the composite is increased by 43.59%. As shown in Figure 2.19, the carboxylic acid functional group in GO reacts with hydration products, such as C-S-H or $Ca(OH)_2$ in the cement pastes. Strong covalent bonds are created at the GO-cement interface, resulting in solid interfacial adhesion between GO and cement. The GO sheets improve the load transfer efficiency, which results in an improvement in the mechanical behaviour of GO cement composites.

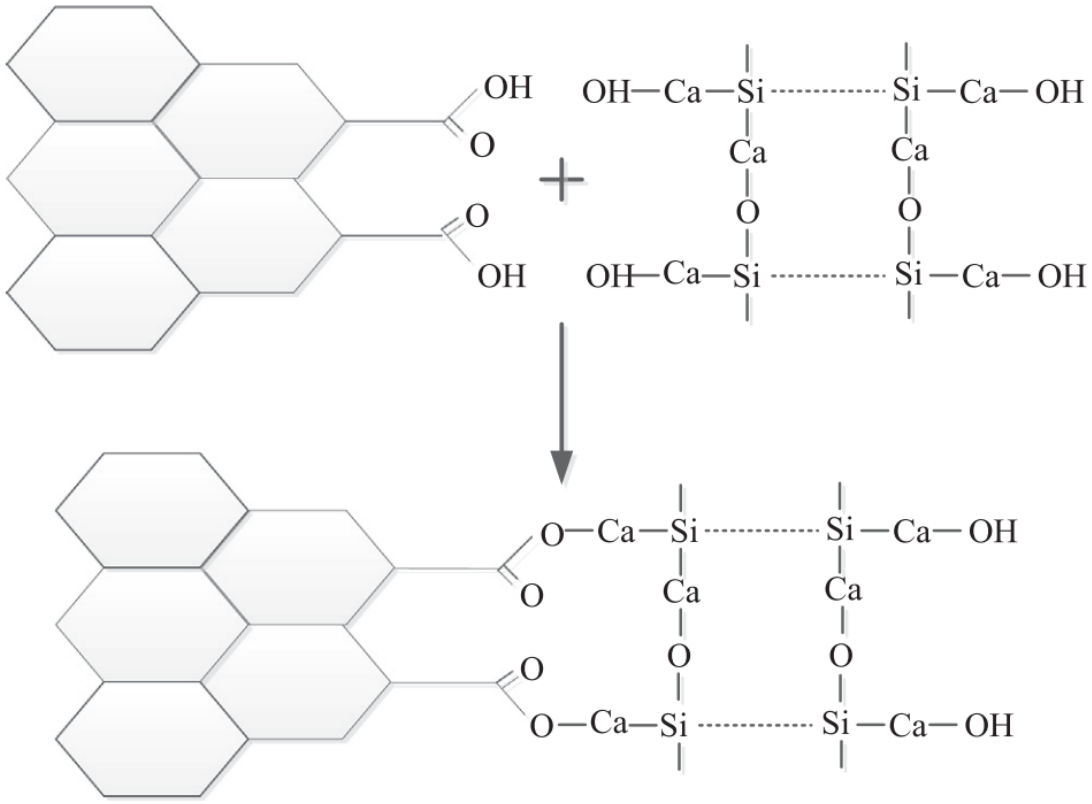

Figure 2.19 The reaction between the GO and hydration productions (Z. Chen *et al.*, 2018)

In summary, the application of 2D nanomaterial GO reinforces the find that cement composites have many advantages. GO has superior dispersibility and high activity in the water, the nucleation effect provides attachment points for C-S-H gel to accelerate the hydration of cement. The improvement of hydration benefits the mechanical properties of cementitious composites, and significantly increases the tensile/flexural strength of cement composites. In addition, GO has the nano-filler effect, bridging effect and bonding effect. GO adjusts the growth and morphology of the hydration phase, pore volume distribution, bridging microcracks, and improves the stiffness and crack resistance of the cementitious matrix. However, GO also has many limitations, such as the high cost of GO, health risks and the agglomeration problem, which prevent its application in large-scale industries.

2.3.3 Nanocelluloses (NCs)

Compared to expensive nanomaterials, cellulose is the most abundant and widely distributed polysaccharide in nature (Crawford, 1981). Cellulose has the advantages of biodegradability, low price, zero carbon footprint, high dispersibility and no apparent hazards (Ardanuy, Claramunt and Toledo Filho, 2015). NCs refer to nanostructured cellulose, which is a bio-based nanostructured product. NCs can be obtained from various cellulose sources such as hardwoods, softwoods, industrial lignocellulosic waste, farm processed fruit and vegetable residues in biorefineries (Chirayil, Mathew and Thomas, 2014; Jonoobi *et al.*, 2015). The diversity of cellulose treatment methods results in NCs including the cellulose nanocrystals (CNCs), cellulose nanofibre (CNF) and bacterial nanocellulose (BC). NCs show several advantages over ordinary cellulose, including higher surface area, excellent stiffness, lighter weight, higher strength and stronger interaction with other materials (water or inorganic and polymeric compounds) (Abitbol *et al.*, 2016; Mondal, 2017). NCs derivatives are utilised in various production and performance applications due to their cellulose properties and nanomaterial characteristics (Klemm *et al.*, 2018).

Fibre incorporation is one of the most effective ways to reduce the brittleness of cementitious materials and improve their toughness. Randomly oriented fibres in cement can prevent the formation and propagation of cracks, improve strength and ductility (Wafa, 1990). Fibre reinforcement materials can be steel, stainless steel, polymers, mineral materials, synthetic fibres and natural fibres. Different properties and sizes (macro and micro) of fibres are used in a wide range of cementitious applications to improve performance (Bentur and Mindess, 2006). Previous research has shown that the addition of cellulose to cementitious composites can improve the bonding capacity, flexural toughness, ductility, bending resistance and impact

resistance (Yao, Li and Wu, 2003; Bencardino *et al.*, 2010; Ardanuy, Claramunt and Toledo Filho, 2015; Balea, Blanco and Negro, 2019).

2.3.3.1 Cellulose nanocrystals (CNCs)

Cellulose microfibres have amorphous regions and crystalline regions. As shown in Figure 2.20, cellulose microfibres are chemically extracted by acid hydrolysis. After removing the amorphous regions the remaining crystalline regions are called CNCs (Moon et al., 2011). The CNC is a highly crystalline, renewable and biodegradable green material extracted from wood and plant materials. CNC has relatively low density (1.6 g/cm^3), high modulus of elasticity (145 GPa) and high tensile strength (7.5 GPa) (Moon *et al.*, 2011; Brinchi *et al.*, 2013). Figure 2.21 shows the TEM images of the CNCs. From the TEM photographs, the estimated average diameter of the needle-like CNC is 6-8 nm, with a length of approximately 150-250 nm (Habibi, A.-L. Goffin, et al., 2008).

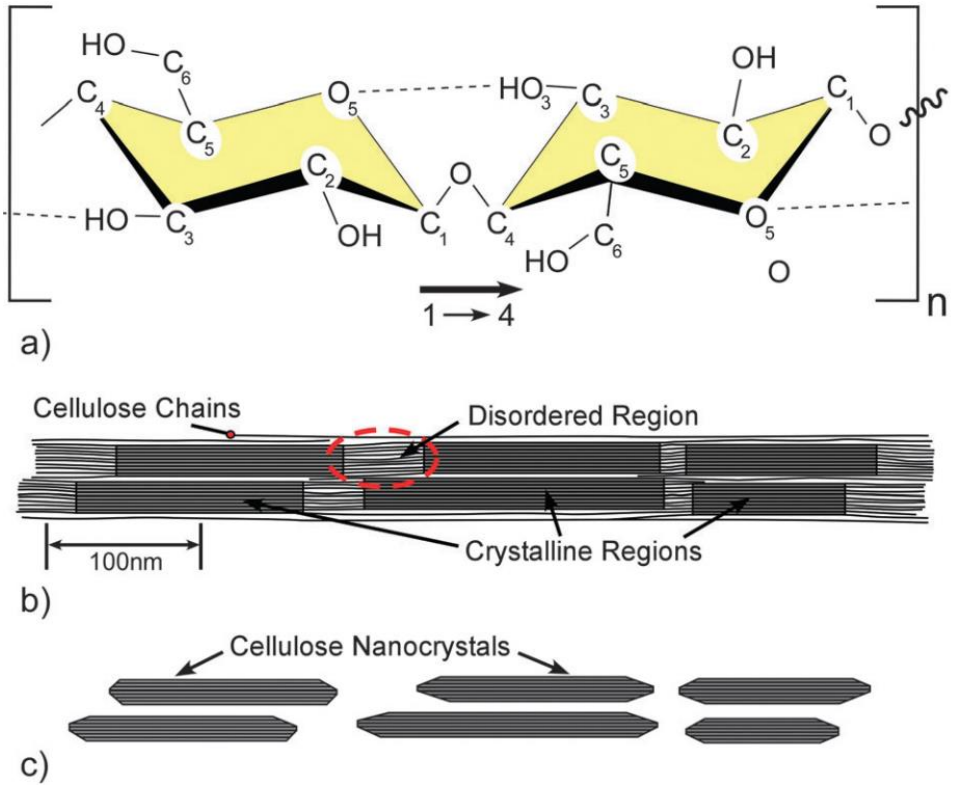

Figure 2.20 The repeating unit of schematics of (a) single cellulose chain of the 1 - 4 linkage and hydrogen bonds in the chain, (b) the idealized cellulose microfibril suggestion in one configuration, (c) CNCs treated with acid (Moon *et al.*, 2011)

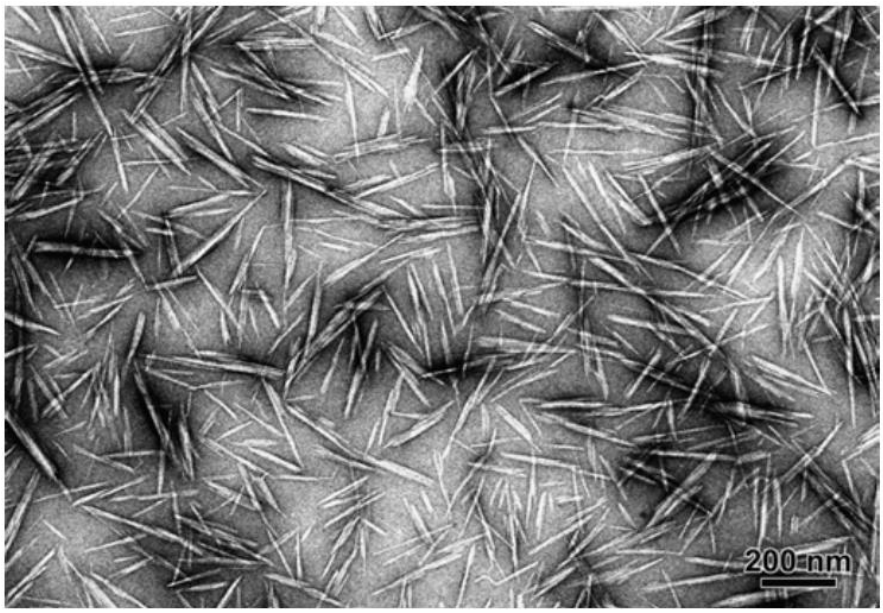

Figure 2.21 The TEM image of CNCs (Habibi, A. L. Goffin, *et al.*, 2008)

Mazlan *et al.* (2016) investigated the effect of CNCs on the compressive strength, density and ultrasonic pulse velocity of cement mortar. The experimental results show that the CNCs addition effectively forms calcium silica hydrate (C-S-H) gels and improves the compressive strength of the mortar. The compressive strength of CNCs mortar at a concentration of 0.2% is increased by 42-45% compared to the control group. The CNCs contain numerous nano-needle fibres enabling it to play a bridging role, making the mortar matrix denser and allowing the mortar structure to withstand the additional loads and increase the UPV value.

Cao *et al.* (2015) researched the influence of CNCs on the performance of cementitious pastes. The mechanical test showed that with 0.2% vol added CNCs, the flexural strength increased by 30% compared to the control group. The results of Isothermal calorimetry (IC) and TGA show that the use of CNCs can increase the DOH of cement pastes. The reinforced hydration degree mechanism can be attributed to the steric stabilisation mechanism of the cement particles and the short-circuit diffusion (SCD) mechanism. The steric stabilisation mechanism is similar to the dispersion of cement particles by water reducing agents, and the SCD is due to the nanofiber network having a faster diffusion of water molecules than the matrix. As shown in Figure 2.22, water molecules are transferred to the interior of unhydrated cement, and the thicker hydration product shell (high-density C-S-H) on the cement particles is attributed to CNCs increase in the hydration rate. These two mechanisms support the CNCs to accelerate the formation of C-S-H gels at the fibre-matrix interface.

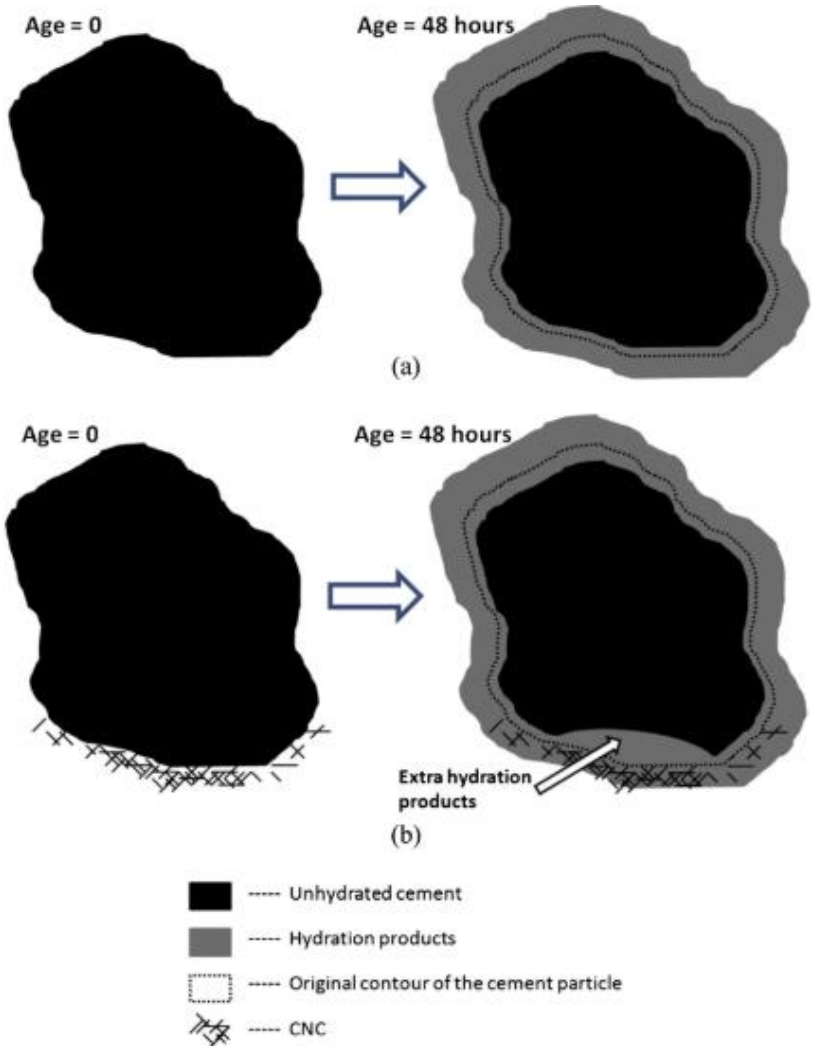

Figure 2.22 Schematics of pseudo-hydration products formed around the cement grains ages from 0 to 2 days (a) ordinary cement and (b) CNCs reinforce cement (Cao *et al.*, 2015)

Subsequently, Cao *et al.* (2016) used ultrasonication to disperse the CNCs in the cement pastes, and investigated the relationship between the agglomeration concentration of CNCs and the hardening strength of the cement pastes. The experimental results show that agglomerates exist when the concentration of CNCs in deionized water exceeds 1.35 vol%. The CNCs placed in pore solutions of cement pastes start to agglomerate at a low concentration (0.18 vol%). The results found that the ultrasonication was effective in dispersing CNCs and with the addition of 0.18% concentration, the flexural

strength was increased by more than 50% in the cement paste. The strengthening effect of dispersed CNCs is better than that of untreated CNCs, along with the 20-30% strength increase. Therefore, the degree of dispersion in CNCs solutions is essential to reinforce the flexural strength of CNCs cementitious composites.

Fu *et al.* (2017) investigated the effects of various material sources and processing techniques on the performance of cement-based CNC systems. The IC, TGA and Ball on three balls (B3B) tests were carried out on nine different CNCs with Type I/II and Type V cement pastes to quantify the effect of CNCs on cementitious composites. The IC and TGA experiment results demonstrate that CNC increases the DOH in all design, with the Type V cement showing a higher total heat release than Type I/II cements. In addition, the I/II and V systems both have been strengthened by up to 20% in flexural strength.

In summary, CNCs has a high SSA and many hydroxyl groups, suitable for various types of surface functionalisation. The advantage of chemical functionalisation is the possibility of introducing different charges from the CNCs material, which ultimately provides better dispersion in any solvent/polymer. The CNCs additive in the cementitious matrix can significantly improve the hydration and bonding rate and increase compressive, flexural strength and fracture properties. However, CNCs has some disadvantages such as low thermal stability and a low crystallization rate. The implementation of CNCs as a cement additive in industrial production can lead to several defects, such as durability, water absorption and thermal stability.

2.3.3.2 Cellulose nanofibres (CNF)

CNF are manufactured from cellulose by mechanical treatment, which is different from the manufacturing process of CNCs obtained by acid hydrolysis. As shown in TEM

Figure 2.23, the CNF dispersion consists of individualized cellulose nanofibres with a 3-4 nm width and a length of a few microns (Saito *et al.*, 2007). CNF are nanocellulose nanomaterials with very high mechanical strength and brittle behaviour. The strength is dependent on specimen size. The average strength of woody CNF ranges from 2 to 6 GPa (Saito *et al.*, 2013). The SSA of cellulose fibres is significantly increased after nanofibrillation (Osong, Norgren and Engstrand, 2016). CNF has a higher hydrogen bonding capacity than cellulose because CNF has more hydroxyl groups, and this specific active surface is more conducive to matrix-CNF interactions in the cementitious matrix (da Costa Correia et al., 2018).

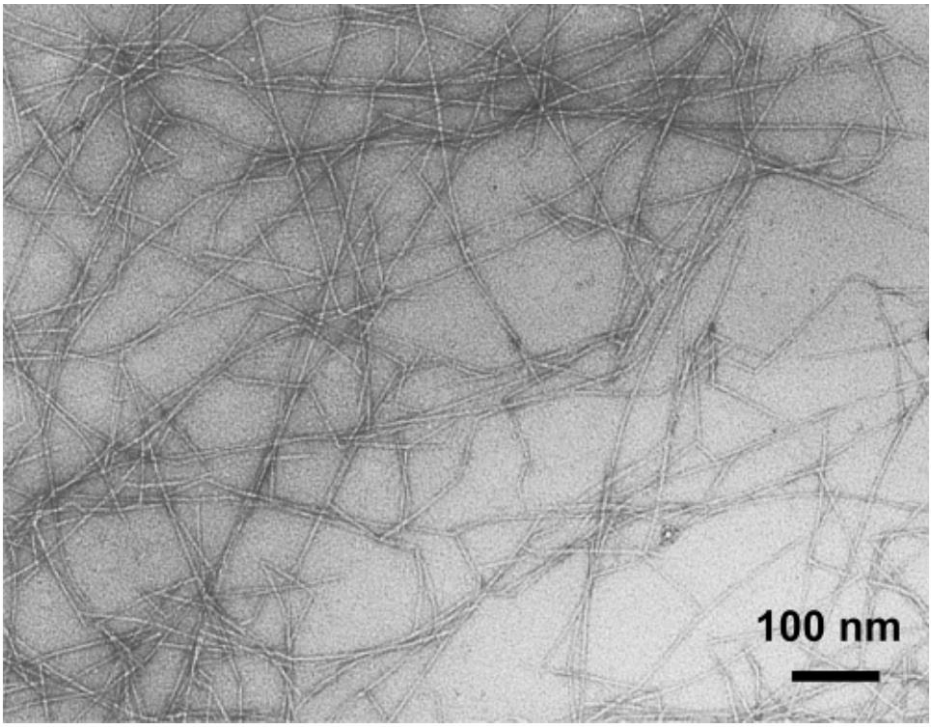

Figure 2.23 TEM of the TEMPO-oxidized cellulose with carboxylate (Saito et al., 2007)

Peters *et al.*(2010) investigated the toughness of reactive powder concrete through a combination of low-cost nano cellulose and micro cellulose fibres. Preliminary results show that the combination of micro and nanofibres with an addition of up to 3%

increases the breaking energy of unreinforced material by more than 50%. However, if the fibre is not positioned at the tip of the crack, this has no effect on preventing the crack initiation.

Onuaguluchi, Panesar and Sain (2014) investigated a relatively low volume fraction of cellulose nanofibers reinforced cement pastes. The results show that the addition of cellulose nanofibers to the mixtures delays the ion diffusion progress of the cement hydration process, which attribute to the viscosity of nanofibre. The delay in cement dissolution only affects early hydration and has no adverse effect on the DOH for 28 days. As the content of nanofibers increases, also does the cumulative heat of hydration and the DOH of cement pastes containing nanocellulose. Compared to the control group, at 28 days the flexural strength and energy absorption of 0.1% nanofiber reinforced cement pastes increased by 106% and 184%, respectively.

In addition, XRD and FTIR have also confirmed that the NFC (also called CNF) leads to cement paste an increase in DOH (Mejdoub *et al.*, 2017). Mejdoub *et al.*(2017) proposed that NFC as a steric stabilisation role in cement particles. The high surface area provided by NFC acts as a nucleus and promotes the hydration process. The amount of DOH is positively correlated with the dosage of NFC. The DOH of 0.5-wt% NFC was significantly higher than that of ordinary cement pastes, reaching 40%, 48% and 58% at day 1, 7 and 28 days, respectively. The increased hydration degree favours the production of more portlandite and calcium silicate gel. The accumulation and precipitation of hydration products in the pores make the matrix densifying and improves its compressive strength. The 0.3-wt% addition of NFC (the optimal amount) in the cement can increase the compressive strength of the cement by 50% and reduce the porosity by 30%.

The nano-reinforcing effect of CNF was also examined by Balea, Blanco and Negro's (2019) research, where the crystals and the fibre surface are bonded during the hydration process of cement. Physical bonding occurs when the fibres come into contact with the cement particles and water-permeable parts. The hydrophilic and hygroscopic characteristics of CNF, as shown in Figure 2.24 provide an internal reservoir of water for the nanofiber network, and the surface of the anionic nanofiber electrostatically attracts high concentrations of Ca^{2+} ions. The ion concentration increase accelerates the fibre-cementitious composite of C-S-H gel during the hydrating process, promote the interface's hydration products (Balea, Blanco and Negro, 2019).

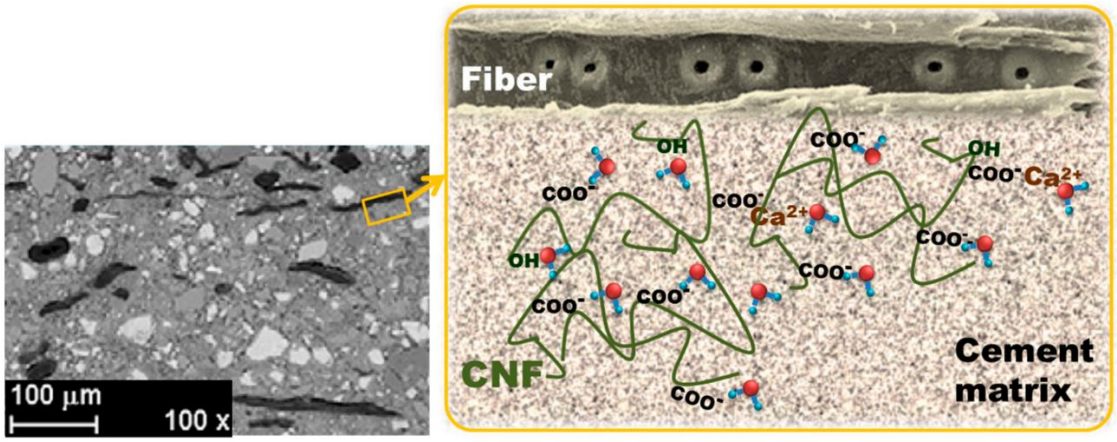

Figure 2.24 The schematic of the CNF–water interactions at the cement matrix (Balea, Blanco and Negro, 2019)

In summary, the CNF has excellent potential to accelerate the cement hydration process efficiently. Moreover, CNF enhance the strength and toughness of the matrix by bridging in the cementitious matrix, which impedes the nanoscale microcracks formation and development in cementitious materials. However, CNC and CNF are one-dimensional fibres, which only contribute to one direction than the 2D GO. The

fibre bridging cannot fundamentally prevent and resolve microcracks forming on the nanoscale, it only transfers water to a limited distance of cement particles.

2.4 Sugar beet

The agri-food sugar production sector is one of the top energy-intensive industries. Sugar is produced in more than 120 countries worldwide (Baldwin, 2011). The major source of sugar production are sugar cane and sugar beet, approximately 20% of the world's sugar is derived from sugar beet. According to the 2019/2020 Season Crop Report, global sugar production is approximately 166.2 million metric tons and is expected to reach 182 million metric tons in 2020/2021 (Statista, 2020). The Food and Agricultural Organisation (FAO) statistics show that in 2018 the 56 most important countries grew sugar beet, harvesting 5.03 million hectares and producing 287 million tonnes of beetroot (the average production per hectare was 57.06 tons of beetroot) (FAO, 2018).

Sugar beet is a common plant whose roots contain a high concentration of sucrose, apart from being a major sugar source, it can be used as a food, food colouring and medicinal plant (European Commission, 2019; Statista, 2020). With 17.25 million metric tons of sugar produced in 2019/2020, the EU is the world's largest beet sugar producer (Statista, 2020; United States Department of Agriculture, 2020). The UK contributes to over 8 million tonnes of sugar beet each year, and in turn the sugar beet production chain promotes the rural and agricultural economy. As sugar beetroot production in the UK has increased by over 25% in the last decade, the widespread use of beetroot has generated many industrial biowastes (Sharon Fisher, 2017). For example, the Wissington plant in the UK produces 400,000 tonnes of sugar each year, with co-products including approximately 350,000 tonnes of sugar beet pulp (SBP),

15,000 tonnes of vinasse and up to 64,000 tonnes of bioethanol yearly (Cárdenas-Fernández *et al.*, 2017).

2.4.1 Sugar beet in industry

Considering the energy consumption of bioenergy carriers and the goal for environmental sustainability, the waste streams produced by the sugar industry can be utilised to produce value-added products (Cohen, 1983; Salazar-Ordóñez, Pérez-Hernández and Martín-Lozano, 2013). Systematical attempts have been employed to decrease the environmental impact of SBP, including bio-methanation, combustion for power generation, bioethanol production, biogas production, fertilizer, animal food (Parawira *et al.*, 2004; Contreras *et al.*, 2009; Alkaya and Demirer, 2011; van Zanten *et al.*, 2014; Cárdenas-Fernández *et al.*, 2017). Typically, the SBP, as a biological route to ethanol production produces 30% of the EU's ethanol production (Zheng *et al.*, 2012); The mixtures of SBP and bio methanation of wastewater that contains soluble carbon compounds can be effective in increasing methane productivity (Alkaya and Demirer, 2011).

In such context, it is essential to maximize cycle energy from sugar beet waste. Figure 2.25 shows the main operational unit of sugar beet processing at British Sugar's Withington biorefinery. The company incorporates the sugar production and the recycling of a range of by-products with value-added products such as bioethanol, animal food feed (SBP and vinasse) and renewable energy (Cárdenas-Fernández *et al.*, 2017). SBP is the main carbohydrate by-product in the sugar beet industry, mainly in the form of cellulose and pectin, containing D-glucose(Glu), L-arabinose(Ara) and D-galacturonic acid (GalAc) (Cárdenas-Fernández *et al.*, 2017). Dried SBP can be conveniently utilised as a low-value animal feed product, and its mixtures can be utilised as a stabilizer, emulsifier or thickener due to the pectin content. The SBP

contained pectin can further work as a biosorbent for the wastewater treatment, recovering elements such as Cu, Pb and Cd (Renouf, Wegener and Nielsen, 2008; Mata *et al.*, 2009).

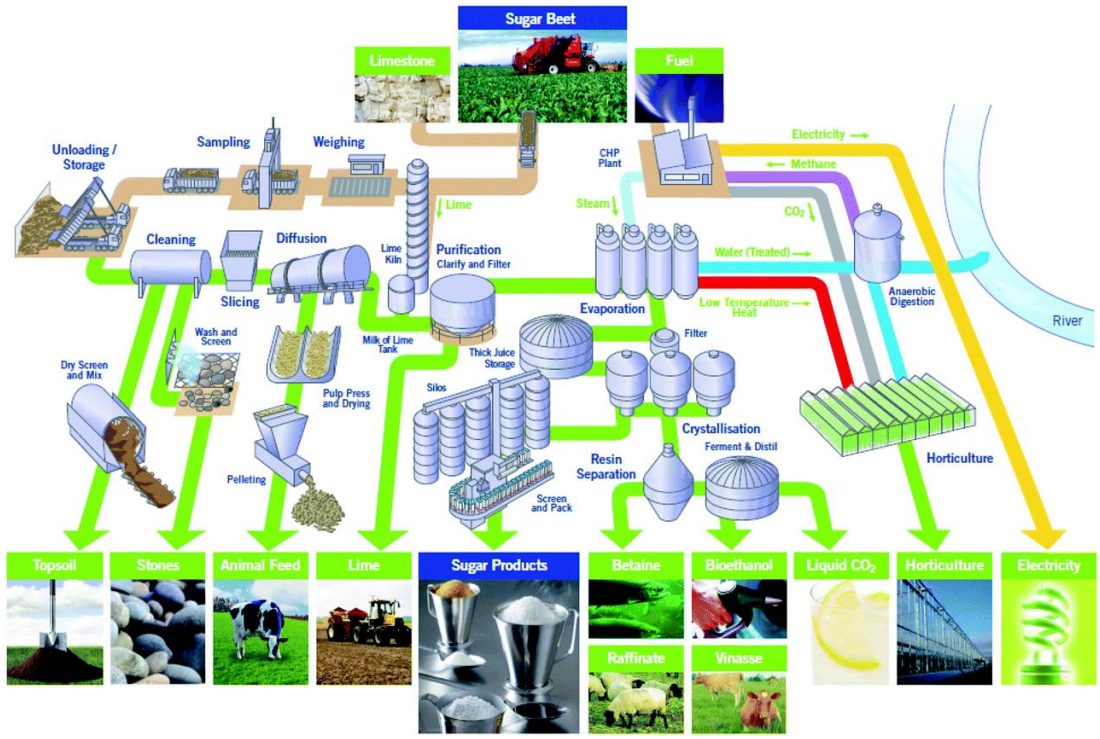

Figure 2.25 British Wissington Sugar beet biorefinery processing (Norfolk, UK) (Cárdenas-Fernández *et al.*, 2017)

Olmos and Hansen propose that pectolytic enzymes can effectively remove the pectin from the SBP, leaving the hemicellulose fraction (Olmos and Hansen, 2012). Lv *et al*'s, research shows that pectin can fully extract from the SBP (C. Lv *et al.*, 2013). The homogeneous depectinated sugar beet pulp (DSBP) cellulose nanofibers (10-70 nm in diameter) can be obtained by chemical treatment (including alkali treatment and bleaching) and high-pressure homogenisation. After pectin removal, the DSBP is a vital biomaterial. FTIR and chemical analysis showed that the chemical treatment efficiently removed the hemicellulose and lignin from DSBP, which serves to increase the cellulose content, crystallinity and thermal degradation temperature. As a result, the

residues contained 40 to 50% cellulose, 20 to 30% hemicellulose and a small amount of lignin (Li *et al.*, 2014).

2.4.2 Depectinated sugar beet in research

Previous research focused more on optimising the sugar manufacturing and waste convenience treated process. Little is known about the potentials for waste products in the beetroot sugar industry. As biorefining DSBP becomes an abundant renewable resource of natural cellulose nanofibers, the DSBP advantages can transform into a fibre additive. Globally available low cost cellulosic fibres can be used in the cement-based composites to decrease the bulk density by 37.3% (Xie *et al.*, 2015), in reinforce cementitious composites to improve the internal curing (Onuaguluchi and Banthia, 2016) and enhancing plasters (Dalmay *et al.*, 2010). As opposed to synthetic fibres with the advantages of lower cost, eco-friendly, no health hazards, bio renewable, sufficiently stiff and strong to be processed and easily recyclable (Tonoli *et al.*, 2009; Mármol *et al.*, 2013; Anju, Ramamurthy and Dhamodharan, 2016; Onuaguluchi and Banthia, 2016). Small volume fractions of fibre additions can significantly improve the concrete toughness and tensile behaviour (Pacheco-Torgal and Jalali, 2011). As reported by Tonoli et al., the fibres enhance the interactive adhesion of the matrix, thus improving the interfacial mechanical properties of cementitious materials (Tonoli *et al.*, 2009).

The sugar beet pulp cellulose nanosheets (SNSs) are the new 2D cellulose material extracted from the sugar beetroot waste. It has the advantages of abundant sources, environmental friendliness, low price, hydrophilicity and affinity (oxygen functional groups). According to an earlier research, the 2D nanoplatelets synthesized from sugar beetroots can be bound with C-S-H in cement matrix with hydrogen bonds or ionic/covalent bonds to form a three-dimensional (3D) network, which significantly

improves OPC's Young's modulus, flexural strength, and toughness. BNPs addition by 0.2 -wt% cement increased the flexural strength and modulus elasticity by 75% and 200%, respectively. Furthermore, the BNPs pastes optimal fracture energy and the fracture toughness were increased by 88% and 106%, respectively (Hasan et al., 2019). However, when the sugar beetroot concentration is higher than the critical value, ultrasonic dispersion shows a limited dispersion effect. The defects formed by agglomeration will reduce the cementitious composites mechanical properties (Hasan *et al.*, 2019). Since the understanding of beetroots pulp raw materials in cementitious composites remains limited, this study investigates the degree of hydration, mechanical and microstructure properties of raw and ultrasonic treatment SNS cementitious materials under the different w/c ratios.

2.5 Summary

This chapter systematically reviews the different dimensions of nanomaterial-reinforced cementitious composites. According to the existing research, extensive experimental and theoretical research of nano-reinforced cementitious has dramatically contributed to the reinforcement and development of nano-engineered high-performance concrete and nanostructures (Table 2.1). The evolution of mechanical properties on the macroscopic scale of cement matrix composites is derived from the mapping of microscopic nanoscale property changes in nature. The hydration of nanomaterials in the cement environment promotes interfacial chemistry and prevents crack extension. Nanomaterials increase and strengthen the C-S-H hydration phase content, improving the pore structure and densification of the cement matrix. However, the large-scale nanoparticles utilised in construction materials are problematic in terms of the difficulty and complicated disperse processes, high cost, potential health and safety implications.

Table 2.1 The advantages of the nanomaterials reinforce cement composites

Nanomaterials	Advantages
CNTs	CNTs reinforced cementitious composites compressive strength increases by 77% (Balasubramaniam, Mondal, Ramasamy, Gadyam S. Palani, *et al.*, 2017), flexural strength by 269% and ductility by 81% (Abu Al-Rub, Ashour and Tyson, 2012); CNTs accelerates the early hydration process of cement (J.M. Makar, Margeson and Luh, 2005), limit the propagation of mixtures' microcracks (Abu Al-Rub, Ashour and Tyson, 2012).
NS	NS improved cementitious composites compressive strength by 51.6% (Najigivi, Khaloo and Rashid, 2013), flexural strength by 27% (Li *et al.*, 2004); NS promotes the cement hydration products' internal structure densification (Kontoleontos *et al.*, 2012); reduces the size and quantity of the $Ca(OH)_2$ crystals (Najigivi *et al.*, 2013). The NS increases the quality of the hydrated C-S-H and ettringite crystals (Ma and Zhu, 2017), reduces the Ca/Si ratio and contributes to the enrichment of CH in the interfacial transition zone (Ma *et al.*, 2019).
G	G increases the cement composite compressive strength by 8% and flexural strength by 24%, raises the DOH and promotes the hydration products (Wang *et al.*, 2016); reduces the cement pastes effective porosity and critical pore diameter by 37% and 30%, respectively (Du and Dai Pang, 2018). GNPs provide more space

	for ion transportation on the cement particle surface and promote the early nucleation effect (Baomin and Shuang, 2019).
GO	GO template effect results in cement composites tensile strength increased by 78.6%, flexural strength increased by 60.7% (S. Lv *et al.*, 2013). Increase in the compressive strength by 46.9% and effectively impeding the crack propagation (Pan *et al.*, 2015). A small proportion of GONPs additives significantly reduced the pore size (M. M. Mokhtar *et al.*, 2017).
CNCs	CNCs supply the steric stabilisation and short-circuit diffusion (SCD) mechanism to the cementitious composites (Cao *et al.*, 2015), improving the compressive strength by 45% (Mazlan, Md Din, *et al.*, 2016) and flexural strength increase by 50% (Cao, Zavattieri, *et al.*, 2016).
CNFs	CNFs heighten the cement composites concentrations of Ca^{2+} ions and accelerate the C-S-H gel generation (Balea, Blanco and Negro, 2019); Increase the compressive strength by 50% and reduce the porosity by 30% (Mejdoub *et al.*, 2017), rise the breaking energy more than 50% (Sarah J. Peters *et al.*, 2010); The flexural strength and energy absorption of the reinforced cement pastes increased by 106% and 184%, respectively (Onuaguluchi, Panesar and Sain, 2014).

Compared with expensive nanomaterials, cellulose fibre-based nanomaterials are relatively inexpensive, and their hydroxyl-rich material properties can effectively reduce agglomeration with cementitious materials. The literature review on

cementitious composites with nano cellulose has confirmed the feasibility of a nanofiber reinforced cementitious base. In theory, a well-dispersed 2D fibre material is helpful in crack bridging and beneficial to improving mechanical and fracture properties. A new type of green 2D nanomaterials SNS has been developed from sugar beet waste, which has the advantages of being extensive, cheaper, and environmentally friendly. Little is known about the SNS additives effect on cementitious hydration behaviour. Our research aims to bridge the gap on 2D SNS that develops a new generation of high-performance, sustainable infrastructure materials with a low carbon footprint. The following chapter will discuss the manufacture of 2D SNS and its material properties.

Chapter 3 The SNS characterisation and SNS aqueous preparation

3.1 Introduction

This chapter introduces the new 2D SNS material and its manufacturing process, followed by the results of a series of characterisation experiments conducted on different SNS suspensions to determine the colloidal properties and stability of SNS.

3.2 Sustainable nanomaterial SNS

The UK sugar industry is one of the most efficient sugar producers globally. The sugar beet supply chain plays the leading role, as sugar beetroot production in the UK has increased by more than 25% in the last decade. The widespread use of beetroot generated a large amount of industrial biowaste (e.g. waste sugar beet pulp). The exits SBP waste treatment process is mainly based on low-value methods. The SBP recycling methods include bio-methanation, combustion for power generation, bioethanol production, biogas production, fertilizer and animal foods (Parawira *et al.*, 2004; Contreras *et al.*, 2009; Alkaya and Demirer, 2011; van Zanten *et al.*, 2014; Cárdenas-Fernández *et al.*, 2017). However, the exploration of the high-value SBP material development is limited. Taking in to consideration the consumption rate of bioenergy carriers and the importance of environmental sustainability, maximizing the recycling of energy from biowaste products through SBP is essential.

Our industrial partner, CelluComp Ltd (Scotland, UK), manufactured the SNS material utilised in this research. SNS is the new 2D cellulose material extracted from the sugar beetroot pulp waste. SNS has cellulose properties that can be compatible with common aqueous polymer systems, such as epoxy, acrylic and polyurethane. Compared to the

popular 2D nanomaterials G, GO, BN research in cement composites, SNS has many advantages: its abundant nature, eco-friendliness, low price, hydrophilicity, and affinity (oxygen functional groups) (CelluComp Ltd, 2020).

3.3 Manufacturing of SNS

The SNSs manufacturing process is shown in Figure 3.1 and detailed in Patent No.: 9,834,664 B2 (Hepworth and Whale, 2017). The first step of the manufacturing process involved diluting SBP with a solid content of 1.0% by weight. The pH of the mixtures was then raised and kept constant at 14 by adding a 0.5M sodium hydroxide (NaOH) solution. Subsequently, the amounts of hemicellulose and pectin were extracted from the mixtures. The mixtures were then homogenised at a temperature of 90℃ for 5 hours, and using a stirring blade with a rotation speed of 11m/s for 1 hour. The stirrer blades rotate at a speed of 30 m/s for 5 minutes before the end of the heating phase. The homogenised solution was filtered to remove the dissolved material, resulting in an SNS paste with a solid content of 8% and an average SNS sheet size of 50μm x 50μm in lateral size and 0.25μm thickness. Finally, the dispersant Span 20 (Croda international PLC) was added to the mixtures to coat the surface of cellulose platelets, preventing them from aggregating and making it easier to redisperse in an aqueous medium. The SNS suspension properties are as shown in Table 3.1.

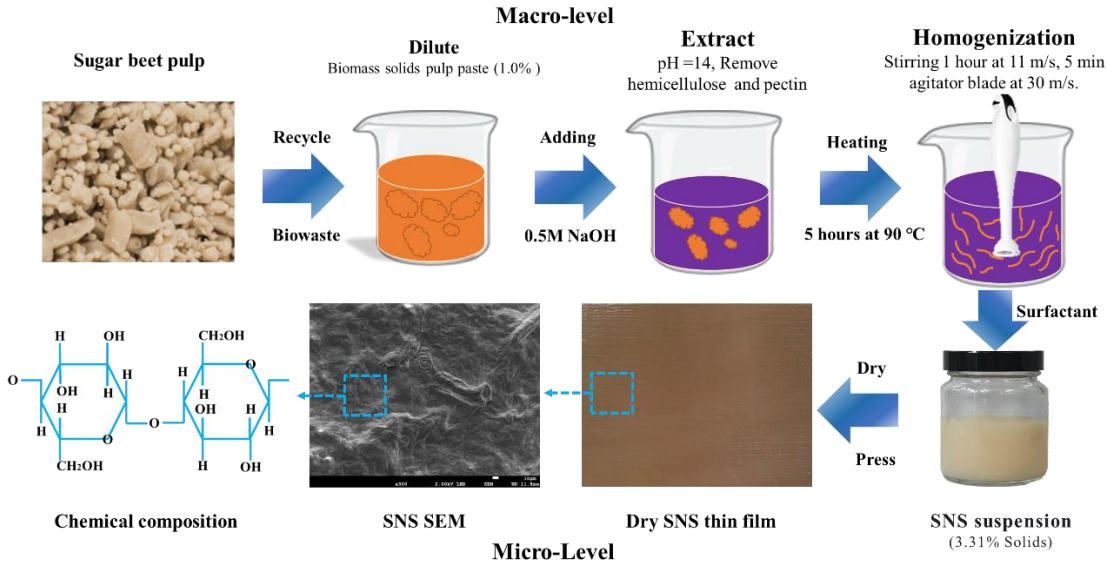

Figure 3.1 Flow chart showing the manufacturing of SNSs

Table 3.1 SNS suspension property

Property	pH	Viscosity (RV, 10rpm Brookfield)	Density g/cm^3
SNS pastes	4.5 – 7.0	500-2000 cps	1.07

3.4 SNS characterisation programme

For the characterisation of SNS properties, the SNS paste is placed in between two absorbent surfaces covered by metal, and then compressed to reduce the excess water. The SNS material eventually forms the sheet of SNS at 0.1 mm thickness.

3.4.1 SEM and EDS

The SEM is a versatile instrument for the visual microstructural characteristics of materials. The SEM can be used as an adjunct to obtaining and identifying high-resolution images of SNS morphology. Furthermore, the EDS is a proper analytical method used to study the SNS chemical characterisation and element distribution.

SEM JEOL JSM-7800F fitted with X-Max50Silicon Drift Detector (SDD) to an area of 50 mm^2 was employed to characterise the microstructure of the SNS sheets. After

coating with gold, SEM and EDS micro images of the air-dried SNS were produced at a voltage of 2-15 kV at room temperature.

3.4.2 Fourier-transform infrared spectroscopy

Infrared spectroscopy is a popular spectroscopic technique. Most of the materials and chemical bonds more or less exhibited absorption in the IR spectral range. FTIR is a technique that can be used to obtain the infrared spectrum to identify the surface groups in the SNS.

The SNS structures were evaluated by Agilent Technologies ExoScan 4100 FTIR with the diffuse sample interface. 128 consecutive scans of each spectrum were in the frequency range of 4000-500 cm^{-1} and at a spectral resolution of 8 cm^{-1}. The SNS molecular functional groups were examined through the infrared absorption spectrum.

3.4.3 X-ray diffractometer (XRD)

The XRD was operated with the SNS spectroscopy, to analyse the crystallinity index. The dried SNS sheet was ground into powders and tested by a single crystal XRD (Agilent SuperNova). The XRD pattern was recorded at a scan rate of 2°/min, with the scan range from 5° to 60° (2θ), Cu Kα radiation (λ = 1.5418 Å), voltage 40Kv and current 40mA.

3.4.4 Transmission electron microscope

To observe the morphology and microstructure of the SNS, the JEM-1010 transmission electron microscope captured TEM images of the SNS. SNS suspension was diluted to 0.2-wt% and ultrasonicated for 30 mins. The prepared SNS suspension was dripped onto carbon-coated TEM grids, and the excess liquid removed with filter paper, leaving the sample air-dried at room temperature. The TEM was run at 80kV acceleration voltages.

3.4.5 TGA and DSC

TGA/DSC was used to evaluate the SNS phase composition, clarifying the SNS crystallisation behaviour and thermal stability. The TGA and DSC were performed through the STA 449 F3 Jupiter instrument. The 30 mg specimen was transferred into the apparatus with an Al_2O_3 crucible, during the experiment chamber temperature was increased from 20℃ to 1100℃ at a constant rate of 10℃/min. The TGA/DSC experiments were conducted under a rate of 25.00 ml/min nitrogen flow and were repeated three times.

3.4.6 Nitrogen adsorption and desorption isotherms

The specific surface area (SSA), pore size and pore volume of the SNS were determined by the BET method using a nitrogen adsorption instrument (MICROACTIVE 3FLEX 3500, Micromeritics, Germany). Prior to testing, the SNS samples were dehydrated in the vacuum and dried at 40℃ for 120 minutes under a pressure of 10^{-6} Pa. According to BS ISO 9277:2010 (Bs Iso 9277, 2010), the dead volume was used to ensure the measurement accuracy of each pressure step. The BET theory identified the SSA of SNS during its method of analysis (Brunauer, P. H. Emmett and Teller, 1938). The relative pressure range of the adsorption isotherm ranges from 0.05-0.35. The isothermal adsorption specific surface area (S) follows the equation as follows (Brunauer, Paul Hugh Emmett and Teller, 1938).

$$S = \frac{V_m N \sigma}{m \times 22400} \tag{3.1}$$

Where, N is the Aphrodro constant (6.022×10^{23}/mol), σ is the cross-sectional area of a single adsorbent molecule, m is the amount (g) of the sample, S is the specific surface area (m^2 /g) of the sample.

$$\frac{1}{V_a\left(\frac{P_0}{P}-1\right)}=\frac{C-1}{V_mC}\times\frac{P}{P_0}+\frac{1}{V_mC} \tag{3.2}$$

Where V_a is the volume (ml) of adsorbed mass at the standard state, V_m is the volume (ml) of adsorbed mass in a single molecular layer on the surface of the test sample in the standard condition, P_0 is the saturation vapour pressure (Pa) of the adsorbent at the adsorption temperature, P is the equilibrium adsorption pressure (Pa) of the adsorbent at 77.4 K (boiling point of liquid nitrogen), C is the constant associated with the adsorption characteristics of the test sample.

The total pore volume and pore size distribution, were identified based on the adsorption and desorption isotherms (relative pressure range of 0.99-0.38), according to the theory of monolayer adsorption and capillary condensation (BJH) (Barrett, Joyner and Halenda, 1951). Kelvin's formula describes the relationship between the capillary coalescence pressure and pore size:

$$r=-\frac{0.414}{\log\left(\frac{P}{P_0}\right)} \tag{3.3}$$

Where, r is pore radius, P is adsorption/desorption pressure (Pa), P_0 is saturation vapour pressure of nitrogen at liquid nitrogen temperature (77.3 K).

The data processing was employed by the instrument's advanced interactive MicroActive 2.0 software.

3.5 SNS characterisation results analysis

3.5.1 SNS chemical components

Figure 3.2 shows the hierarchical structure and molecular structure of SNS. The saccharide units were polymerised to form a single chain. Then, repeat saccharide units covalently formed the SNS crystal molecules by linked β-1-4 glycosidic (C-O-C) bonds.

During the biosynthesis, all the chains involved in nanofibrils are tightly stacked and randomly oriented to form semi-crystalline sheets of SNS. The different functional groups include hydroxymethyl group (-CH_2OH), hydroxyl group (-OH) and methine group (-H) were grafted on the backbone tetrahydropyran ring (Figure 3.3). The high content of hydroxyl and hydroxymethyl groups makes SNS more efficiently and evenly dispersed in aqueous solutions. As shown in the patent report, the SNS suspensions are less likely to agglomerate the outstanding dispersibility performance (Hepworth and Whale, 2017). Specifically, SNS involve at least 1.5 available hydrogens per glucose residue, which could be functionalised for glucose residues significantly compared to those with 0.5 available hydrogens per glucose residue. Moreover, the available hydroxyl groups (-OH) in glucose residues can be used for the proton transfer or functionalisation (Hepworth and Whale, 2017).

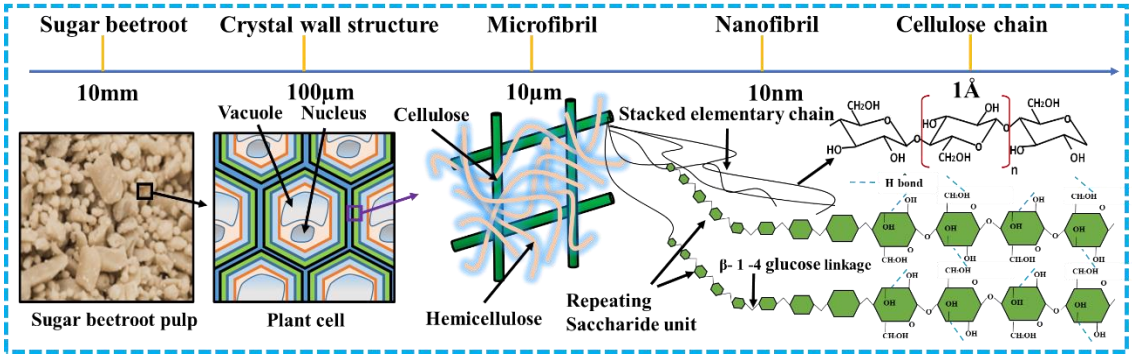

Figure 3.2 The hierarchical and molecular structure of SNS

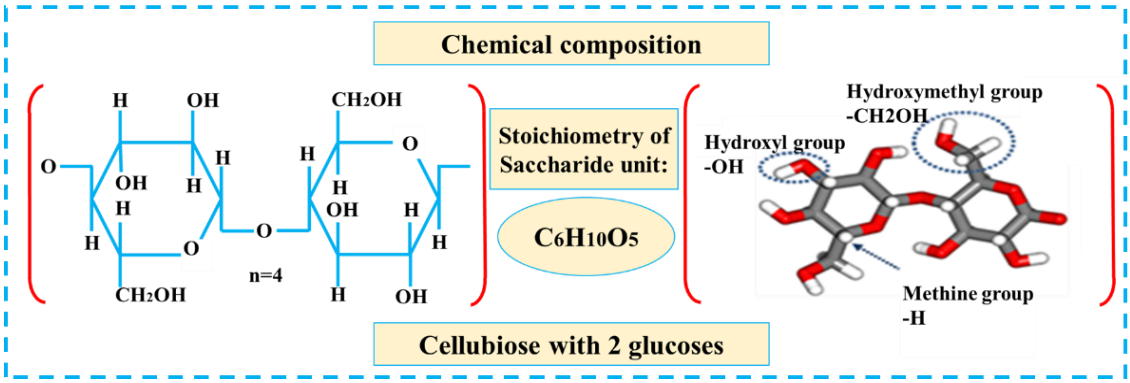

Figure 3.3 Molecular structure and functional groups of the SNS

3.5.2 Energy-dispersive X-ray spectroscopy

The SNS chemical composition obtained from the element analysis of EDS is shown in Table 3.2. The chemical components of SNS are mainly carbon (54.4%), oxygen (43.1%) and impurities that are brought from the preparation process such as calcium (1.3%) and chlorine (0.6%). The element map for EDS content is shown in Figure 3.4.

Table 3.2 SNS chemical composition

Chemical elements	O	C	Ca	Na	Cl	Al	Mg
Amount (%)	43.1	54.4	1.3	0.4	0.6	0.2	0.1

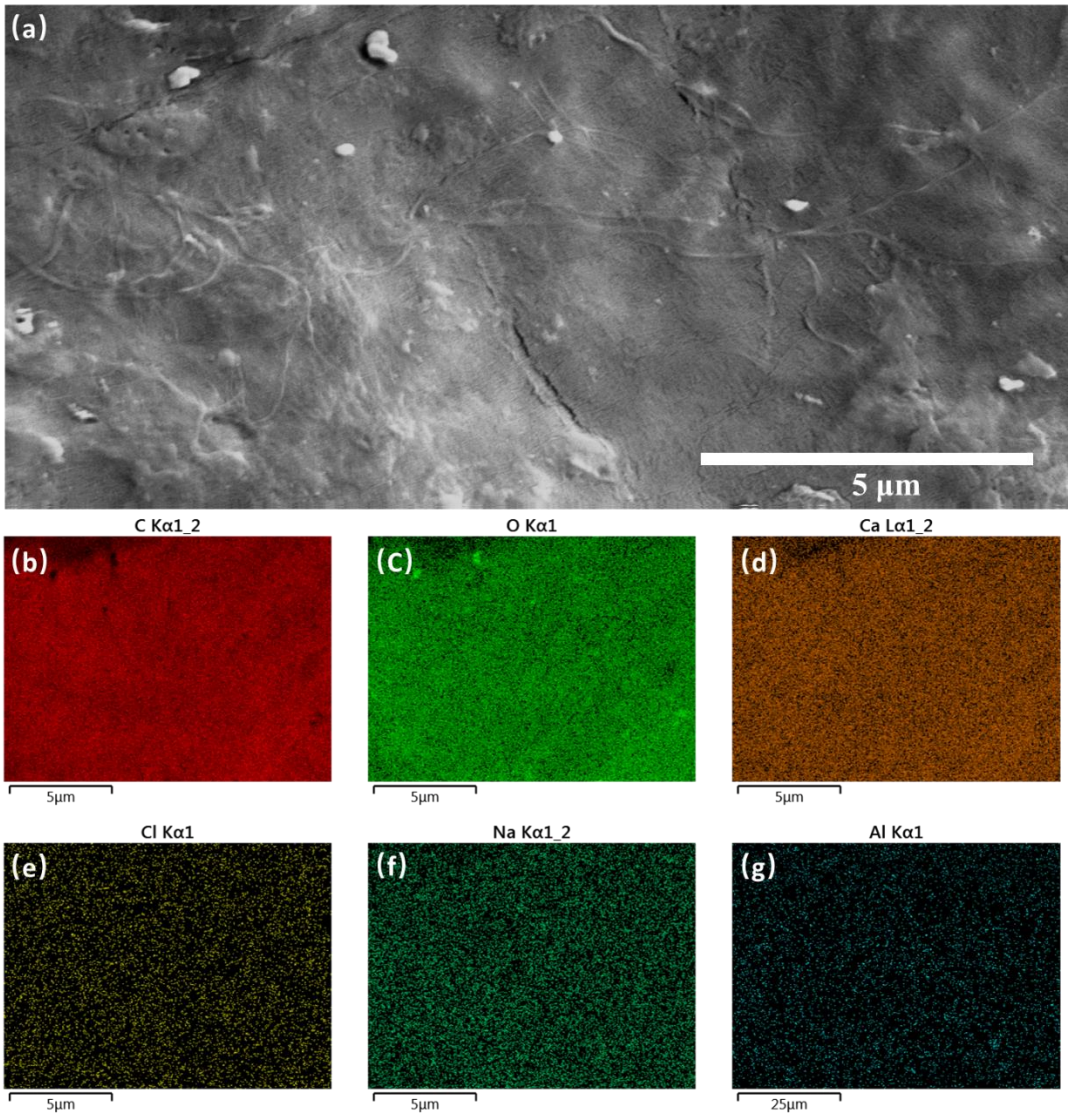

Figure 3.4 SEM and EDS of SNS (a) SEM image, (b) distribution of Carbon element, (c) distribution of Oxygen element, (d) distribution of calcium element, (e) distribution of Chlorine element, (f) distribution of Natrium element map and (g) distribution of Aluminium element

3.5.3 The Fourier-transform infrared spectroscopy analysis

The FTIR spectrum of SNS is shown in Figure 3.5. The absorbance peak nearing 3350cm^{-1} represents the stretching vibration of the hydroxy group (O-H) in the structure, which indicates the hydrophilicity of SNS (Sain and Panthapulakkal, 2006; Kaushik and Singh, 2011). The prominent peak at 2850 cm^{-1} is due to the stretching

and deformation vibration of saturated C-H in cellulose (Alemdar and Sain, 2008). The peak at 1675 cm^{-1} reflects the stretched O-H group, which corresponds to adsorbed water molecules. The 1470, 1420, 1360 and 970 cm^{-1} bands appearing are attributed to C-H stretching of methylene (CH_2) and methyl (CH_3) groups. The signal at 1170 cm^{-1} indicates a C-O-C bond, which is characteristic of cellulose ethers (Abderrahim *et al.*, 2015; Oliveira *et al.*, 2015; W. Chen *et al.*, 2018).

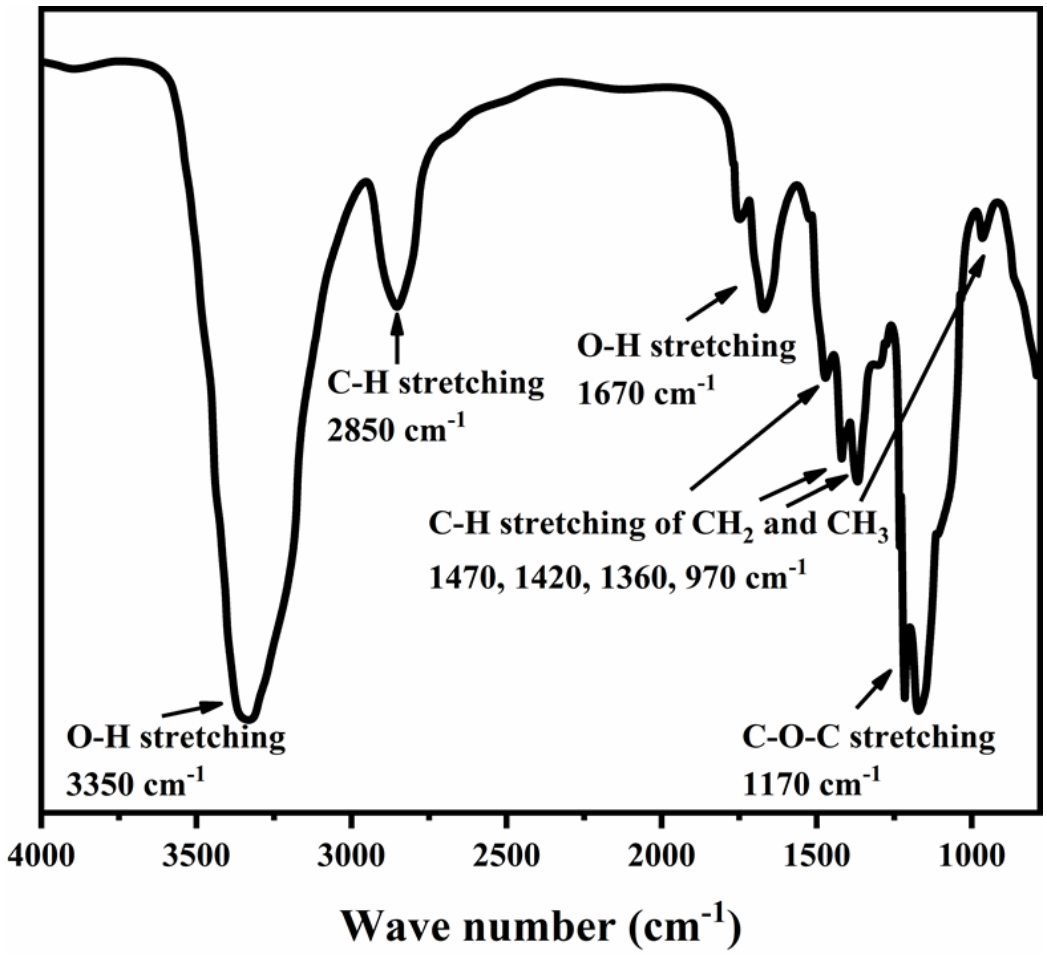

Figure 3.5 FTIR spectrum of SNS

3.5.4 Characterisation of SNS (XRD)

The XRD pattern of the SNS is shown in Figure 3.6. The SNS exhibited diffraction peaks around 2θ=16.5° and 22.5° indicating the typical cellulose-I structural features. These diffraction peaks show that the crystal structure remains intact in the chemically

treated sample, engendering characteristic assignments in the (110) and (200) plane, respectively (Nishiyama *et al.,* 2003; Kumar *et al.,* 2012). The SNS crystalline region appear on the 2θ=16.5°, (110) plane indicate the SNS hydrophilic has hydroxyl groups and easily dispersing in aqueous solution properties. The SNS at the peak of 2θ=22.5° (200) plane appear the wider surface amorphous regions. The amorphous zone are associated to the SNS consist lignin and hemicellulose composite (Li *et al.*, 2014; Gong *et al.*, 2017). The following equation 3.4 (Segal *et al.,* 1959) shows that crystallinity index (*CI*) is correlated with the strength and stiffness of the fibres (Wang, Han and Zhang, 2007) :

$$CI(\%) = 100 \times \frac{(I_{002} - I_{am})}{I_{002}} \tag{3.4}$$

Where I_{002} represents the SNS maximum intensity in the lattice diffraction of the principal peak (200) at (2θ=22.5°) and I_{am} is the SNS amorphous region diffraction intensity.

The average *CI* for SNS is 75.65%, indicating that this cellulose retained its good mechanical strength and stiffness, making it a good candidate for a nanofibre reinforced composite.

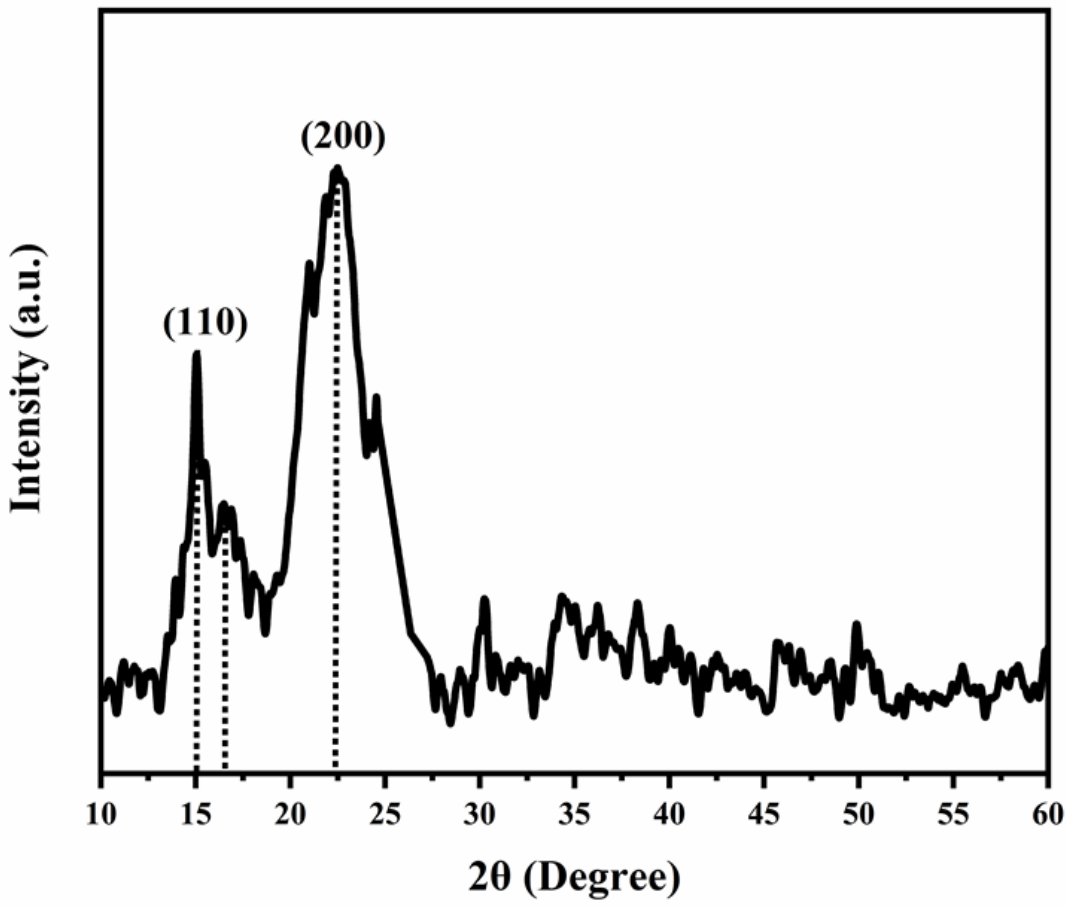

Figure 3.6 XRD spectrum of the SNS

3.5.5 SEM and TEM of SNS

Figure 3.7 shows SEM images of the SNS sample. As shown in Figure 3.7 (a), the SNS exhibit irregular and wrinkled surface textures. The SNS typically consist of partially stacked and randomly oriented cellulose nanofibres. Figure 3.7 (b) shown SEM image of the SNS sample thickness. As can be seen, the sample is composed of stacked and overlapped SNS sheets. It can also be seen that the SNS are wrinkled, crumpled and rippled. These features are also observed in graphene and can greatly reinforce the mechanical properties, as enhanced interfacial mechanical interlocking (Deng and Berry, 2016).

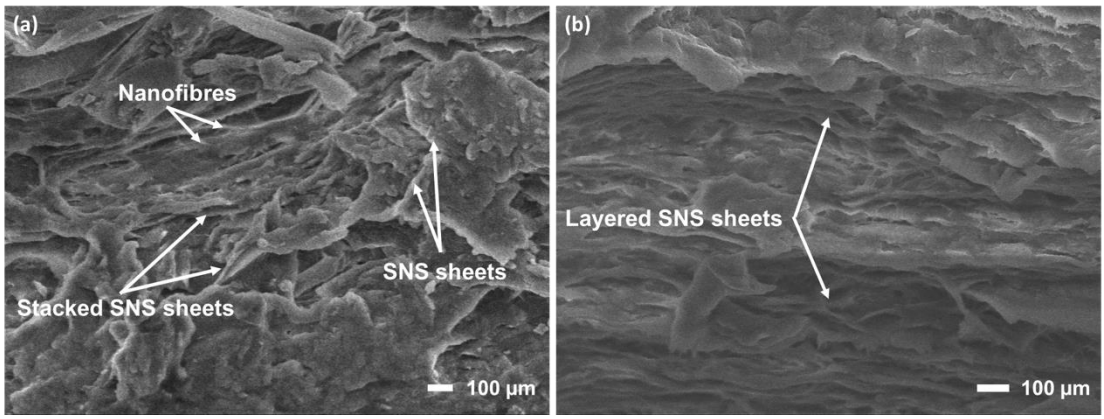

Figure 3.7 The SNS sheets morphology (a) surface, (b) layer

The TEM images of SNS microfibres are shown in Figure 3.8. The purity of the SNS product is high, which clearly shows that most hemicellulose and lignin have been removed during the fabrication process. Figure 3.8(a) demonstrates that the intertwined randomly oriented SNS nanofiber molecular chains were stacked, which exhibited considerable homogeneity in terms of nanometre dimensions. Figure 3.8(b) shows the TEM characterisation of the SNS nanofibrillar structure, and it was observed that the diameters of SNS cellulose are below 100nm, meeting the size requirements of nanofibrils.

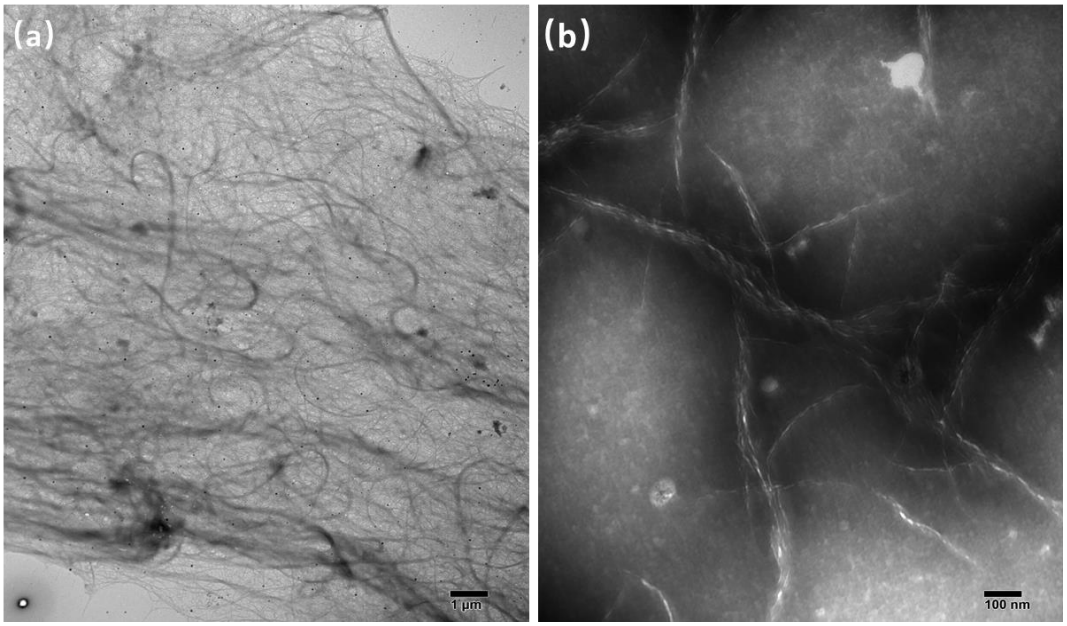

Figure 3.8 TEM images of SNS

3.5.6 TGA and DSC of SNS

The thermal behaviour of SNS is shown in Figure 3.9. Their thermal behaviour of SNS is mainly divided into two stages: slow pyrolysis in the temperature range of 20 ℃ to 200 ℃ and rapid pyrolysis in the temperature range of 200 ℃ to 600 ℃. The slow pyrolysis is the mass loss of the hydrophilic bound water evaporation, whereas the rapid pyrolysis is the sharp mass loss after SNS dehydration. This is due to the thermal degradation the functional group of SNS in the temperature range of 200 ℃ to 380 ℃, and the tetrahydropyran ring backbone structure of SNS in the temperature range of 440 ℃ to 580 ℃. The derivative thermogravimetry (DTG) peaks indicate that the maximum temperature depolymerisation of the SNS functional groups is 329℃ and the depolymerisation temperature of the tetrahydropyran ring of SNS is around 518 ℃. The mass loss of SNS remains unchanged between 580℃ and 1100 ℃, with a residual mass weight of 20%.

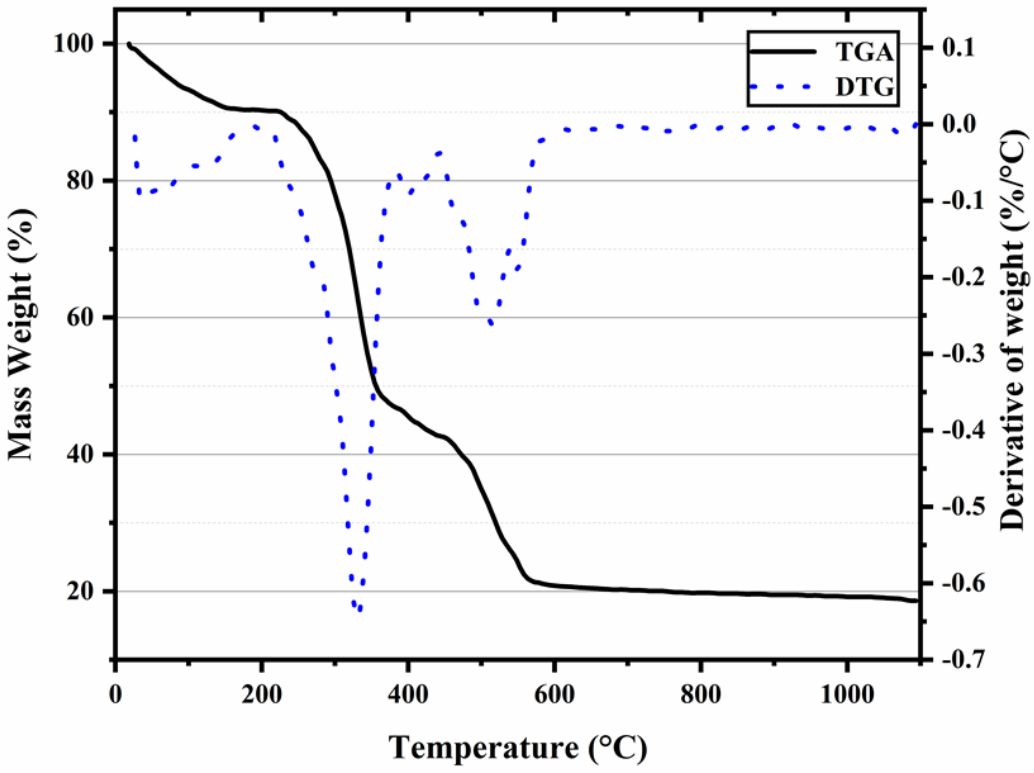

Figure 3.9 Mass and derivative of the weight of SNS

Figure 3.11 shows the DSC thermogram and its derivative of SNS in the temperature range of 20 ℃ to 1000 ℃. From the derivative of the DSC curve, the first endothermic broad peak between 20 ℃ and 200 ℃ corresponds to the rearrangement of the molecular chains of SNS caused by the evaporation of bound water. The second endothermic peak between 200 ℃ and 380 ℃ can be attributed to the colloidal bond cleavage. The third endothermic transition between 440 ℃ and 580 ℃ corresponds to the depolymerisation of cellulose. The occurrence of the endothermic hump and the first peak phenomena are similar to amorphous cellulose (Ciolacu, Ciolacu and Popa, 2011). It is worth noting that conventional cellulose typically completes its depolymerisation over a temperature range of 200 ℃ to 400 ℃, whereas the depolymerisation of the tetrahydropyran ring backbone of the SNS material is completed over a temperature range of 200-580 ℃. This indicates that the SNS material has a higher thermal resistance than conventional cellulose.

Figure 3.10 shows the SNS heat flow graph and the changes over time. The enthalpy of fusion was calculated from the curve area. As shown in Figure 3.11, the first phase of the SNS sheet enthalpy of the fusion area is the heat absorbed from the DSC process (577.911 j/g), the second phase corresponds to the microcrystalline portion of the cellulose (472.366 j/g) and the third phase relates to the tetrahydropyran ring backbone depolymerisation enthalpy of fusion (7105.58 j/g). The SNS sheets exhibit high thermal stability when suspended in water in a temperature range of 20-200℃, which can withstand the hydration heat of cement composites.

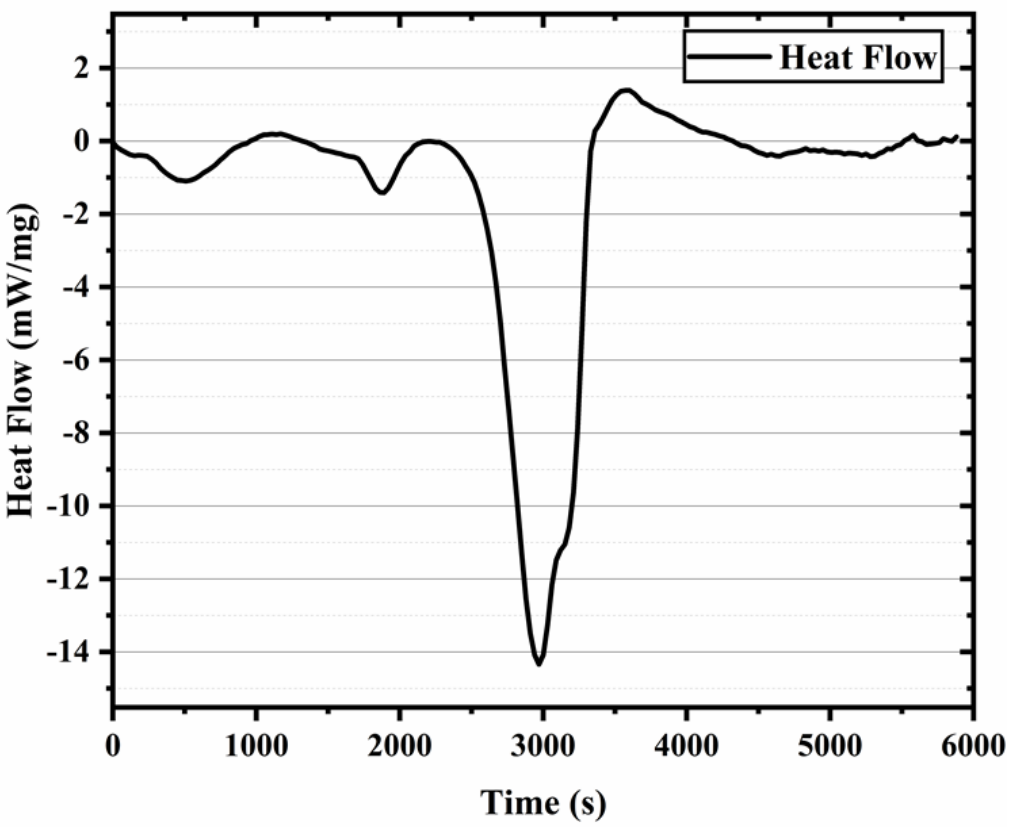

Figure 3.10 SNS enthalpy of fusion

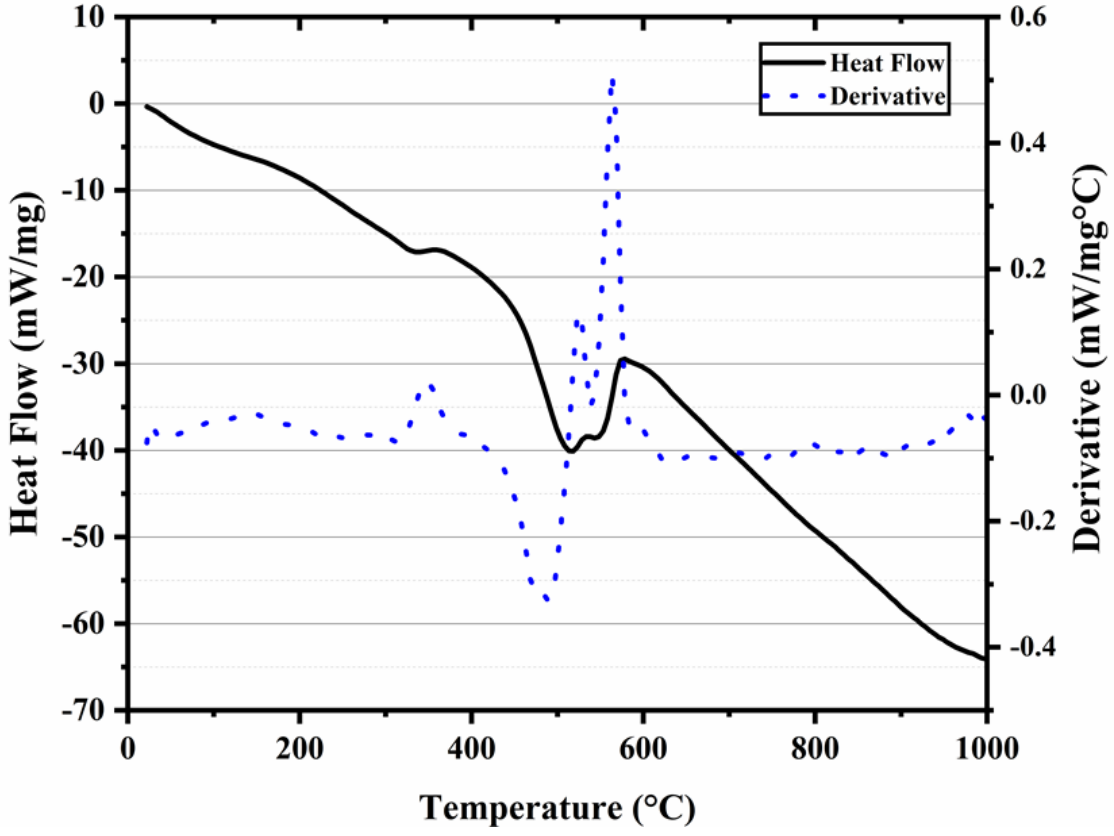

Figure 3.11 DSC and Derivative of SNS sheet

3.5.7 Nitrogen adsorption-desorption isotherms of SNS

The N_2 adsorption-desorption isotherms of SNS are shown in Figure 3.12. This figure shows that the SNS have a BET specific surface area of 68.35 m^2/g. The total pore volume and pore size distribution of SNS calculated according to BJH theory are shown in Figure 3.13. As shown, the pore volume, the BET specific surface area and the average pore diameter of SNS are 0.14 cm^3/g, 68.35 m^2 g^{-1} and 8.19 nm, respectively. The microstructural studies of the previous OPC pastes have shown that the high surface area correlates with the high DOH (Juenger and Jennings, 2001). It is generally accepted that the surface area in cement pastes is directly related to the nature of highly porous C-S-H gel (Thomas, Jennings and Allen, 1999). The surface area of cement pastes is partly derived from the C-S-H gel. Therefore, the addition of SNS to the cement base increases the surface area and possibly promotes hydration.

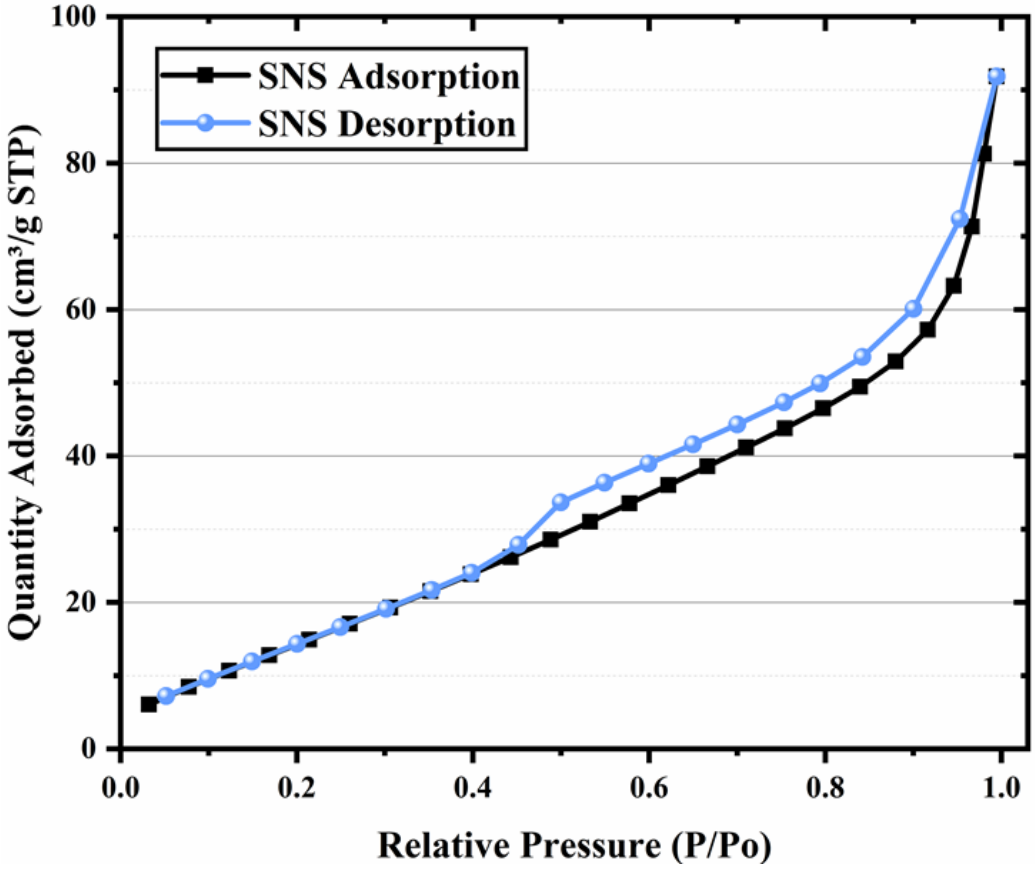

Figure 3.12 SNS Nitrogen sorption isotherm curves

Figure 3.13 shows that the pore size distribution of SNS is a bimodal pore size distribution in the 0-10 nm range and a small number of pores in the 40-80 nm range. The SNS 0-10 nm pores provide more reaction points for the reaction (same size as C-S-H gel). In addition, the hydrophilic SNS (hydroxy group (O-H) in the structure) were absorbed during the early hydration period and had stored excess water into the pores at that stage (Sain and Panthapulakkal, 2006; Kaushik and Singh, 2011). Up until the later stages of the hydration process, the SNS are embedded into the hydration products and built water channels in the cement matrix. The SNS were constant in releasing water molecules which facilitated the C3S reactions during the hydration process.

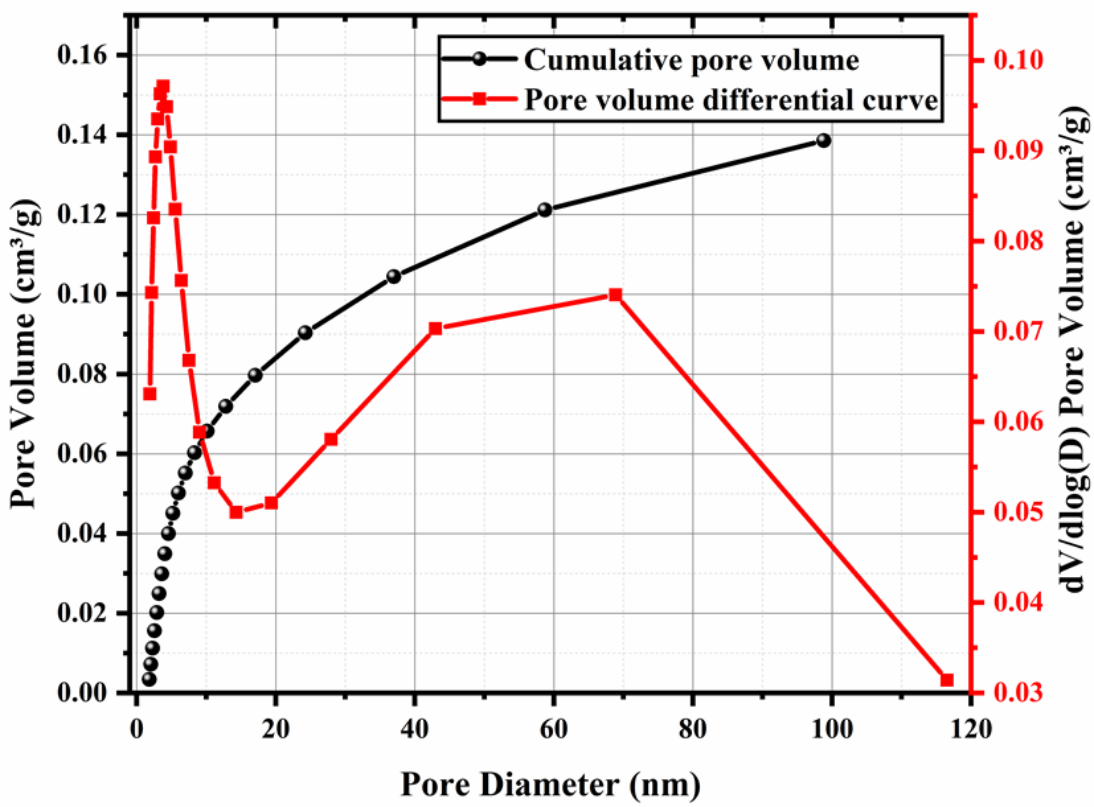

Figure 3.13 SNS Cumulative Pore volume and Pore distribution

The specific surface area of GO is 47.5 m^2g^{-1}, the pore volume and average pore diameter of GO are 0.18 cm^3/g and 9.3 nm, respectively (Guerrero-Fajardo, Giraldo and Moreno-Piraján, 2020). When 0.05-wt% of GO was incorporated into the cement

composite, this lead to the matrix SSA increasing from 27.3m^2/g to 64.9m^2/g and the total pore volume from 0.049 to 0.101 ml/g. The increase in the SSA of the cement matrix is due to the GO addition, promoting the DOH and generating more C-S-H gel (Pan *et al.*, 2015). Table 3.3 shows that the 2D materials Graphene and BN BET pore properties were similar to the SNS. Compared to the 1D materials, the SNS has the advantages of large specific surface area, concentrated small pore size and fast adsorption and desorption speed. The 2D material SNS provides a large number of nano-sized pores that facilitate the ions exchange and are beneficial for the cement hydration process.

Table 3.3 Nitrogen adsorption-desorption isotherms of different materials

Material	Average pore Diameter (nm)	Pore Volume (cm^3g^{-1})	BET Surface Area (m^2g^{-1})
SNS	8.19	0.14	68.35
Graphene (GO) (Guerrero-Fajardo, Giraldo and Moreno-Piraján, 2020)	9.3	0.18	47.5
Graphite (Gr) (Guerrero-Fajardo, Giraldo and Moreno-Piraján, 2020)	7.4	0.04	5.2
oxygen-containing BN (Tang *et al.*, 2008)	1.53	-	26.8
Oxygen-free BN (Tang *et al.*, 2008)	1.31	-	52.7

3.6 SNS aqueous solution dispersion and stability

3.6.1 Dispersion of SNS aqueous solution

The fibril within 2D nanomaterial SNS is a feature which qualifies them for becoming the potential material for cementitious reinforcement. However, the high concentration of fibre dispersed into the cement matrix is problematic. When the fibres are not well dispersed as under the agglomerated states, this creates a weak zone leading to the stress concentration of cement composites during the loading. The weak zone affects the mechanical properties of the matrix and even causes damage (Bentur and Mindess, 2007). Similar to the CNC reinforced cementitious composite, the SNS van der Waals forces under high concentration leads to self-aggregation. The simple mechanical dispersion methods are difficult to achieving SNS agglomeration even distribution.

Previous research developed many methods to improve fibre dispersion (e.g. CNC), such as fibre surface modification, functionalisation, modification of the physical mixing process and external doping of surfactants. Among them, Cao *et al*. (2015) used ultrasound to disperse CNC in the aqueous suspension before mixing the cement. The ultrasound dispersion effectively alleviated the high concentration agglomeration, thereby reducing the occurrence of the stress concentration phenomenon (Cao *et al.*, 2015). Based on the similar structural characteristics of SNS, this investigation considered the surfactant and ultrasonic dispersion methods to overcome the dispersion issue of the SNS aqueous solution.

Firstly, the SNS was treated with surfactant (Span 20) and until leaving the factory. After that, SNS and 1%-wt superplasticisers (SP) were slowly mixed with water and magnetically stirred for 2-3 minutes to produce the raw SNS aqueous solution. Figure 3.14 shows the ultrasonic disperse setup, where the solution was ultrasonically

dispersed through a probe sonicator (Branson Sonifier 450) operated in the pulsed mode with a 50% duty cycle for 30 min to obtain the SNS suspensions. The suspensions were placed in an ice bath throughout the dispersion process to prevent overheating and moisture evaporation. Finally, the stable homogeneous SNS solutions were placed in a sealed container.

Figure 3.14 Sonicate Machine set up, SNS suspension surround with ice

3.6.2 Stability of SNS aqueous

The ultraviolet-visible (UV-vis) spectrum is a standard method that characterises the degree of transparent media dispersion. According to the Beer-Lambert law, higher absorbance implies better dispersion of aqueous solutions (Grinter and Threlfall, 1992). The SNS suspension UV-vis absorption spectra were produced by the Evolution 220 spectrometer. The absorption spectra of SNS suspensions, with a concentration of 1.0-wt%, were obtained at a wavelength between 290 to 750 nm (maximum effective the

absorbance can collect) after ultrasonic treatment for 0, 15, 30, 45 and 60 minutes. Figure 3.15 indicates that the SNS aqueous absorption spectra increase gradually with ultrasonication time, which indicates the SNS dispersion increase. The SNS absorption spectrum has an absorption absorbency peak at 310 nm during different sonication times. The absorbance area of the spectral line were increases with the sonication time increases. The disperse efficiency significantly slows down after ultrasound time reached the threshold (30 min), and there are no peak shifts during the entire experiment.

The dispersion of SNS suspensions can be attributed to three parts. Firstly, the dispersant (Span 20) is uniform mixed with SNS, enabling the electrostatic repulsion SNS to disperse in aqueous media. Secondly, the SNS have natural hydrophilicity and carboxylic groups (-COOH), which greatly dispersed the water. Thirdly, the ultrasound technique transferred vibrating waves to the solution, and the ultrasound technique transferred energy into SNS to achieve uniform dispersal. Figure 3.16 shows after 120-day storage, the SNS suspension dispersion is still stable with no stratification or precipitation.

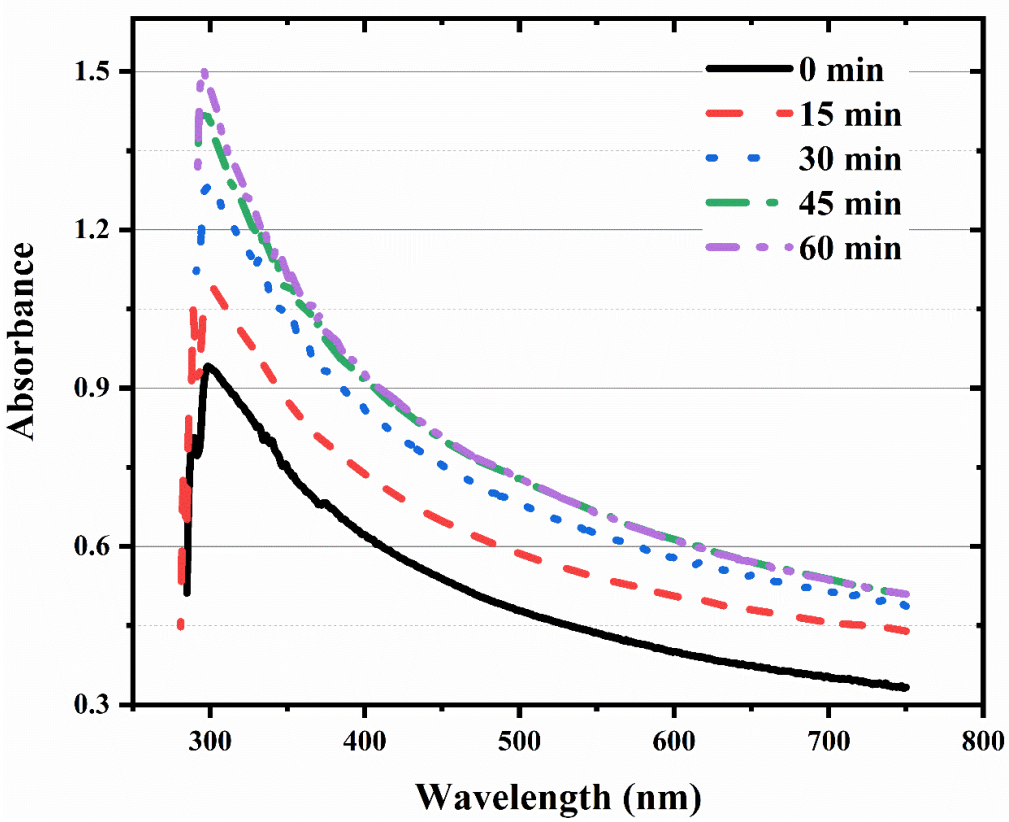

Figure 3.15 Absorption spectra of SNS aqueous solutions with different ultrasonication times

Figure 3.16 120 days SNS suspension

3.7 Conclusions

This chapter presented the SNS manufacturing process, characterisation experiment and SNS suspension dispersion methods. The characterisation results show that SNS have a high specific surface area, high dispersion in aqueous solution (with hydroxy and carboxyl groups), good thermal stability and multilayer folded morphology. Specifically, the EDS elemental analysis results showed that SNS mainly consist of carbon (54.4%) and oxygen (43.1%) elements. The XRD pattern further shows that the structure of SNS was mainly divided into crystalline and amorphous regions. The *CI* of SNS is 75.65%. Compared to the normal CNCs' *CI* it indicates great crystallinity and excellent mechanical properties. In addition, as the FTIR spectra show, the SNS comprise two main types of absorptions: hydroxyl groups (OH) in structure with hydrophilicity and the cellulose saturated C-H stretching vibration. The highly hydrophilic SNS sheet can store water molecules on the surface, while the SNS can act as a reservoir to continue releasing water molecular for hydration.

The TGA, DTA and DSC results show that SNS have excellent thermostability, which meets the cement composites application. The SEM and TEM results show that the SNS similar to the GO, which are wrinkled and stacked enabling the interlayer to fold and overlap flakes. These material properties contribute to filling the hydration products and promoting SNS/C-S-H accumulation to improve the mechanical properties of cementitious composites. The nitrogen adsorption-desorption isotherm results certify that the material has effective mesoporous properties and can accelerate the cement particles exchange to water molecules during the hydration process.

UV-vis experiments demonstrate that SNS suspensions can be well dispersed with ultrasonication (at 30 min). Compare to 2D materials of Graphene and Graphene oxide,

SNS suspension has the advantages of stability, homogeneous distribution and non-agglomeration. It is useful for pre-production of SNS suspension before large-scale construction sites. In the next chapter, the SNS hydration effect of cementitious composites will be investigated.

Chapter 4 Hydration of cement pastes infused with SNS

4.1 Introduction

Cement hydration is a complex physical and chemical process. In this chapter, a series of experiments are conducted to investigate the hydration of cementitious composites containing SNS. Similar to the fluidity investigation, different 2D SNS amounts (0, 0.1, 0.2 and 0.3-wt%) (limited by the SNS cement pastes workability) were used to understand the cement pastes and their hydration mechanism. The experiments include workability tests (Marsh Cone test and mini-slump test), the hydration kinetics of the cementitious composites are studied with the EIS and CV, and equivalent circuit modelling analysis. In addition, TGA and DSC examine the hydration kinetics of the cement pastes and determine their DOH.

4.2 Materials, mix design and experiment methods

4.2.1 Materials

4.2.1.1 Hanson High Strength 52.5N Cement

CEM I, 52.5R commercial ordinary Portland Cement (OPC, Hanson, UK) was used in this study, according to the BN EN 197-1:2001(EN, 2011). The X-ray fluorescence chemical composition of the cement is shown in Table 4.1.

Table 4.1 Chemical components of OPC

Composition	SiO_2	Al_2O_3	Fe_2O_3	CaO	MgO	SO_3	K_2O	Na_2O	Cl
Amount (%)	20.85	5.22	2.25	64.98	2.40	3.37	0.61	0.27	0.05

4.2.1.2 SNS suspension

The manufacturing process of SNS suspension is mentioned in chapter 3.6 SNS aqueous solution dispersion and stability. The SNS suspensions were prepared and utilised on the same day.

4.2.1.3 Superplasticiser (SP)

Due to the addition of the SNS, the workability of the cement pastes has significantly reduced. The SP used in this study is a polycarboxylic ether-based superplasticiser (MasterGlenium®51, BASF, UK), according to the BS EN 934-2 (EN, 2002). This product is a concrete admixture, designed to improve concrete flowability achieve the highest durability and performance. The details of the SP are given in Table 4.2.

Table 4.2 Characteristics of superplasticiser

Appearance	Specific gravity (20 ˚C)	pH-value	Alkali content (%)	Chloride content (%)	Water reduction
Brown liquid	1.10 ± 0.03 g/cm^3	7.0 ± 1	≤ 5.0 by mass	≤ 0.10 by mass	≥ 112%

4.2.1.4 Water

The deionized water supply at Lancaster University Engineering Laboratory was used for the preparation of the cement pastes. It complied with the EN 196-1:2005 specifications (EN, 2005).

4.2.2 Mix design

Four mixtures were used in this study to investigate the effect of SNS on the hydration of cementitious composites. The water/cement (w/c) ratio was kept at 0.35 for all designs. Table 4.3 shows the details of cement paste mixes.

Table 4.3 Mixture proportions of SNS platelet reinforced cement pastes.

Mixtures ID	Unit weight					Additional percent
	Cement (g)	Water (g)	SP (g)	SNS (S) (g)	w/c ratio	
AP00	300	105	3	0.00	0.35	0.00%
AS01	300	105	3	0.30	0.35	0.10%
AS02	300	105	3	0.60	0.35	0.20%
AS03	300	105	3	0.90	0.35	0.30%

Remarks: the capital letter A in the specimen mix numbering indicates the water /cement ratio of 0.35. P refers to the plain cement, S represents the ultrasonicate dispersion sonication methods, following the relative content of SNS additives into the cementitious composites (0.00%, 0.10%, 0.20% and 0.30%), SP represents the superplasticiser.

4.2.3 Manufacturing process

Cement pastes were designed, manufactured and cured in the laboratory following ASTM C302-99 (ASTM, 2014). Firstly, the SNS suspension, SP and deionized water were properly mixed using a magnetic stirrer. Secondly, the mixtures at step 1 were poured into the bowl. The cement was then added and after 30s, when the water was absorbed, it was mixed at low speed (140r/min) for 30s. Thirdly, the mixer was stopped for 15s and a batch was made from scraping down any pastes from the side of the bowl. The mixer was then re-started at medium speed (285r/min) for 120s until SNS evenly dispersed in fresh cement pastes. Fourthly, the fresh cement pastes were poured into the mould and the surface was flattened with a scraper. The mould was vibrated on a shaker for 60s to compact the pastes (no bubbles overflowed), and then a pair of stainless-steel sheets were vertically embedded along the prism length, with the

electrode spacing L for 120 mm. The specimens were covered with a plastic film to prevent the water evaporating during curing and then stored in the laboratory at room temperature. Finally, after curing at room temperature for 24 hours, all the samples were demoulded and specimens were moved into the 20±2℃ standard cured until testing.

4.2.4 Experiment methods

4.2.4.1 Rheology of SNS-cementitious composites

The rheology of SNS-cementitious composites pastes was investigated through the fluidity and workability at the different w/c ratios, SNS concentrations and SP additions.

4.2.4.1.1 Marsh cone experiment

The Marsh cone test is a convenient and reliable method that identifies the cementitious composites flow properties. This test was utilised to characterise the cement pastes and superplasticiser compatibility. The cement pastes manufacturing procedure is described in section 4.2.3, where the viscosity of the cement pastes is indicated from the marsh cone flow time. After 5, 15 and 60 minutes of mixing, 1-litre of cement pastes was poured into the marsh cone vessel, and the time taken for the cement pastes fluid to flow from the marsh cone vessel was recorded (Figure 4.1). The procedure was repeated three times for each set of experiments to calculate the average. The mixtures were stirred throughout the whole test. According to the recommended dosage, the SP admixtures dosage was varied from 0.4 to 1.2-wt% of cement pastes, with a constant increase in 0.2-wt% intervals.

Figure 4.1 Marsh cone experiment

4.2.4.1.2 Mini-slump test

A mini-spread test was conducted to determine the impact of SNS on the workability of the cement pastes by measuring the spread diameters formed by the pastes upon lifting a mini-slump cone (Dubey and Kumar, 2013; Payakaniti *et al.*, 2017), with a top diameter of 70 mm, a bottom diameter of 100 mm and a height of 60 mm (Figure 4.2). The workability test was conducted according to the method used by Collins et al.(2012). During this test, each of the cement pastes was poured into the mould and then vibrated. Subsequently, the excess pastes on the top were removed and the mould

was lifted vertically, leaving the cement pastes to cure for 24 hours. As shown in Figure 4.2, the slump diameter was taken as the average of two direction measurements (d_1 and d_2), for each SNS concentration three measurements were made. The workability was calculated using the following equation (Şanal, Zihnioğlu and Hosseini, 2015):

$$W = \left(\frac{\frac{(d_1 + d_2)}{2} - d_0}{d_0} \right) \times 100 \qquad (4.1)$$

where W is workability, d_1 and d_2 are the two direction spread-out diameters of the pastes and d_0 is the bottom diameter of the cone.

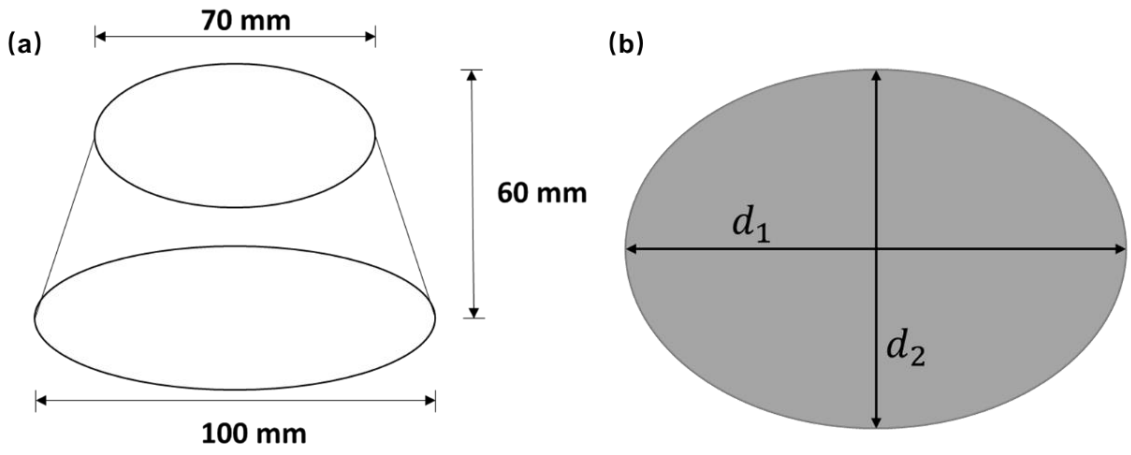

Figure 4.2 Mini slump cone (a) geometric dimensions (b) two directions spread-out diameter

4.2.4.2 EIS, CV and Equivalent circuits models

Cyclic voltammetry (CV) measurements were used to assess the effect of the SNS on the hydration mechanism of the cementitious composites. Potentiostat (Gamry Interface 1000) was employed to obtain the CV characteristics of the cementitious pastes at ages of 7, 14 and 28 days, two-probe method as shown in Figure 4.3. During this test, electrical current was passed through the cementitious composite as the voltage is swept over a voltage range of -0.5 *V* and 0.5 *V* at a scan rate of 0.2 *V/s* for 10

cycles. Gamry software™ was used to produce current vs voltage spectra to extract qualitative hydration kinetics of the cementitious composites.

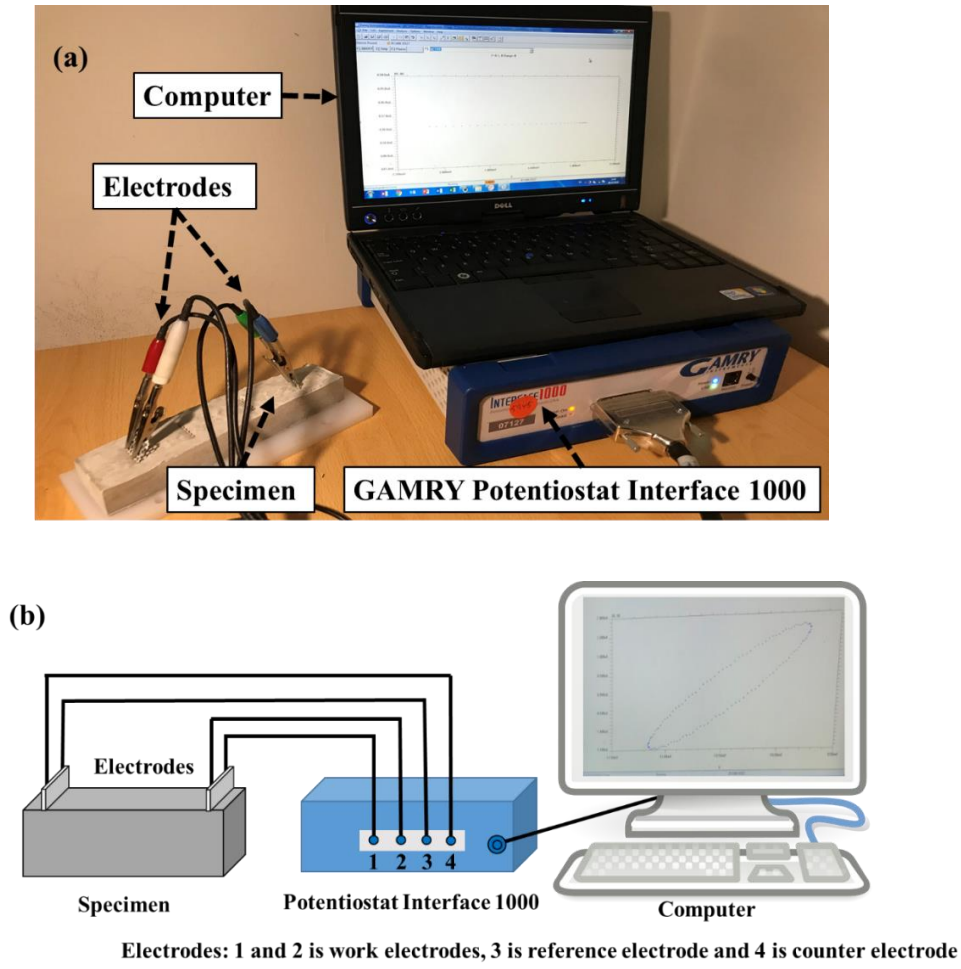

Figure 4.3 Gamry Interface 1000 apparatus two-electrode arrangement for the Electrochemical impedance measurements (a) experiment setup (b) schematic view of the setup

The EIS measurements were also conducted to clarify the influence of SNS evolution of the hydration process of cement pastes at 7, 14 and 28 days over a frequency range of 0.1 Hz to 1 MHz using a sinusoidal voltage of 10 mV. Gamry software™ was used to analyse the EIS results and obtain the equivalent circuit for the cementitious composites.

4.2.4.3 Thermogravimetric analysis and differential scanning calorimetry

The TGA and DSC were performed using the STA 449 F3 Jupiter instrument (Figure 4.4) to characterise the DOH of SNS-cementitious composites. Samples obtained by crushed cube cement specimens were ground into powder with a grinding machine (RETSCH PM 100 Model Planetary Ball Mill). The thermal analysis of the cementitious composites was then carried out at 7, 14 and 28 days. The powdered samples were placed in Al_2O_3 crucibles and transferred into the apparatus chamber. During heating, the chamber temperature was first raised from 20°C to 140°C at 10°C/ min. Then, the temperature was held at 140°C for 30 minutes to remove evaporable water (Pane and Hansen, 2005). Finally, the samples were heated from 140°C to 1100°C at 10°C/min. The TGA/DSC experiments were repeated three times and conducted under a nitrogen flow rate of 25.00 ml/min.

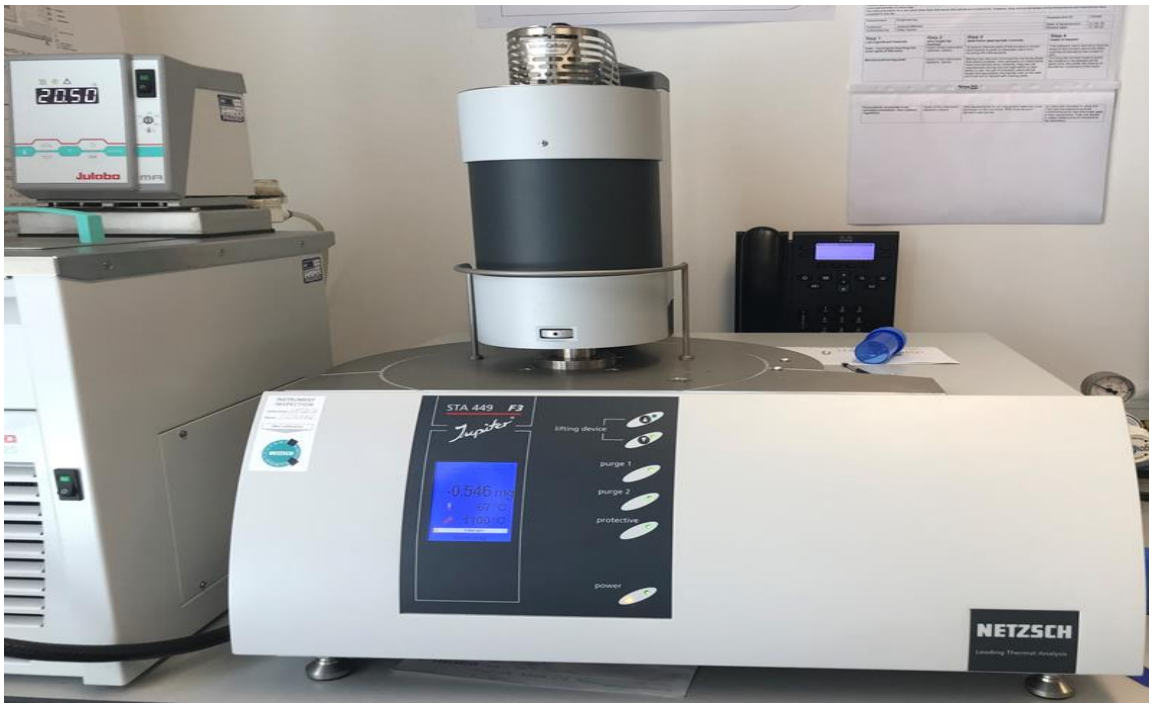

Figure 4.4 Thermal analyser (STA 449 F3 Jupiter instrument)

4.3 Rheology of SNS-cementitious composites

4.3.1 Marsh cone experiment

Figure 4.5 shows the cement pastes (w/c=0.35) marsh cone time related to the SP addition dosage. The experimental results show the marsh cone time decreasing with the increase in SP. The marsh cone flow time of cement pastes reveals the viscosity relationship, in that the longer flow time results in the higher cement pastes viscosity and the lower the fluidity. The optimal dosage of SP admixtures 1.0-wt% which is called the 'Saturation Point', resulting in 55.4% reduction in Marsh cone time compared to the control group. In addition to this, the use of SP reduced the bias of the cement pastes Marsh cone time and increased the stability. However, beyond the saturation point (1.2 -wt% additions), marsh cone flow times drop increase at 5, 15 and 60 minutes. When the SP effect is fully exploited, the excessive admixtures may lead to air entrainment and bleeding issues of the cement pastes.

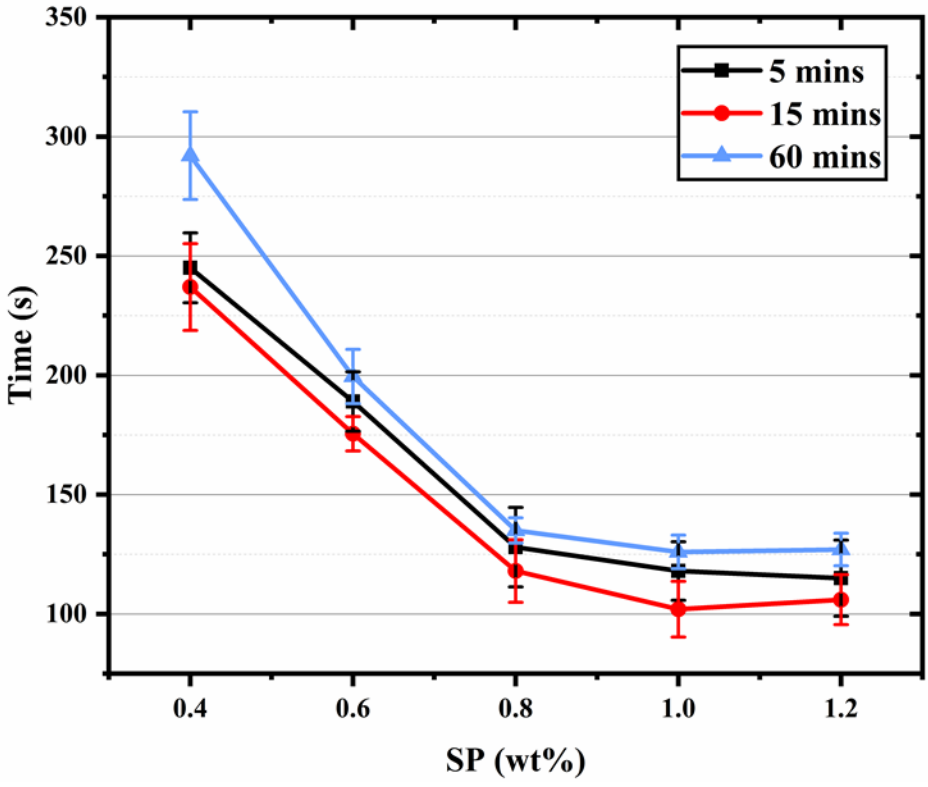

Figure 4.5 Cementitious composites marsh cone test under different SP

4.3.2 Workability of SNS cement pastes

Figure 4.6 shows the workability results of the different SNS dosage cement pastes. After 24 hours, the average spreading diameter of the cement pastes hardening increased by 136.6% compared to the initial diameter of 100mm. The working performance of the slump test decreased as the SNS amounts increased. The experimental results show that incorporating a small amount of SNS does not significantly affect the cement pastes fluidity.

When the SNS addition reaches 0.3-wt%, the workability reduces 33.39% compared to the ordinary cement pastes. When the concentration of SNS is above 0.4-wt%, the workability of cementitious composites drops down significantly. Compared to the control group at the addition of 0.40-wt%, 0.50-wt% and 0.60-wt% SNS, which leads the pastes' slab diameter to decrease 86.59%, 90.75% and 96.05%, respectively.

When SNS is less than 0.3-wt%, the workability between 50% and 150% is suited for research. However, the workability of the cement pastes sharply decreases with a higher concentrate of 0.3-wt% SNS. This can be attributed to the high specific surface area of SNS and SNS dominant hydrophilic functional groups. These two factors could absorb and consume most of the free water in the cement pastes for increasing the friction. The viscosity effect of SNS enhancing the stability of the cementitious composites hardened properties.

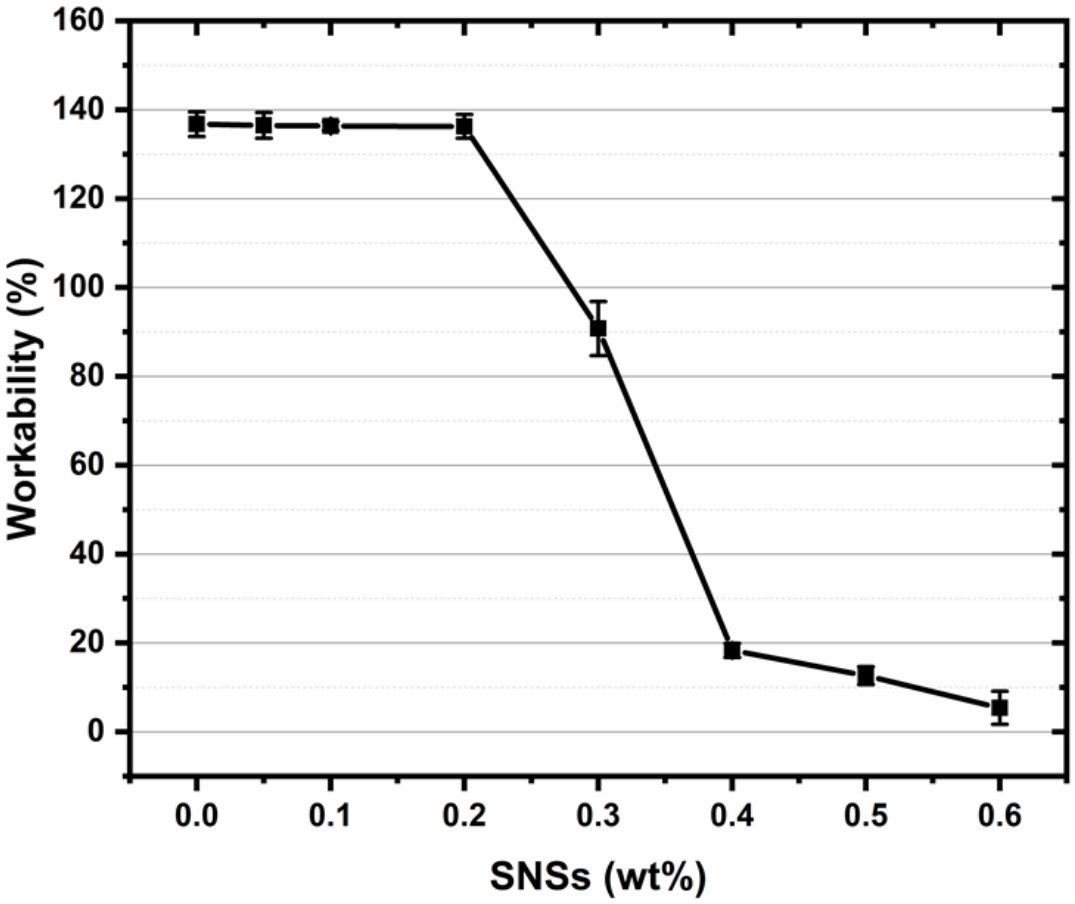

Figure 4.6 Mini-slump workability results of SNS-cementitious composites

4.4 Electrochemical characterisation of SNS-cementitious composites

The DOH of cement pastes is closely related to the electrochemical behaviour. The electrochemical character methods, electrochemical impedance spectroscopy and cyclic voltammetry, can accurately capture the change in ionic concentration and charge transfer mobility. In this section EIS, CV and equivalent circuits were employed to reveal the mechanism of SNS that accelerates the hydration of cementitious composites. The SNS addition along with the formation and area of the CV curve changes, the CV properties of the cementitious matrix were reflected through the storage capability. The Nyquist plot and equivalent circuit simulations show the matrix

result in resistance of pore solution and charge transfer. The sensitive and non-destructive changes in electrical response reflect the cementitious hydration process.

4.4.1 Cyclic voltammetry of SNS-cementitious composites

The effect of SNS on the electrochemical behaviour of the cementitious composites was investigated using CV charge-discharge curves between -0.5 V and 0.5 V. Figure 4.7 and Figure 4.8 show the CV curves at different SNS concentrations and curing ages. As the graphs illustrate, the CV curves exhibit elliptical and symmetrical shapes, indicating that the cementitious composites are behaving like electrical capacitors (Tao *et al.*, 2014).

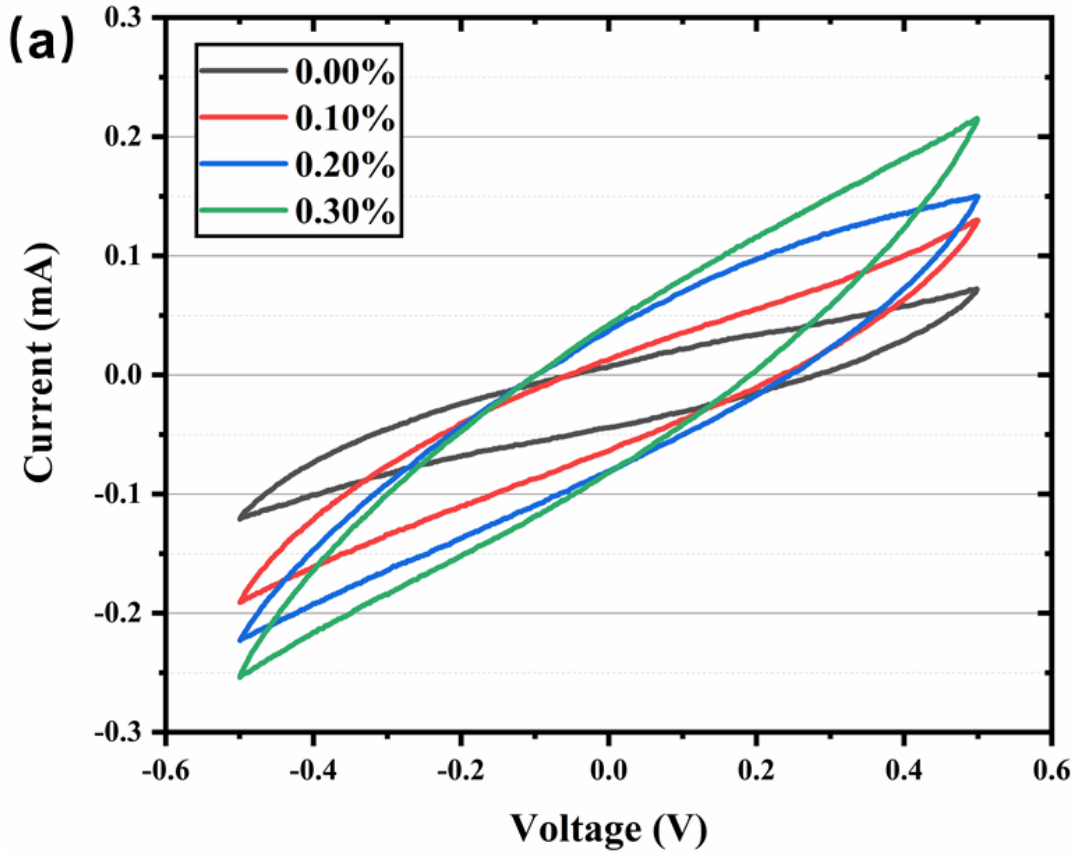

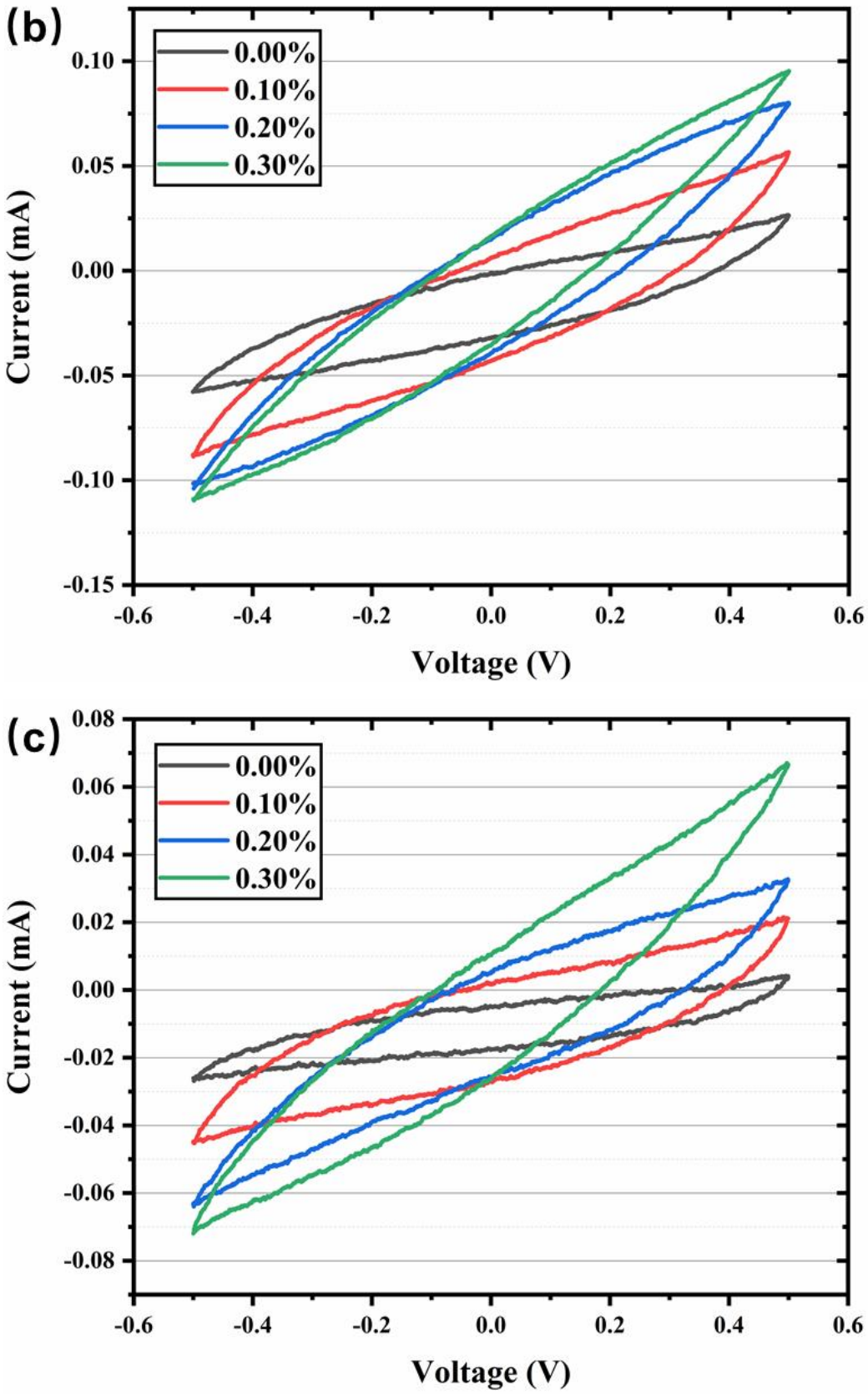

Figure 4.7 CV curves of SNS cement paste at days of (a) 7, (b) 14 and (c) 28

The integrated area of the CV curves provides direct information on the amount of charge transfer Q due to ion diffusion, resulting from the interaction of SNS with cement particles during hydration. The charge transfer Q during hydration is expressed as (Li *et al.*, 2009):

$$Q = \frac{\int IdV}{2v} \tag{4.2}$$

Where $\int IdV$ is the integrated area of the CV curve and v is the scan rate (V/s).

As shown in Figure 4.7(a-c), for a given age, the charge transfer Q increases as the SNS concentration increases, which demonstrates that the SNS promote the transport of ion within the cementitious composites, resulting in good ionic conductivity. On the other hand, Figure 4.8(a-d) shows that for a given SNS concentration, the charge transfer Q decreases as the cementitious composites curing age increases. This means that the transport of ion within the cementitious composites diminishes as the curing age increases.

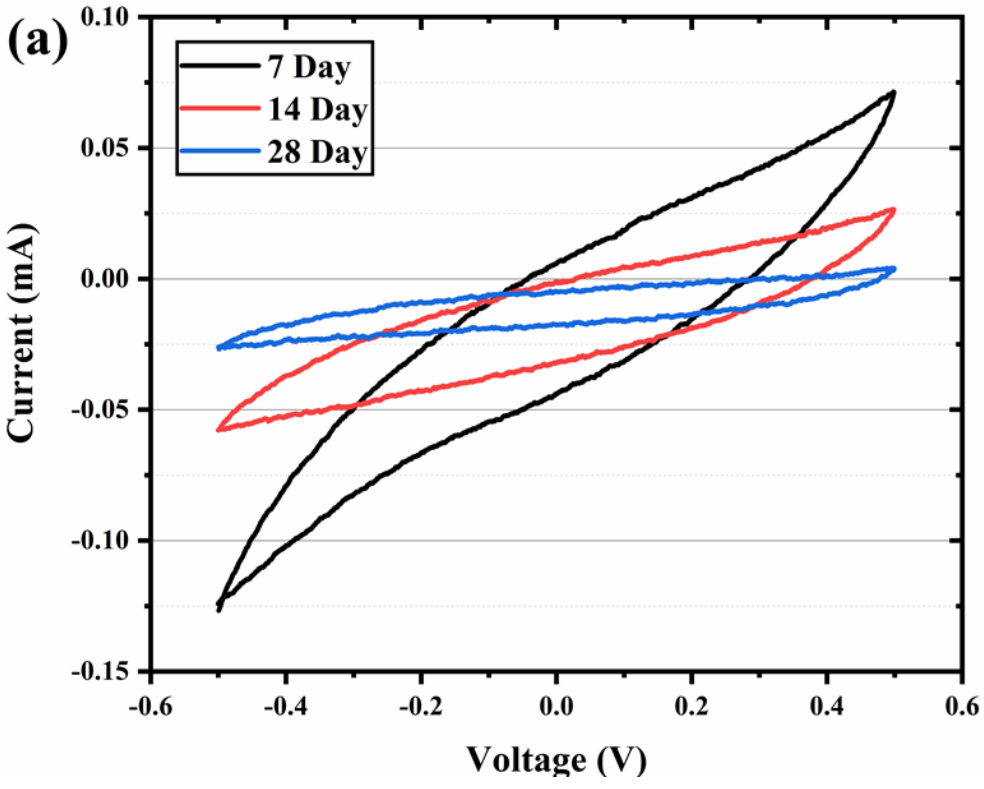

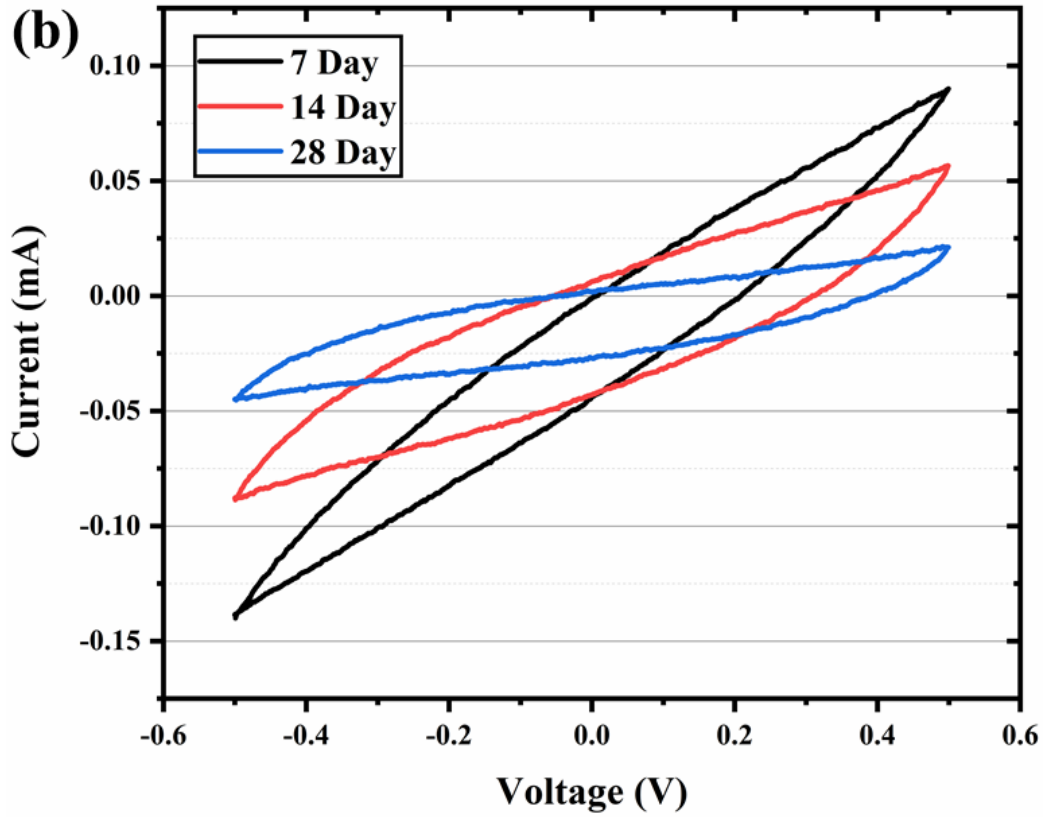
(b)
7 Day
14 Day
28 Day
Current (mA)
0.10
0.05
0.00
-0.05
-0.10
-0.15
-0.6
-0.4
-0.2
0.0
0.2
0.4
0.6
Voltage (V)

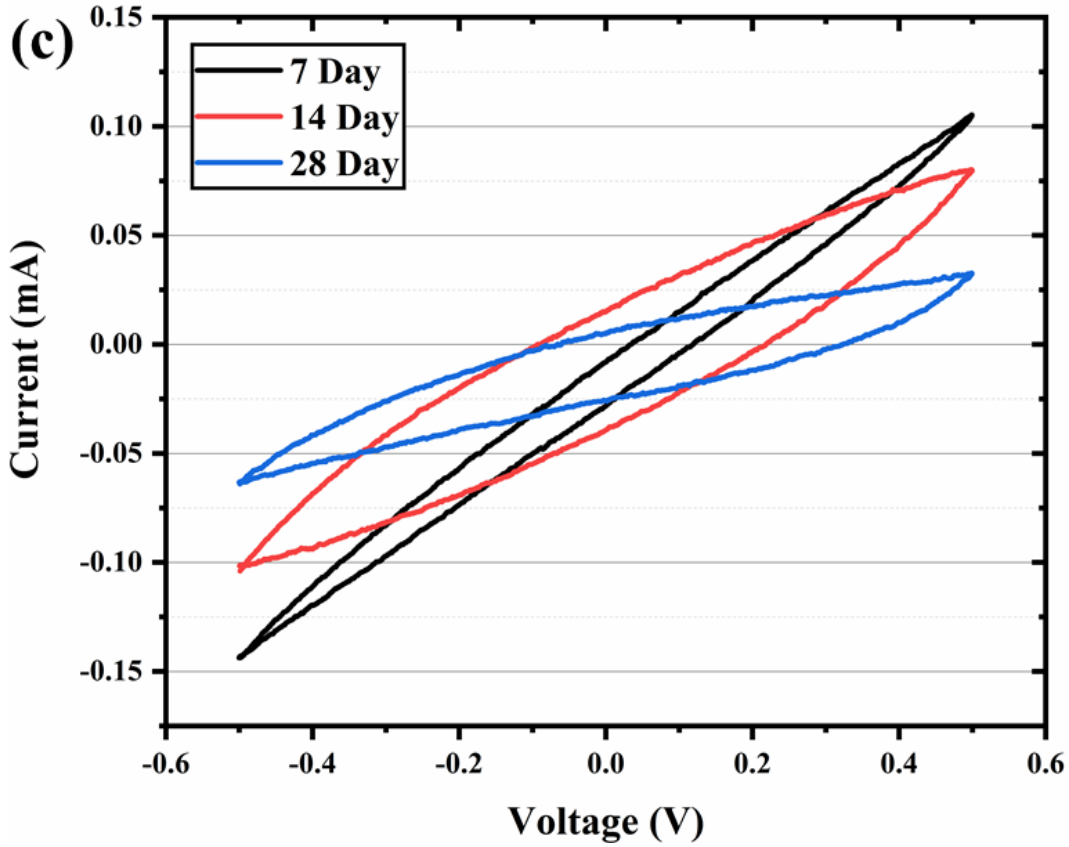
(c)
7 Day
14 Day
28 Day
Current (mA)
0.15
0.10
0.05
0.00
-0.05
-0.10
-0.15
-0.6
-0.4
-0.2
0.0
0.2
0.4
0.6
Voltage (V)

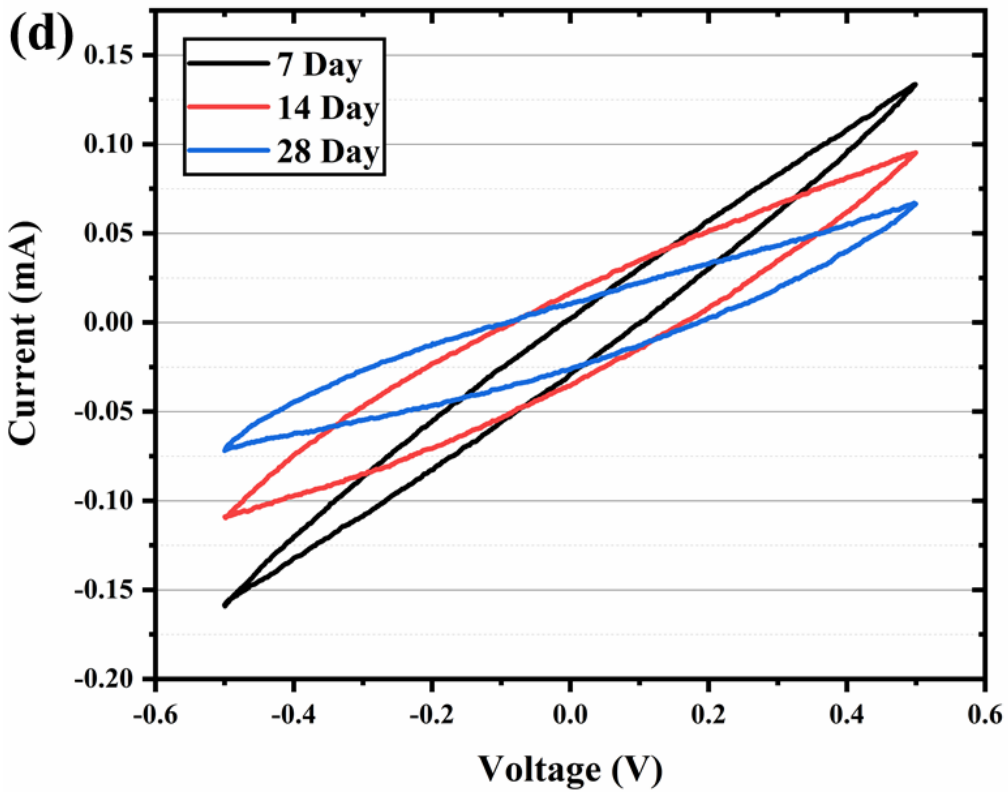

Figure 4.8 CV curves of SNS-cementitious composite at SNS-wt% of (a) 0, (b) 0.1, (c) 0.2, (d) 0.3

Figure 4.7 and Figure 4.8 depicts that for a given curing age, the current increases with increasing SNS concentration and for a given SNS concentration, the current decreases with increasing curing ages. This is attributed to the effect of the SNS and curing ages on the capacitance of the cementitious composites. From the Figure 4.9 CV curves, the peak current is estimated at a potential of 0.5 V and plotted vs SNS concentration. At the same SNS addition, the cement matrix peak current continues to decrease with the hydration process. In addition, the maximum current measured in the matrix gradually increases with the addition of SNS-wt%. The current *I* proportional to the capacitance *C* and is given by the following equation (Fan *et al.*, 2006):

$$I = Cv \tag{4.3}$$

Where *C* is the capacitance of the cementitious composites and v is the scan rate (*V/s*).

From the CV curves, the capacitance C of the cementitious composites was calculated using the following equation (Harrington, 2003):

$$C = \frac{Q}{\Delta V} \tag{4.4}$$

where ΔV is the potential voltage window and Q is the charge transfer and is given by Eq.(4.2). Substituting Eq (4.2) with Eq. (4.4) is shown below:

$$C = \frac{\int I dV}{2\nu\Delta V} \tag{4.5}$$

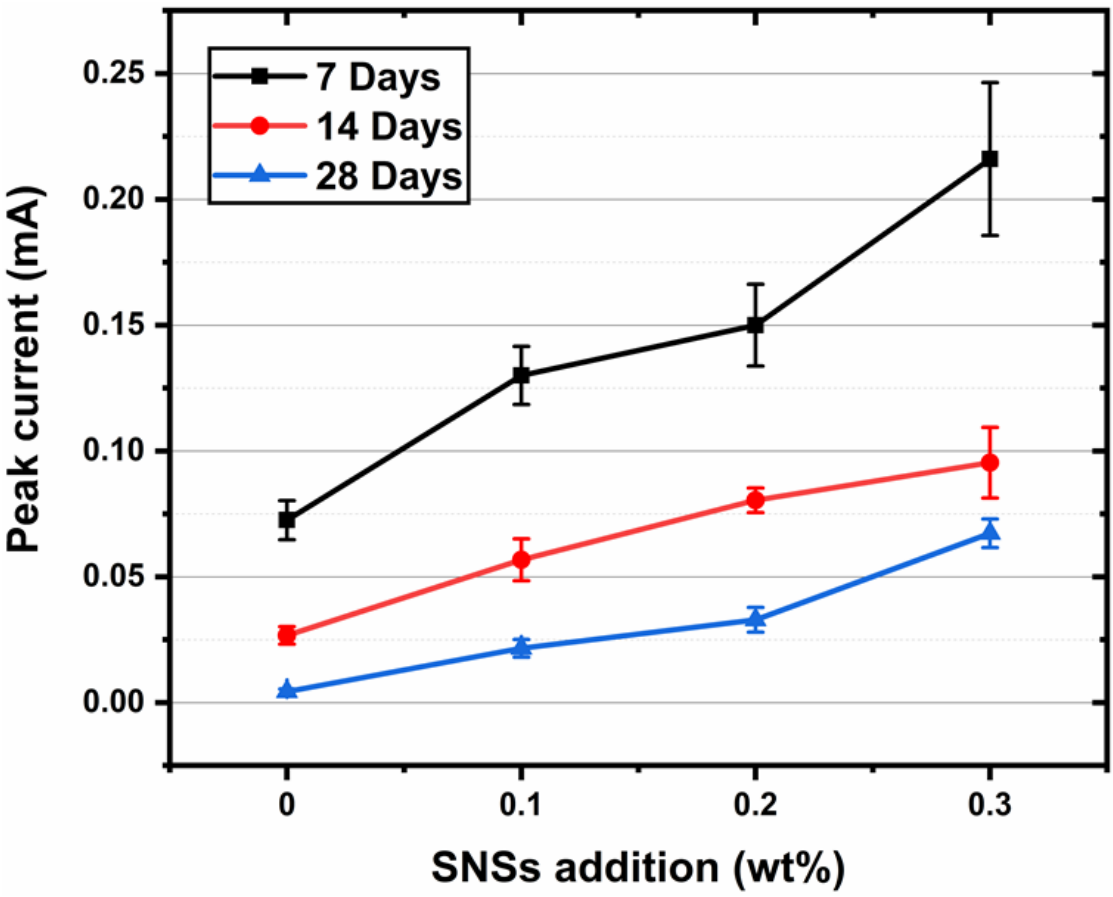

Figure 4.9 Peak current of SNS-cementitious composites

The effect of SNS and curing ages on the capacitance of the cementitious composites is shown in Figure 4.10. Figure 4.10(a) shows that the hydration leads to an increase in matrix resistance and a decrease in capacitance, the capacitance of cementitious

composites significantly increases with increasing SNS concentration. This is attributable to the combined effect of adsorbed SNS (a-SNS) and free SNS (f-SNS) in cementitious composites.

The f-SNS dissolution promotes the chemical interaction on the cement particle interface. Firstly, the f-SNS bond hydroxyl/hydroxymethyl functional group break under the alkaline conditions, brokered SNS backbone and the carbon atoms increase hydrogen and hydroxyl group concentration. Secondly, during hydration the OH^- and C-OH fragments decompose from the f-SNS and the enriched H protons in water allow further ion exchange with C3S. Finally, the concentration of ions increases the penetration depth of protons into the C3S, leading to a more hydrated area allowing C3S to release more Ca^{2+} and Si^{2+}.

Furthermore, the SNSs are adsorbed onto the surface of the cement particles when its contact, and then the a-SNS gradually embed into the hydration products during the hydration process. During the cement hydration process, the hydrated product crystals interact with the evenly distributed a-SNS surface. The hydrophilic nature of the SNS enable them to act as a ‘reservoir’ and a transport pipeline. The SNS sandwiched between the hydration products can store sufficient water to continuously transport water molecules to the deeper part of the hydration products. The water in the capillary of the Ca/Si layer is absorbed by the hydrophilic SNS, forming numerous conductive channels, which accelerate the diffusion of water molecules into the SNS matrix network (Cao *et al.*, 2015).

The large SSA of a-SNS has a bimodal pore size distribution (0-10 nm and 40-80 nm), the SNS 40-80 nm pores are able to store more water molecules, whilst the 0-10 nm pores provide more reaction sites for the C3S reaction. The surface of the highly

reactive a-SNS cementitious enables it to work effectively as an ionic catcher, the Ca^{2+}, Si^{2+}, K^{+} and Na^{+} ions in the cement matrix attracting more easily to the anionic electrostatic surface of the SNS (Voisin *et al.*, 2017; Hisseine, Omran and Tagnit-Hamou, 2018). The f-SNS dissolution increases the concentration of ions, a-SNS promotes C3S hydration and attracts the anionic electrostatic surface which improves the capacitance of cementitious composites. The centrifugation experiment in chapter 6 was used to quantified characterise of a-SNS and f-SNS in the cement particles.

Figure 4.10(b) shows with the hydration age increase, plain and SNS cement capacitance shows a continually decreasing trend. The capacitance decreases with age attributed to the hydration product continuously generated, consuming the ions in the pore solution. The compact cementitious composites internal structure resulting in the capacitance decrease.

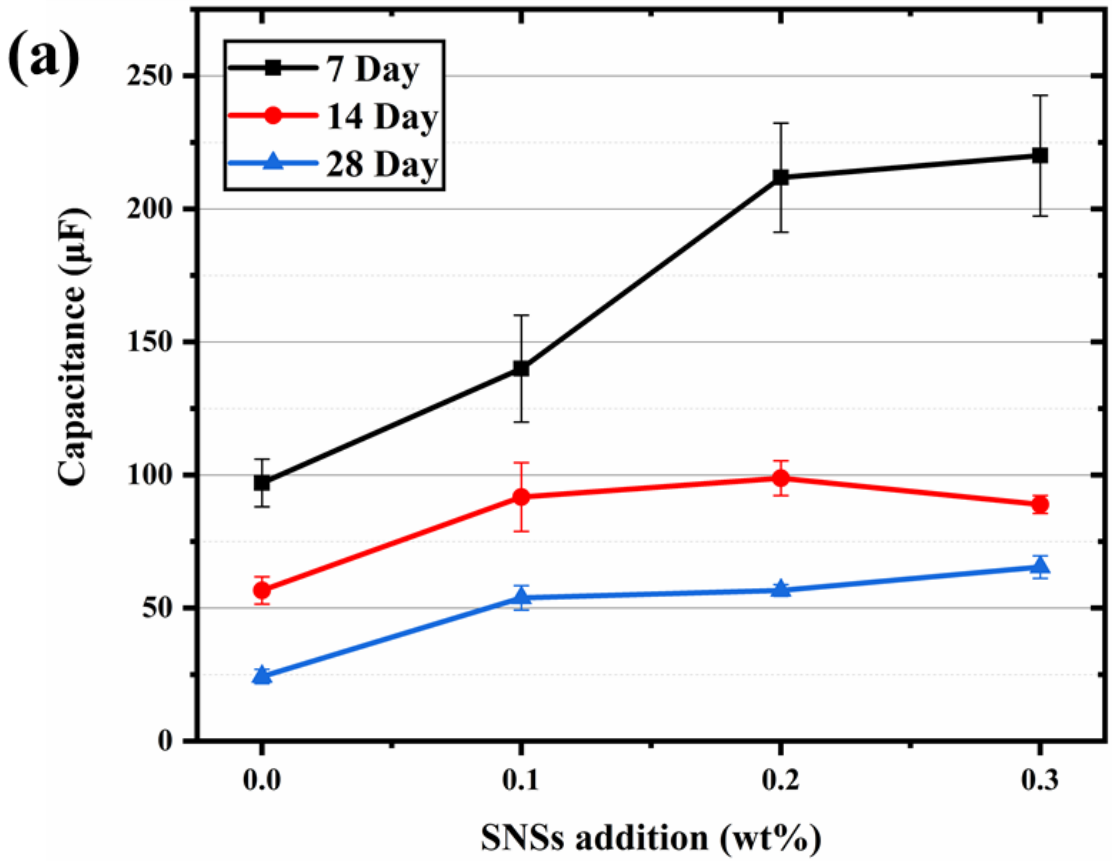

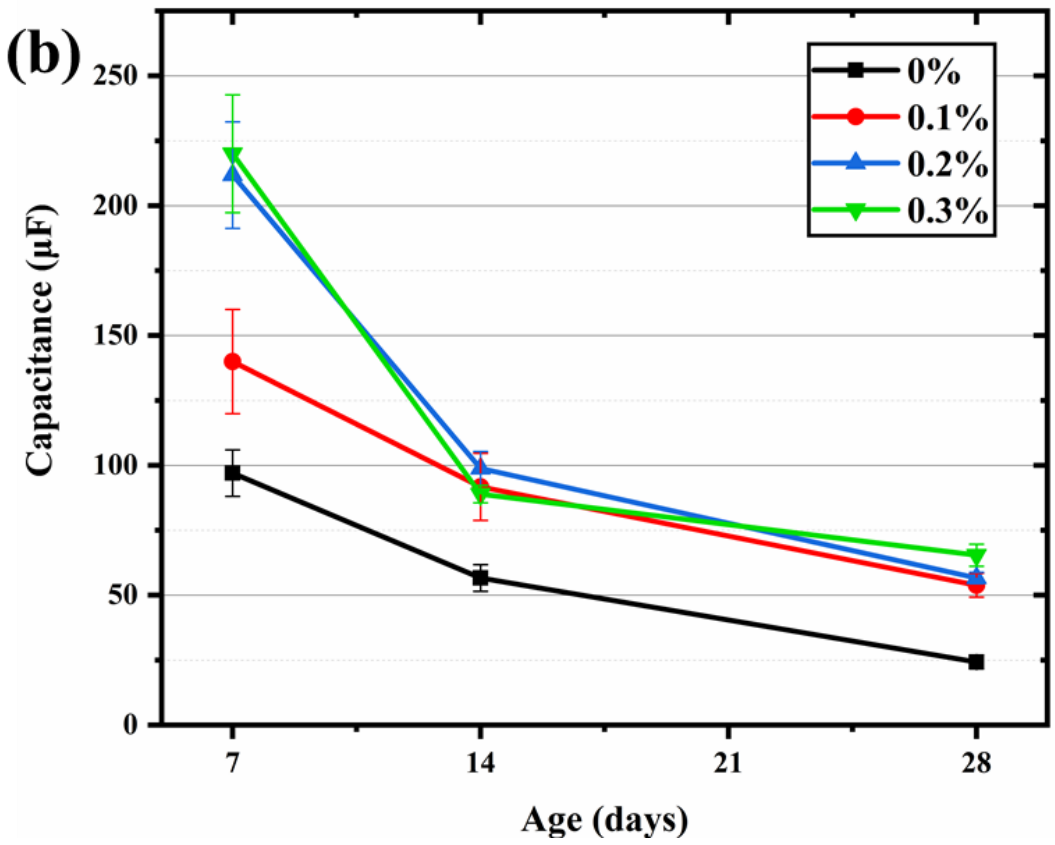

Figure 4.10 SNS-cementitious composites CV curves capacitance at (a) different SNS addition (b) different ages

4.4.2 EIS characterisation of the different hydration stages of cement pastes

4.4.2.1 Impedance of cementitious composites

The different concentrations of SNS cementitious composites are quantified through EIS. The experiment continuously applies the same voltage to the cement pastes within a specific alternating current (AC) frequency range, calculating the real (resistance) and imaginary (reactance) parts of the complex impedance ω based on the input signal and the amplitude of the AC. Impedance magnitude, the real part of impedance and the imaginary part of impedance are defined as follows:

$$Z(\omega) = R + jX \tag{4.6}$$

$$R = |Z(\omega)| \cos \alpha \tag{4.7}$$

$$X = |Z(\omega)| \sin \alpha \tag{4.8}$$

Where $Z(\omega)$ is impedance magnitude, ω is operating frequency, R is the resistance, j is the imaginary unit, X is the reactance and α is the phase difference between voltage and current (phase shift).

Figure 4.11 shows the 28 days 0.3-wt% SNS cementitious pastes Nyquist plot. From left to right, Figure 4.11 shows the range of 1MHz to 0.1 Hz under AC signal scanning the cementitious pastes results, the horizontal axis Z' represents the real part of the impedance and the vertical axis Z'' represents the imaginary part of the impedance. The impedance Z can be calculated by the following equation (Rajabipour *et al.*, 2005).

$$|Z| = \sqrt{(\mathrm{Z}')^2 + (\mathrm{Z}'')^2} \tag{4.9}$$

Figure 4.11 is a typical SNS-cementitious composites Nyquist plot, which mainly composes on two semi-arcs: (i) the high-frequency arc (100KHz-1000KHz) is related to the overall properties of the nanocomposite and (ii) the low-frequency arc (0.1 Hz-100KHz range) is related to the interface characteristics of the stainless steel electrode with the specimen (McCarter and Brousseau, 1990). The value of the real part resistance (Z') of the impedance is related to the charge transfer resistance and electron transfer, which is inversely proportional to the electron transfer rate. The imaginary part of impedance (Z'') includes capacitive reactance and inductive reactance. The reactance value is related to the energy storage capacity of the metal/insulator/metal sandwich structure. In addition, the angular frequency $\omega = 1/RC_{dl}$, the C_{dl} is a double-layer capacitor representing the maximum storage capacitor of electrical energy (Hsu *et al.*, 2004; Chung, 2010).

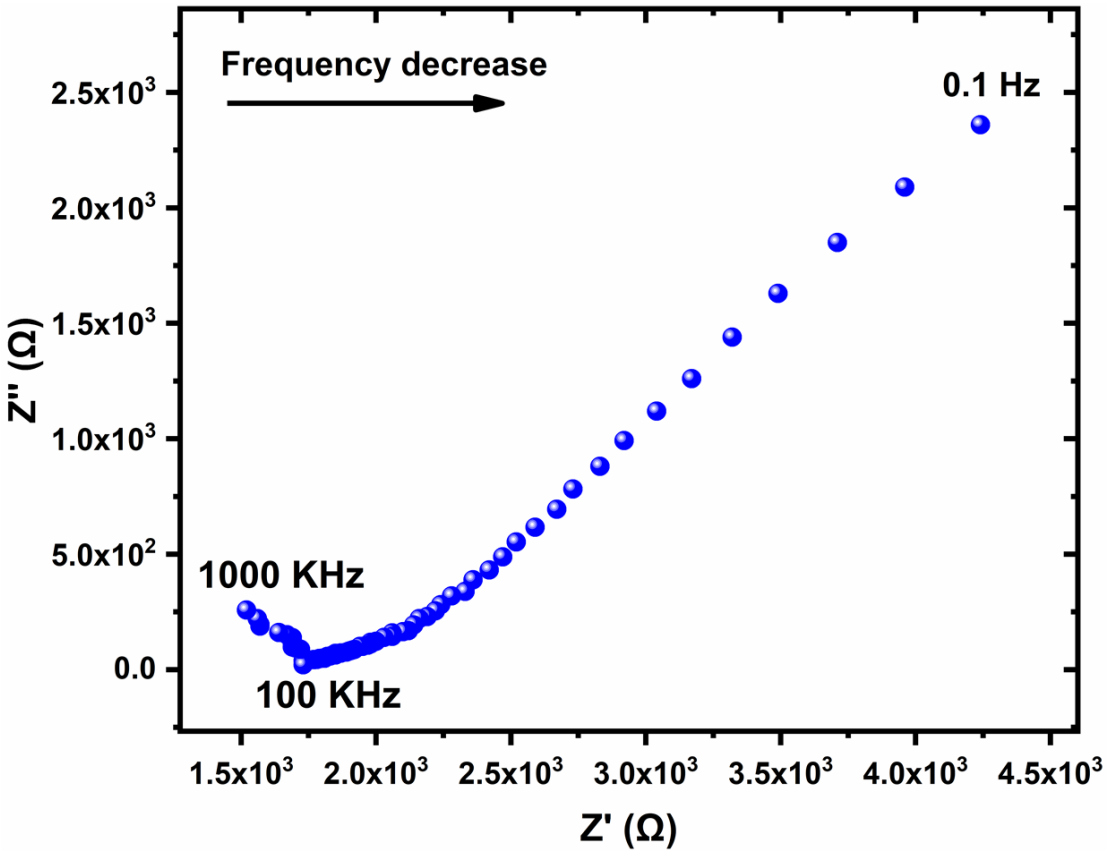

Figure 4.11 Nyquist plot of 28 days cementitious composites with 0.3-wt% addition

4.4.2.2 EIS Nyquist plot and Bode plot of SNS cement pastes

Figure 4.12 shows the 7-day Nyquist plot of SNS-cementitious composites. In the early hydration stage, the high-frequency Nyquist plot is presented as a semi-circular arc, and the low-frequency diagonal line shows a deviation of less than 45°. The low frequency of cementitious composites impedance real (Z′) and imaginary (Z′′) values continually decreases with the increase in the SNS amount. The high-frequency semi-circular arc slightly shifts to the right as the SNS addition amount rises. The Nyquist plot was similar to cementitious composites blended with CNTs, indicating that the SNS cement matrix has a complex electrochemical system (Han et al., 2019).

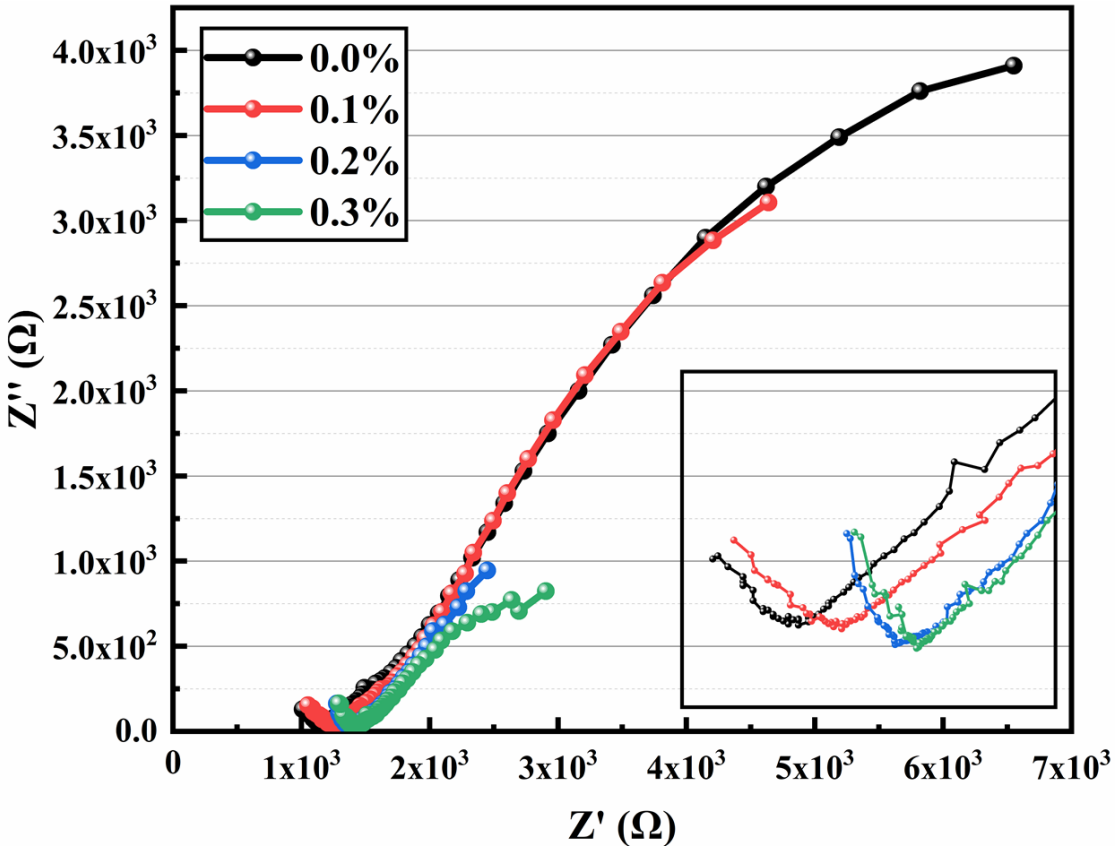

Figure 4.12 Nyquist plot of SNS-cementitious composites at 7 days

Figure 4.13 shows the Nyquist plots of SNS cementitious composites at days of 7, 14 and 28. It can be observed that the plain and SNS-cementitious composites real impedance (Z') and imaginary impedance (Z'') both increase with the curing ages (Figure 4.13). This is because the matrix curing accompanies the densification of the microstructure, as matrix DOH improvement which gradually increases the electron transmission impedance. At 28 days the low frequency diagonal line leans closer to 45 degrees, the corresponding impedance values (resistance of solution) increase and the Nyquist plot's high frequency maintains the same shift trend as at 7 days. The increasing amount of SNS results in an increase in the matrix resistance of the pore solution, and the high-frequency Nyquist plot semi-circular arc slightly shifts to the right. Furthermore, the low frequency of cementitious composites Z' and Z'' values continually decrease with the increase in SNS amounts. With the increase of SNS

addition and curing age, the low frequency of SNS cement paste continued to decrease compared to the control group.

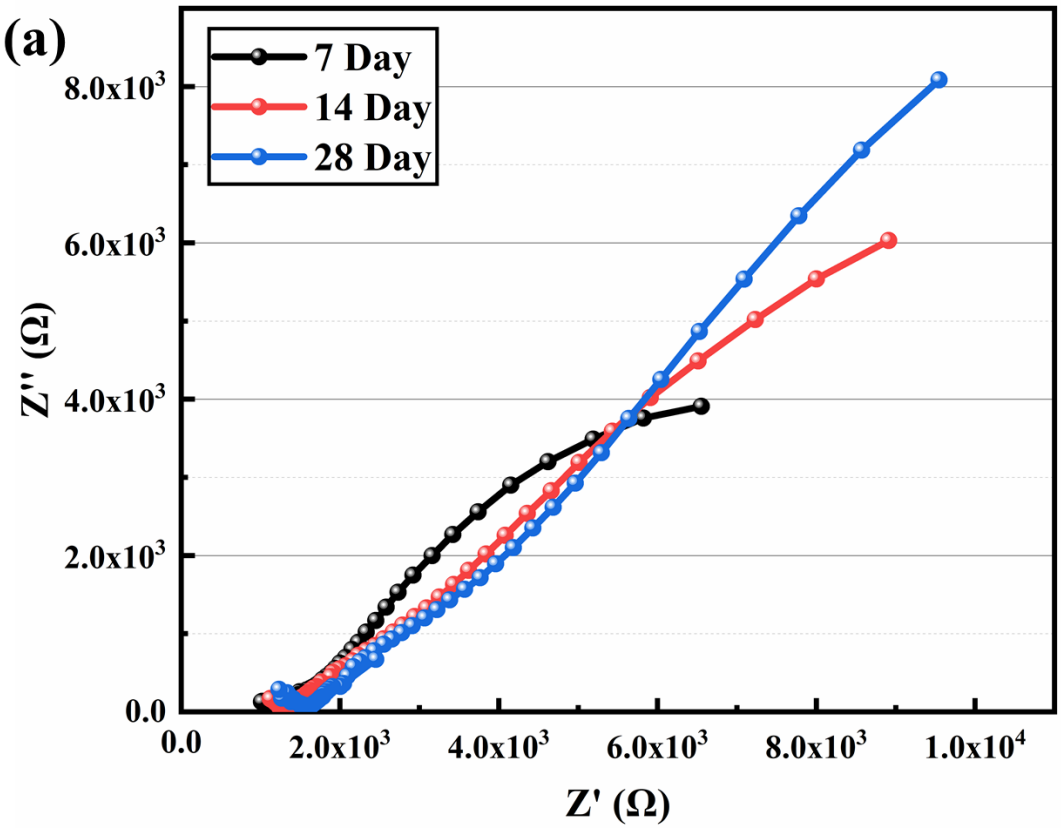

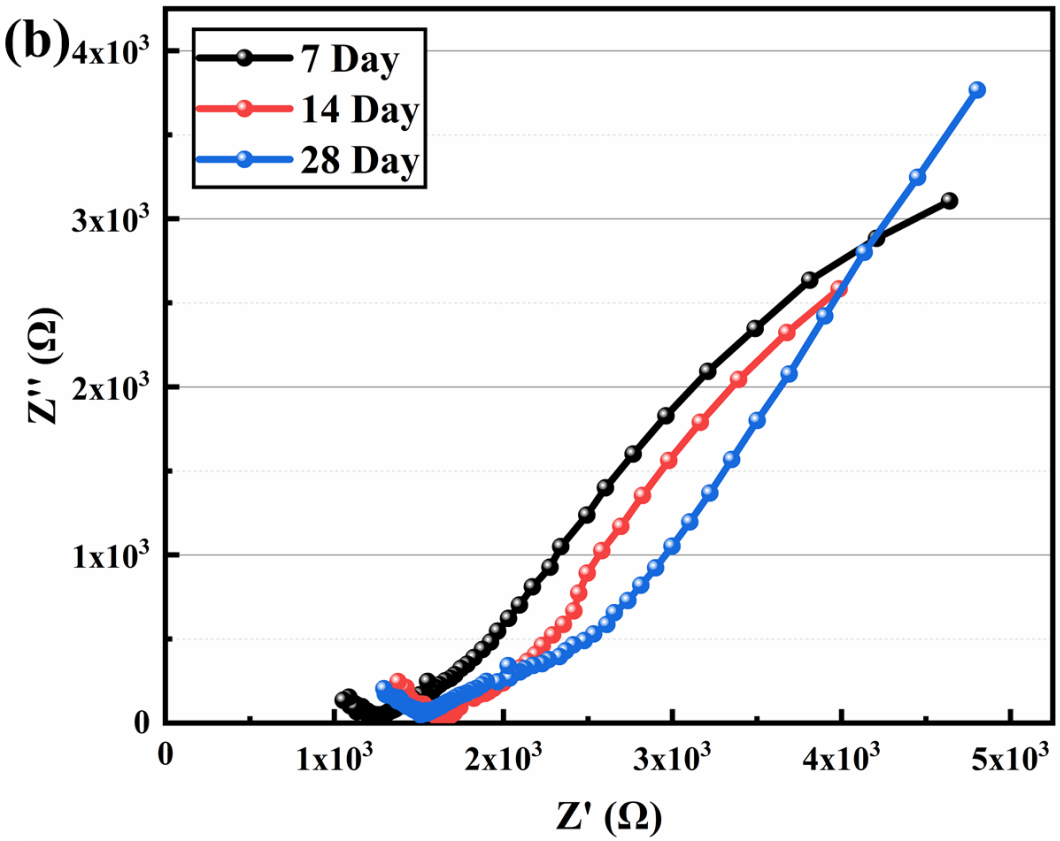
(b)
7 Day
14 Day
28 Day
Z'' (Ω)
Z' (Ω)
0
1x10³
2x10³
3x10³
4x10³
5x10³

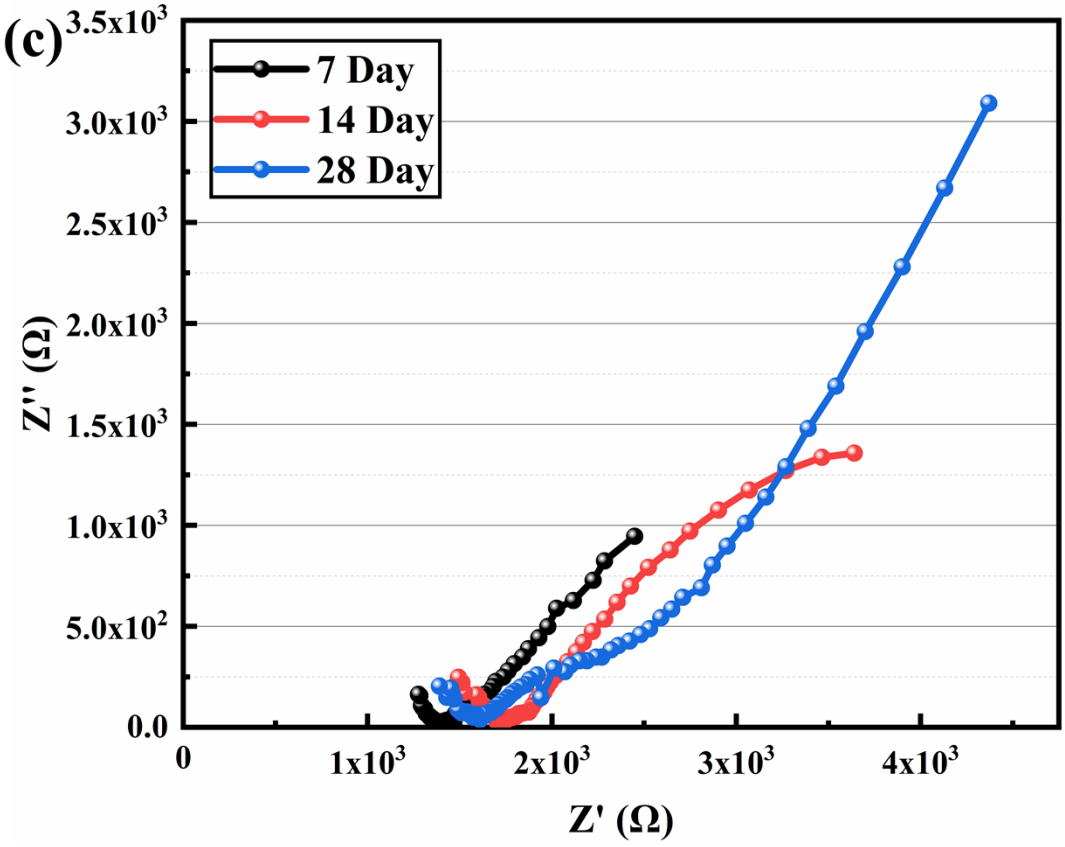
(c)
7 Day
14 Day
28 Day
Z'' (Ω)
Z' (Ω)
0.0
5.0x10²
1.0x10³
1.5x10³
2.0x10³
2.5x10³
3.0x10³
3.5x10³
0
1x10³
2x10³
3x10³
4x10³

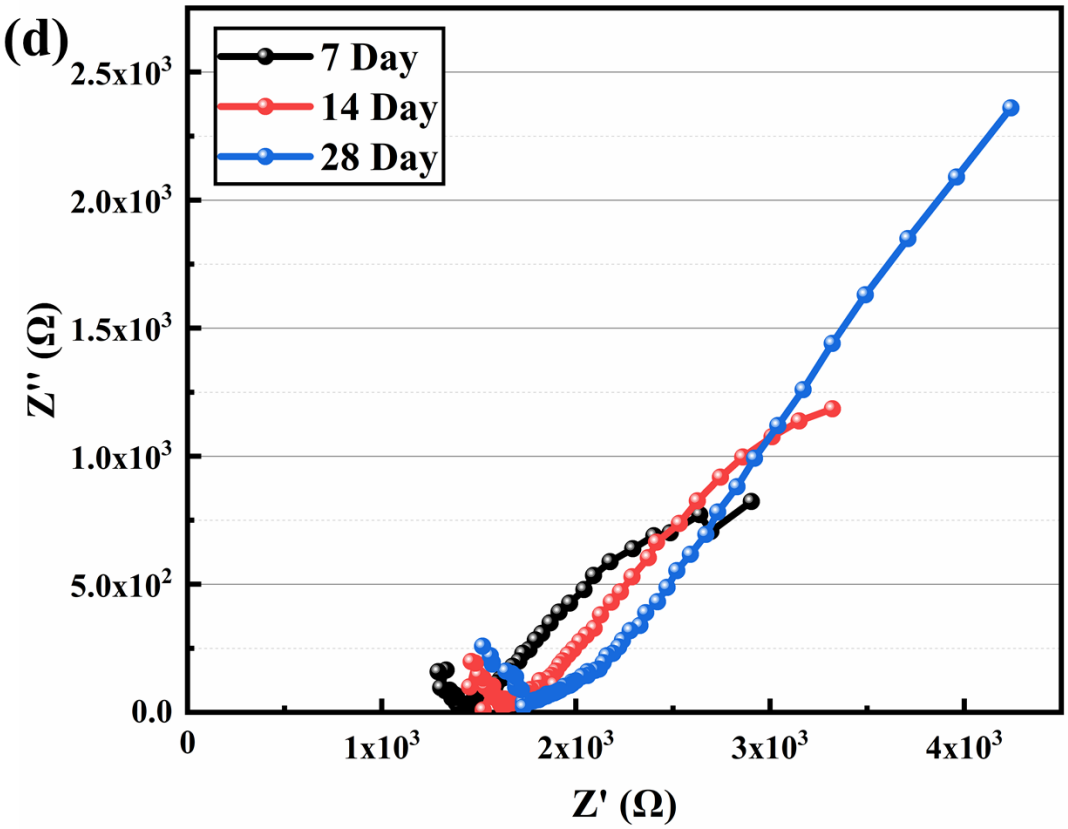

Figure 4.13 Nyquist plot of SNS-cementitious composites at SNS-wt% of (a) 0, (b) 0.1, (c) 0.2 and (d) 0.3

Figure 4.14 shows the impedance of SNS-cementitious composite at 7, 14 and 28 days. The incorporation of SNS significantly decreases the cementitious composites low-frequency impedance. With the increase of the SNS additions, the formation of the conductive electronic network of a-SNS matrix is gradually superimposed. The encapsulated moisture of a-SNS with C-S-H and $Ca(OH)_2$ actives the path of conductivity. With the increase of SNS additions, the conductive electronic network of the SNS matrix gradually superimposed its formation.

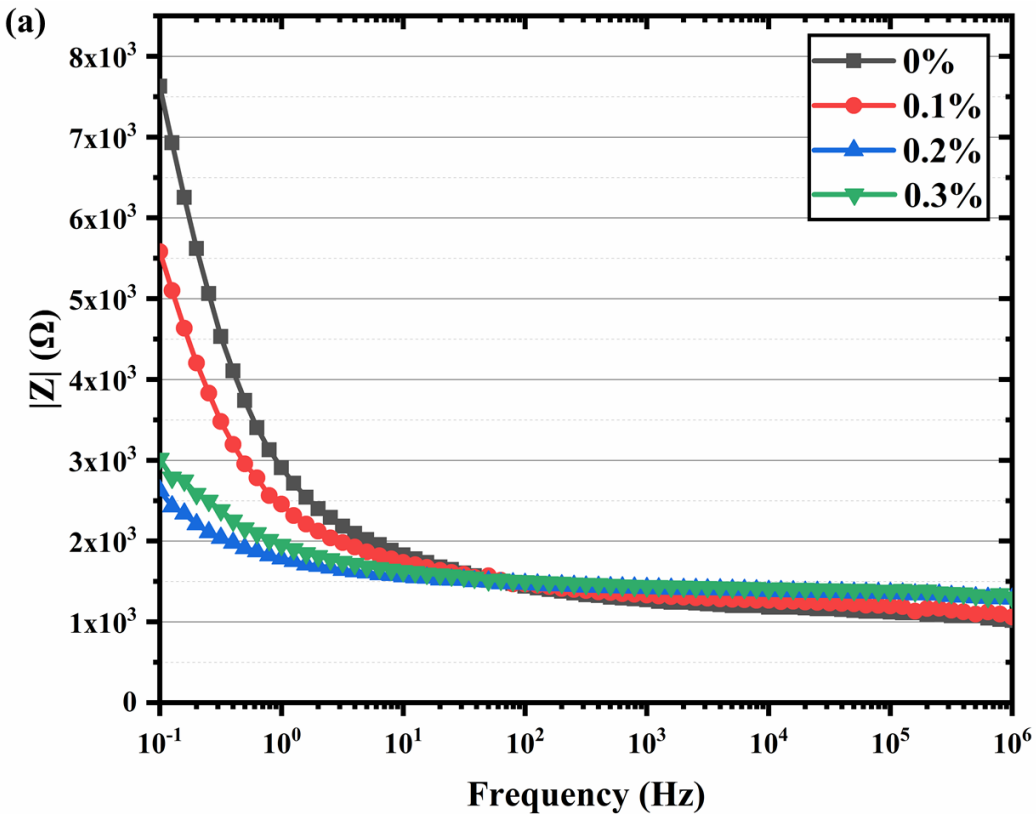
(a)
8x10^3
7x10^3
6x10^3
5x10^3
4x10^3
3x10^3
2x10^3
1x10^3
0
|Z| (Ω)
10^-1
10^0
10^1
10^2
10^3
10^4
10^5
10^6
Frequency (Hz)
0%
0.1%
0.2%
0.3%

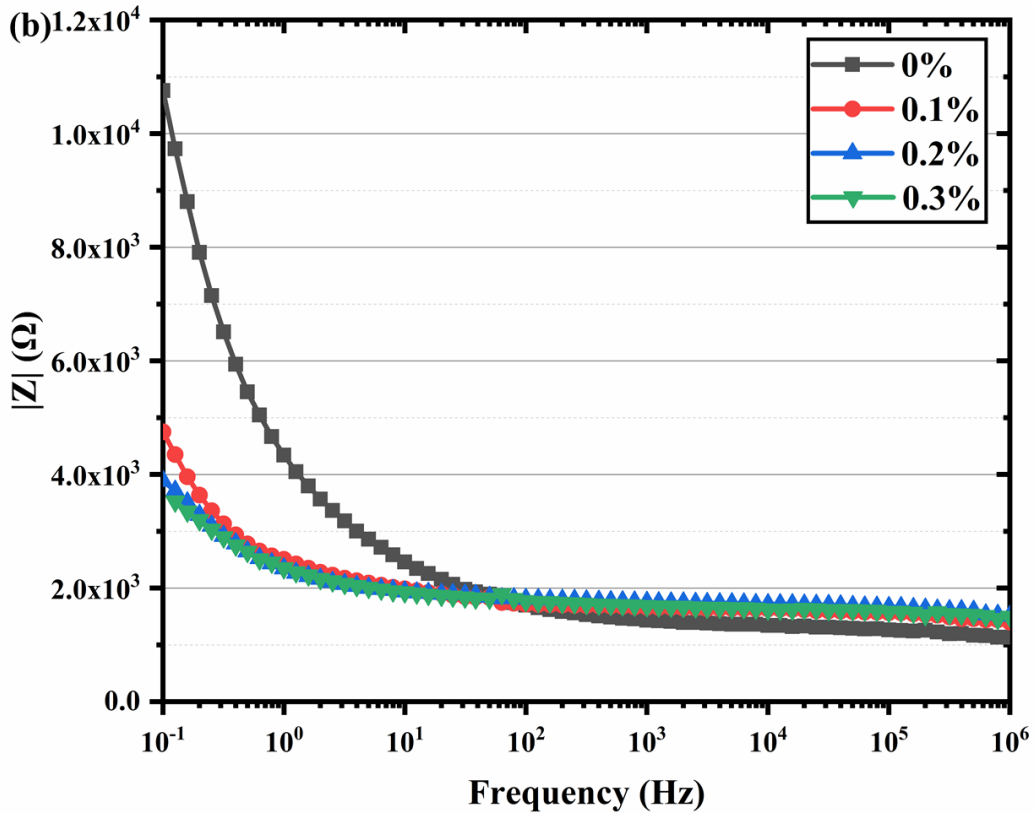
(b)
1.2x10^4
1.0x10^4
8.0x10^3
6.0x10^3
4.0x10^3
2.0x10^3
0.0
|Z| (Ω)
10^-1
10^0
10^1
10^2
10^3
10^4
10^5
10^6
Frequency (Hz)
0%
0.1%
0.2%
0.3%

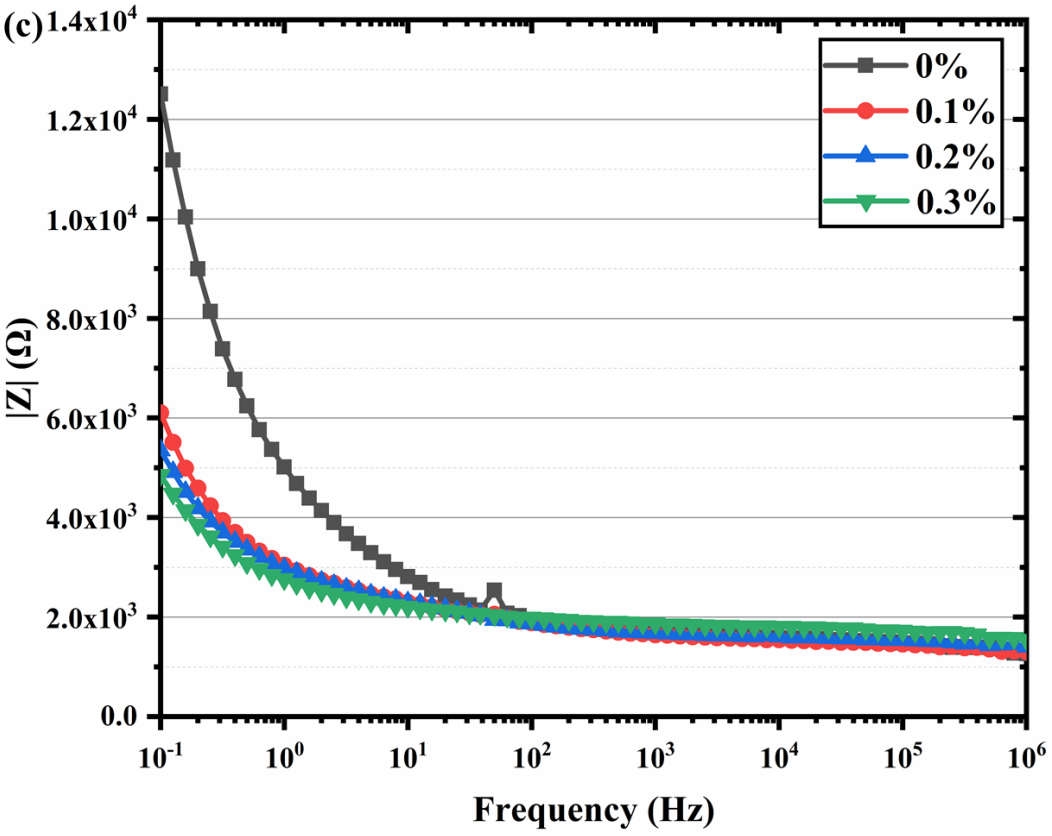

Figure 4.14 Impedance for the different SNS addition cementitious composites at days of (a) 7, (b) 14 and (c) 28

As shown in Figure 4.15, the phase angle of SNS-cementitious composites is related to the age and frequency. The phase angle (θ) calculates the equation as below:

$$\tan\theta = \frac{Z''}{Z'} \tag{4.10}$$

The impedance of cementitious composite is positively related to the phase angle, which corresponds to the Nyquist plot (Figure 4.14). The cementitious composite phase angle slightly increased with the curing ages. Additionally, as seen from Figure 4.15 the cement pastes low frequency phase angle smoothly decreases as the SNS additive increases. For example, the first phase peak is shown between 0.1 to 1 Hz, at 7 days the 0% SNS addition phase value is 35° and with 0.3% SNS addition decreases to 16°.

During the hydration process, the phase angle of SNS-cementitious composites is steadily lower than the control group. As shown in Figure 4.15, the SNS samples have the same trend and shape in phase plots with plain cement pastes. Furthermore, the second phase took place between 10 to 100 Hz due to the electrode and the matrix building a solid-solid interface. The above result phase angle effectively reflects the cementitious composites.

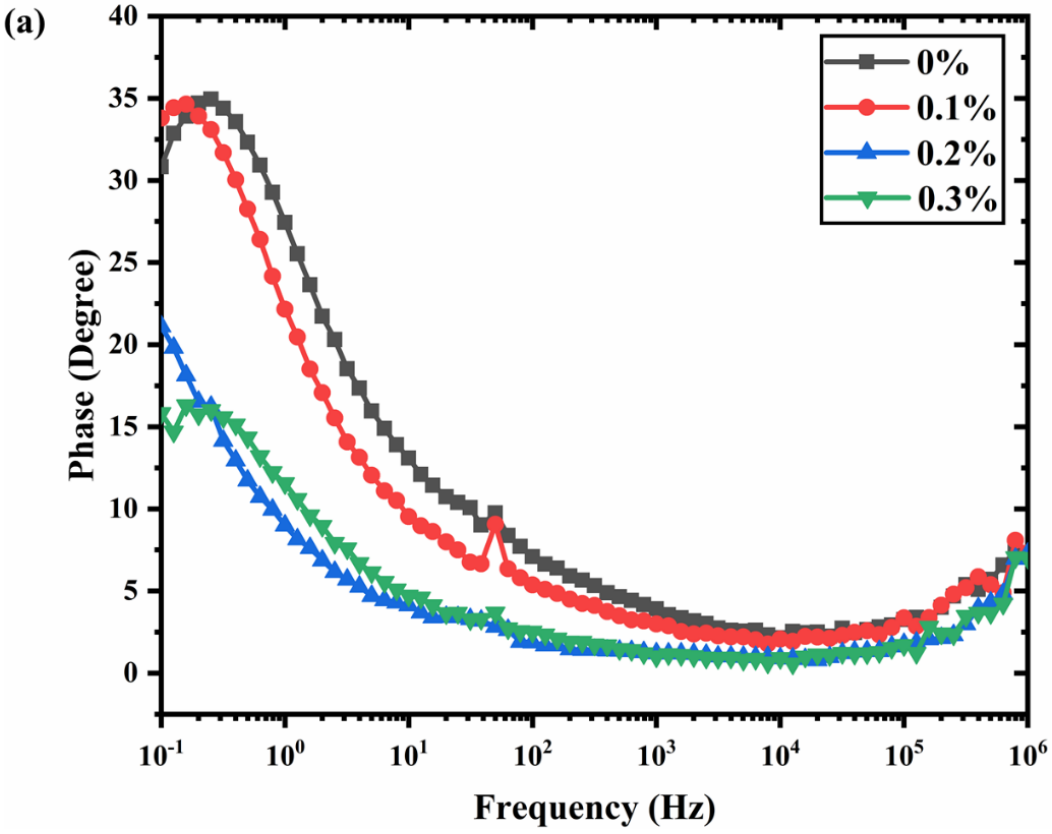

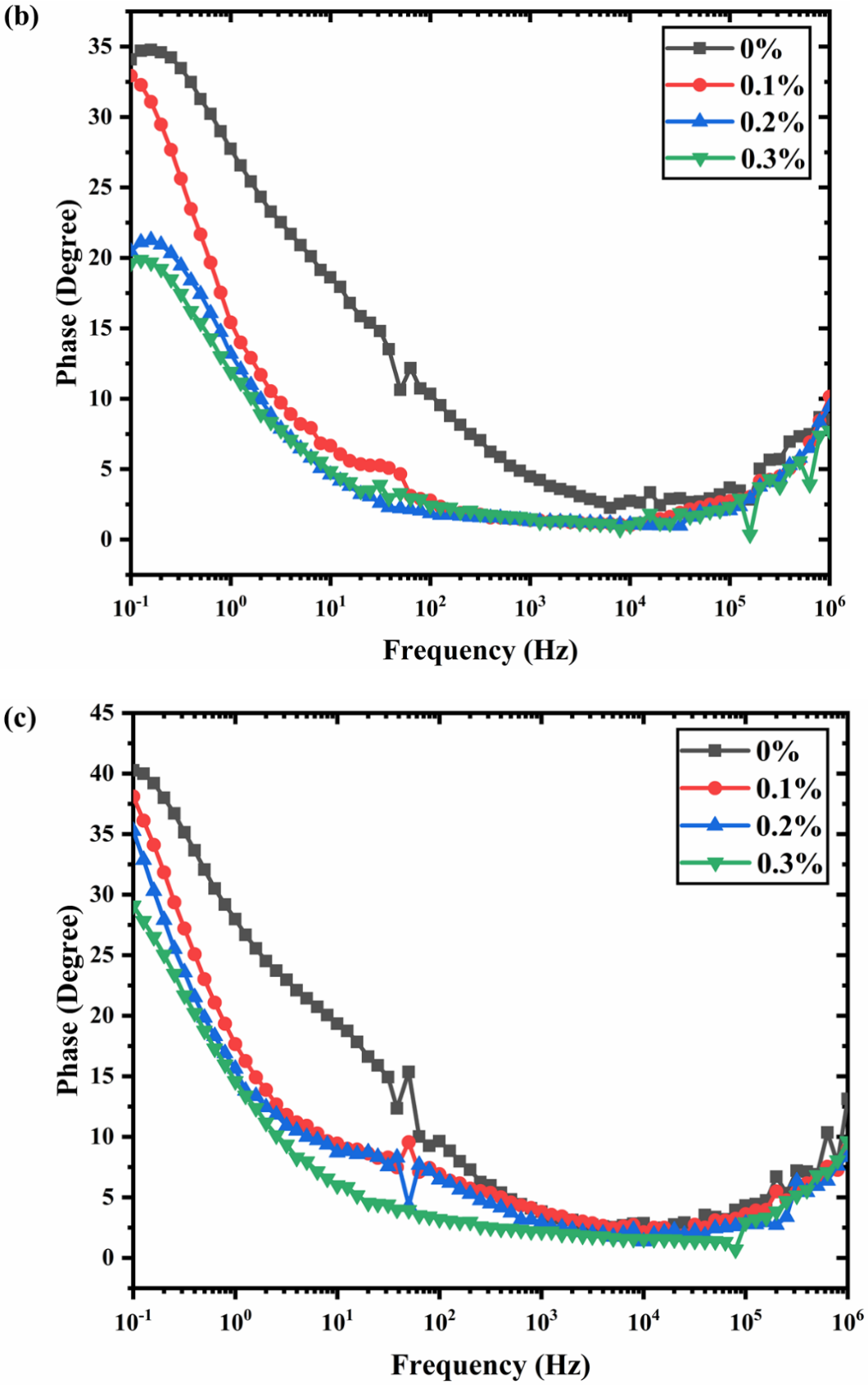

Figure 4.15 SNS cementitious composites EIS Phase angle Vs Frequency (a) 7 days, (b) 14 days, (c) 28 days

Figure 4.16 shows the cementitious composites impedance (log |Z|) and phase relates to the log f. In theory, the phase value in the high frequency approach to zero reveals the specimen impedance. However, the EIS experiment result shows that the phase of cementitious composites cannot reach zero, the closest to zero area phase angle threshold (PAD) is considered to reveal the close impedance data (Belli *et al.*, 2020). As shown in Figure 4.16, the PAD happened between the middle and high frequency range. The cementitious composites bulk resistance is calculated on the average of log |Z|, corresponding to the PAD area.

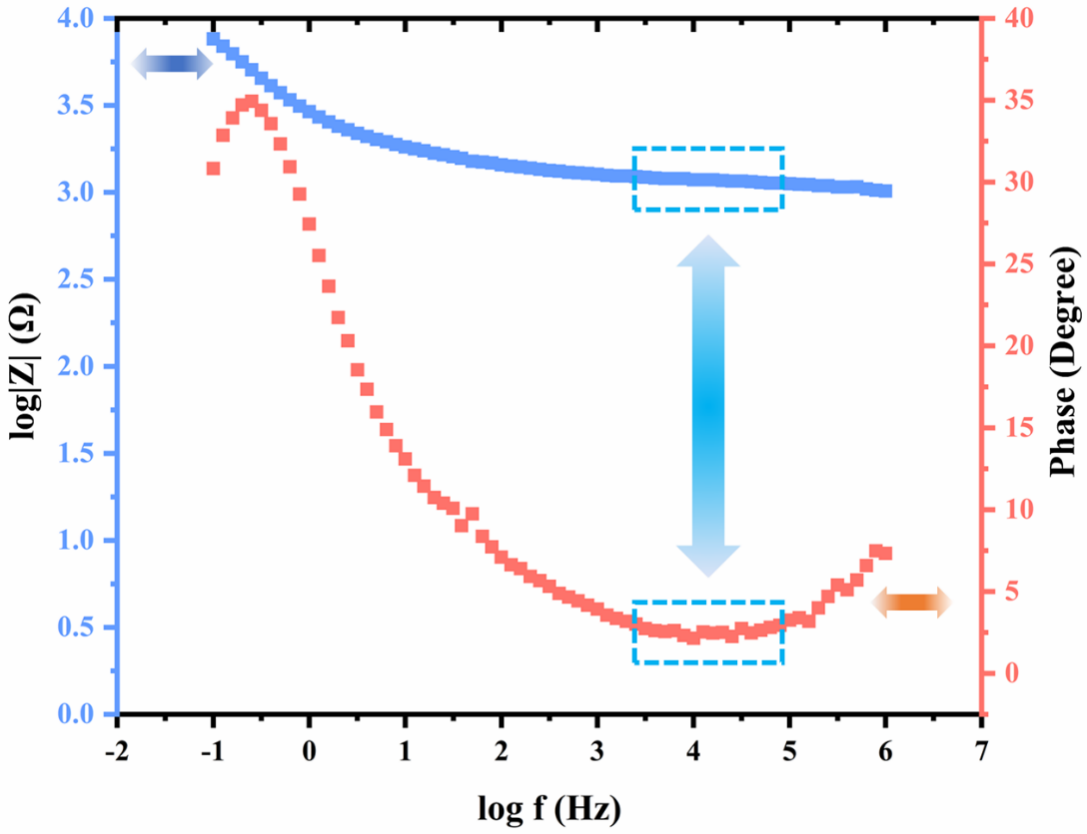

Figure 4.16 Impedance and phase of cementitious composites at 7 days, the average values of log |Z| are calculated relating to the phase PAD values close to the 0

Corresponding to the PAD value of the average Log |Z|, the bulk electrical resistance *R* of the cementitious composites was calculated through the Eq. (4.11)

$$R = 10^{\overline{\log|Z|}} \tag{4.11}$$

Figure 4.17 shows the bulk electric resistance of SNS cementitious matrix at days of 7, 14 and 28. The logarithmic histogram indicates that the resistance of cement matrix continuously improves with the ages. The resistance increases can attribute to pore water loss and hydration, with age which is continually denser in the matrix microstructure. Furthermore, Figure 4.17 indicates the SNSs promote the cementitious composites electrical resistance at different ages. At 28 days, compare to the control group, the 0.3-wt% SNS additive cementitious composites denser structure shows an increase of up to 14% bulk electric resistance. The ability of SNS to affect the electrical resistance of the cement matrix is attributed to the accelerated hydration mechanism.

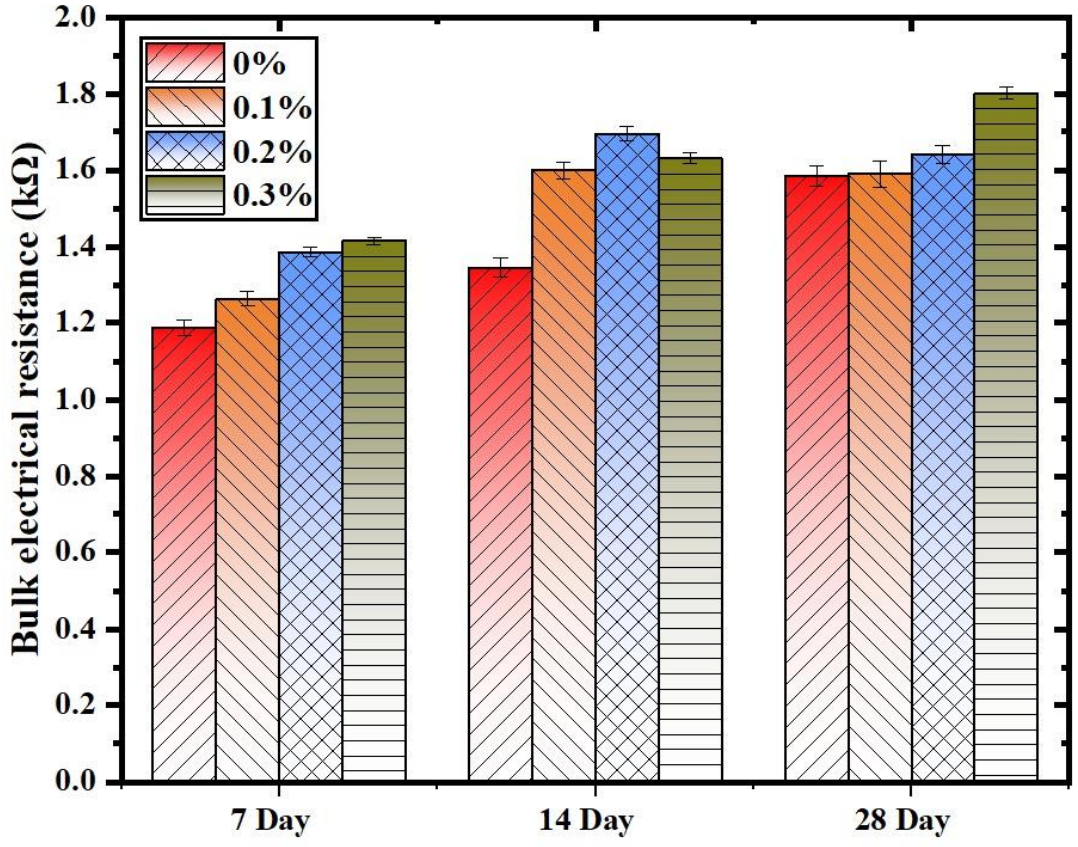

Figure 4.17 The bulk electrical resistance of SNS cementitious pastes at the days of 7, 14 and 28

4.4.2.3 Equivalent circuit models of cementitious composite

The cementitious materials are defined as a particular electrochemical system. Figure 4.18 show the idea of plain cementitious composites impedance spectroscopy equivalent Randles circuit. The interface of cementitious materials exists of solution resistance (R_s), electrolyte and electric double layer capacitance (C_{dl}) and the Warburg impedance (Z_w). The AC impedance spectroscopy electrochemical system equivalent circuit model can be simplified and described as $R_s(C_{dl}(R_{ct}Z_w))$ (Li *et al.*, 2016).

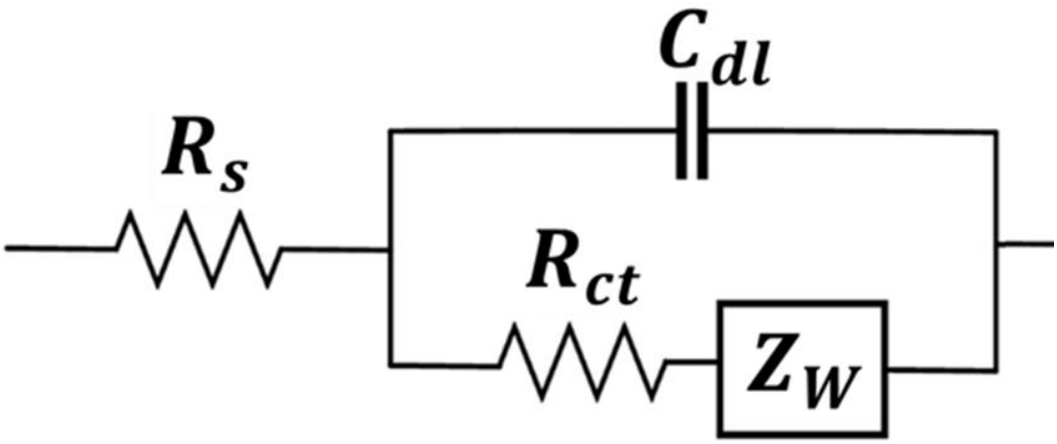

Figure 4.18 Randles equivalent circuit

The EIS experimental Nyquist plot data was used to develop an equivalent circuit model to analyse the SNS-cementitious composite. According to the Nyquist plot and Bode plot, the equivalent circuit of SNS cement-based contains three components, including the pore solution, cement matrix and electrodes. The equivalent circuit $R_s(C_eR_e)(C_{dl}(R_{ct}Z_w))$ is shown in Figure 4.19. The pore solution is the resistance of solution, which represents R_s. The cementitious matrix represents the AC passing through the uniform SNS substrate conductive path $C_{dl}(R_{ct}Z_w)$. The resistance of charge transfer is represents R_{ct}. The electric double-layer capacitance (C_{dl}) and the diffusion behaviour refer to the ion penetration process in the solution Warburg impedance (Z_w) (Naderi et al., 2013; Emran and Hanaa, 2017). The electrodes represent

the resistance and capacitance (C_eR_e) introduced by the electrodes and matrix solid-solid interface. According to the equivalent circuit, the SNS-cementitious composites impedance can be shown in Figure 4.20.

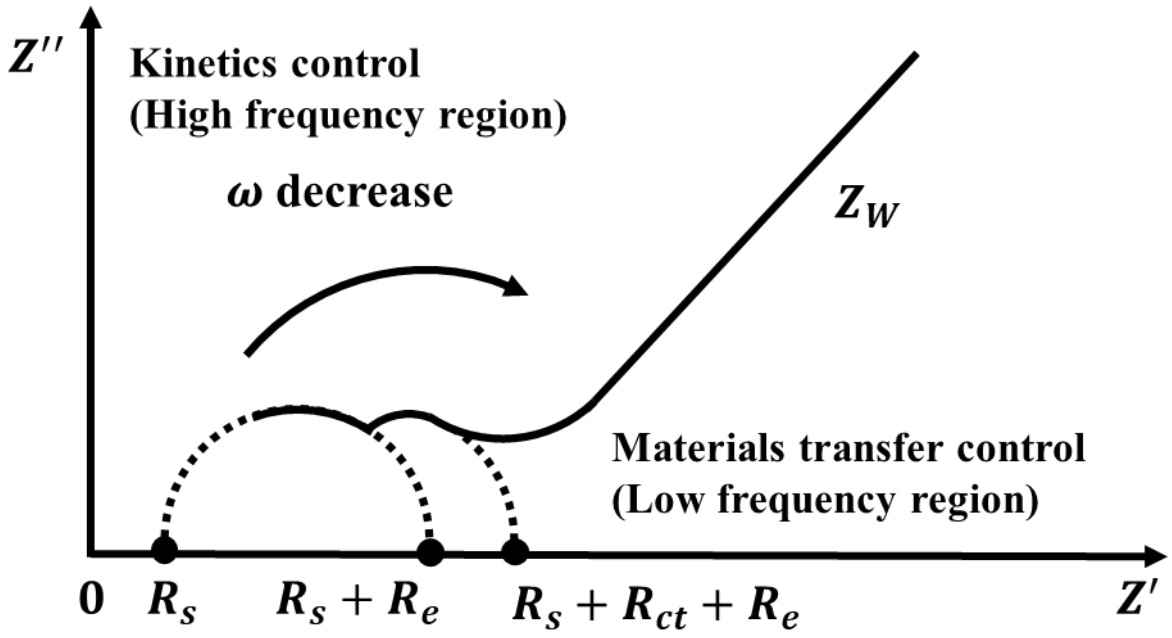

Figure 4.19 $R_s(C_eR_e)(C_{dl}(R_{ct}Z_w))$ equivalent circuit of the curve in the cementitious composites

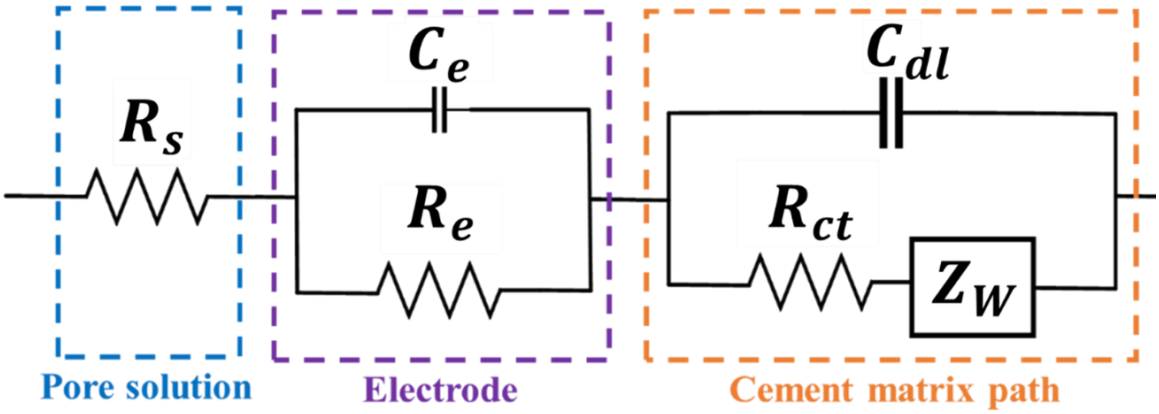

Figure 4.20 SNS-cementitious composite equivalent circuit $R_s(C_eR_e)(C_{dl}(R_{ct}Z_W))$

The entire electrochemical process consists of high and low frequencies. The high-frequency region appears as two semicircles, corresponding to R_s and R_e, respectively, in which the reaction process is controlled by kinetics. The low frequency region is a

straight line with a slope of 1, which is controlled by charge transfer (diffusion) in this region, where the Faraday impedance caused by the Faraday process of the cement material is represented by Z_F (Yuan *et al.*, 2010).

$$Z_F = R_{ct} + Z_w \tag{4.12}$$

The relationship between the angle frequency (ω) and Z_w is given by

$$Z_w = \sigma(\omega)^{-\frac{1}{2}}(1 - j) \tag{4.13}$$

$$\omega = 2\pi f \tag{4.14}$$

In Equation 4.13, σ is the Warburg impedance coefficient defined as:

$$\sigma = \frac{RT}{n^2F^2A\sqrt{2}}\left(\frac{1}{C_O^*\sqrt{D_0}} + \frac{1}{C_R^*\sqrt{D_R}}\right) \tag{4.15}$$

Where f is frequency, R is the ideal gas constant, T is the absolute temperature, n is the number of electrons involved, F is Faraday's constant, A is surface area of the electrode, ω is radial frequency, C_O^* is the concentration of oxidant, D_0 is diffusion coefficient of the oxidant, C_R^* is the concentration of the reductant on the electrode surface, D_R is the diffusion coefficient of the reductant.

According to Srinivasan and Fasmin (2021), in the introduction of electrochemical impedance spectroscopy, the total impedance Z of the equivalent circuit model (Figure 4.19) can be expressed in Equation 4.16, as follows:

$$Z = R_S + \frac{Z_F}{1 + j\omega Z_F C_{dl}} + \frac{R_e}{1 + j\omega R_e C_e} \tag{4.16}$$

By substituting Equation (4.12) and (4.13) with Eq. (4.16), the equation below is obtained:

$$Z = R_s + \frac{R_{ct} + \sigma\omega^{-\frac{1}{2}}(1-j)}{1 + j\omega R_{ct}C_{dl} + j\omega Z_W C_{dl}} + \frac{R_e}{1 + j\omega R_e C_e} \tag{4.17}$$

The real part of Z' can be expressed as below:

$$Z' = R_s + \frac{R_{ct} + \sigma\omega^{-\frac{1}{2}}}{\left(1 + \omega^{\frac{1}{2}}\sigma C_{dl}\right)^2 + \omega^2 C_{cl}^2\left(R_{ct} + \sigma\omega^{-\frac{1}{2}}\right)^2} + \frac{R_e}{1 + (\omega R_e C_e)^2} \tag{4.18}$$

And the imaginary part of Z'' is:

$$Z'' = j\left[\frac{\omega R_{ct}^2 C_{dl} + 2C_{dl}\sigma^2 R_{ct}\omega^{\frac{1}{2}} + 2\sigma^2 Q_1 + \sigma_1\omega^{\frac{1}{2}}}{\left(1 + \omega^{\frac{1}{2}}\sigma C_{dl}\right)^2 + \omega^2 C_{dl}^2\left(R_{ct} + \sigma\omega^{-\frac{1}{2}}\right)^2} - \frac{\omega R_e^2 C_e}{1 + (\omega R_e C_e)^2}\right] \tag{4.19}$$

Complex relative permittivity (Kim *et al.*, 2016)

$$\varepsilon^* = \varepsilon' - j\varepsilon'' \tag{4.20}$$

The dielectric constant ε' and the dielectric loss ε'' of the specimen calculate according to the followed equations (Zihlif, Ayish and Elimat, 2013)

$$\varepsilon' = \frac{Z''}{2\pi f C_o Z^2} \tag{4.21}$$

$$\varepsilon'' = \frac{Z'}{2\pi f C_o Z^2} \tag{4.22}$$

Where Z is the impedance, C_o is the capacitance of two plates of the cell without the sample and is given by the followed equation.

$$C_o = \epsilon_0 \frac{A}{d} \tag{4.23}$$

Where A is the contact area of the electrodes and the cement pastes, d is the distance between the electrodes and ε_0 is the value of vacuum permittivity.

By substituting Equation (4.23) with Equation (4.21) and (4.22), the equation below is obtained:

$$\varepsilon' = \frac{dZ''}{2\pi f Z^2 \epsilon_0 A} \tag{4.24}$$

$$\varepsilon'' = \frac{dZ'}{2\pi f Z^2 \epsilon_0 A} \tag{4.25}$$

The dielectric constant (ϵ') of different aged SNSs additions cementitious composites at 25, 50 and 80 kHz are shown in Figure 4.21. The ε' is related to the stored energy within the matrix medium. The dielectric constant continually decreases as the cementitious composites age increase. This is attribute to the slow diffusion of CH and C-S-H generated. During this process, some polymerisation of silicates also took place (Zhang *et al.*, 1996). Furthermore, the higher frequency results in cementitious composites being the smaller dielectric constant.

Figure 4.21 also indicates that the dielectric constant of cementitious composites at different frequencies decreases as the SNS amount increases. The dielectric constant decreases could be attributed to two reasons. First, the dielectric constant of the SNSs material itself is low (Torgovnikov, 1993). Second, the SNSs promote the growth of hydration products. The nanopore size distribution and the fine microstructure of C-S-H reduce the dipole orientation of the cementitious composites, which might slow down the segmental mobility of the polymer (Zhang *et al.*, 1996).

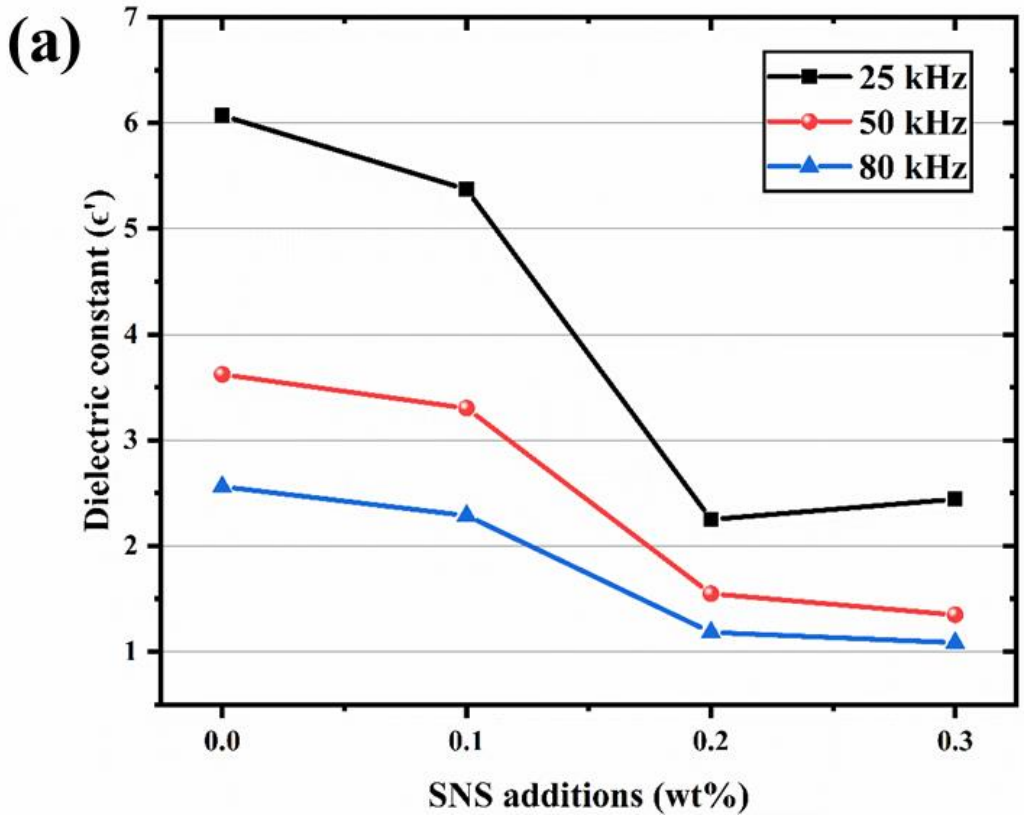
(a)
25 kHz
50 kHz
80 kHz
Dielectric constant (ϵ')
SNS additions (wt%)
0.0
0.1
0.2
0.3
1
2
3
4
5
6
7

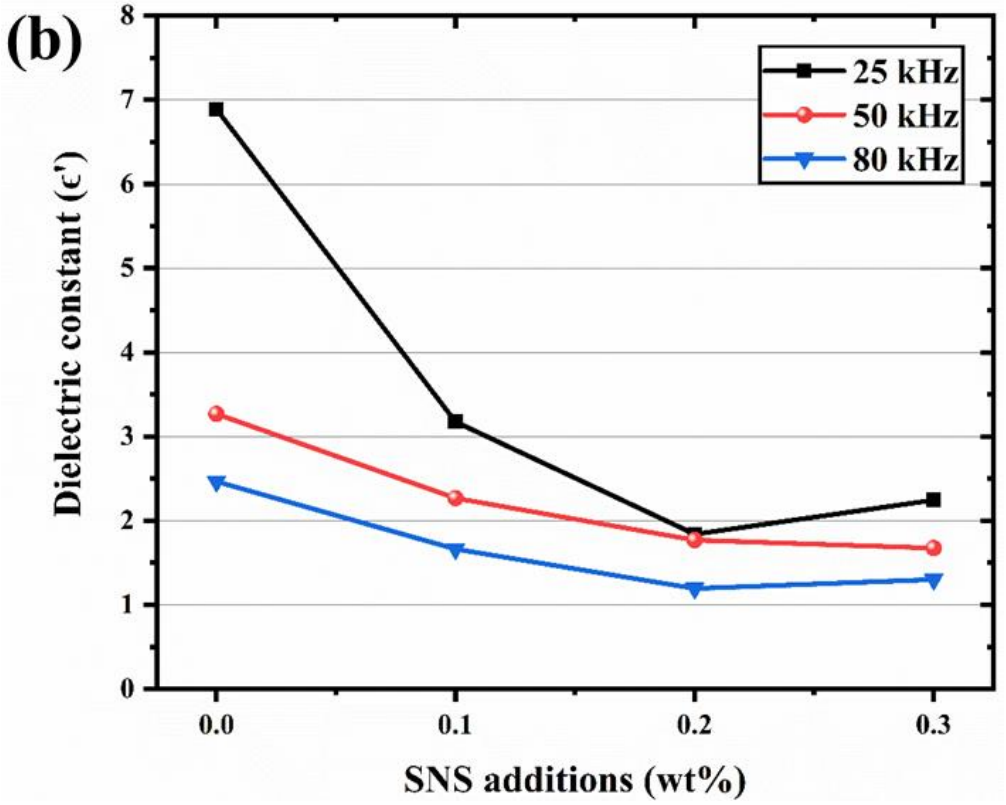
(b)
25 kHz
50 kHz
80 kHz
Dielectric constant (ϵ')
SNS additions (wt%)
0.0
0.1
0.2
0.3
0
1
2
3
4
5
6
7
8

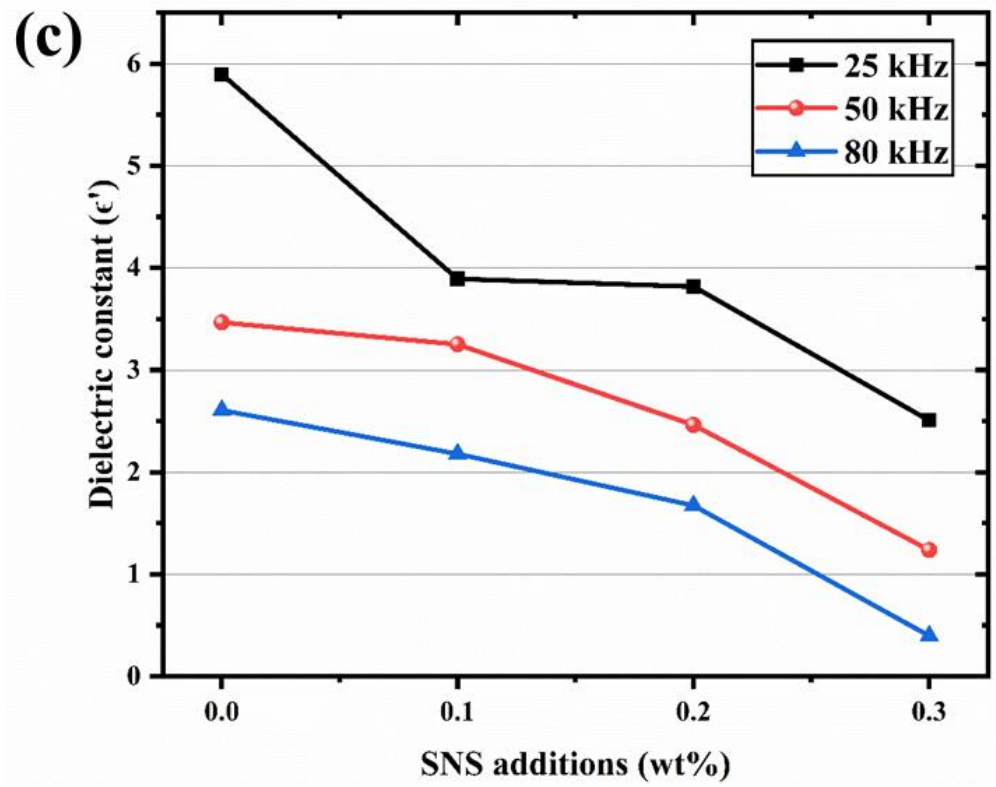

Figure 4.21 The dielectric constant of SNS cementitious composites at (a) 7 days (b) 14 days and (c) 28 days

Figure 4.22 shows the dielectric loss of cementitious composites at 25, 50 and 80 kHz with variation in SNS amounts and ages. It is found that the dielectric loss curves trend is similar to the dielectric constant at different frequencies. The ε'' relates to the dielectric energy loss within the medium, depending on the material composition interaction among charge carriers (Arya and Sharma, 2018). The dielectric loss continually decreases with the frequency increase attributed to the higher conductive behaviour (Psarras, Manolakaki and Tsangaris, 2003; Zihlif, Ayish and Elimat, 2013).

Figure 4.22 also shows the matrix dielectric loss decreases with specimen age, attributed to the lowering of the dielectric constant reducing the binding ability of charge. Furthermore, it was found that the dielectric loss of the cementitious composites continually decreases with the increase in amounts of SNS additives. The

SNS accelerate hydration promoting a denser cementitious composites structure which demonstrates relative lower dielectric loss properties.

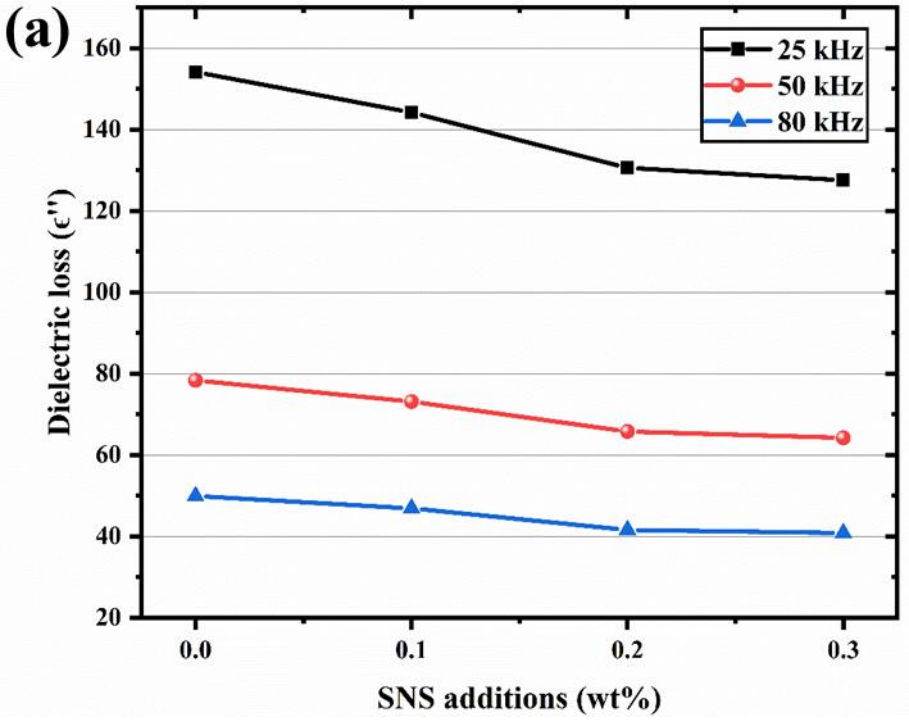

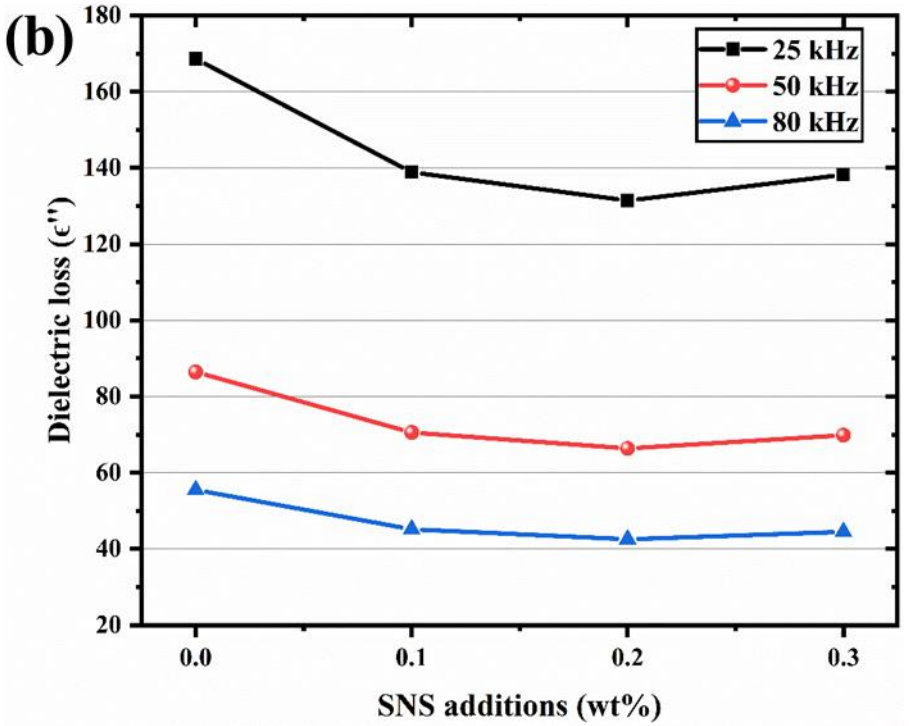

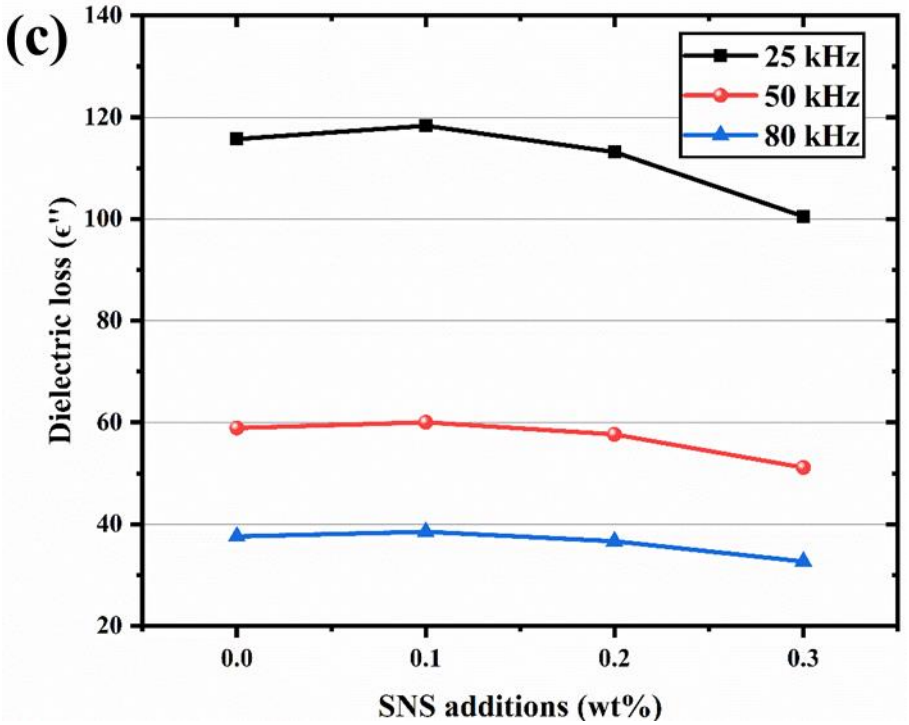

Figure 4.22 The dielectric loss of SNS cementitious composites at days of (a) 7, (b) 14 and (c) 28

The hydration of cementitious composites is a complicated dynamic reaction process, where matrix properties and internal structure keep changing with time. Model analysis of the equivalent circuit was performed under the same experimental conditions at ages of 7, 14 and 28, respectively. Figure 4.23 shows the 28 days cementitious composite equivalent circuit ($R_s(C_eR_e)(C_{dl}(R_{ct}Z_w))$) simulation impedance real, imaginary and absolute Bode numerical results compared with the experimental conditions. The results demonstrate the high degree of consistency between the experiment and the equivalent circuit model; the experiment results of cementitious composites are analysed by the equivalent circuit model for each characteristic parameter. Table 4.4 shows the cementitious composites equivalent circuit model characteristic parameters with different amounts of SNS.

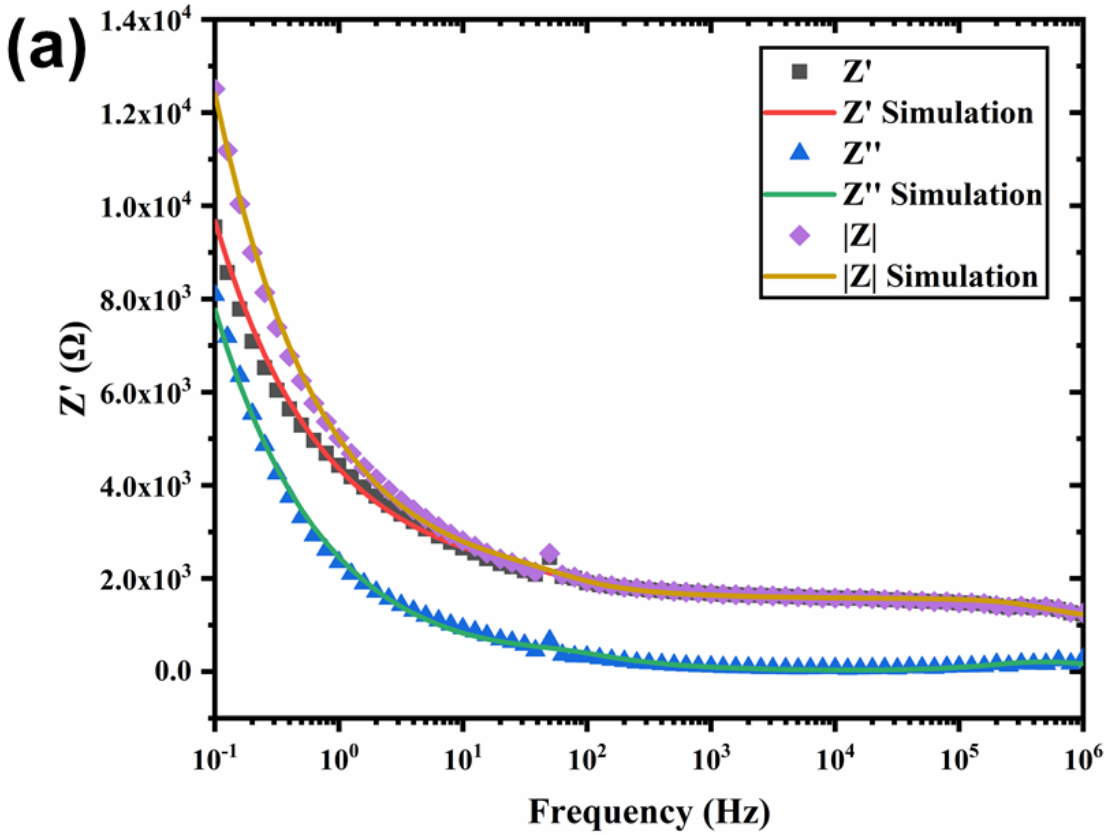
(a)
Z'
Z' Simulation
Z''
Z'' Simulation
|Z|
|Z| Simulation
Z' (Ω)
Frequency (Hz)

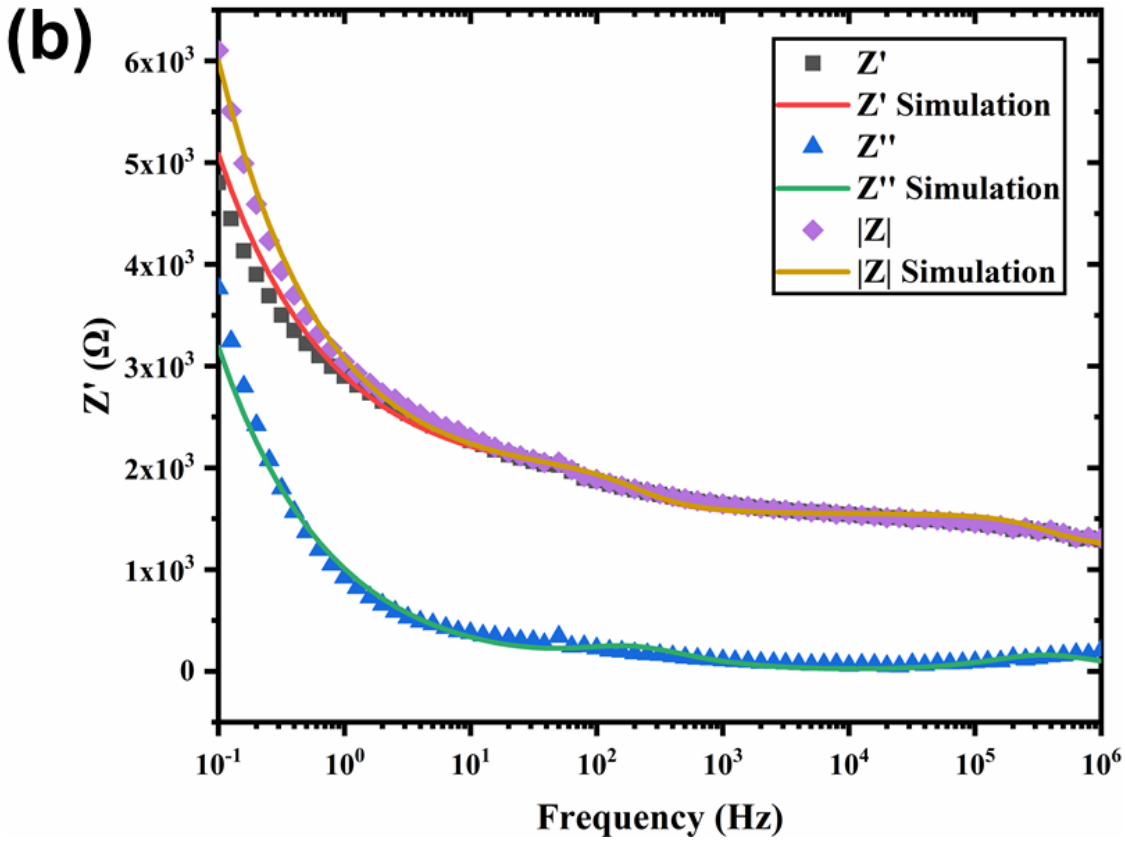
(b)
Z'
Z' Simulation
Z''
Z'' Simulation
|Z|
|Z| Simulation
Z' (Ω)
Frequency (Hz)

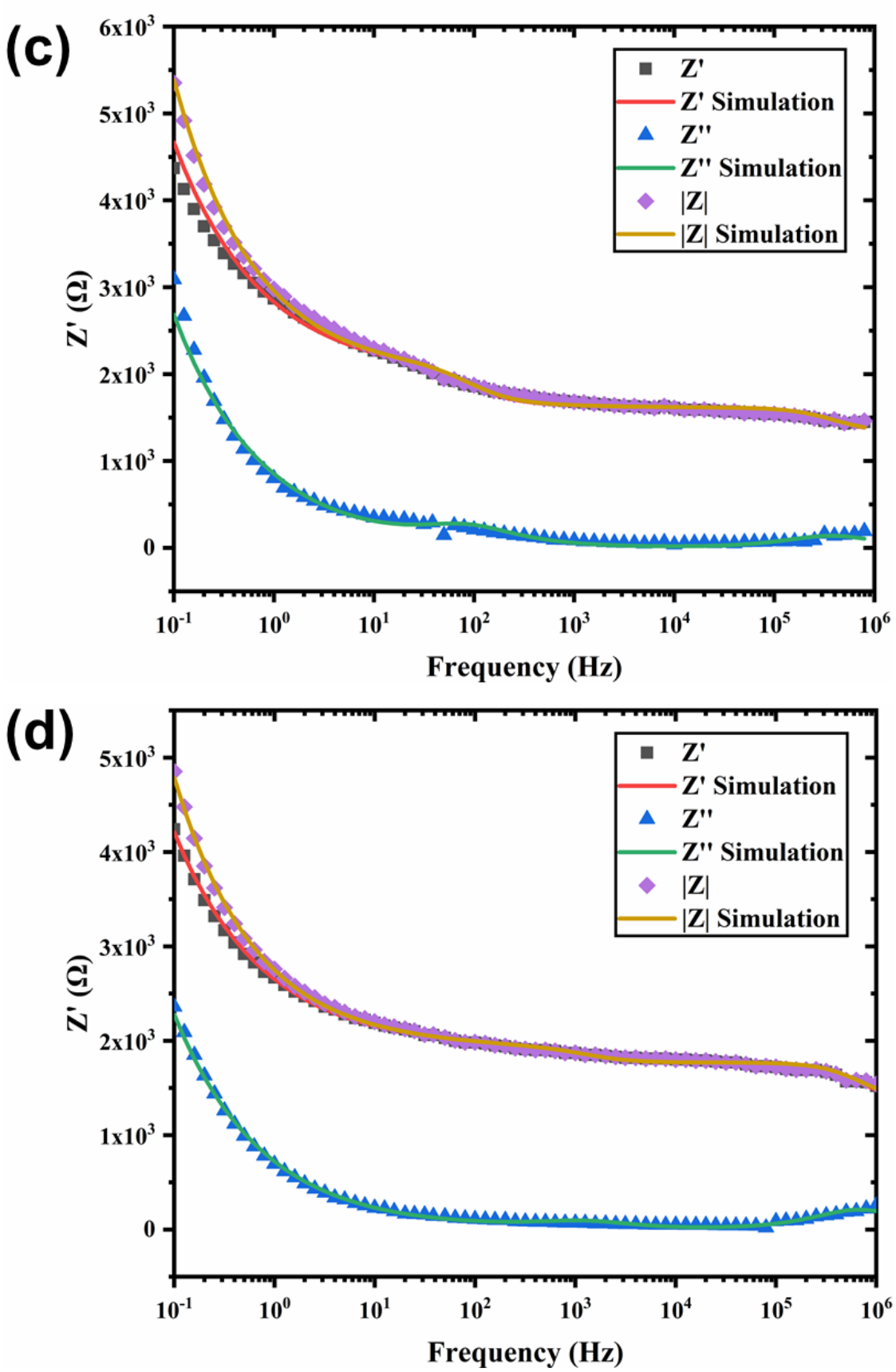

Figure 4.23 SNS-cementitious composite Nyquist and Bode experiment and equivalent circuit results at SNS-wt% of (a) 0, (b) 0.1, (c) 0.2 and (d) 0.3

Table 4.4 SNS Equivalent Circuit Character- $R_s(C_eR_e)\left(C_{dl}(R_{ct}Z_w)\right)$

Day	SNS (-wt%)	R_s (Ω)	C_{dl} (μF)	R_{ct} (Ω)	Z_w (Ω/cm^2)	C_e (μF)	R_e (Ω)
7	0	928.9	4.84E-01	156.5	2.02E-04	1.28E-03	231.6
	0.1	1004	5.92E-01	141.2	2.91E-04	1.58E-03	234.8
	0.2	1074	1.58	87.65	9.55E-04	4.70E-4	298.3
	0.3	1163	8.68	148.6	7.71E-04	7.53E-4	258.7
14	0	1041	1.30E-03	295.7	1.34E-04	7.42	337.4
	0.1	1113	5.39E-02	113.3	3.81E-04	3.22E-4	436.6
	0.2	1239	2.54E-01	84.95	5.21E-04	3.66E-4	439.1
	0.3	1313	1.67	140.5	6.04E-04	7.73E-4	306.9
28	0	1142	7.895E-04	421.7	1.148E-04	7.512	337.3
	0.1	1222	1.40E-03	320.2	2.800E-04	2.30	353.7
	0.2	1335	1.53E-03	279	3.320E-04	5.04	367.8
	0.3	1348	6.68E-01	166.9	3.920E-04	5.58E-4	421.6

Figure 4.24 shows the resistance of pore solution (R_s) of SNS cement composites under different cure ages. The R_s is the resistance of the electrolyte in the pores of the hardened cement pastes, the DOH of the matrix can be characterised by R_s changes. The results show that the R_s is reflected by hydrated product pore solution and hydrated electrons, the matrix hydration age increases when accompanied by the improvement of R_s and the denser material structure results in higher R_s. Furthermore, Figure 4.24 shows the R_s value increasing as SNS additions increase. The high surface area of SNSs exhibit an increasingly stronger adhesion to the hydrated cement matrix along with a deepening of hydration. The fibres fill in capillary pores and microcracks reinforcing the hydrated product growth (Sun and Xu, 2009). The experimental results are highly consistent with the molecular-scale dynamics simulation of fibre repair-defective calcium silicate hydrates (Chi et al., 2020).

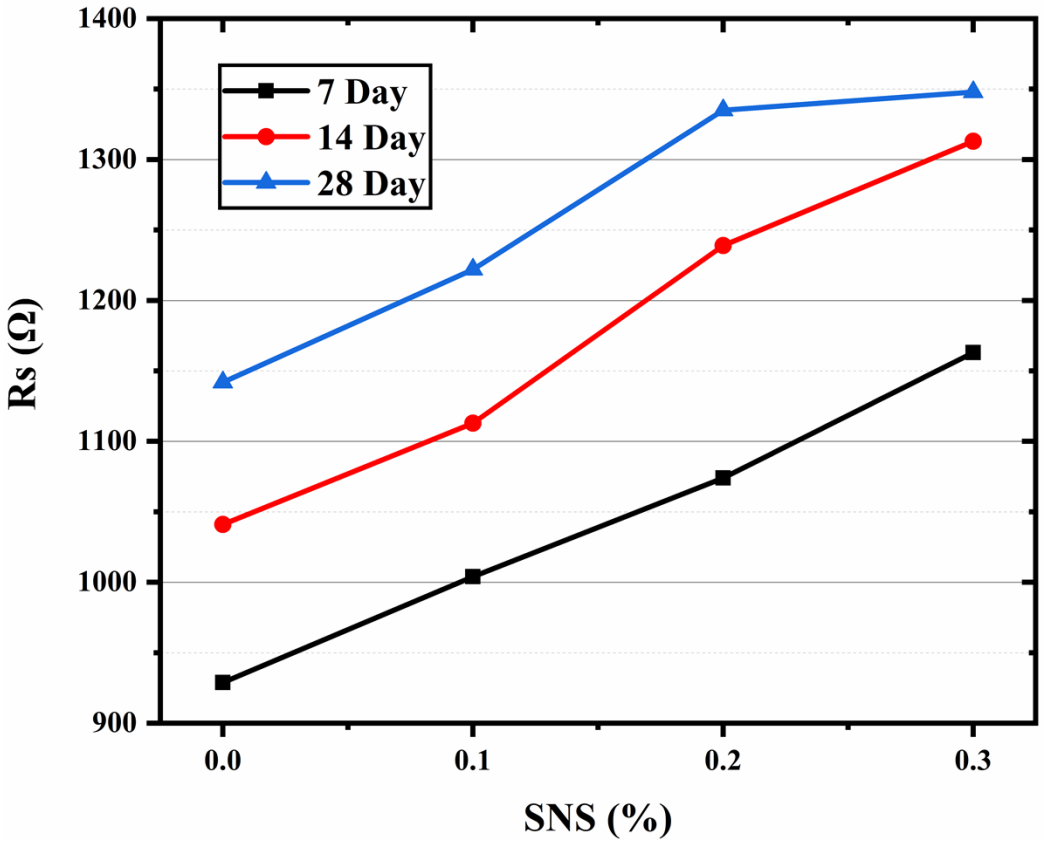

Figure 4.24 R_s of SNS-cementitious composites equivalent circuit

Figure 4.25 shows the cementitious composites' relationship between the charge transfer resistance (R_{ct}) and the SNS-wt% at 7, 14 and 28 days. The R_{ct} reflected the resistance of the cementitious composites electrons charge transfer. The R_{ct} is inversely proportional to the concentration of ions (e.g. Na^+, K^+, OH^-, Ca^{2+}, etc) that exist in the cement pastes. Therefore, R_{ct} can be used to characterise the concentration of ions in solution, which infers that the resistance of charge transfer becomes larger as the hydration of the cementitious composites increases. This is because the hydration process reinforced the pastes' microstructure and the charge transfer resistance was raised from one phase (e.g. electrode) to another (e.g. liquid or solid).

Furthermore, Figure 4.25 shows cement pastes that incorporated SNS significantly reduced the R_{ct} values. The SNS embedded into cement particles built the new structure of a-SNS/$Ca(OH)_2$ and a-SNS/C-S-H. These new structures generated new

conductive path networks and accelerated the electron transfer rate. The SNS-cementitious composites constructed the conductive contact between the cementitious network and the electrode, leading to a proton hopping exchange at a higher diffusion rate. The highly attracted and conductive SNS pathway promotes charge transfer. However, the threshold value of 0.3-wt% SNS was observed during the whole ageing progress. The occurrence of this phenomenon is because a small amount of agglomeration occurs after the dispersal of high concentration SNS. The unevenly distributed 0.3-wt% SNS were constituted as showing similar R_{ct} during all of the ages.

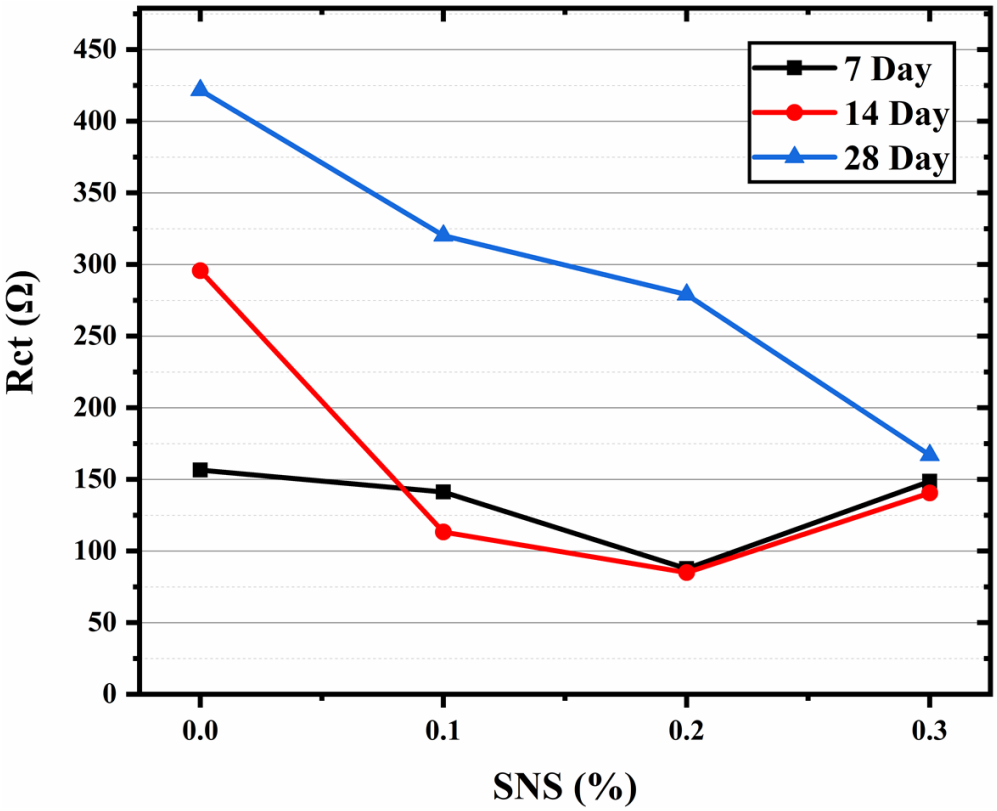

Figure 4.25 R_{ct} of SNS-cementitious composites equivalent circuit

Figure 4.26 shows the relationship between cementitious matrix double-layer capacitance (C_{dl}) and SNS additions on different days. The double-layer capacitance tends to decrease during the progression of hydration, and the capacitance of the samples increases significantly as the usage of SNS increases. The C_{dl} represents the

hydrated product (e.g. C-S-H gel) double-layer capacitance, which is determined by various factors such as the porosity of the material, the average pore size, and ionic concentration of the pore solution. The cementitious composites capacitive enhancement effect can be attributed to the uniform dispersal of SNS in the matrix, modifying the pore size distribution. Furthermore, the f-SNS dissolution results in the ionic concentration improvement of SNS conductive path accumulation.

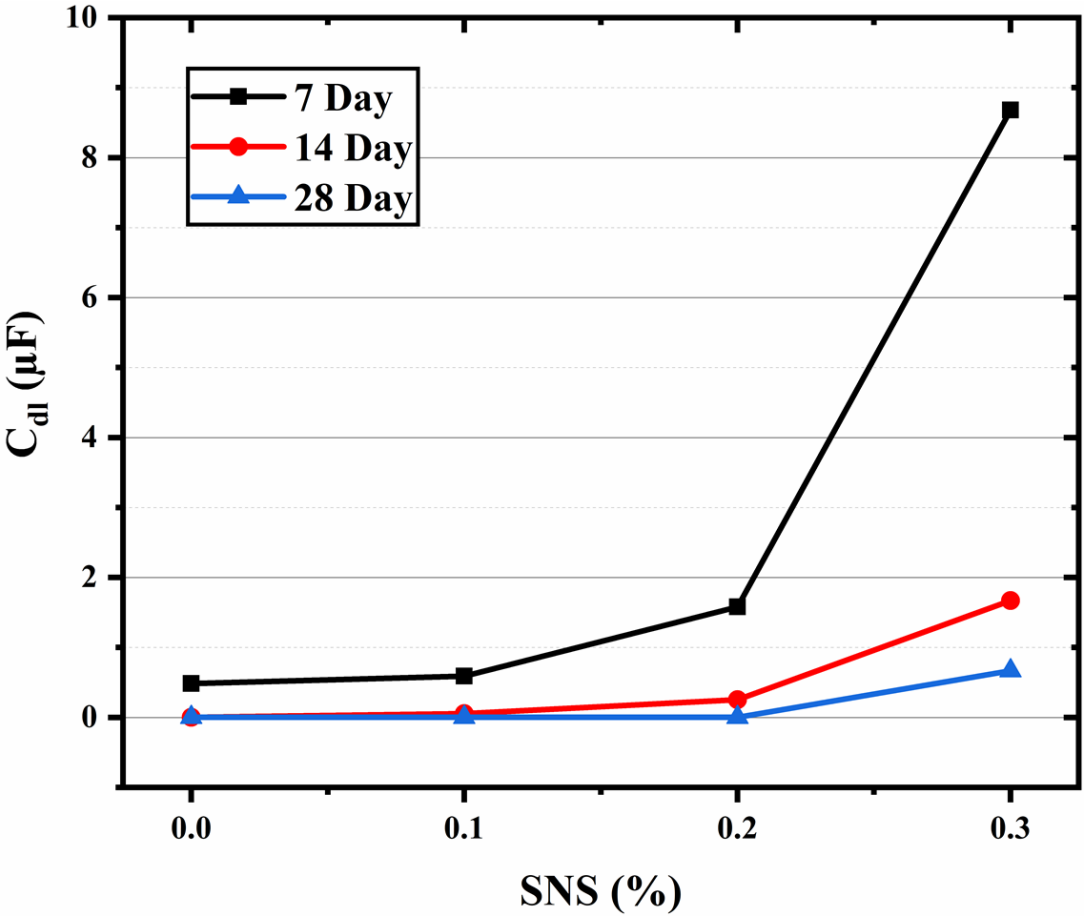

Figure 4.26 C_{dl} of SNS-cementitious composites equivalent circuit

Figure 4.27 shows the relationship between Warburg Impedance (Z_w) and SNS additions. The Z_w is caused by the electrochemical and concentration differential polarisation when the electric current passes through the interface between the electrolyte and electronic conductor. The Z_w results are influenced by the chemically

bound water and diffusion of OH^- ions during the hydration. In this case, the result in Figure 4.27 shows the Z_w decreases with the hydration process. Furthermore, the Z_w associates with the increase in SNS additions, resulting in an increase in the diffusion of free hydrogen atoms (H^+) and hydroxyl groups (OH^-) during the hydration process. The electrical conduction of the cementitious composite proceeds to improve through the conduction path of SNS, leading to the difficulty of ionic diffusion elevation.

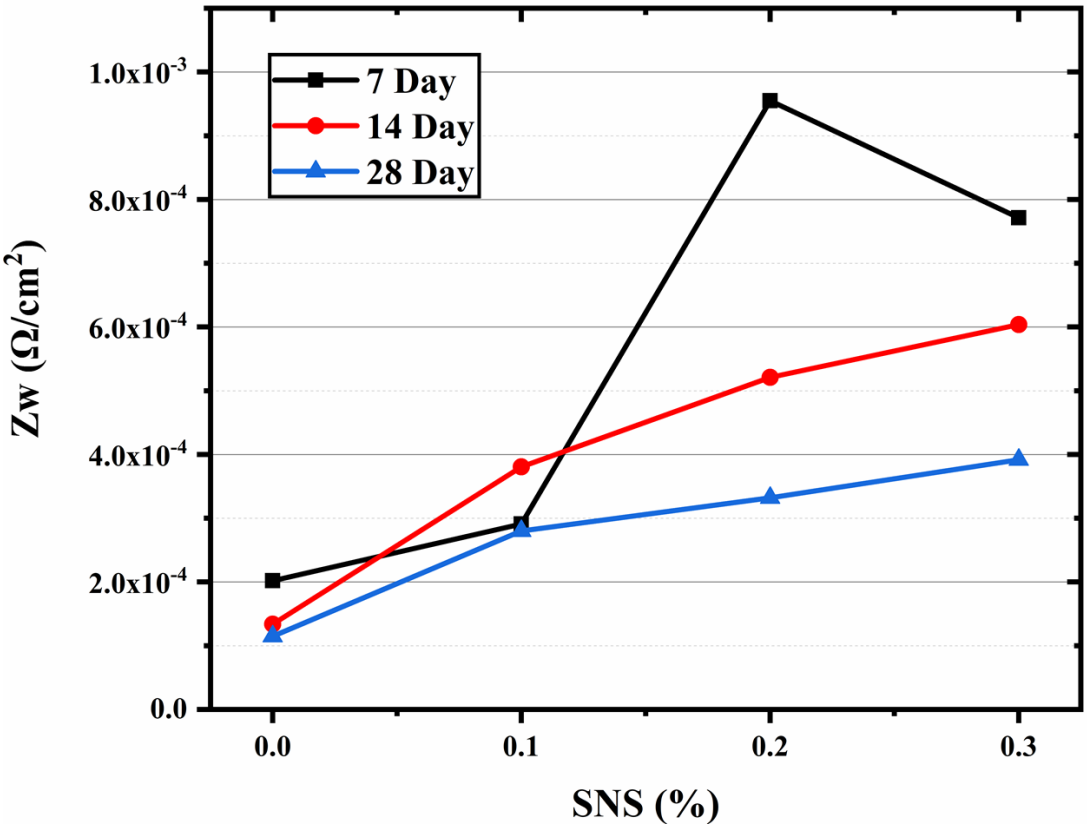

Figure 4.27 Z_w of SNS-cementitious composites equivalent circuit

Figure 4.28 and Figure 4.29 show the resistance (R_e) and capacitance (C_e) of the electrodes and wires that work on the cement pastes. These resistance and capacitance changes were not as stable as in the cementitious matrix. The hydration products accumulate at the electrode surface during hydration process, the solid-solid interface leads to increases in R_e and C_e. The SNS additions cause increase in R_e and decrease in C_e at the electrode and matrix interface, which can be attributed to the fact that the

a-SNS reinforced ionic concentrate improved the passive layer. The corrosion resistance and stability of the electrode part, what has been inserted into the cement, have been improved (Kakooei *et al.*, 2012).

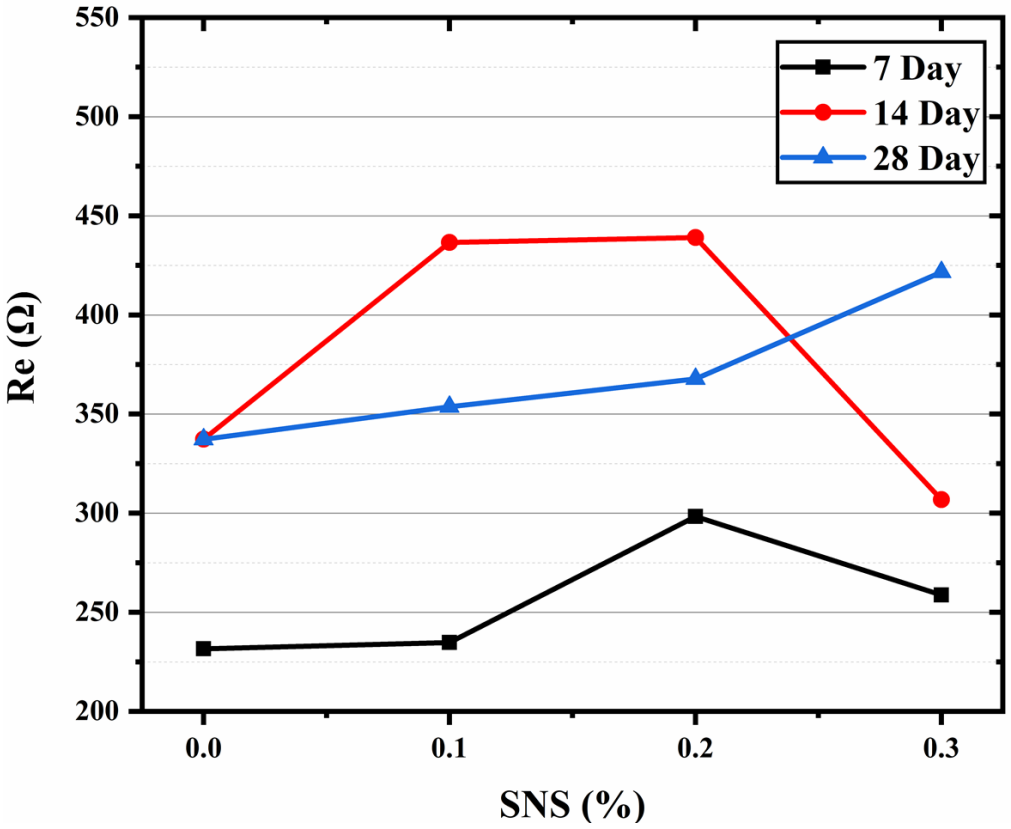

Figure 4.28 R_e of SNS-cementitious composites equivalent circuit

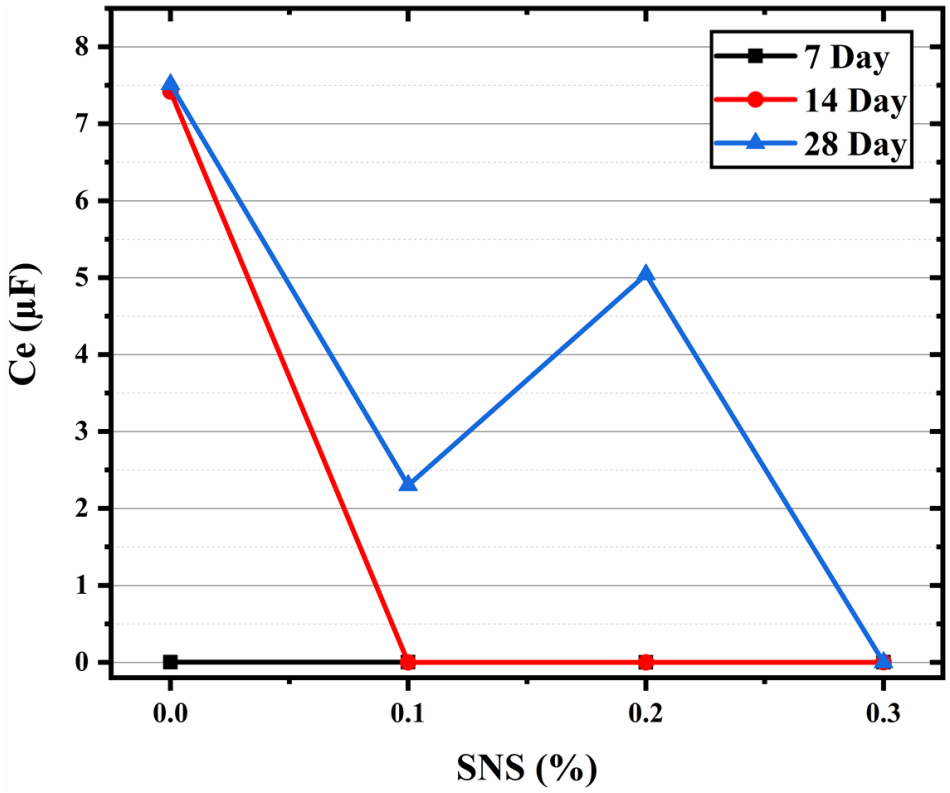

Figure 4.29 C_e of SNS-cementitious composites equivalent circuit

Electrochemical characterisation including the CV, EIS experimental results and the equivalent circuit model, reveals that the SNS is an effective additive to promote the hydration process of the cementitious composites. The experimental results show that the addition of SNS is not influential on the shape of the cementitious CV curves and the Nyquist plot. A new equivalent circuit model $R_s(C_eR_e)(C_{dl}(R_{ct}Z_w))$ was proposed for the SNS-cementitious composites, which considers the solid/liquid phase inside the matrix, and the solid/solid phase generated from the electrode inserted into the cementitious composite. The equivalent circuit model reflects the change in the internal structural in the SNS-cementitious composites. The equivalent circuit analysis includes the resistance of pore solution, the resistance of charge transfer and other parameters. The EIS, CV and the equivalent circuit provide a qualitative analysis of the hydration mechanism of the SNS cementitious composites. Electrochemical experimental results

show that the SNS can effectively facilitate the hydration process of the cementitious composites. The DOH of SNS-cementitious composites were further analysed quantitively in the following section.

4.5 SNS-cementitious composites DOH analysis and discussion.

4.5.1 Thermogravimetric analysis

Figure 4.30 shows the TGA results of different SNS contents cementitious composite at 7, 14 and 28 days. Under the same experimental conditions, the mass loss amount gradually increased with the increase of SNS concentration. During the calcination process, there were mainly three stages of the thermal decomposition, including C-S-H and aluminium carbonate phases that lost bound water in the temperature from 140 to 300℃, the dehydroxylation of calcium hydroxide performed between 420 and 480℃, and the decomposition of calcium carbonate which occurred between 600 to 780 ℃ (Cao, Tian, *et al.*, 2016). The experiment results showed that at 28 days the control group's final weight was 86.1%, whereas the cementitious composites with 0.1, 0.2 and 0.3-wt% SNS burned an extra 1.0, 1.2 and 1.3% compared to the controlled specimen, respectively.

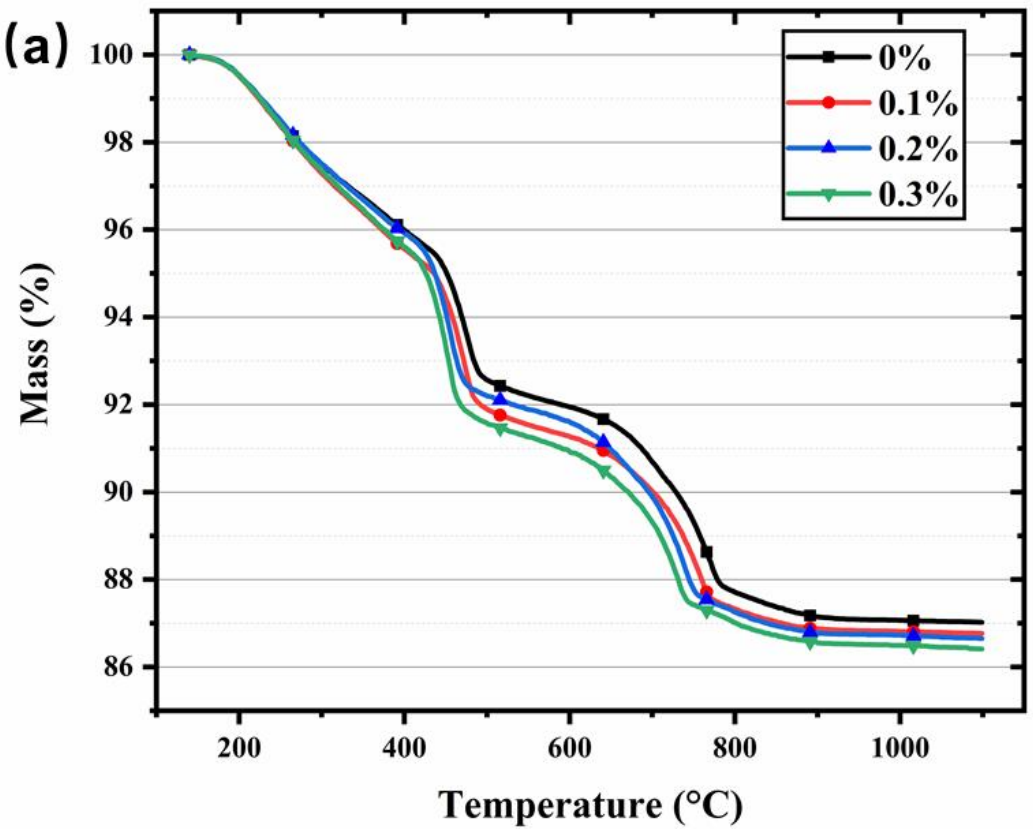
(a)
100
98
96
94
92
90
88
86
Mass (%)
200
400
600
800
1000
Temperature (°C)
0%
0.1%
0.2%
0.3%

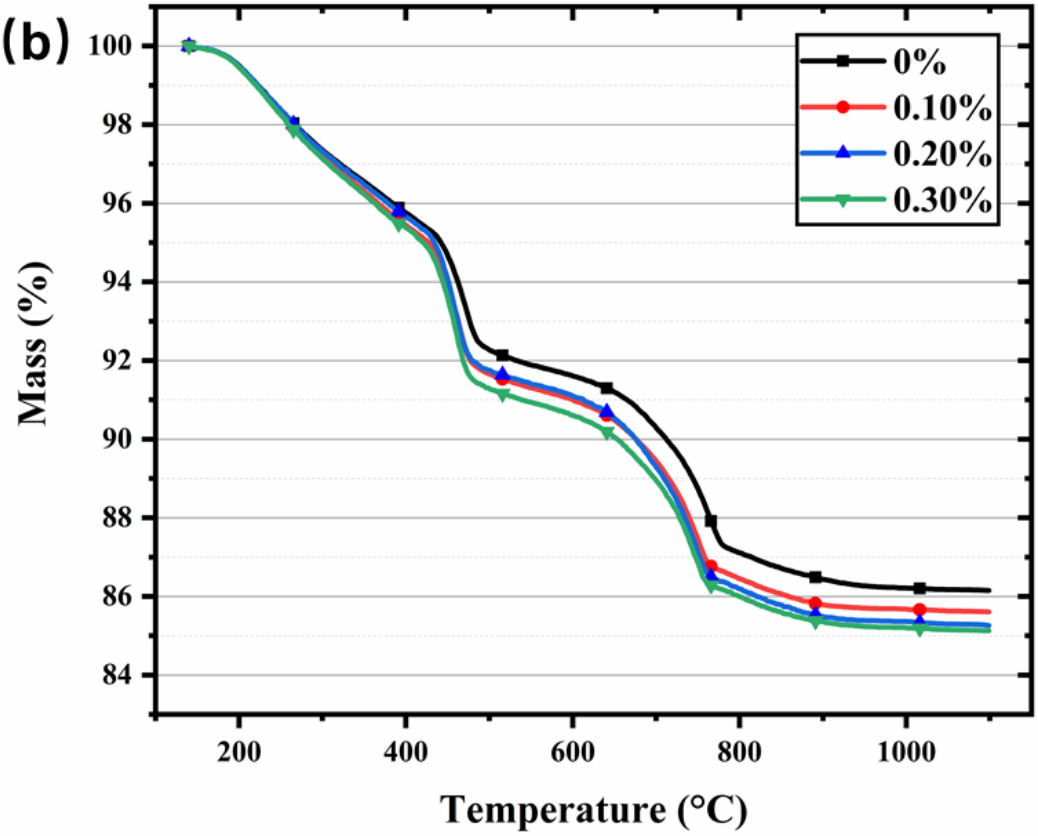
(b)
100
98
96
94
92
90
88
86
84
Mass (%)
200
400
600
800
1000
Temperature (°C)
0%
0.10%
0.20%
0.30%

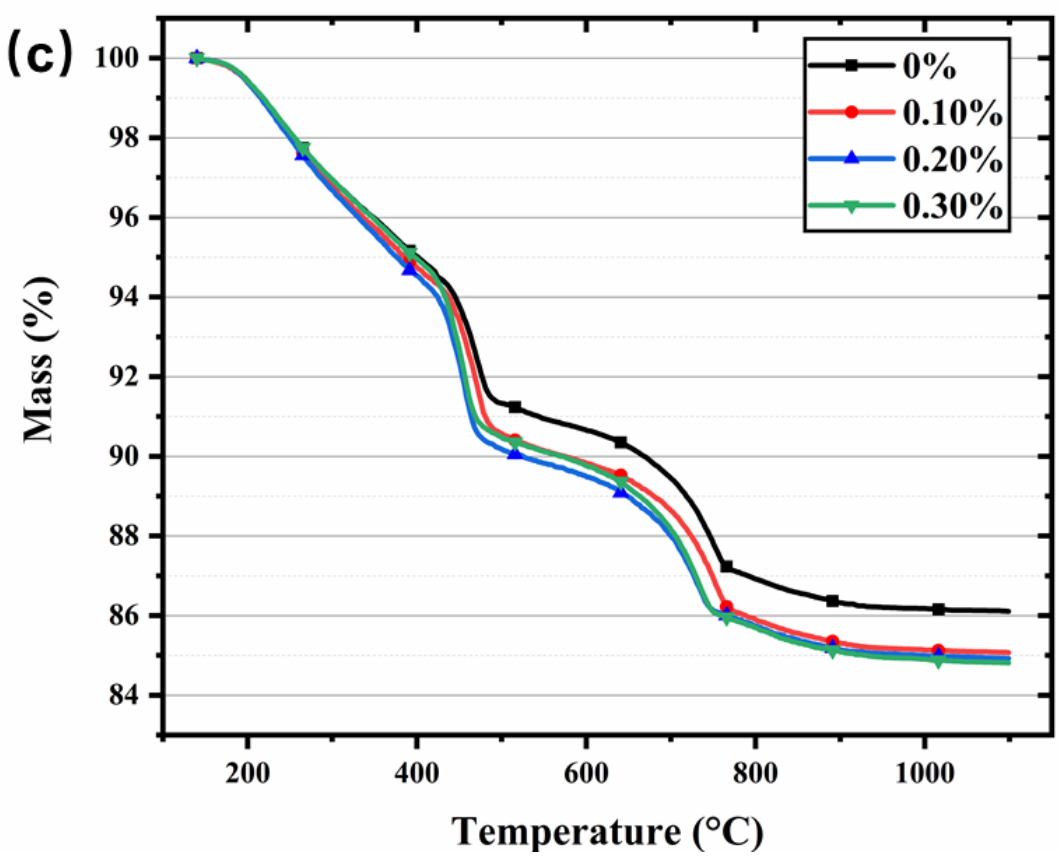

Figure 4.30 SNS-cementitious composites TGA curves at days of (a) 7 (b) 14 and (c) 28

The above mentioned cementitious composites mass loss is related to the DOH. The DOH refers to the fraction of cement that completely reacts with water. Following to the empirical formula of T.C Powers (Powers and Brownyard, 1948), one gram of fully hydrated cement could combine with 0.23 grams of non-evaporated water. The amount of bound water calculated from the weighing difference between the TGA results. The DOH calculation is based on the method described in (Taylor, 1997; Pane and Hansen, 2005). During the experiment process, the weight loss occurring between 140 and 1100℃ equates to the amount of chemically bound water (CBW). The final remaining weight can calculate the content of DOH in the experiments divided by 0.23 grams of non-evaporated water. The DOH calculation equation is as follows:

$$DOH(TGA) = \frac{\frac{m(cbw)}{m(remain)}}{0.23} \quad (4.26)$$

Figure 4.31 shows the cementitious nanocomposites DOH at 7, 14 and 28 days. The DOH indicates the upward trend with the increase of SNS concentration. Compared to the plain specimen, the SNS cement pastes containing 0.3-wt% have a DOH increase of 3.5%, 6.1% and 5.6% at 7, 14 and 28 days, respectively. Cao *et al.*(2016) approved that the hydrophilic CNCs effectively promote the disperse of cementitious composites during the mix. The deepening DOH comes from SNS that promote the water molecules to penetrate the cement particle interior. The cement particle embedded SNS acts as a water channel, transferring water from the external pore solution to the incompletely hydrated cement matrix during hydration, promoting the hydration of cement particles.

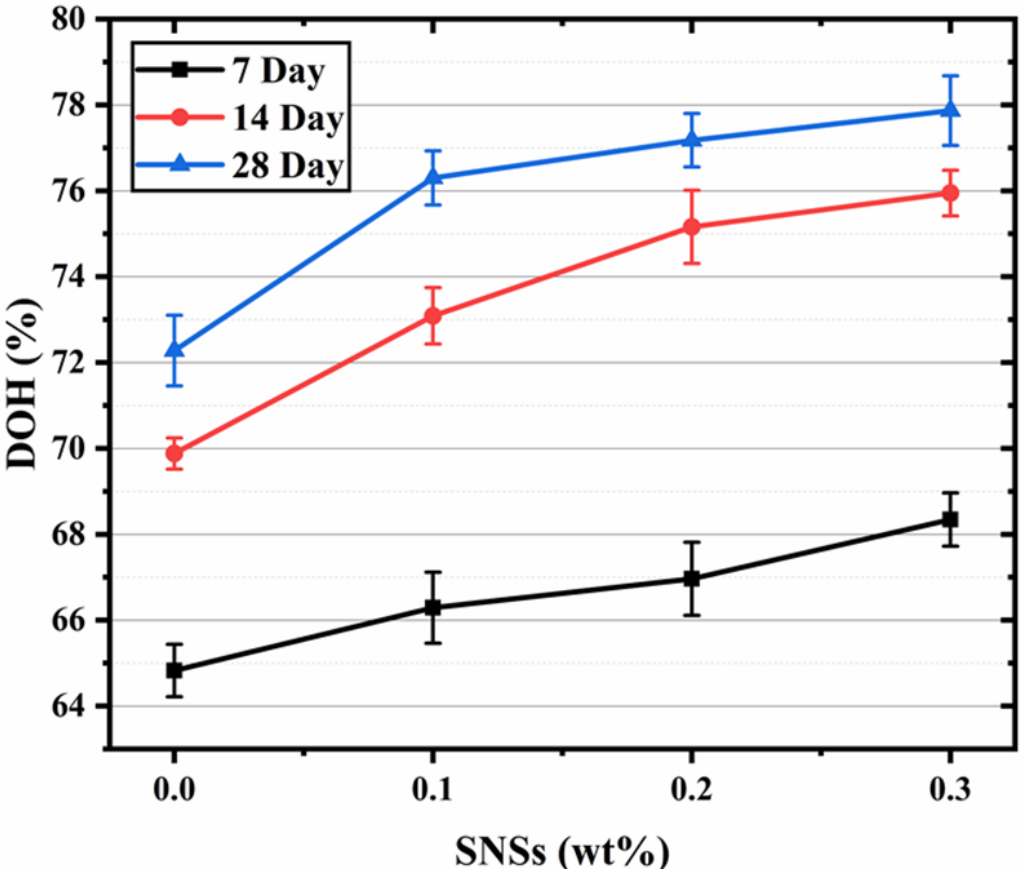

Figure 4.31 DOH of SNS-cementitious composites content

Figure 4.32 shows the calcium hydroxide amount under different SNS addition. The amount of $Ca(OH)_2$ was calculated through the thermogravimetric experiment mass loss of the dehydroxylation reaction (temperature range of 420-480℃). As shown in Figure 4.32, the amount of $Ca(OH)_2$ increases with SNS concentration throughout, similar to the DOH trend. At 28 days, the 0.1, 0.2 and 0.3 -wt% SNS-cementitious composites calcium hydroxide production amount increased by 5.04%, 10.29% and 13.45% compared to the control groups. CH results indicate that the SNS addition filled the matrix pores, accelerated more $Ca(OH)_2$ product, and deepened the cement-based hydration.

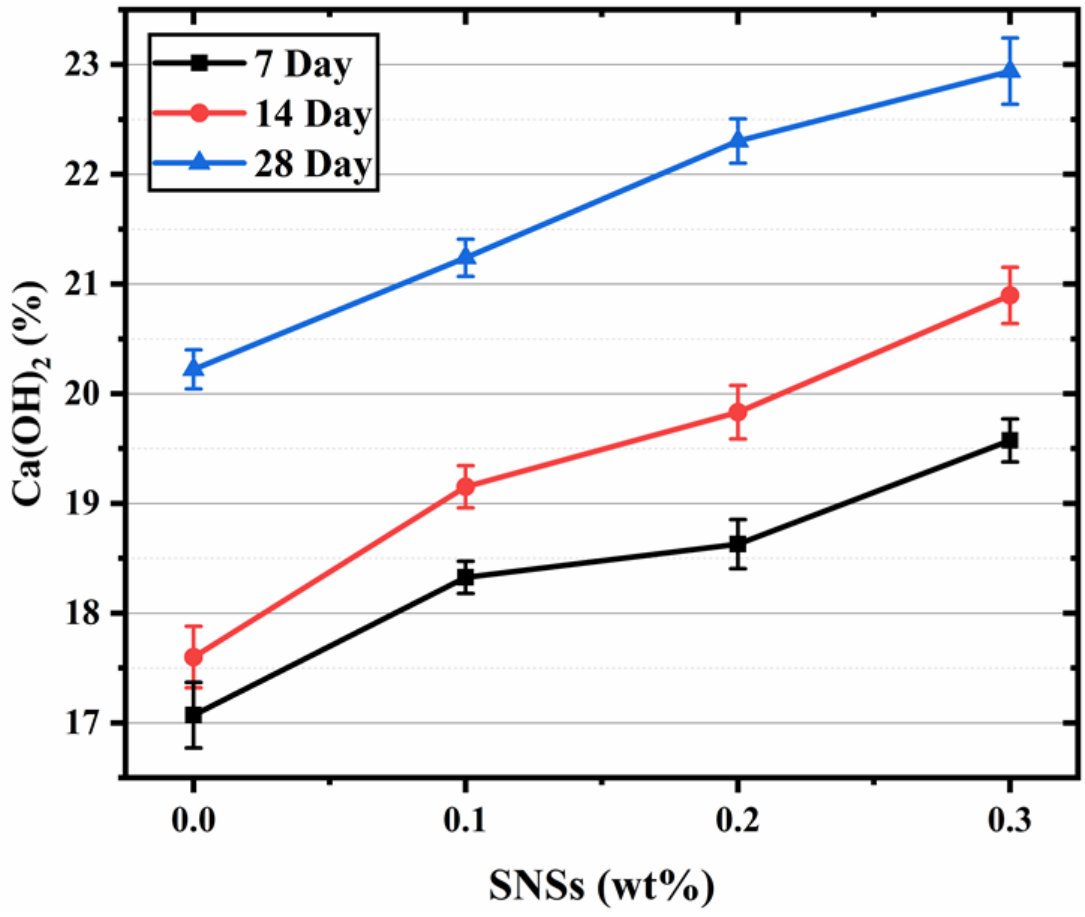

Figure 4.32 SNS-cementitious composites calcium hydroxide content

4.5.2 Differential thermal analysis

Figure 4.33 illustrates different SNS-cementitious composites derivative thermogravimetry (DTG) curves at 7, 14 and 28 days. The peaks in Figure 4.33(a-c) show all the cementitious composite either lost their CBW or decomposed at the specific temperature range during all of the curing ages, regardless of SNS addition. The range of the pyrolysis peak, as shown in Figure 4.33, confirms that the C-S-H, $Ca(OH)_2$ and $Ca(CO_3)$ phases weight was lost specifically in the temperature ranges of 140-300°C, 420-480°C and 600-780°C. Compared to the control group, the higher SNS content enhanced the peak intensity, which resulted in higher hydration products being produced at the same conditions. Furthermore, the decomposition peak of the $Ca(CO_3)$ phase gradually shifted towards the left (decomposition temperature decreased around 10°C) with the increase of SNS addition. This is because the SNS were inserted into the pore gaps of hydration products, the hydration product explored the surface with lower heat resistance, then it decomposed prior to the main hydration products. The DTG results further improved the properties of SNS materials in increasing the DOH and producing high-density nano-composites such as SNS/C-S-H and SNS/$Ca(OH)_2$.

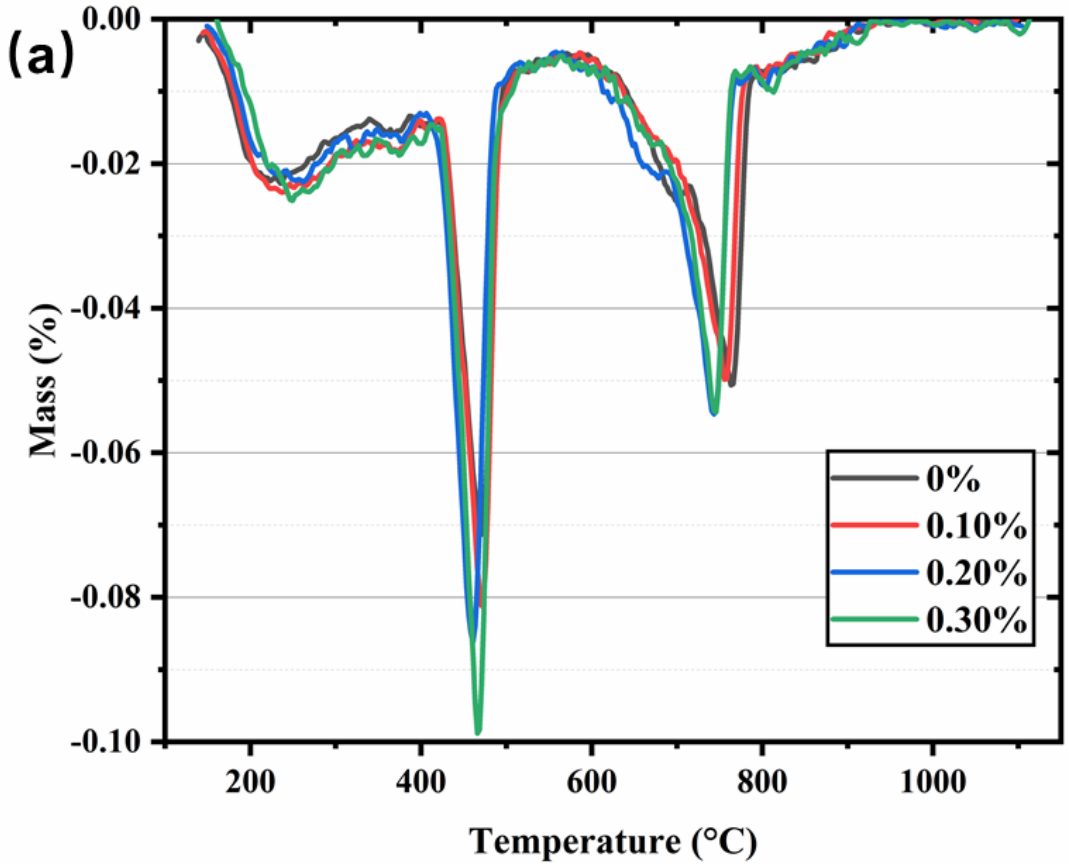
(a)
0.00
-0.02
-0.04
-0.06
-0.08
-0.10
Mass (%)
200
400
600
800
1000
Temperature (°C)
0%
0.10%
0.20%
0.30%

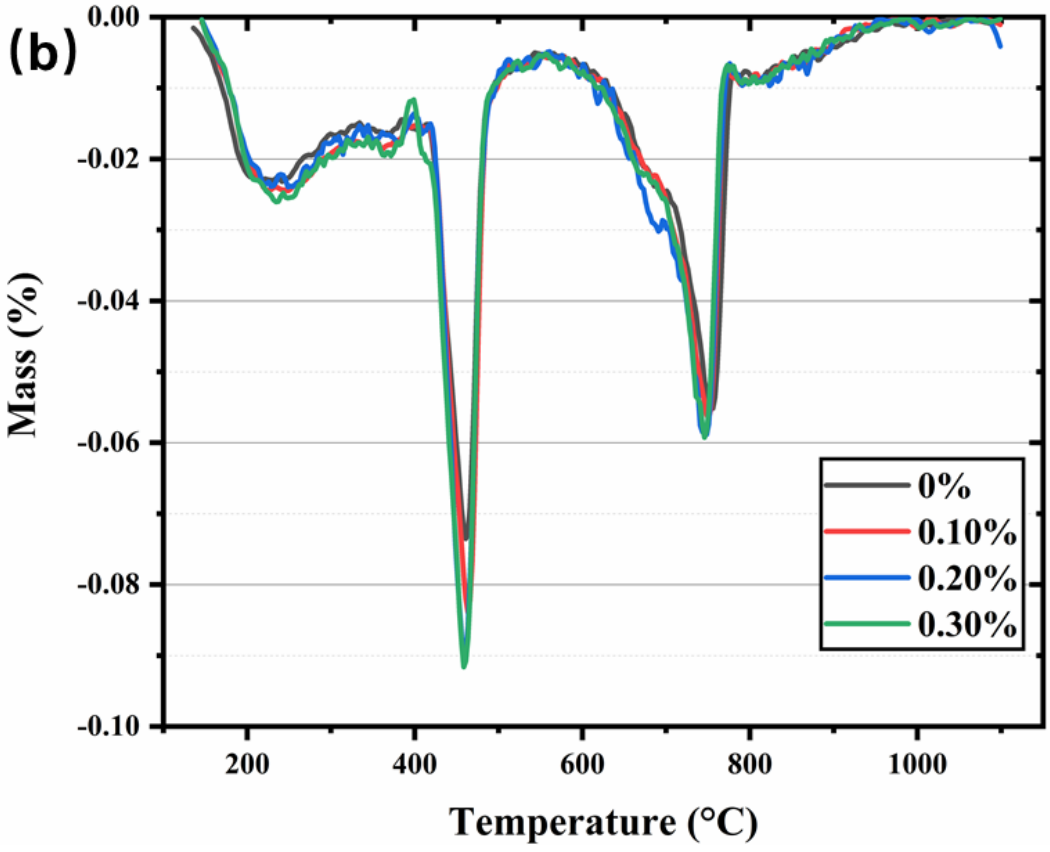
(b)
0.00
-0.02
-0.04
-0.06
-0.08
-0.10
Mass (%)
200
400
600
800
1000
Temperature (°C)
0%
0.10%
0.20%
0.30%

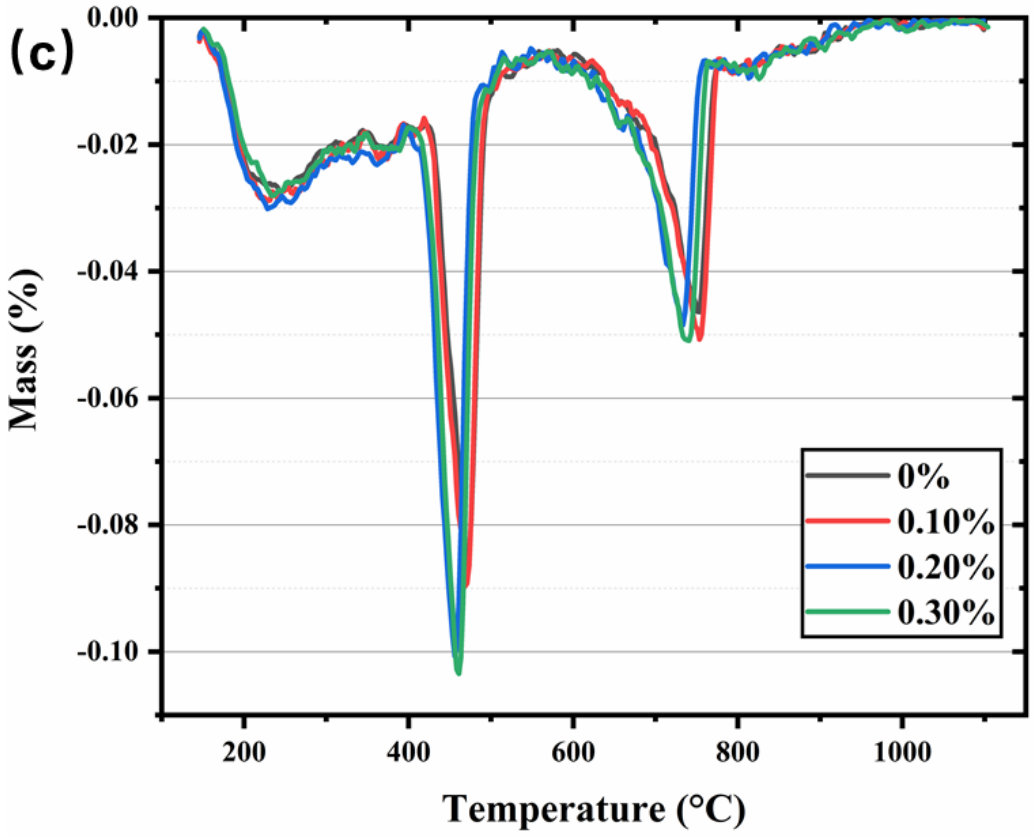

Figure 4.33 DTG of SNS-cementitious composites at days of (a) 7 (b) 14 and (c) 28

4.5.3 Differential scanning calorimetry

Figure 4.34 shows the DSC thermogram for the SNS reinforced cementitious nanocomposites. The experimental temperature ranges from 20 °C to 850 °C. The curves in Figure 4.34 show that the specimen's first endothermic reaction happened between 200 and 400 °C. The process is broken colloidal bonds caused by the thermal loss of C-S-H crystals CBW, the chemical when combined with water evaporation leads to the molecular chain rearrangement. The second endothermic reaction happened from 420 to 480 °C, corresponding to the $Ca(OH)_2$ microcrystalline portion containing SNS. As a result, calcium hydroxide were thermally decomposed, and the attached SNS body was pyrolyzed. The following endothermic reaction occurs ranges from 600 to 800 °C, the calcium carbonate decomposition is mainly demonstrated. It is noted that before the crystal decomposition, the thermal instability of embedded SNS

can cause the decomposition reaction peak to slip towards the low temperature. This phenomenon disappears as the ageing increases, the $Ca(OH)_2$ and $CaCO_3$ hydration productions gradually cover the whole SNS, which leads to the simultaneous decomposition of crystals and SNS. The absorbed/released heat flow of cementitious composites were calculated from the heat flow and time curves within the temperature range (Figure 4.35).

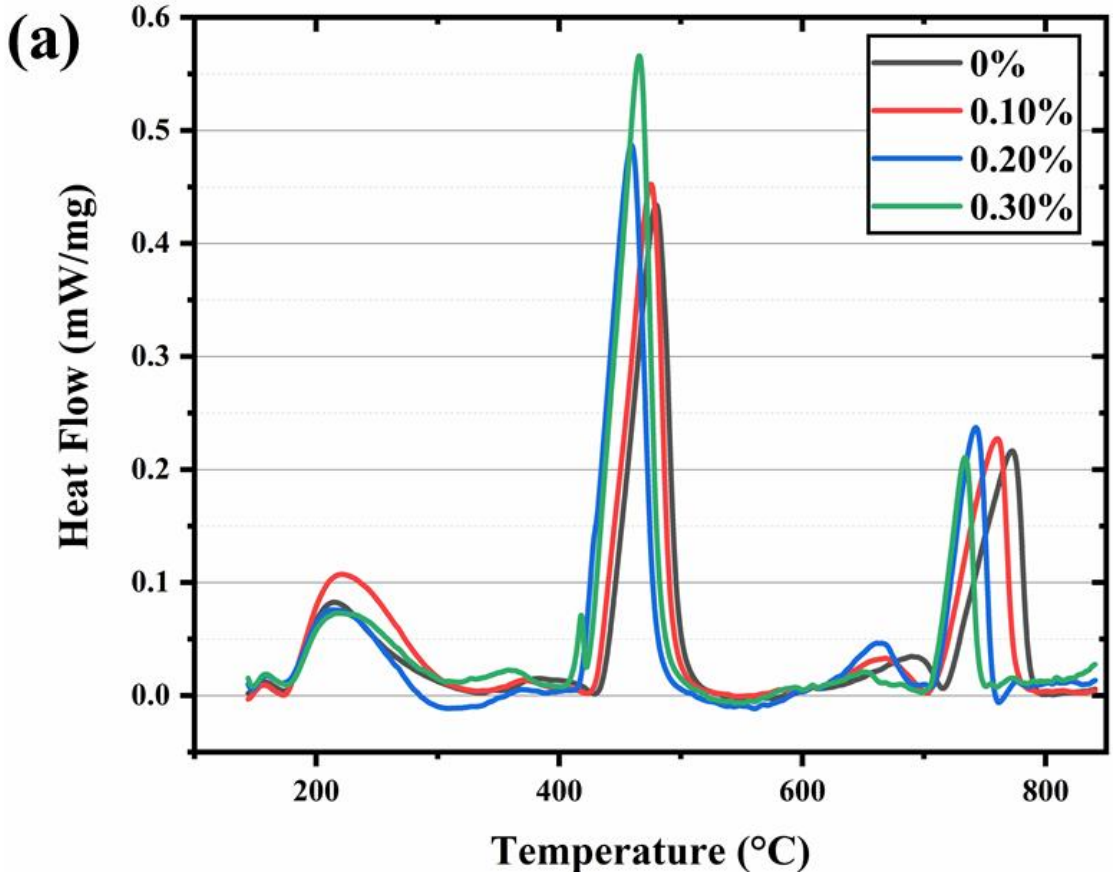

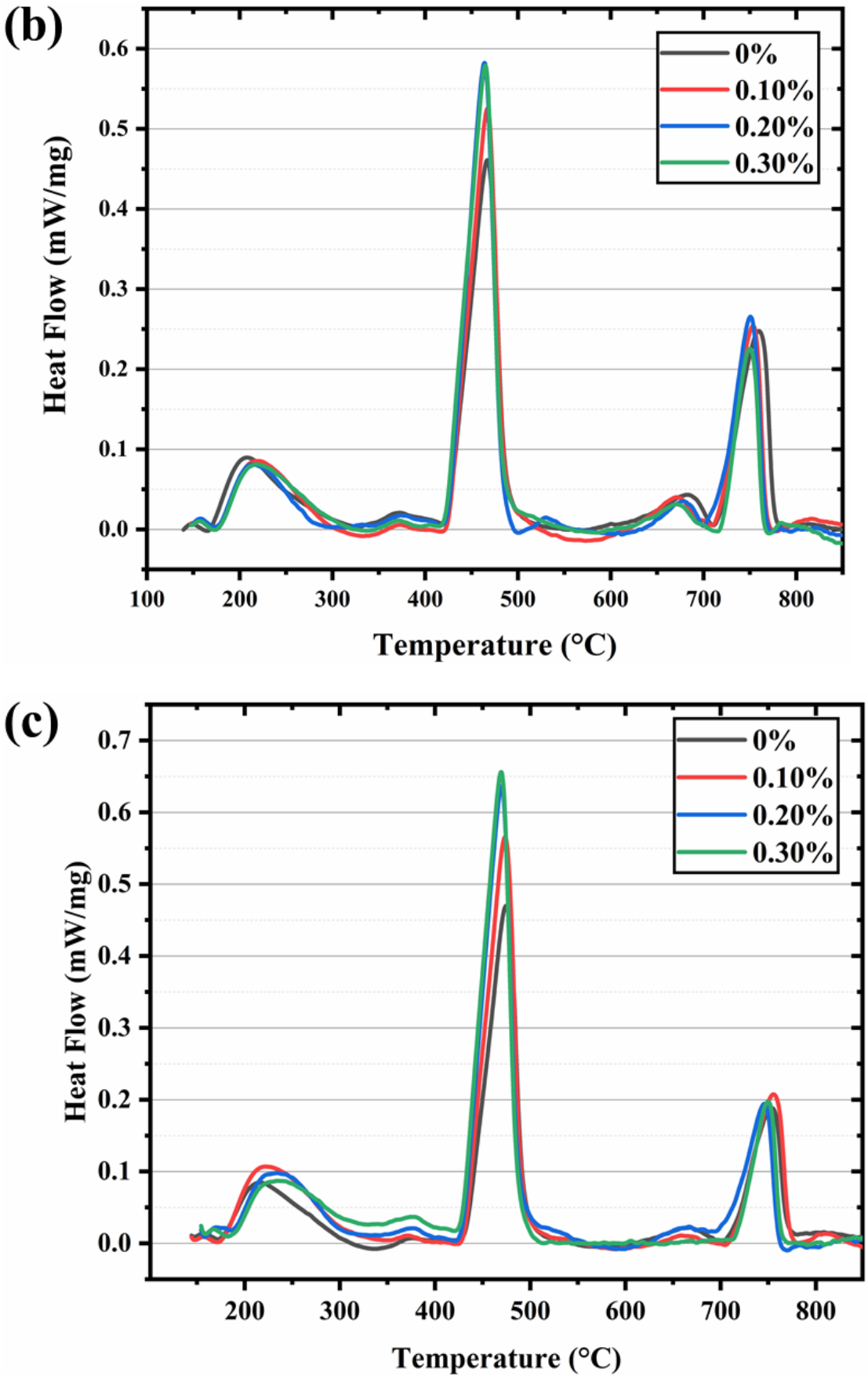

Figure 4.34 DSC curves of SNS cementitious at (a) 7 days (b) 14 days (c) 28 days

DSC endothermic reaction peak generation position simultaneously matches the TGA（Figure 4.30）and DTG (Figure 4.33) degradation positions. The thermogravimetric loss in the temperature range of 420-480 ℃ is the portlandite crystals pyrolysis process. The portlandite amount can be calculated through the heat flow related to time (Figure 4.35). The $Ca(OH)_2$ enthalpy of fusion amount is shown in Figure 4.36, with the SNS concentration increased from 0~0.3-wt%, the content of portlandite enthalpy of fusion raised 2.82%, 10.36% and 24.86% at 7 days, 6.97%, 14.05% and 19.84% at 14 days and 6.95%, 18.70% and 21.76% at 28 days. The DSC results shows that $Ca(OH)_2$ increases with the increase of SNS. The DSC results further confirm the TGA results that SNS accelerate the DOH improvement and generate denser hydration products, generating more C-S-H and ettringite phases.

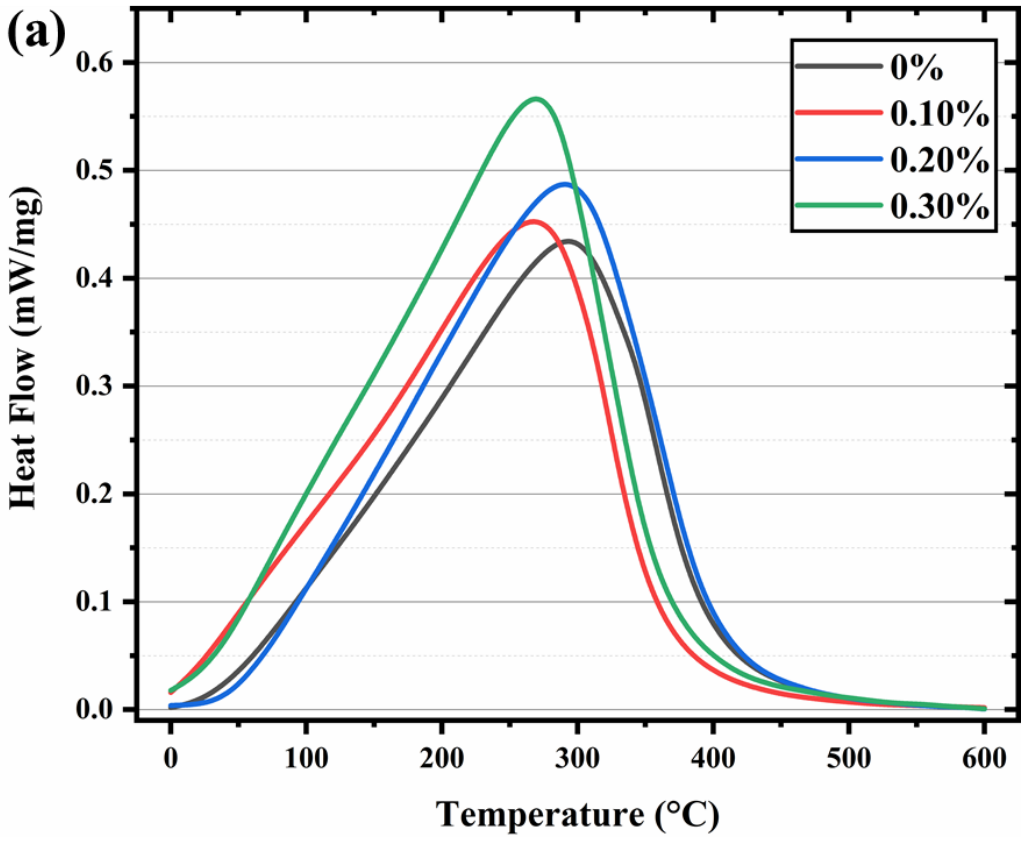

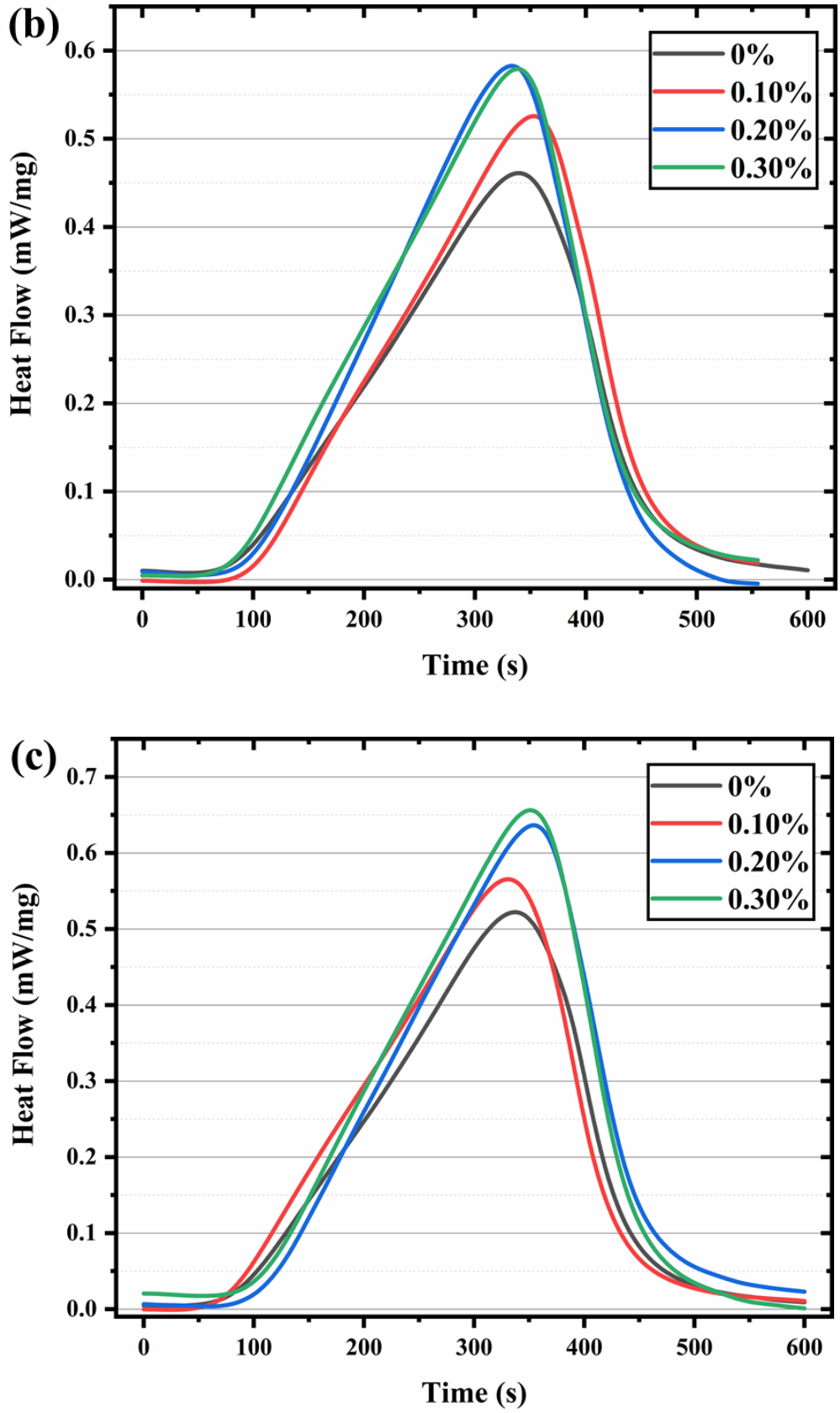

Figure 4.35 $Ca(OH)_2$ crystal decomposition heat flow and time relationship curves at days of (a) 7 (b) 14 and (c) 28

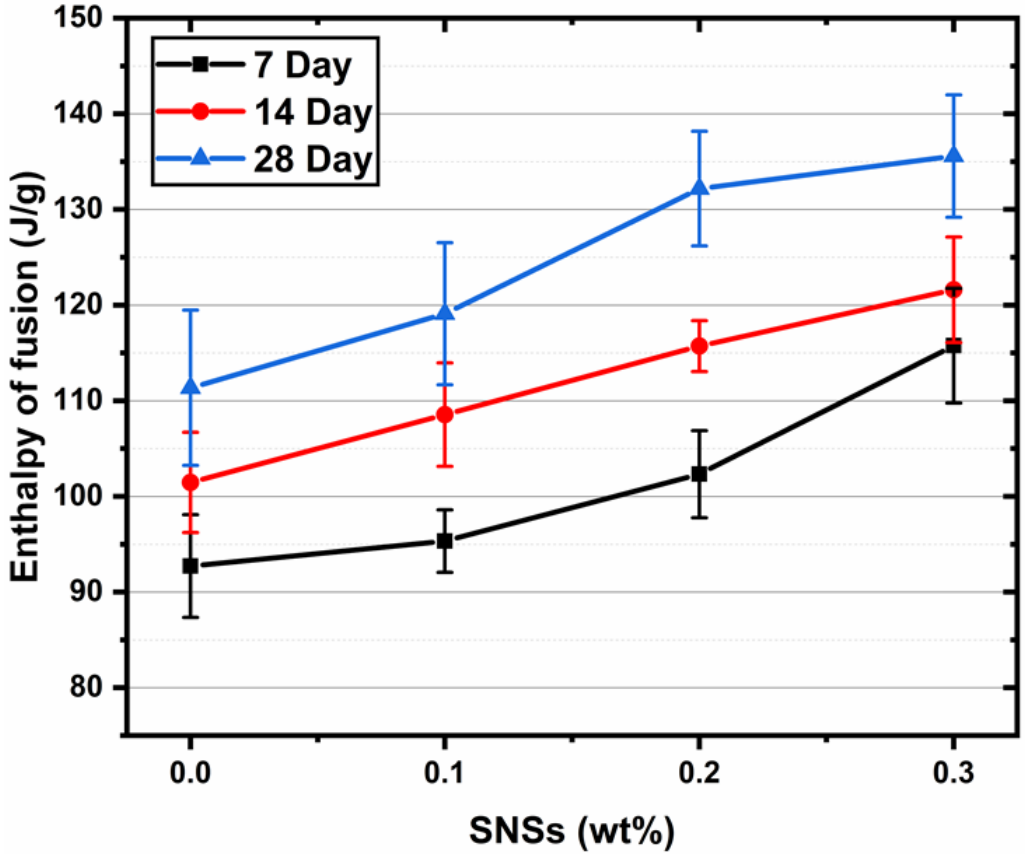

Figure 4.36 Portlandite enthalpy of fusion

4.6 SNS accelerate cementitious composites hydration mechanism

SNS reinforced cementitious DOH mechanisms can be mainly divided into the following three mechanisms. Firstly, SNS construct the cementitious composites steric stabilisation mechanism. Figure 4.37 (a-b) demonstrates the possible agglomeration of ordinary cement particles during mixing, including the cementitious composite DOH. The SNS effect on cementitious composites rheology was verified and characterised through the SNS-cementitious composites mini-slump workability test. As is shown in Figure 4.37 (c), the high-affinity H-bond of hydrophilic additive SNS interacted with the cement particle Ca-O. The SNS adsorbed into the cement particles can reduce the

agglomeration, enabling the cement particles to disperse, and diffuse helping cementitious composites steric stabilisation.

Secondly, the free partly fragmented SNS promote the chemical interaction on the particle interface. The SNS bond exists hydroxyl/hydroxymethyl functional groups, which might break under cementitious composites alkaline conditions (pH=11.7). As shown in Figure 4.37 (c-d) the SNS chains near the C3S surface dissolve to generate organic chemical compounds, which break down the water film on the SNS/C3S interface (Chi *et al.*, 2020). During the hydration, the OH^- and C-OH fragments decompose from the SNS and the enriched H^+ protons in water enable further ion exchange. The brokered SNS backbone and the carbon atoms are reassembled with the oxygen and hydrogen atoms. The ionic concentration increase is consistent with the results of CV, EIS and equivalent circuit simulations. Furthermore, the dissolution of SNS functional group promotes the increase of concentration of hydroxyl groups in the solution, and Ca^{2+} ions react with the dissolved hydroxyl groups and precipitate to the formation of $Ca(OH)_2$ (Hasan *et al.,* 2019).

Thirdly, the SNS attached to the cement particles' surface demonstrated the short-circuit diffusion (SCD) mechanism. The ordinary cementitious reaction formed a high-density hydration products layer on the surface of cement particles. This phenomenon significantly slows down the hydration rate and decreases water molecule diffusion depth into the cement particle interior, which results in a low DOH in the cement particle core. As shown in Figure 4.37 (c-d), the adsorbed SNS encapsulated on the cement particles' hydrate layer illustrates the SCD mechanism. These mechanisms contributed towards building the embedded water-conducting channel structure and generated further reactions to facilitate the hydration. The SNSs dispersed on the surface of C3S generate the new intercalation a-SNS/C-S-H and a-SNS/$Ca(OH)_2$,

which burst the existing hydration shell. Like reservoirs, the SNS promote the movement of water molecules and continuously transport them into the unhydrated cement particle cores, accelerating the hydration process evolution and increasing the hydration phase formation. The SNS in cementitious composites promote more calcium hydroxide and C-S-H formation and improve the DOH. These conclusions have been validated by the TGA and DSC results.

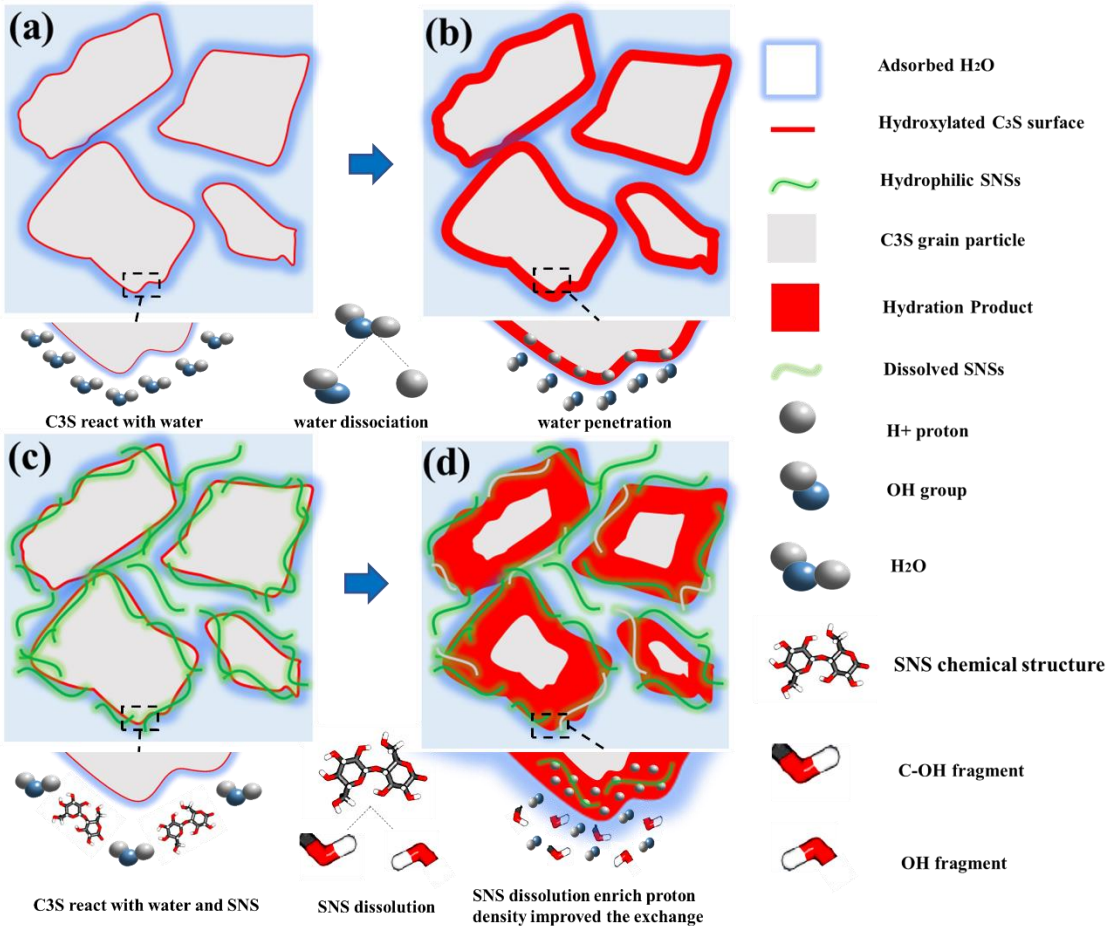

Figure 4.37 Cement pastes' particle hydration progress (a) plain cement particle reaction with water, (b) cement pastes' hydration products, (c) SNS steric stabilisation effect, (d) SNS SCD mechanism and SNS dissolution

4.7 Conclusion

This chapter discussed the workability, hydration degree, type of hydration product phase, and cementitious composites impedance and CV properties with different SNS concentrations during the cementitious hydration interaction progress. The given experimental results revealed the following three SNS reinforced cementitious composites hydration mechanisms:

(1) SNS 2D steric stabilisation dispersal of cement particles. The Marsh cone experiment shows that under the w/c of 0.35, SP optimal addition was 1.0-wt%. The mini-slump test verified that at the 1.0-wt% SP addition, the evenly distributed SNS filled the cement particle gap and stabilised the cement matrix. The high hydrophilic SNS can effectively accelerate the cement particles' reaction with water molecules. Within 0.3-wt% SNS did not significantly affect the workability of the cement pastes.

（2) The short circuit diffusion mechanism explains that the SNS attached to the surface of cement particles. The SNS work as a water transport channel, transferring free water molecules to the interior of unhydrated cement particles and enhancing the degree of hydration. The TGA results indicated that the SNS promoted the DOH from an early age. The thermal mass loss (chemically bound water content) of cement composites hydration products increased with the extension of curing time and the increased SNS concentrate. When the amount of SNS was 0.3-wt%, the matrix DOH increased by 6.8%. The DTG curve shows that the amount of hydration products increases with SNS additions without affecting the hydration phase types. The DSC experiment results further confirmed that the hydration products increase through the enthalpy of fusion, and the content of calcium hydroxide is correlated with the additions of SNS.

(3) SNS promote the formation of new intercalation crystal structures SNS/$Ca(OH)_2$ and SNS/C-S-H, and provide more reaction sites for the further cementitious hydrate. In addition, partial SNS decompose under the alkaline conditions to generate some organic chemical compounds, which break down the water film effect of the SNS/C3S interface. The hydroxyl groups generated by the dissolution of SNS react with Ca^{2+} ions to precipitate the $Ca(OH)_2$. The CV curve shows the composite peak current and volt-current curve area effectively improved when SNS was added, the larger peak current and the curve area show the better cement matrix capacitance. This can be attributed to the fact that SNS promote the formation of organic compounds and enable the cement matrix to carry a higher ion concentration.

The Nyquist plot of EIS results shows the cementitious impedance significantly decreases as the SNS amount increases. Combining with the equivalent circuit model $R_s(R_eC_e)(C_{dl}(R_{ct}Z_w))$, the basic characteristic parameters of the SNS-cementitious matrix can be inferred. With the increase of SNS, the cementitious R_s, C_{dl} and Z_w are also increasing, whereas R_{ct} show a continuous decrease. The changes in the equivalent circuit characteristic parameters reveal the evolved mechanism of SNS enhances cement composite. The overlap and degradation of SNS in the cement composite contributes to a series of proton exchanges and a high diffusion rate of C3S.

Chapter 5 SNS reinforced cementitious composite mechanical properties

5.1. Introduction

This chapter investigates the effect of SNS on the mechanical properties of the cement matrix. The SNS-cementitious composites design considered three different additions of SNS, two different water-cement ratios, two different SNS dispersion conditions and three curing ages. A total of 448 SNS-cementitious samples were tested to determine the mechanical properties, including compressive strength, flexural strength and splitting tensile strength. The fracture properties were also determined. The series of experimental results revealed the mechanical properties of the SNS effect on cementitious composites.

5.2 Experiment design

5.2.1 Raw materials

The raw materials used in the research contained CEM-52.5 R commercial OPC, polycarboxylic acid ether-based superplasticiser (SP), deionized water and the SNS suspension. Details on the materials used has been described in section 4.2.

5.2.2 Cementitious mix proportions

The cementitious composites research considered different SNS mix proportions under the laboratory condition: SNS with weight contents of cement (0, 0.1, 0.2 and 0.3 - wt%), the as-received SNS (raw) and ultrasonically dispersed for 30 min (soni), water-cement (w/c) ratios of 0.35 and 0.40 and curing ages at ages of 7, 14 and 28. The 14 different mix proportions of SNS mixtures are shown in Table 5.1. A total of 168 cubes,

168 prisms, 56 pre-notch prisms and 56 cylinders were prepared in order to investigate the mechanical properties of the SNS-cementitious composites. Four specimens of each mix design were tested on the same ages and the averages were taken to minimize the errors caused by the random factors. The specimen dimensions and test methods are shown in Table 5.2 according to ASTM C 109 (ASTM, 2013), ASTM C78 (ASTM, 2010), BS EN12390-6:0229 (EN, 2009) and RILEM (1985).

Table 5.1 Mixture proportions of SNS platelet reinforced cement pastes

Mix No.	Unit weight						SNS additional percent (-wt%)
	Cement (g)	Water (g)	SP (g)	SNS(R) (g)	SNS(S) (g)	w/c Ratio	
AP00	300	105	3	0.00	0.00	0.35	0.00
AR01	300	105	3	0.30	0.00	0.35	0.10
AR02	300	105	3	0.60	0.00	0.35	0.20
AR03	300	105	3	0.90	0.00	0.35	0.30
AS01	300	105	3	0.00	0.30	0.35	0.10
AS02	300	105	3	0.00	0.60	0.35	0.20
AS03	300	105	3	0.00	0.90	0.35	0.30
BP00	300	120	3	0.00	0.00	0.40	0.00
BR01	300	120	3	0.30	0.00	0.40	0.10
BR02	300	120	3	0.60	0.00	0.40	0.20
BR03	300	120	3	0.90	0.00	0.40	0.30
BS01	300	120	3	0.00	0.30	0.40	0.10
BS02	300	120	3	0.00	0.60	0.40	0.20
BS03	300	120	3	0.00	0.90	0.40	0.30

Remarks: the capital letter A and B in the specimen mix numbering refer to the water-cement (w/c) ratio 0.35 and 0.40. P means the plain cement, R and S represent the dispersion methods raw and soni SNS, followed by the relative content of SNS additives into the cementitious composites (0.00%, 0.10%, 0.20% and 0.30%), SP represents the superplasticiser.

Table 5.2 Specimens, dimensions, test type and quantity of specimens in mechanical properties

No.	Specimens	Dimensions (mm)	Test method	Quantity
1	Cube	50×50×50	Compressive	168
2	Prism	40×40×160	Flexural	168
3	Cylinder	100×200	Splitting	56
4	Notched Prism	40×40×160 (3×13 notch)	Fracture	56

5.2.3 Manufacturing process and curing condition

Prior to using the SNS suspension, the soni SNS were ultrasonically treated with water by Analog Ultrasonic homogenizer (Branson Ultrasonics™ Sonifier™ S-450A). The SNS suspension was sonicated for 30 minutes with 50% duty cycles. During the ultrasonicated process, the suspension was surrounded with ice to ensure the SNS stability at low temperature. Then ready SNS suspensions were added into the water and mixed with 1% superplasticiser. Finally, the prepared suspension was mixed with OPC for 7 minutes (ASTM, 2014). Prepared cement pastes were slowly poured into the different sized moulds (depending on the test type). Filled cement pastes moulds were compacted with a standard electric vibrator, the surface was sealed and the mixture were cast in moulds. After 24 hours, the solid cement pastes were demoulded and continuously maintained at the standard cure conditions (20 ± 2 ℃ and relative humidity 95 ± 5%) until tested. Part of the samples as shown in Figure 5.1.

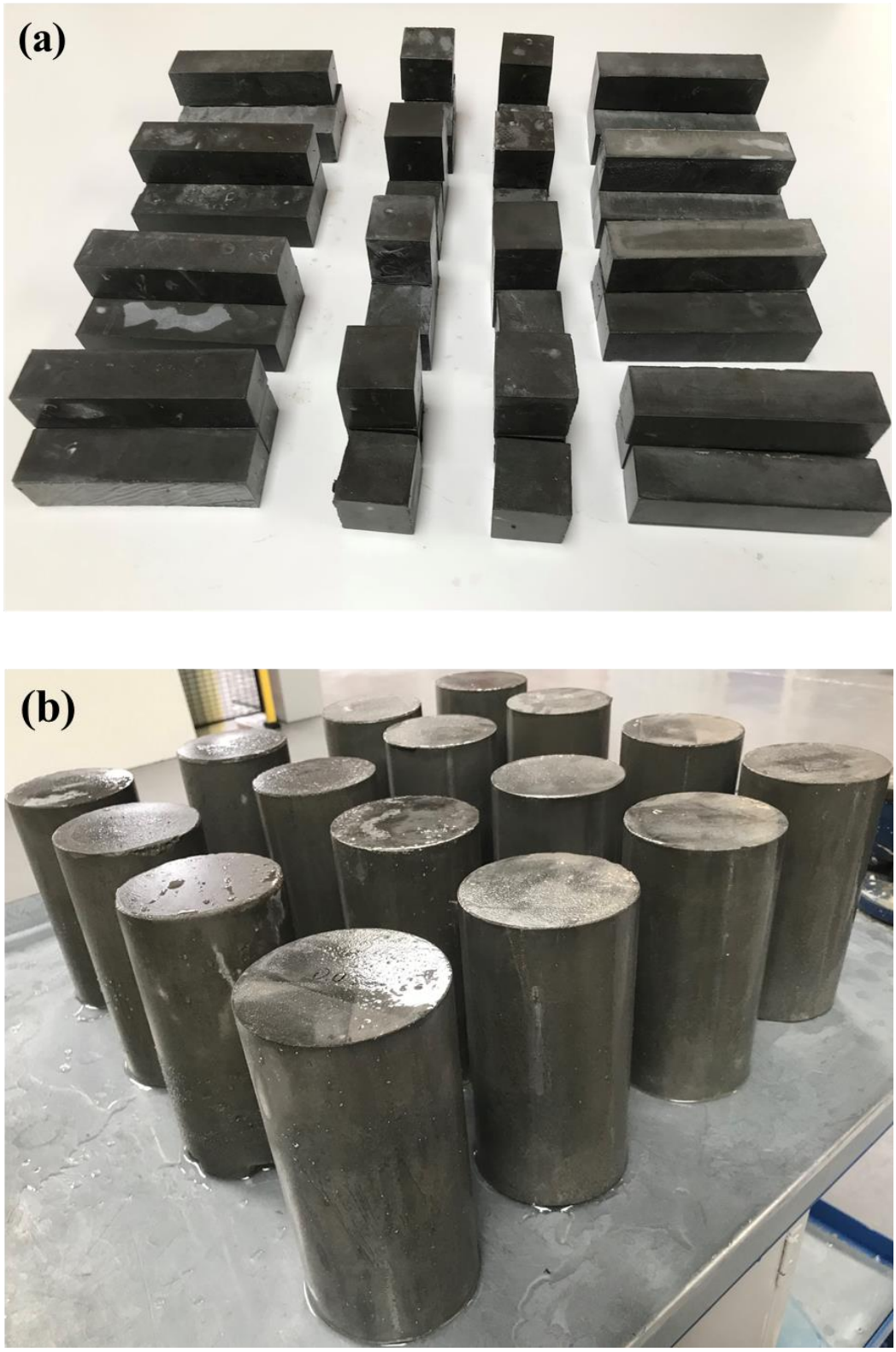

Figure 5.1 Part of the specimens used in study (a) cube and prism (b) cylinder

5.2.4 Experiment methods

5.2.4.1 Compressive strength tests

The compressive strength of cementitious composites was tested according to ASTM C 109 (ASTM, 2013). The samples were tested with the universal testing machine (UTM, Instron 8802J5219, 250KN) at 0.5 MPa/s loading rate. The experiment setup is shown in Figure 5.2. A total of 168 cubes were tested at 7, 14 and 28 days, to investigate the effect of different SNS amounts on the compressive strength of cementitious composites. The experiment was performed at the hydraulic mechanical test systems (MTS) under load control. The cubes compressive strength (σ_c) is calculated from the following equation: (ASTM, 2013).

$$\sigma_c = \frac{P}{A} \tag{5.1}$$

Where P is the maximum applied load, A is the area of the loaded surface (mm^2).

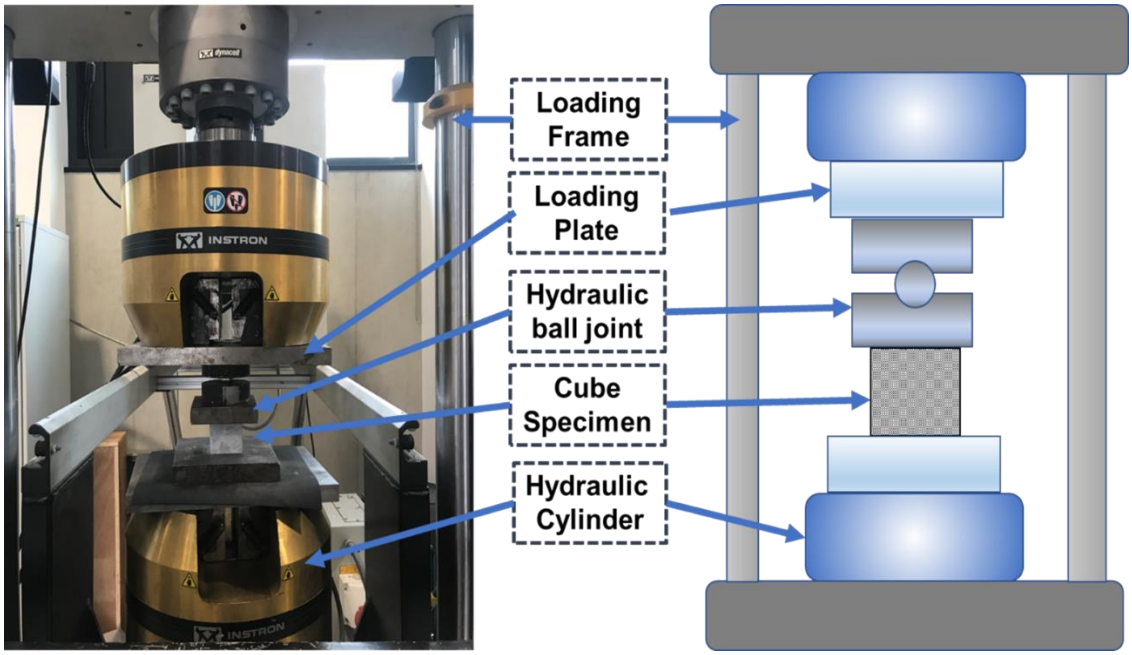

Figure 5.2 Compressive strength of test cube setup

5.2.4.2 Flexural strength four-point bending tests

The bending behaviour of the cement pastes was tested at days of 7, 14 and 28 through the four-point bending experiment. The flexural strength test was following by ASTM C78 (ASTM, 2010). The experiment setup is shown in Figure 5.3, 168 pieces of prisms test on ASTM Zwick Roell Z020 (C090204019, 20KN, Germany). Before the test, a cutting machine was used to polish the prism surface to eliminate stress concentration effects. The bending test was performed with the displacement control at a constant loading rate of 0.01 mm/min. The prism flexural strength (σ_f) was calculated from the following equation: (Saafi *et al.*, 2015)

$$\sigma_f = \frac{3Pa}{b^3} \tag{5.2}$$

Where P is the maximum applied load, a is the distance between the support and the load point and b is the thickness and width of the prism.

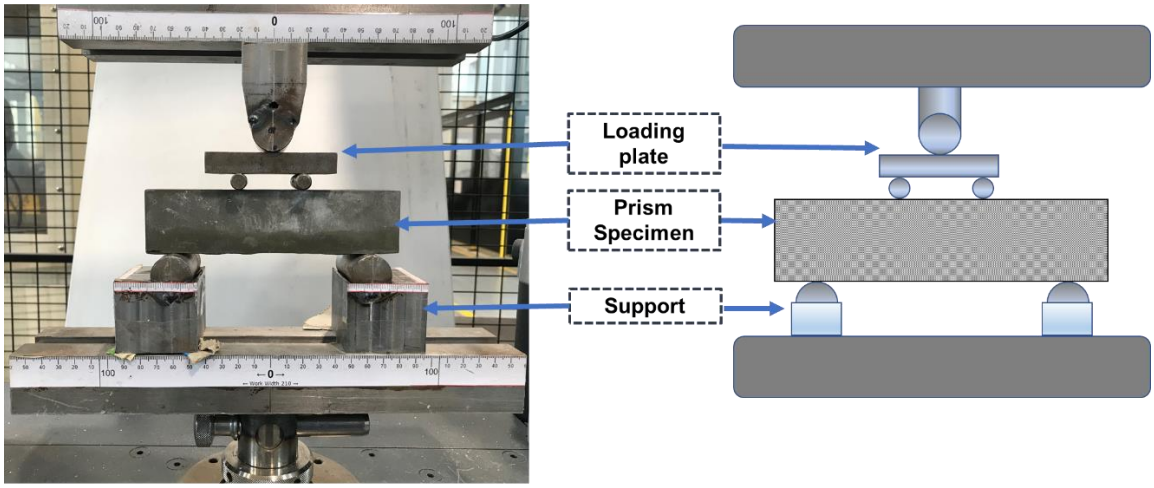

Figure 5.3 Flexural strength of four-point bending test prism set up

5.2.4.3 Splitting tensile strength tests

The splitting tensile strength was measured following the BS EN12390-6:0229 (EN, 2009) splitting tensile strength test. The cured cylinder samples were tested at a

universal testing machine (UTM, Instron 8802J5219, 250KN) as shown in Figure 5.4 with a constant loading speed of 0.06 N/mm^2/s. Figure 5.4 shows the cementitious composite cylinder setup with a supplementary steel bar. The plywood strip is placed on the upper and lower surfaces, to ensure the specimen stress generated by the compression load can be uniformly distributed along the vertical diameter. The experiment involved preparing four specimens in each mixed design and the maximum failure load test at 28 days. The splitting tensile strength (σ_{ct}) is calculated from the following equation according to BS EN12390-6:0229 (EN, 2009).

$$\sigma_{ct} = \frac{2P}{\pi \times D \times L} \tag{5.3}$$

Where P is the maximum load (N) recorded during the test, D is the cross-sectional diameter of the specimen (mm) and L is the length of the specimen (mm).

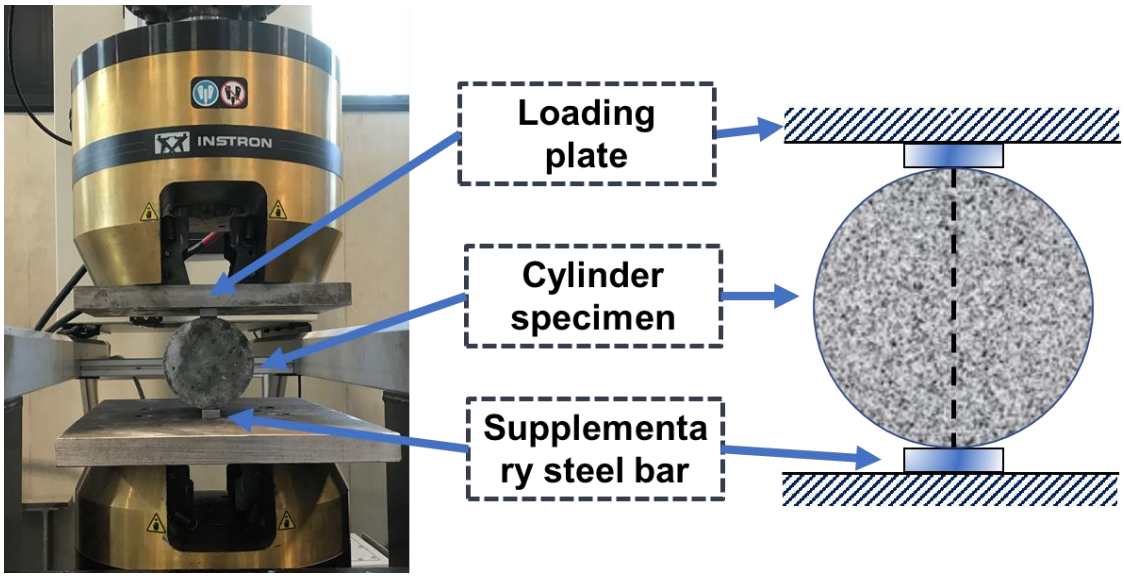

Figure 5.4 Splitting tensile strength of the cylinder specimen

5.2.4.4 Fracture strength three-point bending tests

The fracture was tested by three-point bending methods according to RILEM (1985). A total of 56 pieces of SNS-cementitious composites prisms (40×40×160mm) with pre-

notch (3×16mm) were performed with a Universal testing machine (ZWICKZ005), at a 0.02 mm/min constant loading rate. The Video gauge™ (Imetrum Ltd) method was involved in measuring the crack mouth opening displacement (CMOD) change. The video gauge consists of two camera lenses, an IMetrum controller and computer data acquisition and analysis systems. The experimental setup is shown in Figure 5.5, where clear and uniform black dots are imprinted near the prefabricated notch of the prism to assist in recording the relative displacement in the video area (Figure 5.6). The camera was set up at a distance of 1.2m from the prism surface for continuous monitoring, and the entire camera acquisition frequency is 15Hz. The prism experimental load (P), loading point deflection (δ) and CMOD variation were recorded by the video measuring device and universal testing machine. The calculation of fracture energy (G_F) and fracture toughness (K_{IC}) were based on the stress-deflection curve and calculated through the equations below (Hu *et al.*, 2014).

$$G_F = \frac{mg\delta_0 + W_0}{t(h-a)} = \frac{mg\delta_0 + \int_0^{\delta_0} P(\delta)d\delta}{t(h-a)} \tag{5.4}$$

$$K_{IC} = \frac{P_{max}S}{th^{\frac{3}{2}}} f\left(\frac{a}{h}\right) \tag{5.5}$$

$$f\left(\frac{a}{h}\right) = 2.9\left(\frac{a}{h}\right)^{\frac{1}{2}} - 4.6\left(\frac{a}{h}\right)^{\frac{3}{2}} + 21.8\left(\frac{a}{h}\right)^{\frac{5}{2}} - 37.6\left(\frac{a}{h}\right)^{\frac{7}{2}} + 38.7\left(\frac{a}{h}\right)^{\frac{9}{2}} \tag{5.6}$$

Where G_F is the fracture energy of the cement pastes, m is the mass ($m = m_1 + m_2$), m_1 is the mass of the prism between support, m_2 is the loading fixture without attaching to the machine mass, g is the acceleration under gravity, δ_0 is the final failure of the sample displacement, W_0 is the area of the load relate to displacement plot, t is the thickness of the sample, h is the height of the sample, a is the depth of the notch,

K_{IC} is the fracture toughness of the cement pastes, P_{max} is the peak load and S is the span of the sample.

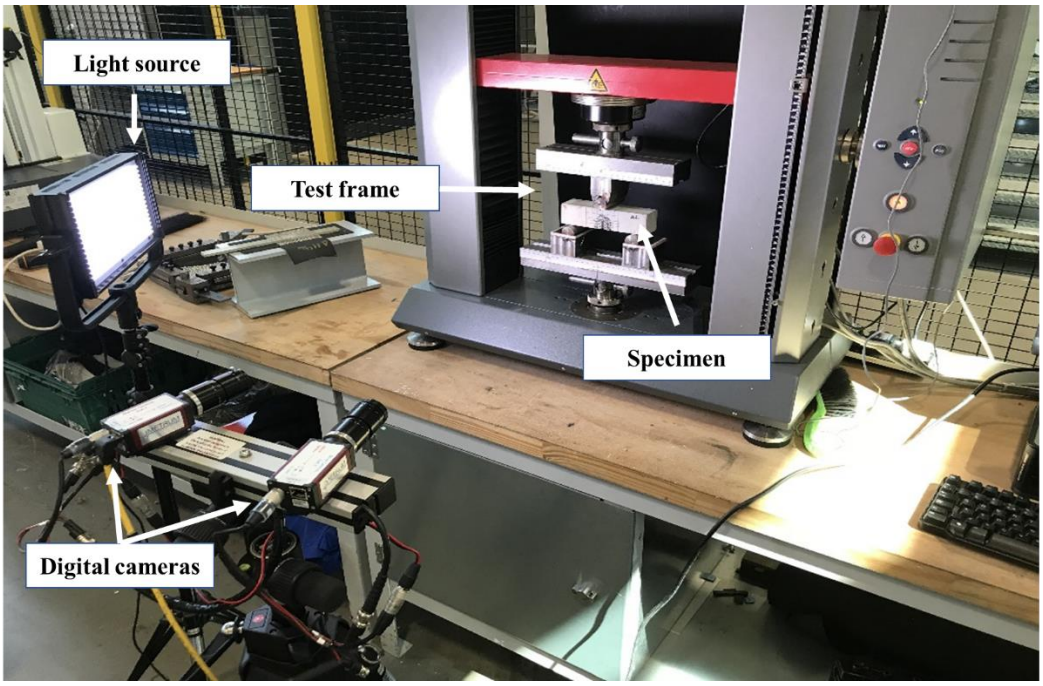

Figure 5.5 Fracture toughness of three-point bending test prism set up with a video recording machine

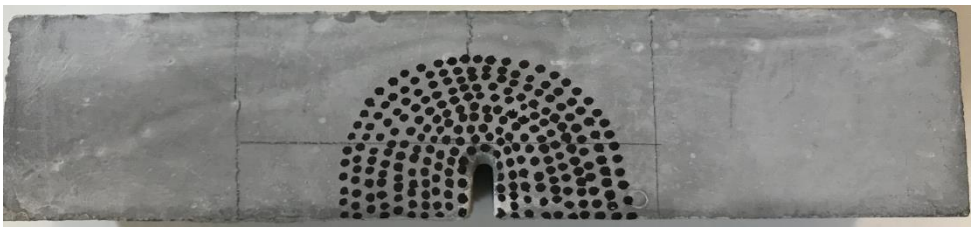

Figure 5.6 Manufactured SNS-cementitious composite specimen

5.3 Results and discussion

5.3.1 Compressive strength of SNS-cementitious composites

Figure 5.7 shows the compressive strength of cement matrix (w/c=0.35) effects of raw and soni SNS at 7, 14 and 28 days. The experimental results are the average of four samples compressive strength in each design. Figure 5.7(a) and Figure 5.7(b)

compressive strength show a similar trend, where the increase of SNS addition and curing ages improve the cementitious composite compressive strength. The optimal SNS addition amount for the cementitious composites was constant at 0.2-wt%. Compared to the control group, the optimal AR02 and AS02 compressive strengths increased by 8.33% and 10.69% at 28 days. At 28 days, compressive strength did not show a significant difference between the raw and soni SNS-cementitious composites.

Notably, ultrasonic-treated SNS show a significant improvement of compressive strength in the early stages of cement-based hydration. Compare to the control group, AR02 and AS02 compressive strength increased by 4.89% and 11.32% at 7 days. This is because the ultrasonically further assistant SNS uniformly distributed them in the aqueous solution, which effectively improved the fibre distribution in the cement matrix and accelerated the matrix early age hydration rate.

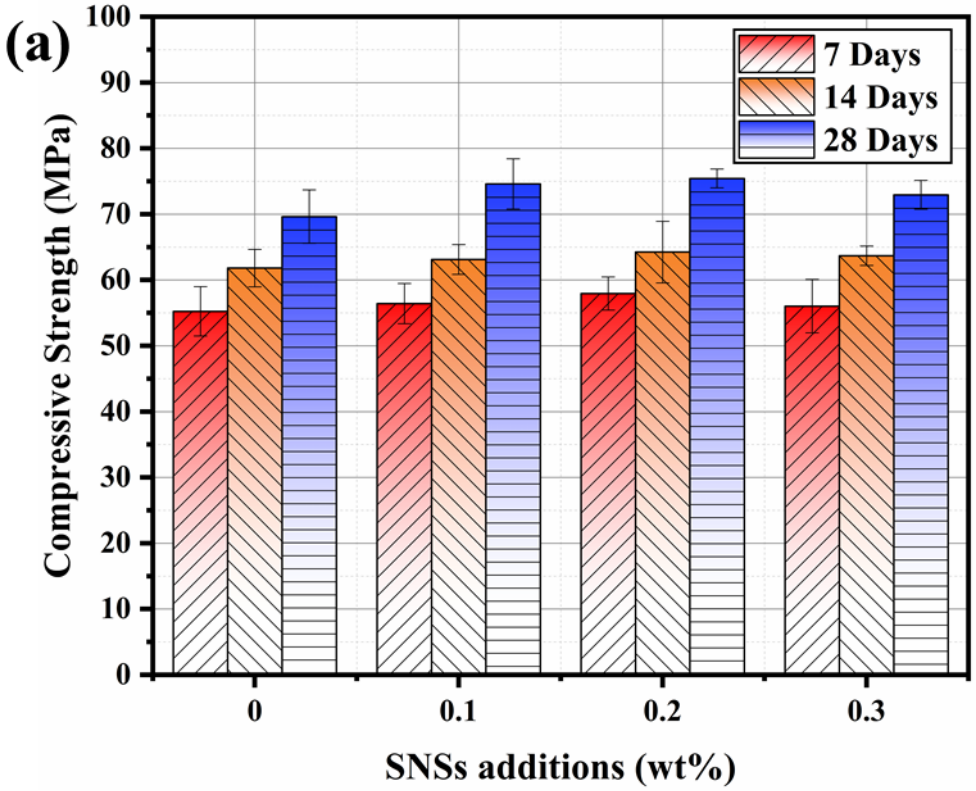

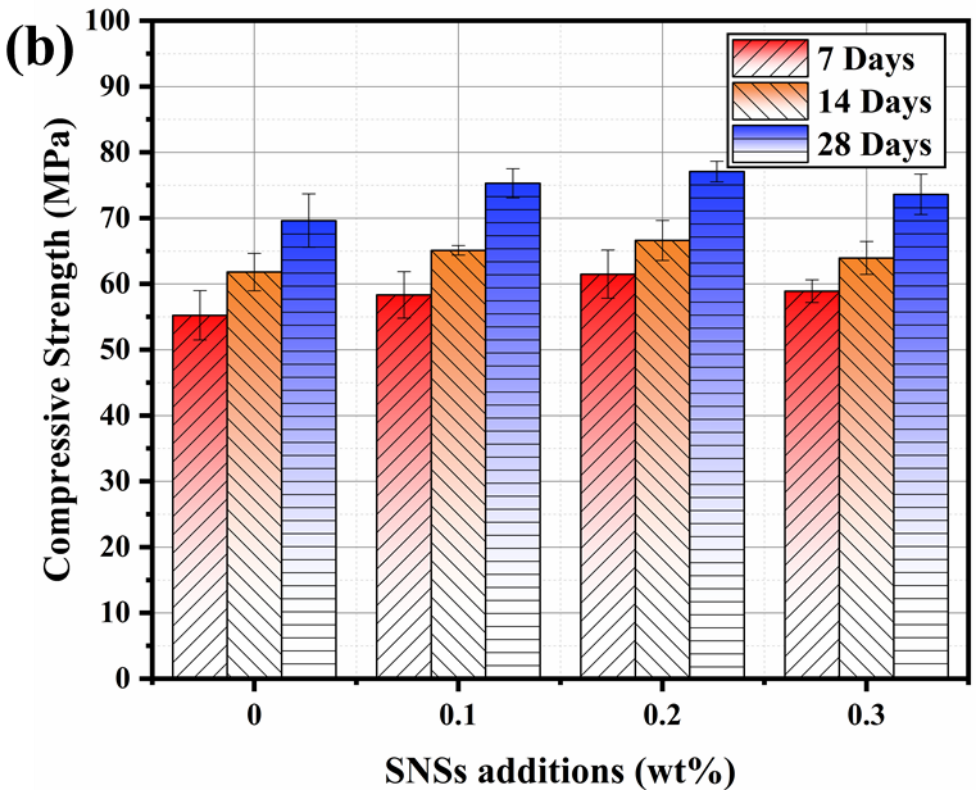

Figure 5.7 Compressive strength of SNS-cementitious composite at 7 days, 14 days and 28 days (w/c=0.35) (a) raw SNS, (b) soni SNS

Figure 5.8 shows the compressive strength of raw and soni SNS-cementitious composites (w/c=0.40) at 7, 14 and 28 days. Figure 5.8 shows that compared to the control group, the compressive strength of optimal design BR02 and BS02 increased by 10.29% and 11.73%, 7.06% and 10.19%, 10.03% and 12.15% at 7, 14 and 28 days, respectively. The ultrasound-treated SNS show a better effect on the compressive strength of cementitious composites under higher water-cement ratios.

When comparing Figure 5.8 with Figure 5.7, the compressive strength results show that SNS expressed a similar reinforced trend under different water-cement ratios. Furthermore, Figure 5.8 shows the w/c ratio increase which reinforces the efficiency of the cementitious composites SNS. The improvement in w/c enhanced the fluidity of the matrix and reduced the raw SNS agglomeration that exists in cementitious

composites. During the mixing, the high hydrophilicity and specific surface area SNS require a large amount of water. The free water molecules promote the hydration reaction process. The insufficient water supply may cause the uneven distribution and agglomeration of SNS, which affects the early hydration efficiency of the cementitious composites. The compressive strength will be enhanced when SNSs are diffused in ultrasonicated, or operated in a better fluidity cement matrix.

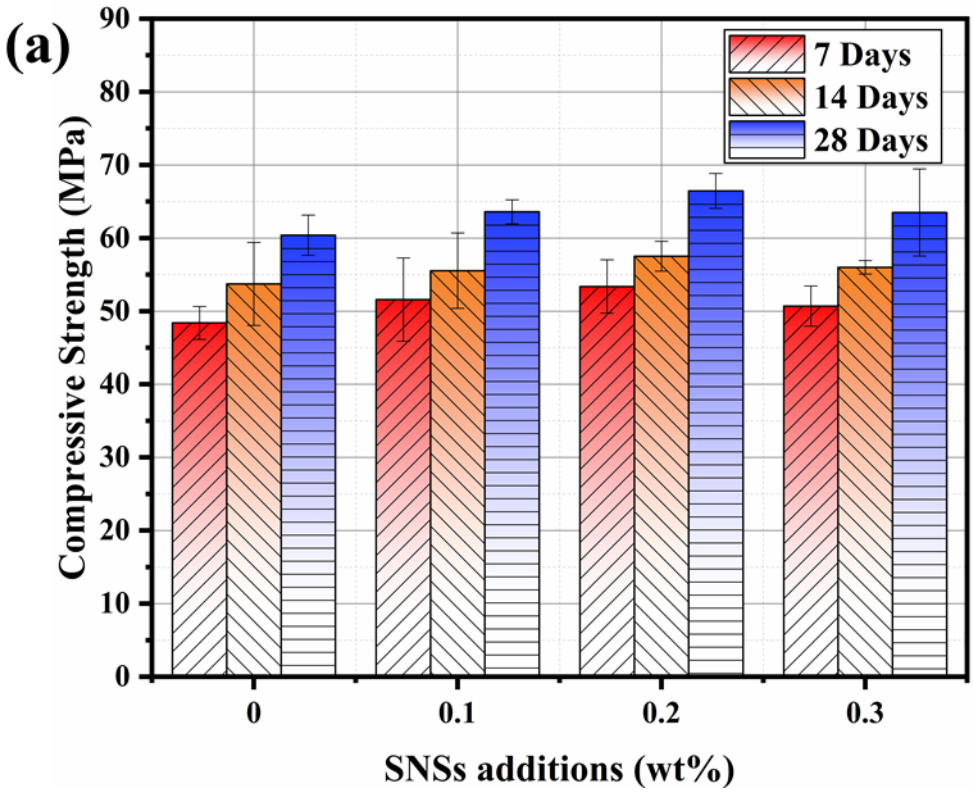

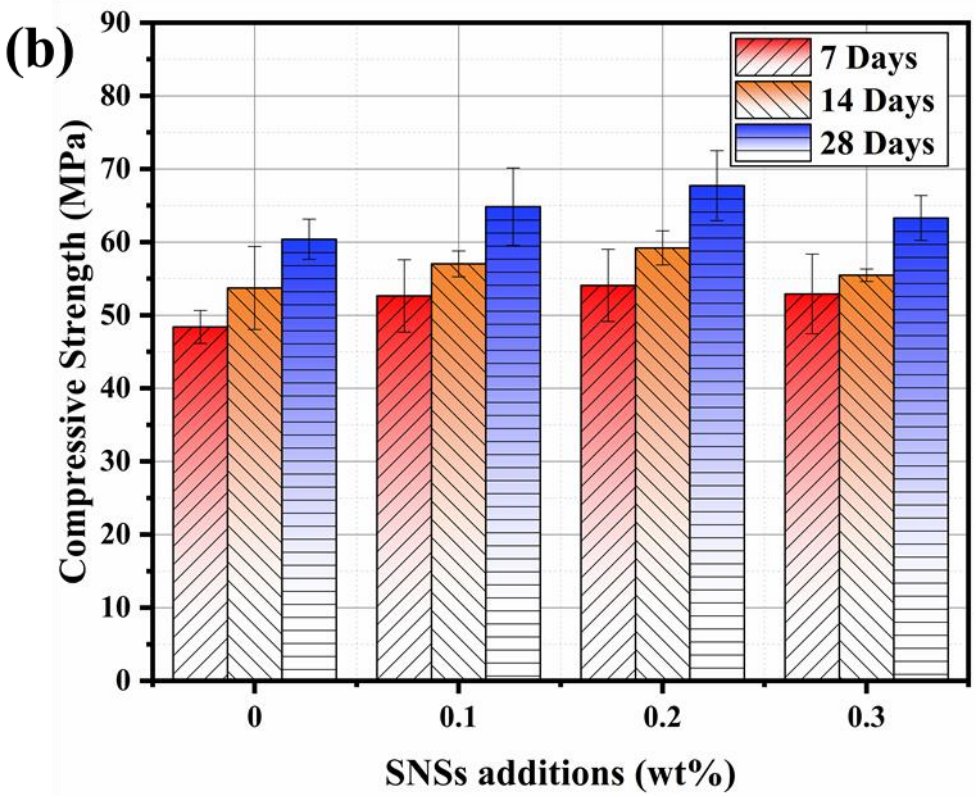

Figure 5.8 Compressive strength of SNS-cementitious composite at 7 days, 14 days and 28 days (w/c=0.40) (a) raw SNS, (b) soni SNS

Figure 5.7 and Figure 5.8 show the compressive strengths of SNS-cementitious composites under 0.35 and 0.40 w/c ratio. The experimental results showed that SNS were able to increase the compressive strength of cement pastes under 14 different formulation conditions at all ages. The results demonstrated that the compressive strength of cementitious composite increased with increasing SNS and matrix curing time. The compressive strength of the cementitious composites reduces with the w/c ratio increase, which is consistent with the Neville point (Neville, 1995). At 7 days, all samples reached 70-80% of the 28-day compressive strength, and all the different additions of SNS had positive effects on the strength. These experimental results are consistent with the finding in CNCs reinforced cement paste (Ghahari *et al.*, 2020) in

that cement pastes at the w/c ratio of 0.35 show that the compressive strength increases 10% at the 0.2% CNCs additive to cement.

Figure 5.9 illustrates the comparison of the increase in the percentage of various SNSs cement matrix compressive strength at 28 days. The SNS formed the cementitious internal reinforcement network, the optimal SNS additions were constant at 0.2-wt%. The mix design of AR02, AS02, BR02, and BS02 at 28 days when compared to the control group showed the compressive strength increased 8.33%, 10.69%, 10.03%, and 12.15%, respectively. The SNS reacts with calcium hydroxide in the cementitious composites, generating more C-S-H and filler in the micro-pore structure.

However, the compressive strength improved by SNS was limited due to the constraint properties of the cementitious materials. When the incorporation of SNS exceeded 0.2-wt%, the increase of cementitious compression resistance tended to decrease the excessive SNS agglomeration forming in the cement matrix. The SNS agglomeration formed the weakest area in the composite material, which were affected the cementitious matrix compressive strength.

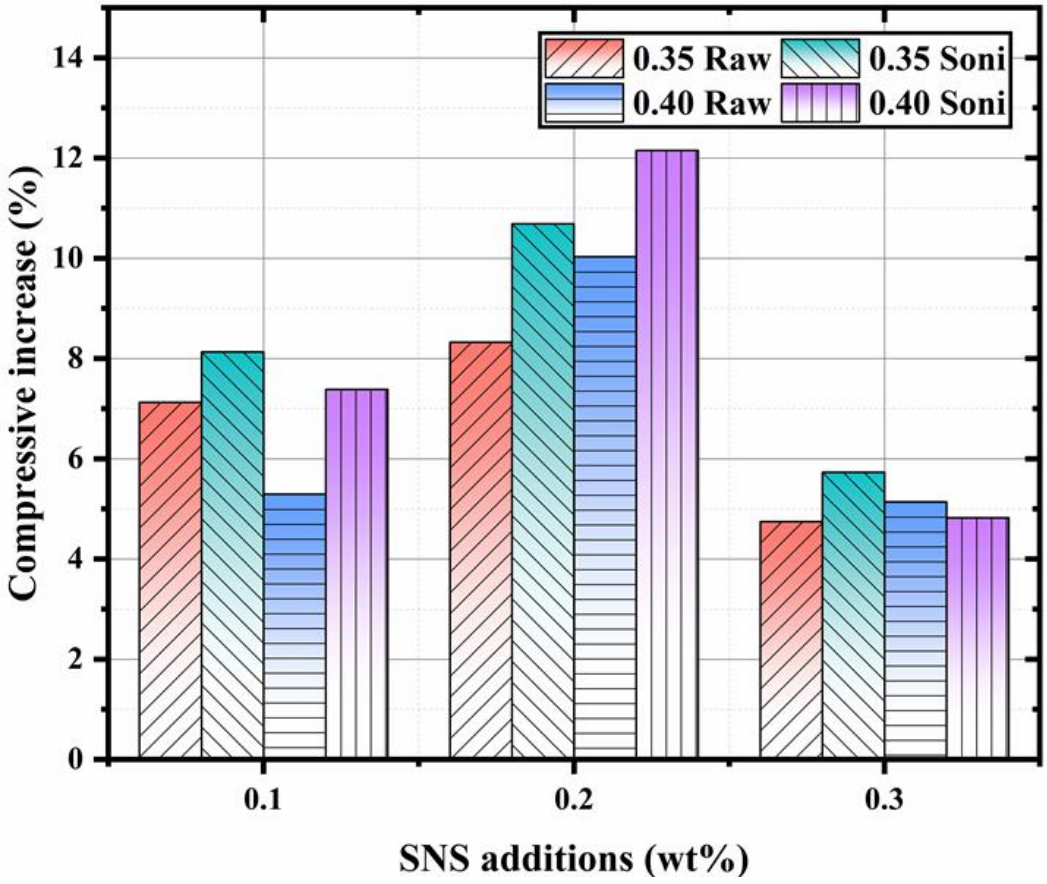

Figure 5.9 Compressive strength of SNS-cementitious composite percentage increase at 28 days

5.3.2 Flexural strength

Brittle materials cementitious composites have high compressive resistance and low flexural properties, which are easily damaged under bending load. The tensile behaviour of SNS-cementitious composites is evaluated by the four-point bending test and splitting tensile test. Figure 5.10 (a-b) and Figure 5.11 (a-b) show the average flexural strength of SNS-cementitious composites under the AR, AS, BR and BS conditions. The flexural strength of cement pastes increased with age, and the strength also increased with the SNS concentrations. The 0.2-wt% SNS additions showed around 20-30% increase in the optimal amount, compared to the control group.

Furthermore, the flexural strength compared to the compressive strength ratio was 4.8-6.5%.

Figure 5.10 indicates the flexural strength of cementitious composites with SNS additions, expressing a parabolic growth trend at 7, 14 and 28 days. The optimum design AR02 increasing by 13.16%, 34.63% and 31.56%, and 20.08%, 48.59% and 38.06% in AS02, respectively. The better fibre filling and cracks bridging in the cement matrix composite can be attributed to more uniformly distributed soni SNS. At 7 days, the addition of 0.1-wt% raw and soni SNS produced about 8% enhancement. The improvement of the ultrasound treated SNS significantly increased at 14 days, the 34.67% increase was double that of the ultrasound untreated SNS cement pastes 14.9%. At 28 days, both SNS and SNS being diffused increased the cement composite by 20.39% and 34.76%. When the SNS addition amount reached 0.3-wt%, the raw and soni SNS matrix flexural showed a limited increase of 3% at 7 days, the flexural strength increased by 14.67% and 28.69% at 14 days, and by 21.92% and 28.82% at 28 days.

The effect of SNS strengthened the internal interface transition zone and inhibited the development of cracks. This phenomenon is consistent with the concrete microstructural internal ITZ reinforce theory (Rashid *et al.*, 2015; Giustozzi, 2016). However, when the SNS addition was increased from 0.2 to 0.3 -wt% there was a certain decrease in flexural strength. This phenomenon is attributed to too much SNS added that cannot be uniformly adsorbed on the surface of the cement particles, a certain amount of agglomeration occurring on the cement pastes surface resulting in stress concentration and reduction in the strength.

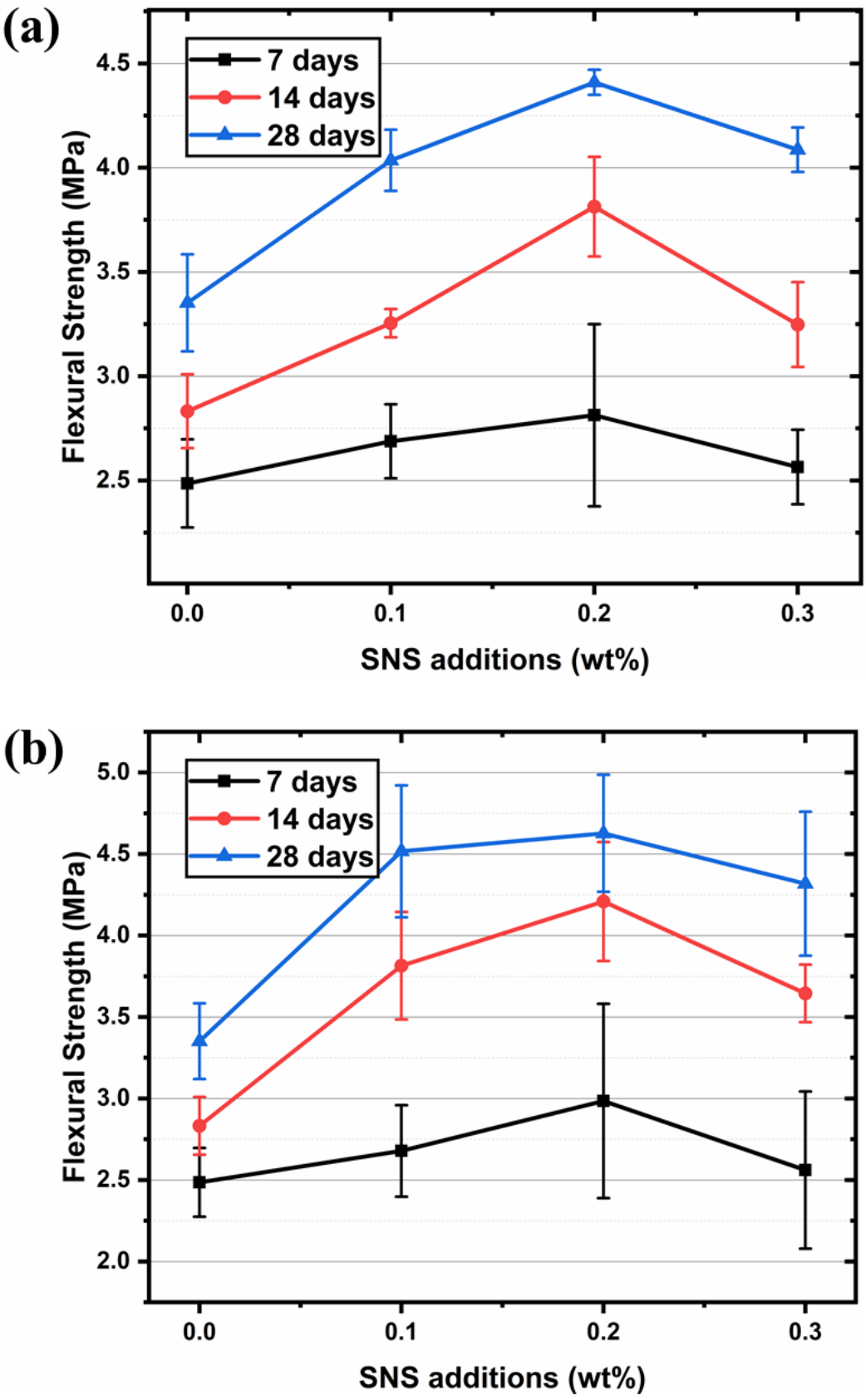

Figure 5.10 Flexural strength of SNS-cementitious composite at the w/c of 0.35 (a) raw SNS (b) soni SNS

Figure 5.11 shows the raw and soni SNS effects on the flexural strength of cement pastes (w/c ratios =0.40) at days of 7, 14 and 28. The optimal design BR02 and BS02 increased by 24.21% and 31.81% at 7 days, 15.34% and 25.40% at 14 days and 28.73% and 39.91% at 28 days. At the concentration of 0.1-wt% and 0.3-wt% of raw SNS-cementitious composite, there was no significant improvement at 7 and 14 days. The 28-day 0.1 and 0.3-wt% raw SNS had only 11.67% and 9.24% increases, respectively. Furthermore, the addition of 0.1 and 0.3-wt% soni SNS showed a significant improvement, increased by 37.94% and 24.31%, respectively at 28 days. As soni SNS was uniformly distributed to the cementitious matrix under the tensile application, more SNS took up part of the tension loads and obstructed the existing crack propagation.

When comparing Figure 5.11 to Figure 5.10, it is evident that the increase in w/c ratio leads to the decrease of flexural strength, but that the SNS that reinforces the matrix keeps a similar trend. Compared to the control groups, the increases in w/c ratio led SNS more efficiently to the enhancement of cementitious composites.

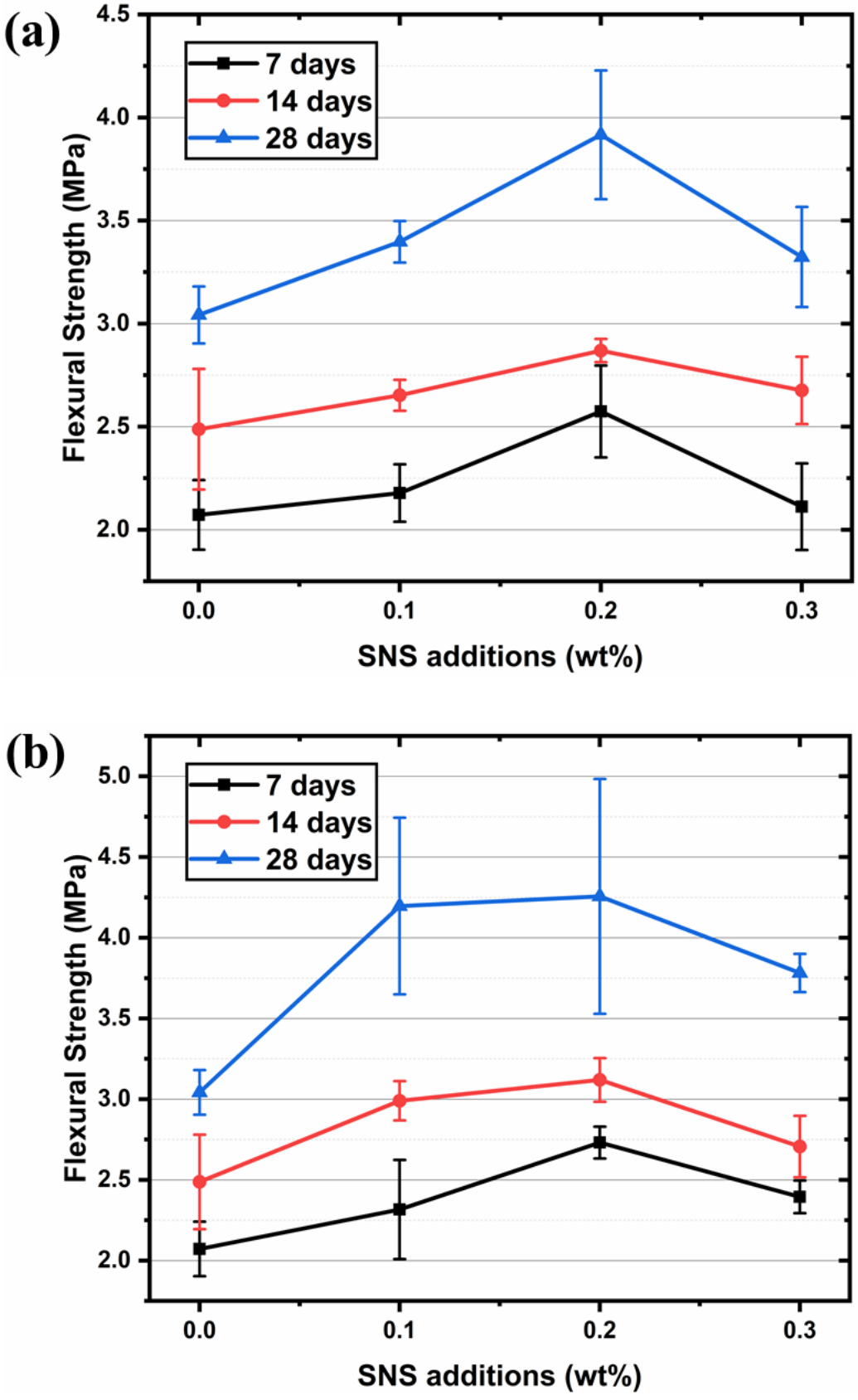

Figure 5.11 Flexural strength of SNS-cementitious composite at the w/c of 0.40 (a) raw SNS (b) soni SNS

Figure 5.12 shows the flexural strength percentage increase of SNS pastes during the 28 days under different conditions. The 0.3-wt% raw SNS amount results in limited strength improvement attributed to the SNS adsorbed to the cement particle, resulting in agglomeration. The results show that the ultrasound treated SNS express a significant increase in flexural strength between the SNS concentration ranges of 0.2 to 0.3-wt%. The high and low concentrations of raw SNS under ultrasonic treatment can result in improved dispersion, presenting more opportunities to exchange water molecules with the cement matrix. Under the same experimental conditions, sonicated SNS cementitious composites contributes to the strength reinforcement because of the higher DOH.

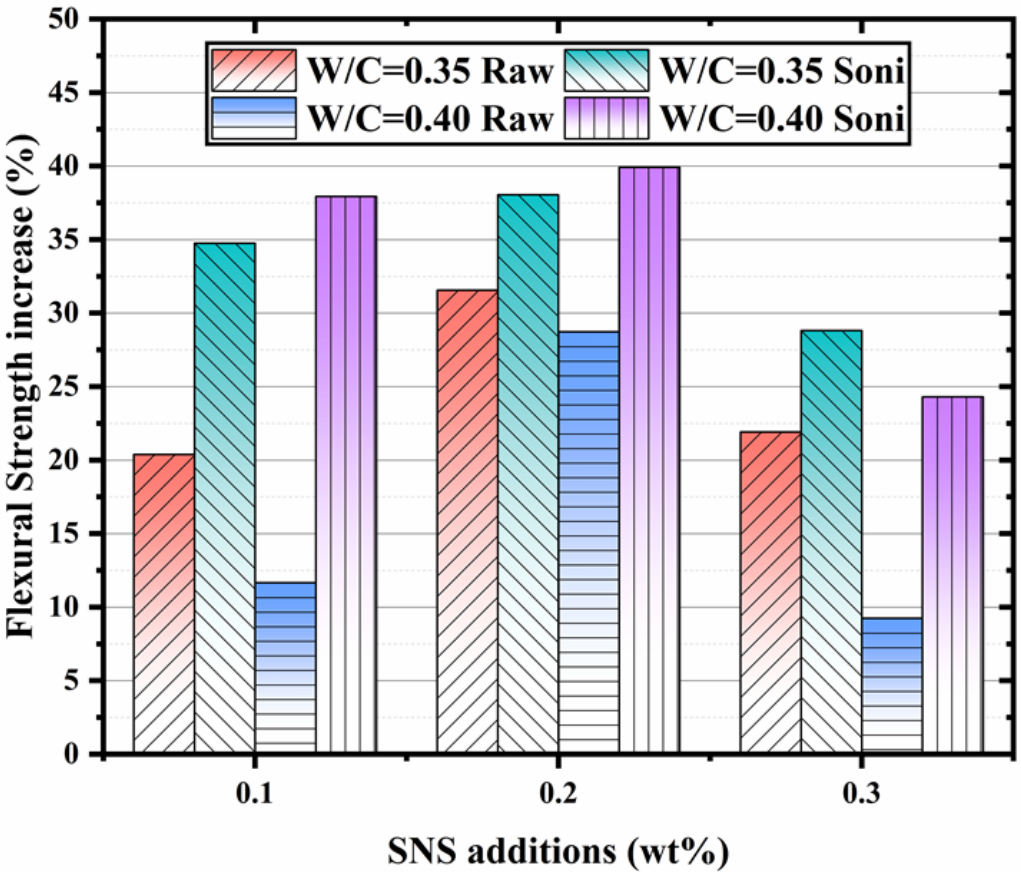

Figure 5.12 Flexural strength of SNS-cementitious composite percentage increase at 28 days

Figure 5.13 visually presents the plain and SNS-cementitious composites prism crack behaviour. The plain cement specimen mode of failure is a predominantly flexural failure, the crack starts in the middle of the span and vertical development. During the experiment, a crack immediately appeared at the surface of the prism and then without warning the specimen separated into two parts. This was attribute to be due to the brittle nature of the plain specimen. The cracks in the plain cementitious composites did not distribute the load and the flexural crack that occurred continued to propagate.

The SNS reinforced cementitious composites prism crack developed closer to the side of the middle in specimens. During the experiment, SNS restraint the cracking was propagated, sufficiently to giving warning during the crack. This demonstrates that SNS is an effective material for bridging of cracks and increasing flexural strength. The bond stresses of SNS in the matrix supplied the crack resistance that happened in the cementitious matrix. With the increase in SNS addition, there is an increase in middle cracking propagation resistance, which then correlates to the maximum load sustained increase. The results obtained from the maximum load sustained from the specimens, suggested that there SNS matrix was better resistance to the cracks.

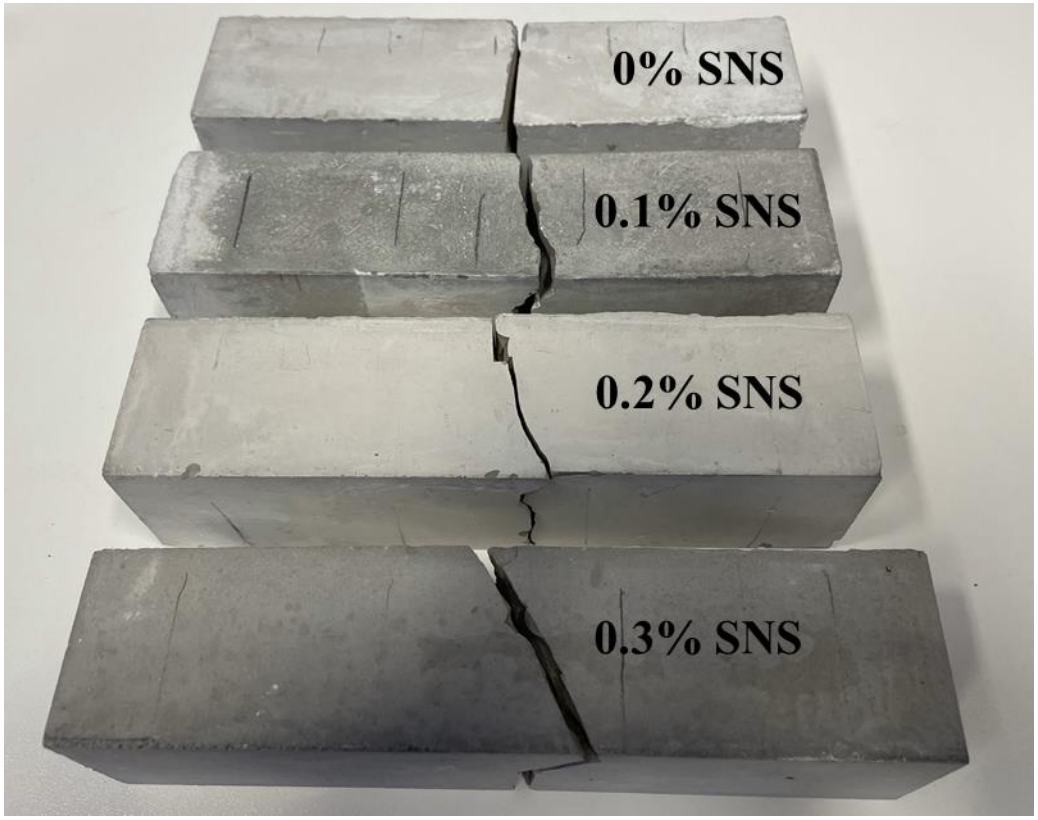

Figure 5.13 Cracks of SNS-cementitious composites prism after test

5.3.3 Splitting tensile strength

In the development of cementitious components design, STS usually triggers tensile cracking at lower load capacities. Figure 5.14 shows the SNS-cementitious composites cylinder indirect tensile composites under the AR, AS, BR and BS conditions at 28 days. At different w/c ratio conditions, the splitting tensile strength of cementitious composites increases peak strength with the SNS addition amount up to 0.2-wt%. Furthermore, the STS of SNS-cementitious composites ratio to the compressive strength was 4.3-5.6%.

Figure 5.14(a) shows the splitting tensile strength of the cementitious composite at 28 days is 3.00 MPa, which significantly increases up to 3.98 MPa and 4.11 MPa when 0.2-wt% raw and soni SNS are added. The splitting strength of cementitious composites with the addition of 0.1, 0.2 and 0.3-wt% SNS was increased by 22.53%, 32.55% and

19.87%. Whereas, the increases in ultrasonically dispersed SNS-cementitious composite were 29.53%, 36.87% and 22.79%, respectively. The splitting tensile strength had improved due to the SNS filling effect, which enhances the bonding between the cement paste matrix ITZ.

Figure 5.14(b) shows the 0.40 water/cement ratio splitting tensile strength of the SNS-cementitious composites. The optimal cementitious addition of the 0.2-wt% raw and soni SNS led to an increase of 31.2% and 32.9%, reaching to 3.65 MPa and 3.70 MPa respectively. When the additional amounts were 0.1% and 0.3%, raw and soni SNS SNS-cementitious composite were increased by 9.18% and 26.92%, and 23.69% and 27.76%, respectively. The SNS filling of the pore leads to a continuous three-dimensional network, generating a structure built from the strong bonds in the cement matrix.

The 0.1-wt% non-dispersed SNS show a limited enhancement effect due to the uneven distribution in the cement matrix. It is noted that similar to Figure 5.14(a), the enhancement amplitude decreases when SNS concentration is higher than 0.2-wt% cement. This phenomenon is the same as with the nano fibrillated cellulose (NFC) agglomeration, in which the NFC agglomeration led to the reduction of the specimen's stress concentrators and STS (Cao, Zavattieri, *et al.*, 2016).

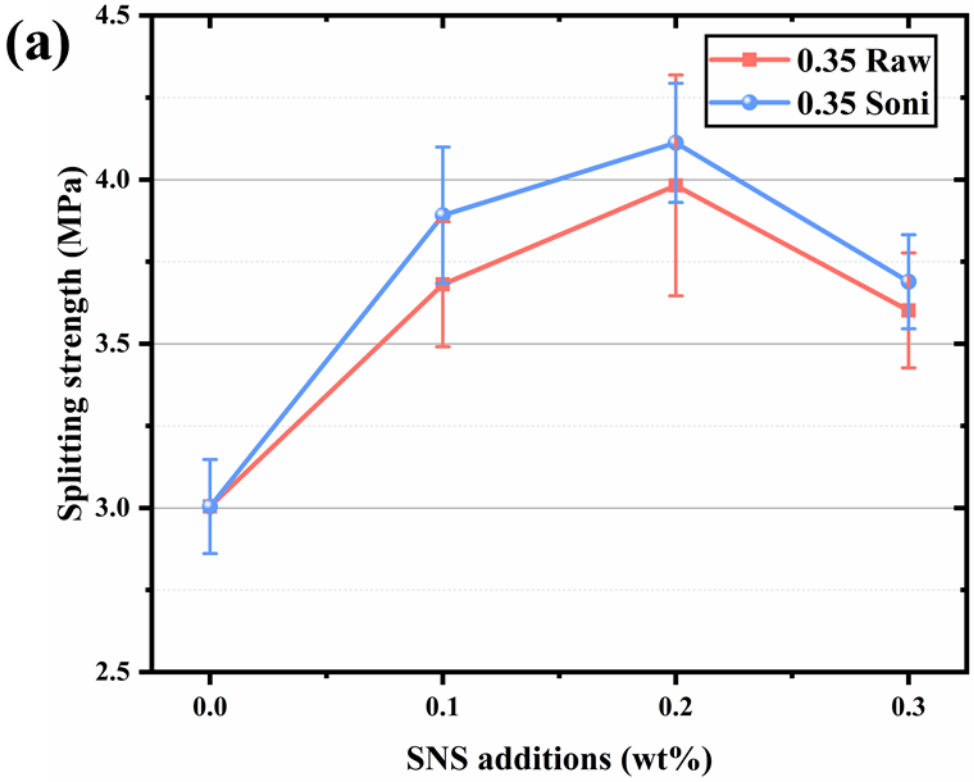

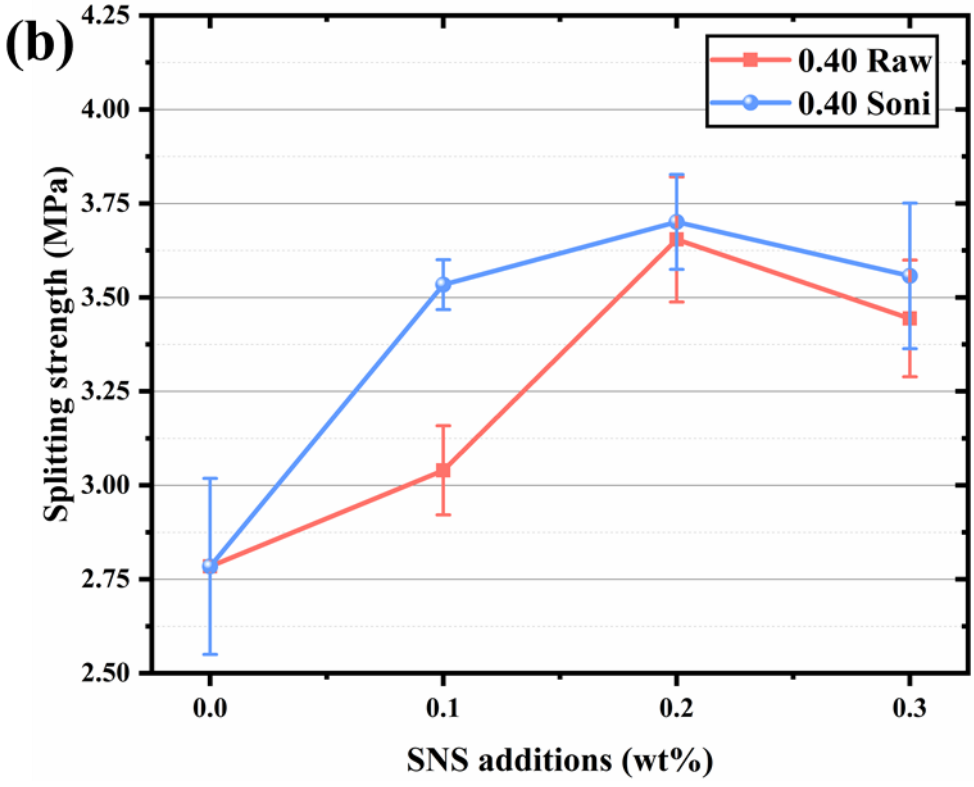

Figure 5.14 Splitting tensile strength of SNS cement pastes at 28 days (a) w/c=0.35 (b) w/c=0.40

5.3.4 Influence of SNS on the cementitious composites fracture energy and fracture toughness

Figure 5.15 shows the prism load-deflection(δ) curves of SNS reinforced cementitious composites under AR, AS, BR and BS conditions for 28 days. As shown in the figure, the ordinary cement has the lowest stiffness and loading capacity, it does not exhibit any post-failure characteristic. The results were anticipated considering that the ordinary cementitious composites are brittle materials. However, the sudden drop of the load-deflection curves at their post crack performance (an abrupt drop of the load after the peak) is detrimental to the building material's performance. Compared to the control group, the specimen's elastic stiffness of the cementitious composite steadily improved with the increase in the addition of the SNS-wt%. At 0.2-wt% SNS additions, the cementitious composite stiffness increased up to 48%. However, when the amount of SNS additions rose to 0.3-wt%, the maximum peak value and the increasing stiffness trend slightly decreased.

Figure 5.15(a-b) shows that at the water-cement ratio of 0.35, the fracture deflection of different SNS added specimens is kept at 0.11 mm. The fracture strength and deflection increases with the increase of SNS addition, but in the ultrasonically treated SNS sample in particular, shows more efficient increase. Figure 5.15(c-d) shows that the samples with the w/c ratio of 0.40 expresses a similar trend as shown in Figure 5.15(a-b) and the fracture deflection is around 0.13 mm. However, as the amount of the added SNS increases, the deflection of the samples increases. The SNS addition enabled the cementitious prisms deflection to increase up to 23.7%, which significantly improves the cementitious failure strength reduction curve and showed better post-cracking performance.

The SNS worked as a fibre supply to hook the stresses transfer properties, the fibres enhanced the cementitious matrix's post-cracking behaviour (Feng et al., 2014). The efficiency of the cracked fibres in transmitting the applied stresses depends on the interfacial bonding properties between the SNS and the matrix. Although the improvement brought by the SNS fibres of the cementitious composites does not enhance the post-cracking performance as significant as the steel fibres, the improved load-deflection curve area of the SNS cementitious composites indicates the improvement in the ductility, fracture energy and fracture toughness properties.

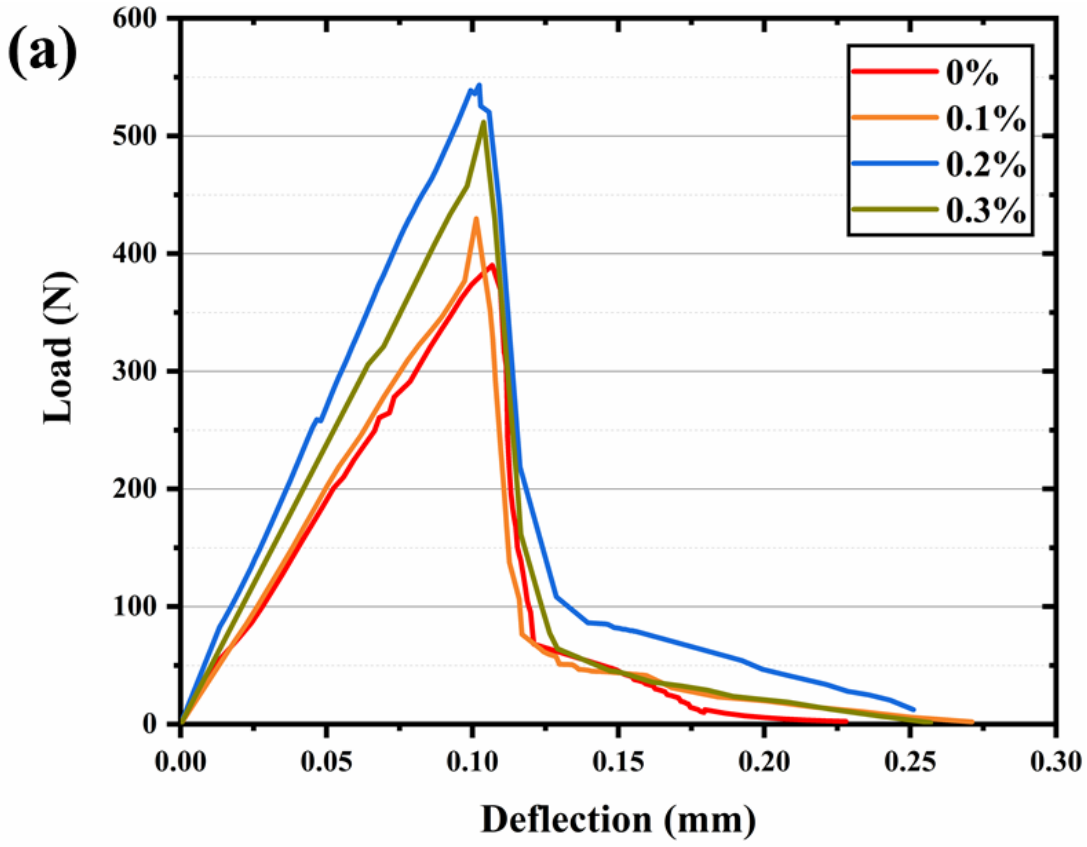

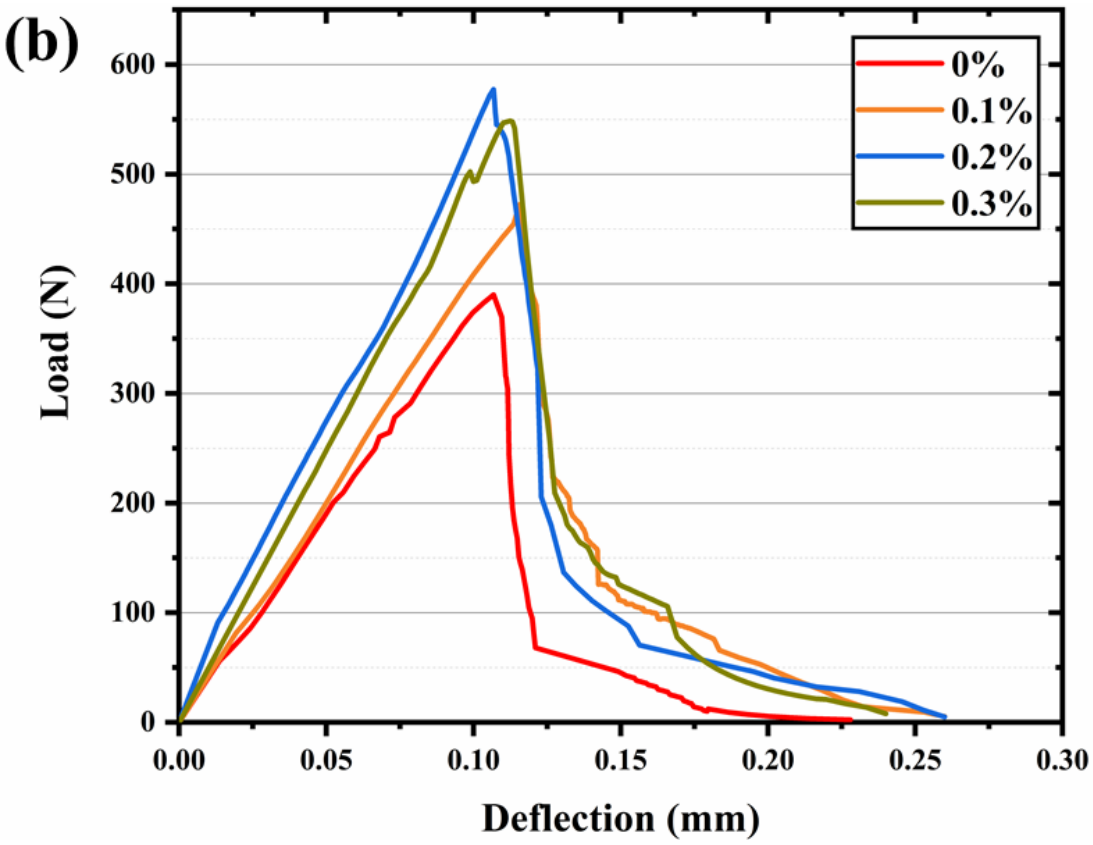
(b)
Load (N)
Deflection (mm)
0%
0.1%
0.2%
0.3%
0
100
200
300
400
500
600
0.00
0.05
0.10
0.15
0.20
0.25
0.30

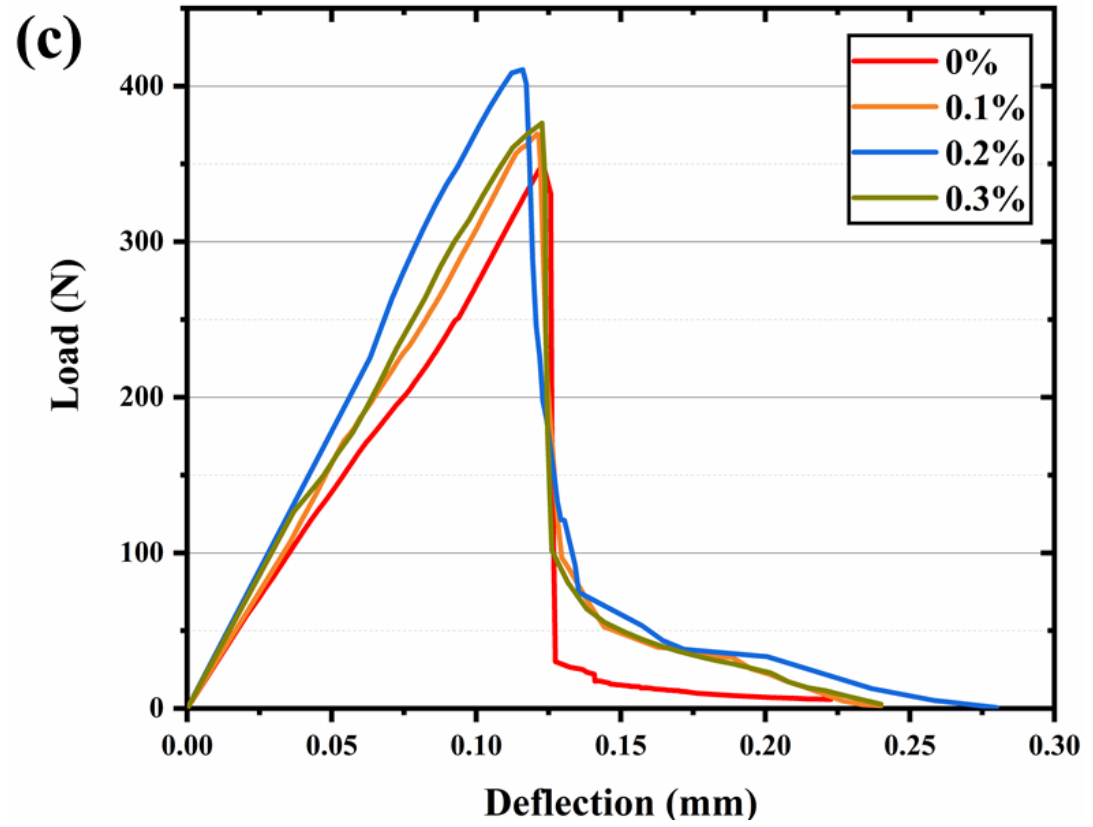
(c)
Load (N)
Deflection (mm)
0%
0.1%
0.2%
0.3%
0
100
200
300
400
0.00
0.05
0.10
0.15
0.20
0.25
0.30

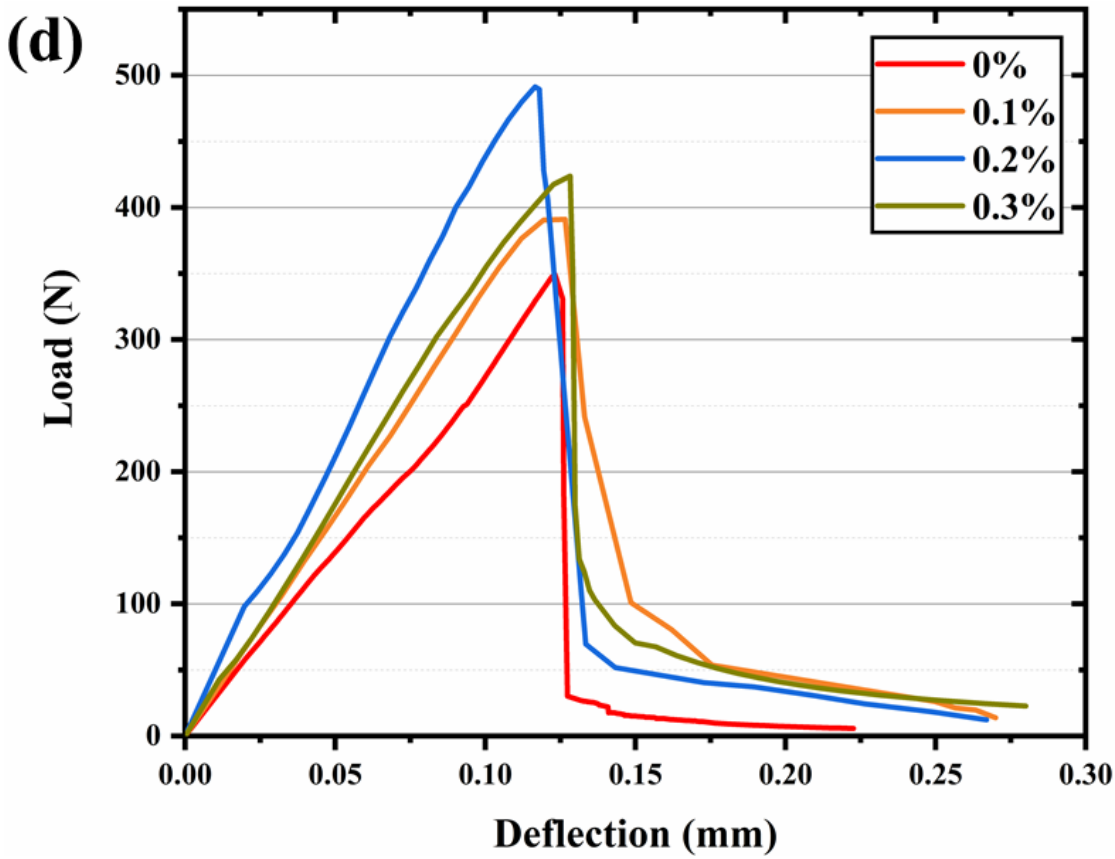

Figure 5.15 P-δ of SNS-cementitious composites three-point bending (a) 0.35 raw (b) 0.35 soni (c) 0.40 raw (d) 0.40 soni

Figure 5.16 shows the fracture energy of SNS-cementitious composites at 28 days. As expected, the results indicate that SNS additions significantly improve the fracture energy performance of the cementitious composites at different water-cement ratios. Figure 5.16(a) shows that the cementitious composites AR2 was the optimal group amount of fracture energy at 46.09 N/m, which is 55.61% higher than the control group. At the raw SNS concentration of 0.1-wt% and 0.3-wt%, the fracture energy was increased by 4.66% and 27.11%, respectively. Furthermore, at the same additional amount, soni SNS were significantly higher than raw SNSs. The fracture energy of the AS01 group was 43.09% higher than the control group. The soni SNS with 0.2-wt% addition showed a considerable improvement of 69.01%. Afterwards, the increased

value slightly decreased to 48.14 N/m (improve of 65.19%) when 0.3-wt% SNS was added.

Figure 5.16(b) shows the fracture energy of SNS cement pastes when the w/c ratio is 0.40. Under the optimum conditions, the fracture properties of BR02 and BS02 are increased by 38.69% and 65.49%, similar to Figure 5.16(a) (w/c=0.35) strengthening trend. When comparing AR group to BR group, AS and BS modified the post-failure feature of cementitious composites. The soni SNS matrix load-deflection curves show a slower strength reduction trend under the different SNS additions, especially when SNS reaches 0.3-wt%. With the propagation of cracks, the residual stress of the matrix resistance gradually decreased. The evenly dispersed high concentration of SNS withstood more cross-sectional stress until the SNS was pulled out.

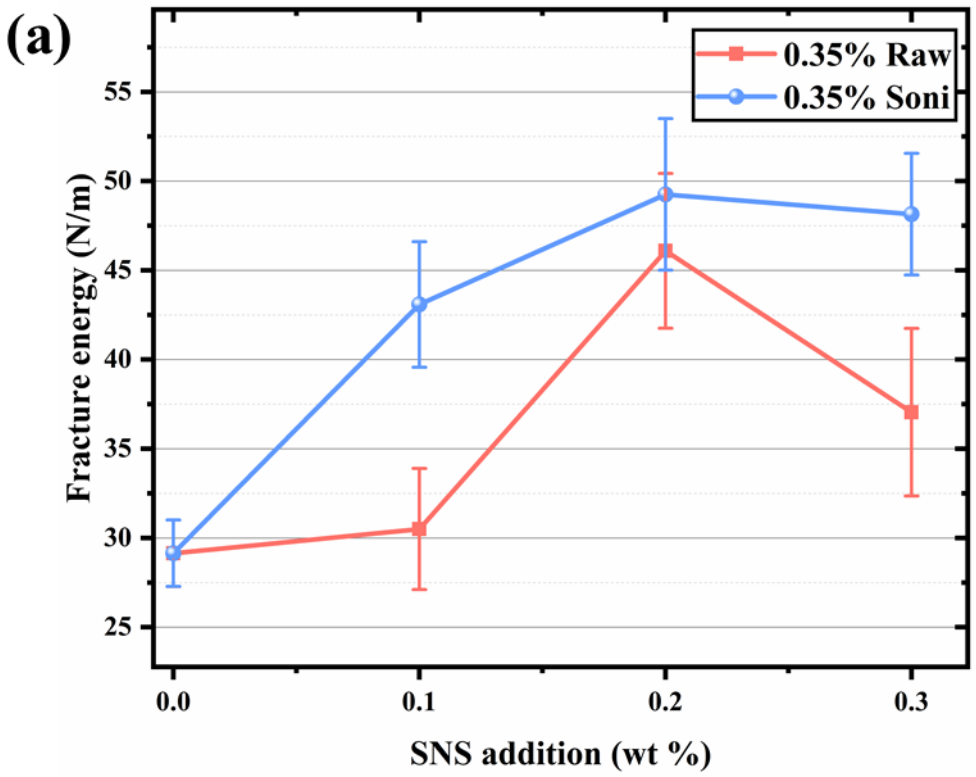

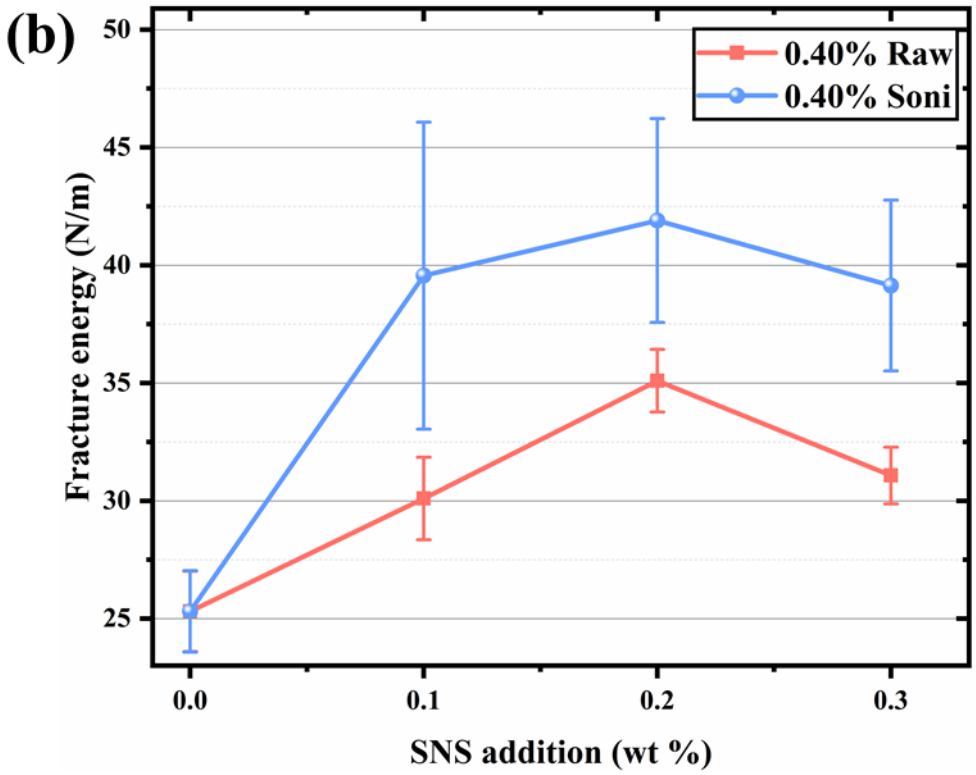

Figure 5.16 Fracture energy of SNS-cementitious composites at different dosages (a) 0.35 w/c ratio (b) 0.40 w/c ratio

Figure 5.17 demonstrates the fracture toughness of SNS-cement pastes at 28 days, with the plain cementitious matrix (w/c ratio of 0.35 and 0.40) showing the lowest fracture toughness. The SNS, under all circumstances of the AR, AS, BR and BS conditions, show fracture toughness to follow a similar trend to fracture energy, the SNS additive effectively improving the cementitious composites fracture toughness. Figure 5.17(a) show the experiment results show that the optimal addition amount of AR02 fracture toughness was 0.40 MPa*$m^{1/2}$, 40.28% higher than the control group. The addition of 0.1-wt% and 0.3-wt% represents an improvement of 5.90% and 27.82%, respectively. Furthermore, under the conditions of 0.1-wt%, 0.2-wt%, and 0.3-wt%, the ultrasonically treated SNS increased the fracture toughness of cement pastes by 19.36%, 49.06%, and 41.66%, respectively.

Figure 5.17(b) shows the relationship between the fracture toughness of cement pastes (w/c ratio=0.40) and the SNS addition. The addition of 0.1, 0.2 and 0.3-wt% raw SNS increased by 5.56%, 17.41% and 7.59% respectively. However, compared with the raw SNS, the results of the ultrasonically treated SNS were almost twice the enhancement percentage of the raw SNS. In particular, the increments of 0.1%, 0.2% and 0.3% increased by 11.84%, 40.50% and 21.18%, respectively.

These results reveal that the ultrasonically treated SNS had distributed more effectively into the cement pastes, significantly affecting fracture energy and toughness. The sharp increase in fracture energy and fracture toughness can be attributed to the SNS crack bridging effect with the cement particle. When the developing crack approaches, the SNS generate perpendicular tensile stress to impede the development of cracks, the matrix withstands more energy before rupturing.

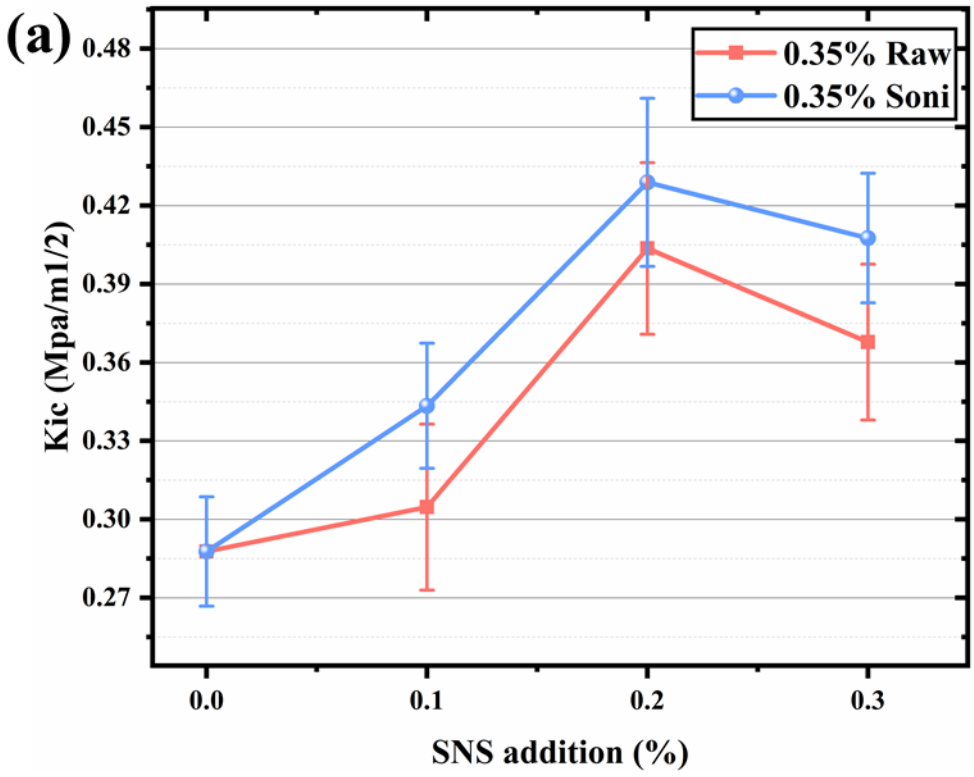

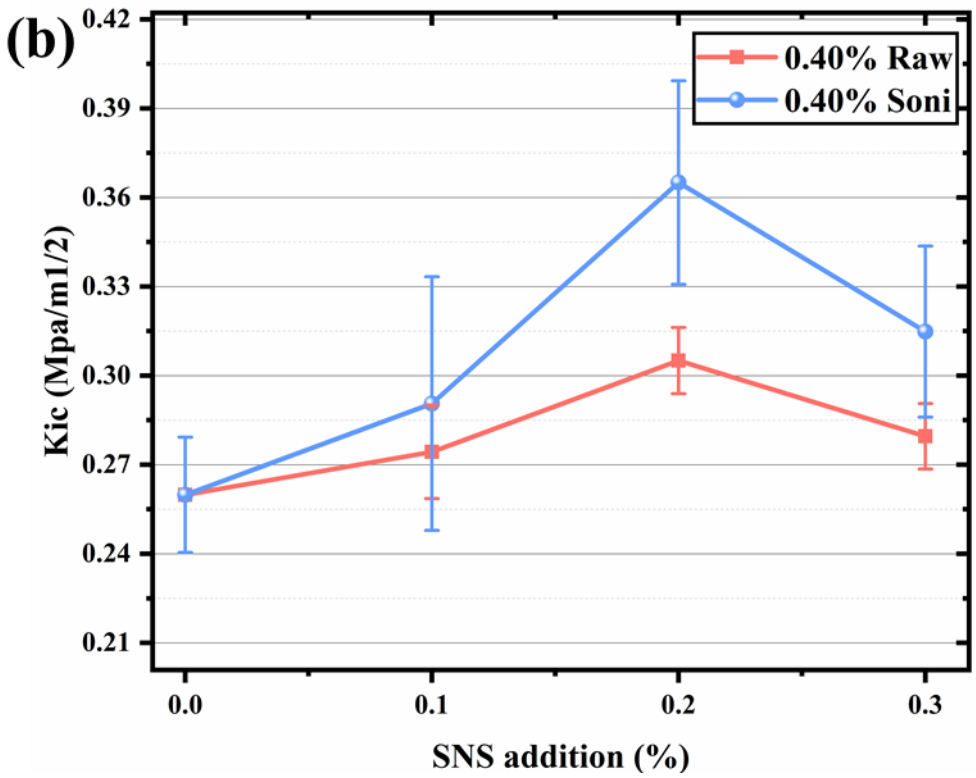

Figure 5.17 Fracture toughness of SNS-cementitious composites (a) 0.35 w/c ratio (b) 0.40 w/c ratio

Figure 5.18 is the Load-CMOD curve of the SNS-cementitious composite prismatic notched beam at 28 days. Figure 5.18 shows that P-CMOD has three stages of non-linear features. The first stage is the linear elastic phase before the crack occurs. The initial portion of the stress-CMOD curve is almost linear until it is close to the maximum load, where the line starts to change. The second stage is non-linear, where the load at the specimen is subjected to the maximum tensile initial cracking load. The stable crack propagation happened after the first crack and before failure, the tension at the tip of the notch reaches the peak of the curve as the load gradually increases. The third stage is the instability of the specimen crack propagation, the specimen tensile strain gradually decreases and turns to compression stress.

The P-CMOD result shows that under AR, AS, BR and BS conditions, the failure load of SNS-cementitious composites was higher than the control group. As the concentration of SNS increases, the cement pastes show slower loads decrease, the peak strength after crack propagation is significantly improved, and the CMOD distance becomes longer. This phenomenon occurs because SNS bond the cement particle and increase the internal integrity of the cement matrix. The SNS binder slows down the crack propagation, absorbs more energy before the first visible crack, and extends the CMOD after the crack.

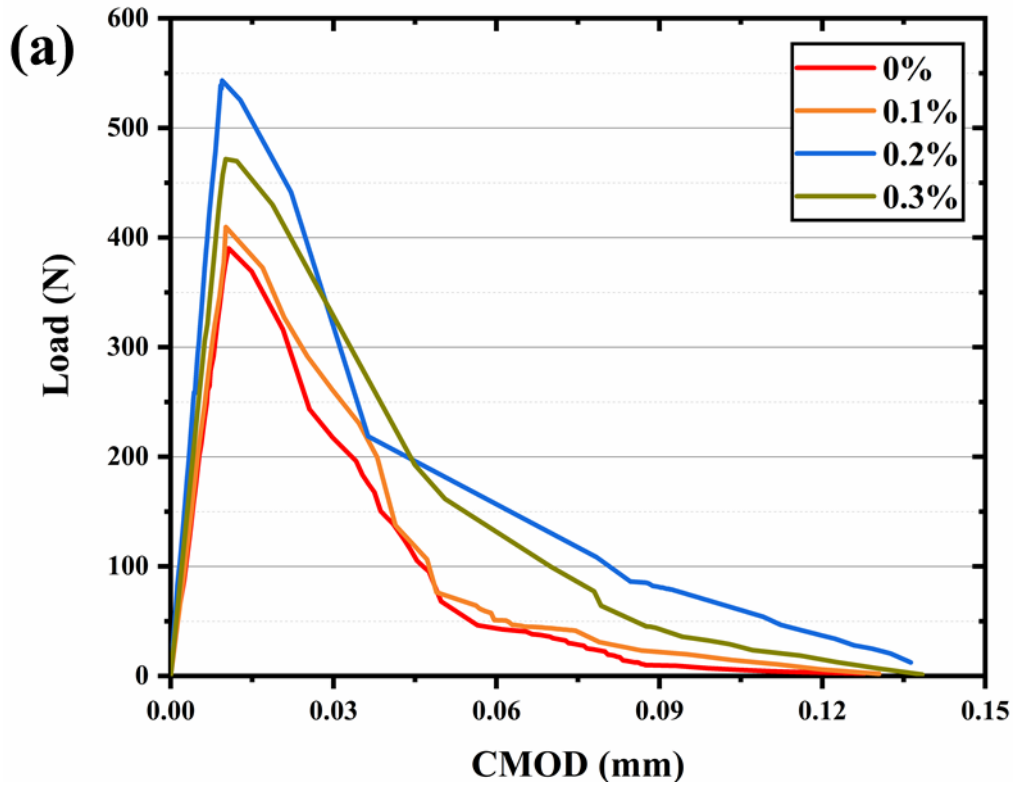

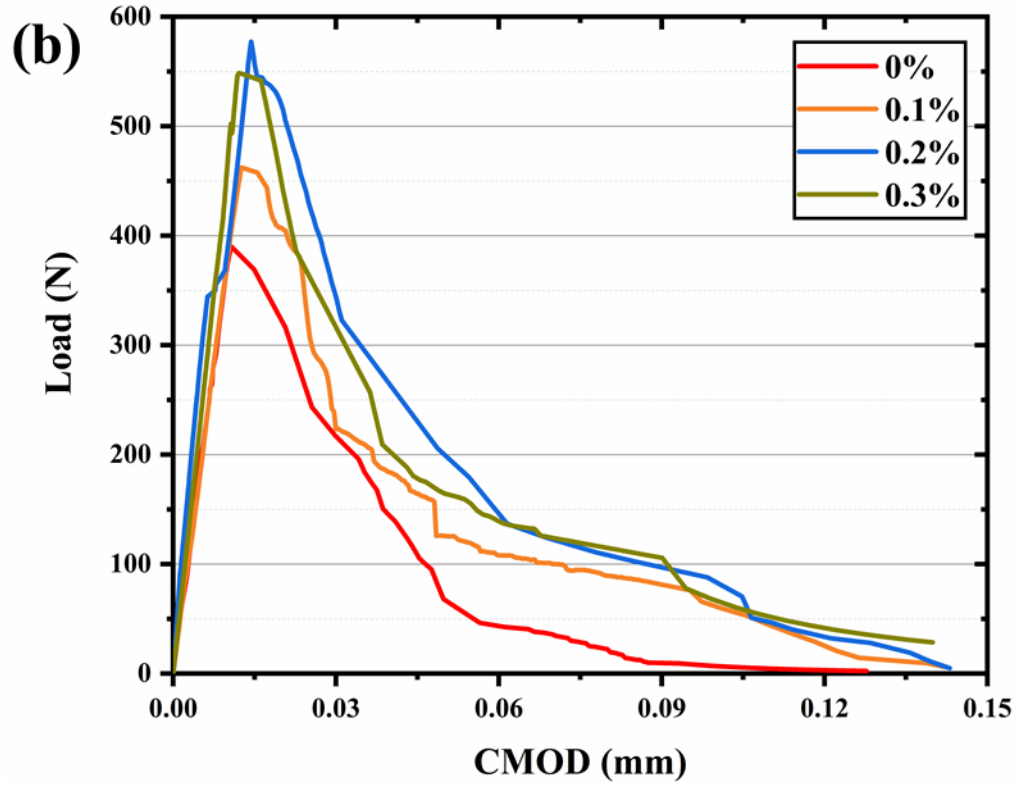
(b)
600
500
400
300
200
100
0
Load (N)
0.00
0.03
0.06
0.09
0.12
0.15
CMOD (mm)
0%
0.1%
0.2%
0.3%

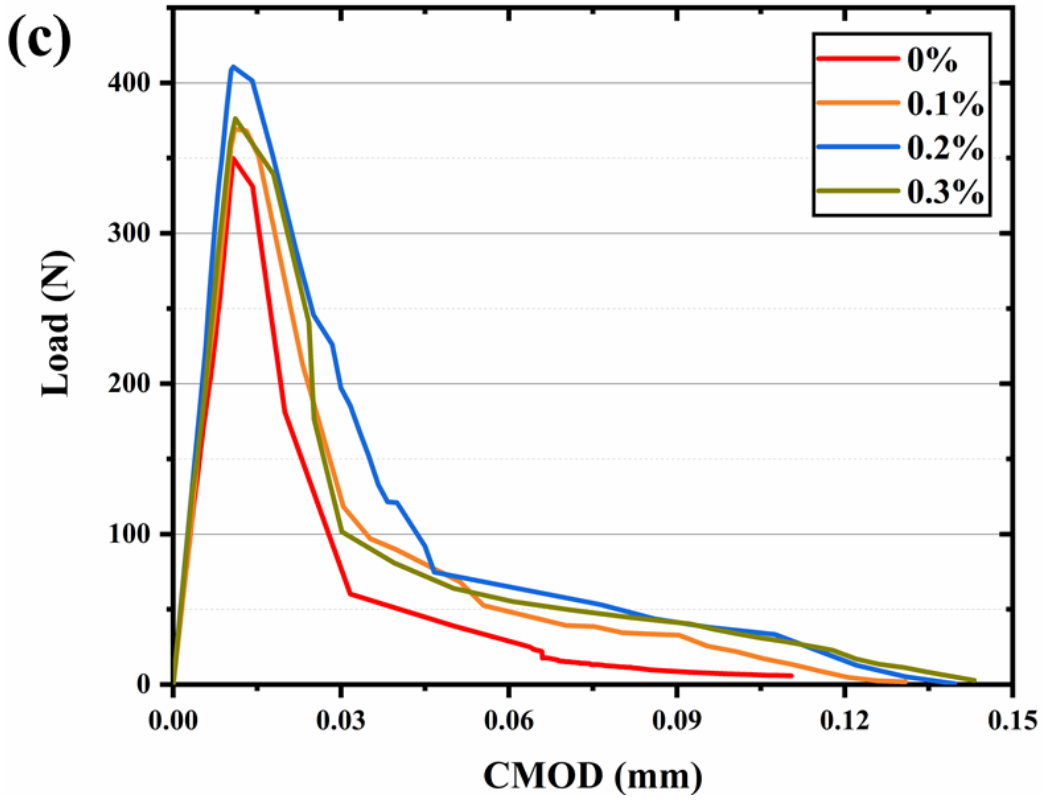
(c)
400
300
200
100
0
Load (N)
0.00
0.03
0.06
0.09
0.12
0.15
CMOD (mm)
0%
0.1%
0.2%
0.3%

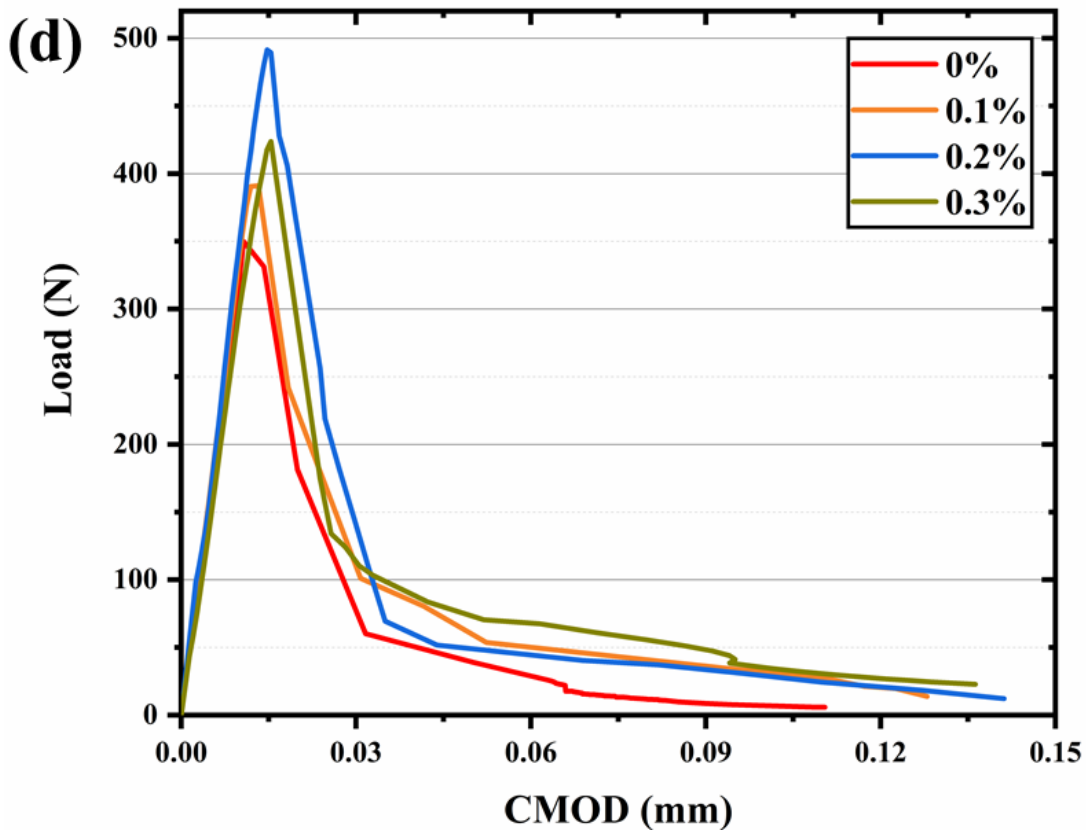

Figure 5.18 SNS-cementitious composites load-CMOD curves (a) raw SNS (w/c=0.35), (b) soni SNS(w/c=0.35) (c) raw SNS(w/c=0.40), (d) soni SNS(w/c=0.40)

5.4 Conclusion

This chapter discusses how the SNS effectively improves the mechanical strength of cementitious composites. A series of mechanical tests were undertaken in fourteen differently designed conditions, including compressive strength, flexural strength, fracture properties and splitting strength. According to the experiments results and discussions above, the following conclusions can be drawn.

(1) As the SNS concentration increases, the mechanical properties of cementitious composites are reinforced. The mechanical result corresponds with the workability result shown in Chapter 4 in that the addition amount of 0.2-wt% SNS reaches the optimum value. The workability is accompanied by mechanical strength, both of them

showing a significant decrease in the SNS addition above 0.2-wt%. The optimal 0.2-wt% of raw and soni SNS in the cementitious matrix at 28 days shows the compressive strength increased by 8.33 to 12.15%, the flexural strength increased by 28.73 to 39.91%, the fracture energy increased by 38.69 to 69.01%, the fracture toughness increased by 17.41 to 41.66% and the splitting strength increased by 31.25 to 36.87%. Compared to the traditional steel and plastic fibre mechanical reinforcement cementitious mixtures, by incorporating SNS significantly changes mechanical properties, which can be attributed to the nanofiber filling and crack bridging functions in the cement matrix, enhancing the strength of the internal and interfacial transition zone and inhibiting the appearance and development of the cracks. The results indicate that SNS additions dominate the bridging effect of the matrix crack. Compared to the reinforcement in compressive stress, SNS is more effective in improving the flexural performance and fracture properties of cementitious composites. The reinforced strength of the cement pastes benefits the production of concrete structures in construction, which can eventually lead to the reduction of cement consumption.

(2) Ultrasonic treatment is beneficial to the dispersion of SNS in cementitious composites, which can indirectly improve the mechanical properties of the matrix. The experiment results confirm that under the same SNS addition, the soni SNS can improve the raw SNS-cementitious composites mechanical strength on average by 10%. When the concentration of SNS exceeds the critical concentration (0.2-wt%), the SNS easily accumulate on the cement matrix. The agglomeration of SNS can be reduced by ultrasonic treatment to promote dispersal and distribution in the matrix.

(3) The water-cement ratio greatly influences the mechanical properties of the SNS cement matrix. With the increase of water/cement ratio, the compression, splitting, flexural and fracture properties of the SNS cement matrix decrease. However, the

variation of the water/cement ratio does not affect the SNS optimal amount and reinforcing effect of SNS. The increase of the water-cement ratio is favourable to the synergistic effect of SNS in that more water molecules promote cement hydration. The high hydrophilicity and high specific surface area of SNS require sufficient water to mix and promote hydration reactions. Insufficient water can easily cause the agglomeration of SNS, affecting the early hydration enhancement on cementitious composite. When the concentration of SNS is relaive high, or the water content is relative low in cementitious composites, the high van der Waals repulsion can lead to a piling up of agglomeration on the SNS sheet. The increase in water-cement ratio brings more water molecules into the cementitious composite, while the agglomeration decrease reduces the defects and avoids the deterioration in mechanical properties.

Chapter 6 Analytical characterisation of the microstructure of SNS reinforced cementitious composites

6.1 Introduction

This chapter focuses on studying the effect of SNSs on the microstructure of the cementitious composites. In addition, the relationship between the microstructure and the overall properties is also discussed. Methods and tools such as SEM, EDS, XRD, BET and TEM were employed to understand the hydration mechanism of the cement pastes, determine the morphology of their microstructure and quantify the growth of their hydration phases. Centrifugation tests were also conducted to investigate the interaction of SNSs with the cement particles in the cement paste.

6.2 Experiment methods

6.2.1 Centrifugation test

It is hypothesised that the improved hydration of the cementitious composites incorporating SNS is attributed to the synergetic interaction between the cement particles and the SNS sheets. The requirement for this synergetic interaction is the adsorption of the SNS sheets on the surface of the cement particles in the fresh cement paste. The amount of SNS (raw and soni) adsorbed on the cement particles (a-SNS) influence this synergetic interaction and its effect on the hydration. Therefore, the following centrifugation test was carried out (Cao, Tian, *et al.*, 2016) to determine the concentration of the a-SNS using an MSE Mistral 2000 centrifuge.

A sample of 200 g cement pastes containing SNS at the concentrations of 0, 0.05, 0.1, 0.2, 0.3 and 0.5-wt% were centrifuged for 10 minutes after mixing. The pastes were placed in the centrifugal bottles and centrifuged at 3000 rpm for 20 minutes. Subsequently, the centrifuged supernatants were collected and filtered through Cole-Parmer Sterile Cell strainers (40 μm) to remove the cement particles. The filtrates were then oven dried at 45°C for 48 hours for water evaporation. The dried filtrates from the plain cement pastes contain supernatant salt and alkali in their pore solution (Rajabipour, Sant and Weiss, 2008). The dried filtrates from the cement pastes with SNS contain free SNS (f-SNS), cement pastes supernatant salt and alkali in the pore solution. The amount of f-SNS was obtained by subtracting the weight of the dried filtrates of the plain pastes from the weight of the dried filtrate of pastes with SNS. The amount of a-SNS was obtained by subtracting the weight of f-SNS from the weight of SNS added to the pastes as outlined in (Cao, Tian, *et al.*, 2016).

6.2.2 SEM and EDS

SEM and EDS were employed to characterise the microstructure and element distribution of the SNS-cementitious composites. The experiment was performed in the JEOL JSM-7800F fitted with a X-Max50Silicon Drift Detector (SDD) in an area of 50 mm^2. After the specimen was coated with a gold sputter through the Q150R Plus (Figure 6.1), the SEM micro images and EDS energy spectrum of the fractured surface of the cement samples (prepared at the 7, 14 and 28 days) were produced at a voltage of 2-15 kV at room temperature (Figure 6.2).

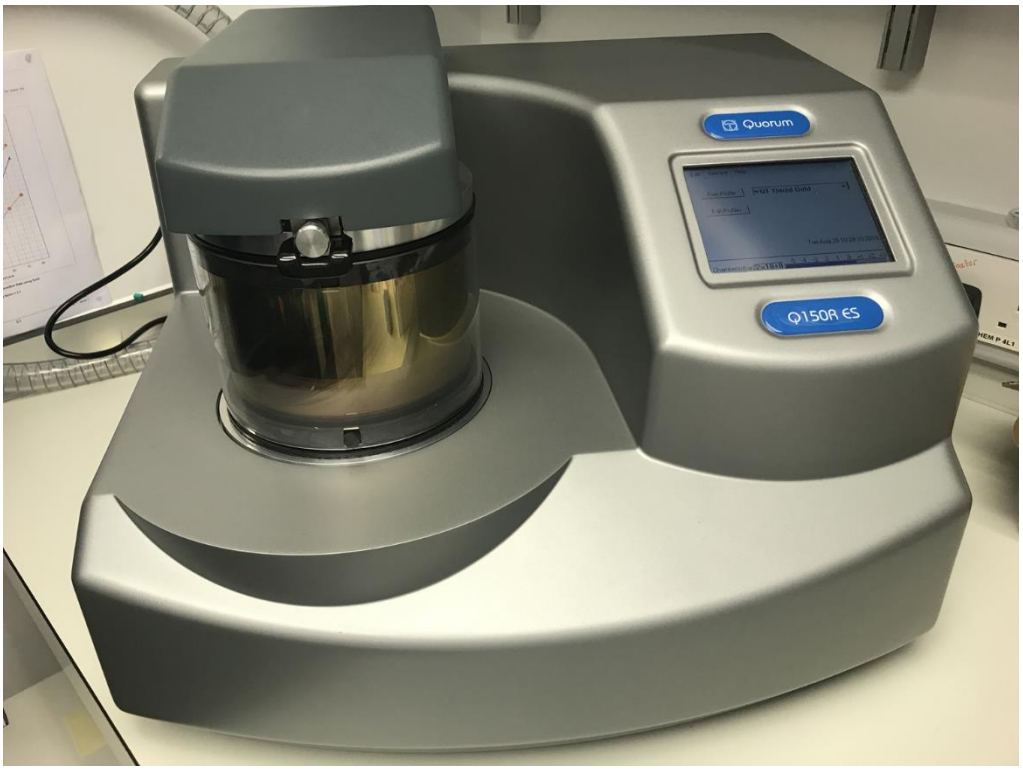

Figure 6.1 Gold rotary pumped coater

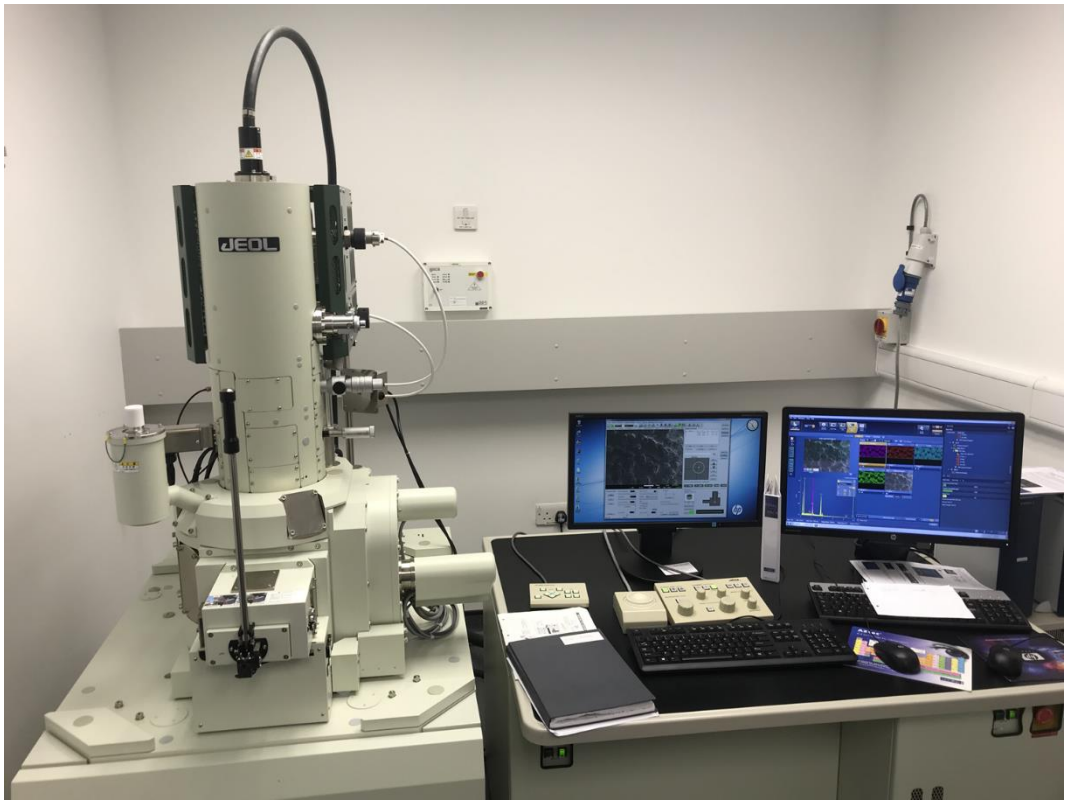

Figure 6.2 Scanning electron microscope (JEOL JSM-7800F)

6.2.3 SNS-cementitious composites X-ray diffraction (XRD)

Cement pastes were ground into powder by a ball mail grinder machine (PM 100 Planetary ball mill) at 7, 14 and 28 days. XRD analysis was performed on a single-crystal X-ray diffractometer (Agilent SuperNova). The XRD patterns scanning ranged from 5° to 65° (2θ) with Cu Kα radiation (λ = 1.5418Å) and at the scanning rate of 2°/minutes. The operating voltage is 40kV, the filament current is 40mA and the step size is 0.02° at ambient conditions.

6.2.4 SNS-cementitious composites Nitrogen adsorption-desorption isotherms

The specific surface area, pore size and the pore volume of the SNS and the cementitious composite samples were determined by the nitrogen adsorption and desorption isotherm, according to BS ISO 9277:2010 (Bs Iso 9277, 2010) using the MICROACTIVE 3FLEX 3500 (Micromeritics, Germany) instrument at 77.35 K. Prior to the testing, the SNS-cementitious composites powder samples were sieved (less than 1 mm), dehydrated in the vacuum and dried at 100℃ for 180 minutes under the pressure of 10^{-6} Pa. During the experiment, a dead volume was used to ensure the measurement accuracy of each pressure step.

The specific surface area of SNS is assessed by the Brunauer, Emmett and Teller (BET) theory (Brunauer, P. H. Emmett and Teller, 1938) method, with the relative pressure range of the adsorption isotherm ranging from 0.05 to 0.35. The total pore volume and pore size distribution were measured following the theory of monolayer adsorption and capillary condensation (Barrett, Joyner and Halenda (BJH)) (Barrett, Joyner and Halenda, 1951), where the relative pressure range of adsorption and desorption

isotherms is 0.99-0.38. The data processing was assisted by the instrument's advanced interactive MicroActive 2.0 software.

6.2.5 Transmission electron microscopy

The TEM images of SNS-cementitious composites were acquired using the JEM-1010 instrument. The process of obtaining TEM images of the SNS-cementitious composites is as follows. First, the cementitious composites were ground into powder (ball mill machine, PM100) at day 28, and the powder was mixed with the acetone solution to prevent further hydration. Subsequently, the SNS-cementitious composite solution was dropped onto the carbon-coated copper mesh and dried naturally. Finally, the experiment was carried out at an acceleration voltage of 80 kV.

6.3 Results and Discussion

6.3.1 Concentration of the adsorbed and free SNS in the cement pastes

The SNS in the cement paste is classified into two categories: a) the adsorbed SNS (a-SNS) and b) free SNS (f-SNS). The centrifugation experiment results were used to determine the amount of a-SNS that adhered to the surface of the cement particles. Figure 6.3 shows that the change of the mass of a-SNS per gram in the cement can be considered as a function of the SNS concentration. In fact, the mass of a-SNS is directly proportional to the concentration of SNS. The SNSs were continually attached to the surface of the cementitious composites by increasing the SNS addition up to 0.5-wt%. The a-SNS adsorbed on the surface of the cement particles, and were wrapped and embedded into the hydration products during the hydration process. The additional hydrophilicity of SNS acts as a transfer channel, connecting the core of the unhydrated cement particles and the water molecules. This approves the SCD mechanism of SNS that accelerates the hydration process.

It is worth noting that the amount of a-SNS of cement slightly decreased after the ultrasonic treatment. This is because the ultrasonic disperses further, reducing the agglomeration of SNS sheets on the surface of the cementitious particles. The a-SNS agglomerates attached to the cement-based surface were partially transformed into f-SNS, which appears in a free state in the suspension.

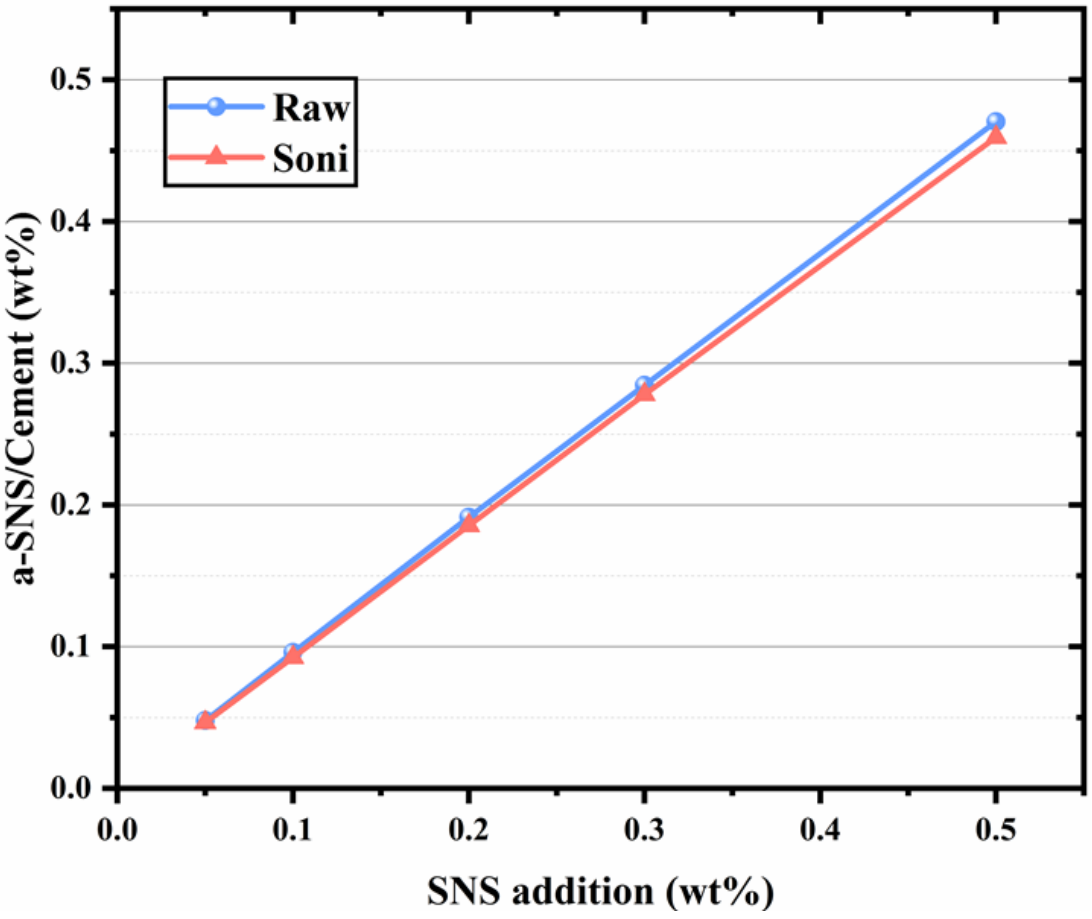

Figure 6.3 The mass of a-SNS per gram of cement

Figure 6.4 shows the change in the percentage of a-SNS (i.e. a-SNS/(a-SNS+f-SNS)) as a function of SNS concentration. The experimental results indicate that the lowest adsorption rate of raw SNS was 94.2%, however in the ultrasonic disperse SNS, it dropped to 91.8%. The f-SNS content slightly increases after the ultrasonic treatment, and also a correlation remains between f-SNS and the amount of added SNSs. The increase in the amount of f-SNS can be attributed to the homogeneous distribution of

the SNS suspension, and the fact that there is no agglomeration or precipitation occurring during the centrifugation process. The f-SNSs that were not bound to cement particles were centrifuged into the supernatant.

The experiment results prove that the SNS have great adsorption capacity to the cement matrix, regardless of being treated by ultrasonication. This phenomenon is because during the hydration progress, hydrophilic SNS surface has hydroxymethyl groups (-CH_2OH) and hydroxyl group (-OH). The functional groups can pull the water molecules towards the SNS and interact with the cement particles. The anionic electrostatic force on the SNS surface effectively attracts the Ca^{2+}, K^+ and Na^+ ions in the cement particles (Voisin *et al.*, 2017; Hisseine, Omran and Tagnit-Hamou, 2018). The C_3S acts as an electron acceptor, the interaction of Ca-O coordination with the hydroxyl group results in the SNS being firmly adsorbed onto the cement particles.

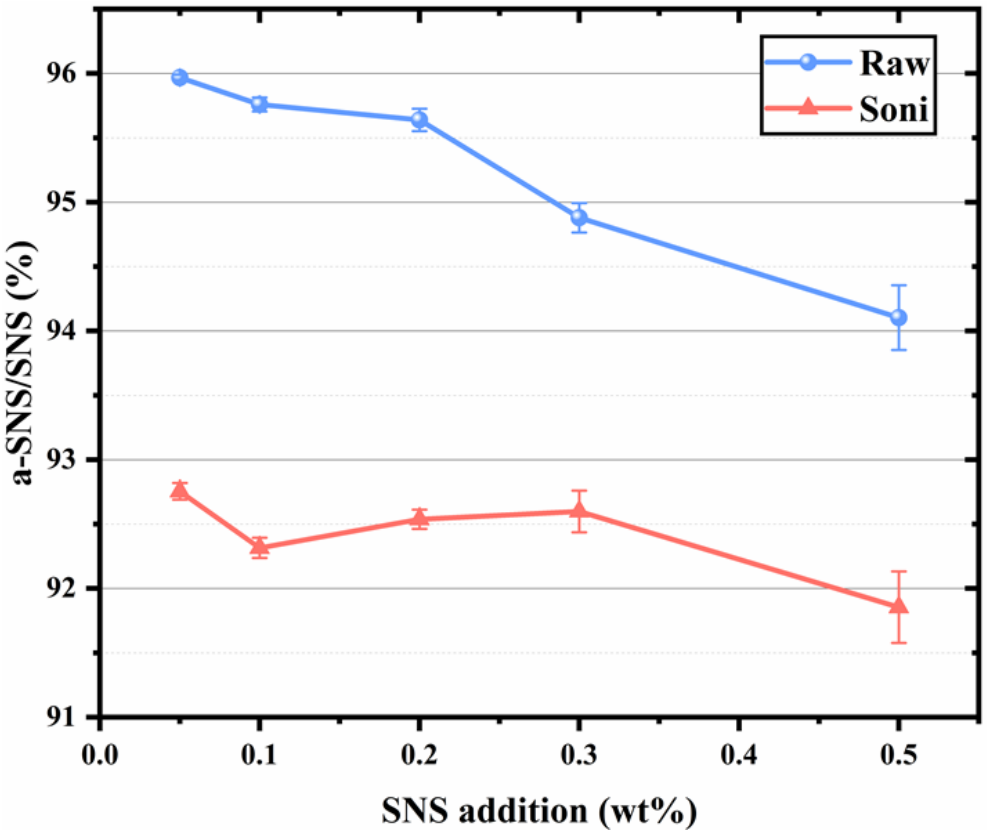

Figure 6.4 The mass of a-SNS percentage out of SNS

According to the Figure 6.3 and Figure 6.4, the effective adsorption capacity of a-SNS on the cement-based particles surface is limited. A large amount of a-SNS on the cementitious surface is more likely to cause agglomeration. Ultrasonic diffused SNS suspension increases the f-SNS content, which indirectly increases the dissolved content of f-SNSs in the cement matrix and the chemical compounds in the cement pastes. Although more work is needed to investigate the interaction of the SNS with the cement particles in the pastes, the hypothesis is valid that SNSs cover most of the cement surface due to their high specific area. As a result, it leads to a superior chemical reaction between the cement and the SNSs, enhancing the hydration kinetics.

6.3.2 SNS-cementitious composites morphology and microstructure (SEM)

6.3.2.1 The microstructure impact of SNS on the cement pastes

Figure 6.5 shows the microstructure of cement pastes with different SNS content at day 7. Figure 6.5(a) shows the microstructure of the ordinary cement pastes including microcracks, partially hydrated cement particles, a small amount of calcium hydroxide (CH) and the irregular particles of calcium-silicate-hydrate (C-S-H). Figure 6.5(a) SEM depicts the cementitious microstructure at a typical and low DOH at the early hydration stage. Figure 6.5(b) shows the cementitious microstructure with 0.1-wt% SNS addition. A small amount of SNS/C-S-H structure is generated at the surface of $Ca(OH)_2$ cubes. The SNSs are intertwined with the C-S-H gel. The SNS/C-S-H structure is added to the surface of the hydration product and therefore fills the cracks.

Figure 6.5(c) shows the SEM of the cementitious pastes at 0.2-wt% SNS additions. Compared with Figure 6.5(b), the hydration product SNS/C-S-H increases with higher SNS addition. Furthermore, in the substrate surface, the needle-like hydration product

of ettringite has significantly increased. Figure 6.5(d) shows the SEM of cementitious pastes material with 0.3-wt% SNS additions. Due to the relatively high amount of SNS, the flocculent a-SNS were not completely intercalated with the hydration products, C-S-H and some SNSs were visible on the surface of the cementitious particles. In this situation, the hardness of the cementitious composites decreases and it becomes unstable. The external matrix unstable led to the microstructure being weak, which is consistent with the experimental mechanical results.

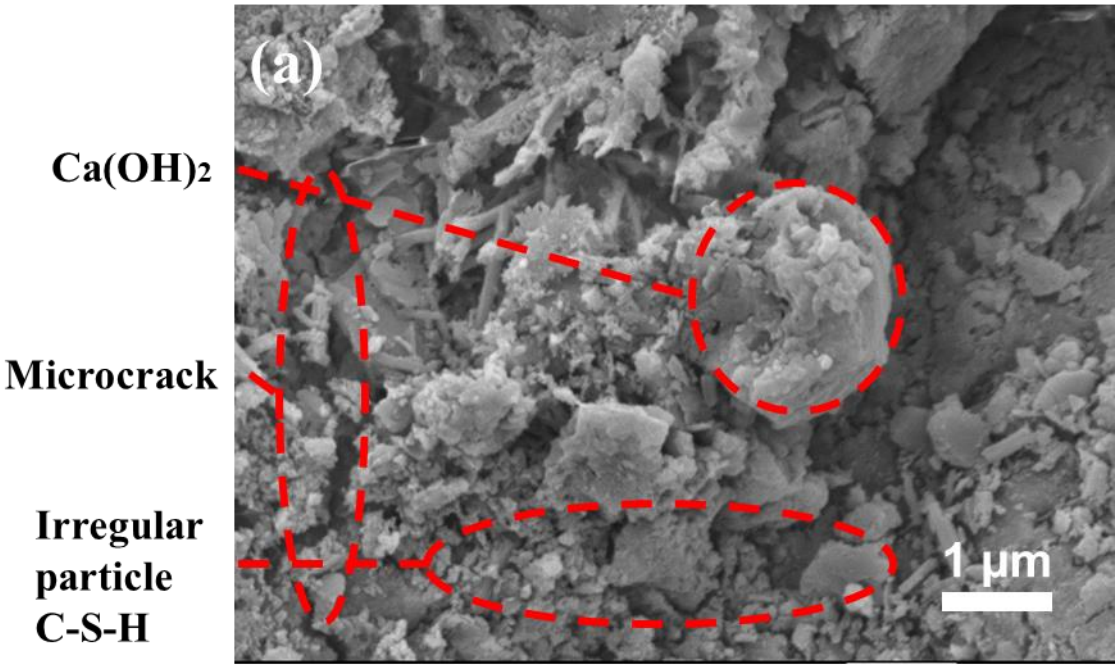

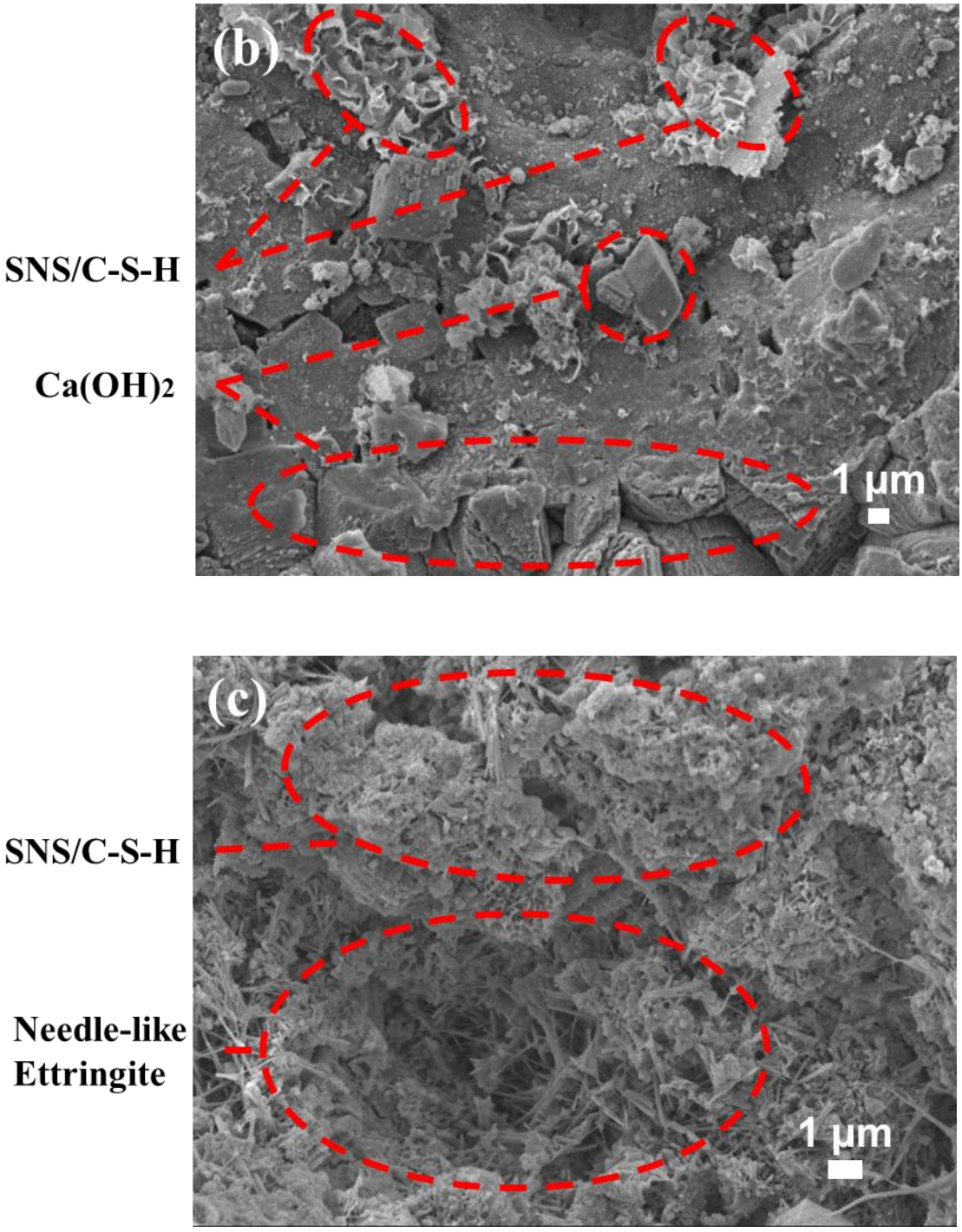
(b)
SNS/C-S-H
Ca(OH)2
1 μm
(c)
SNS/C-S-H
Needle-like
Ettringite
1 μm

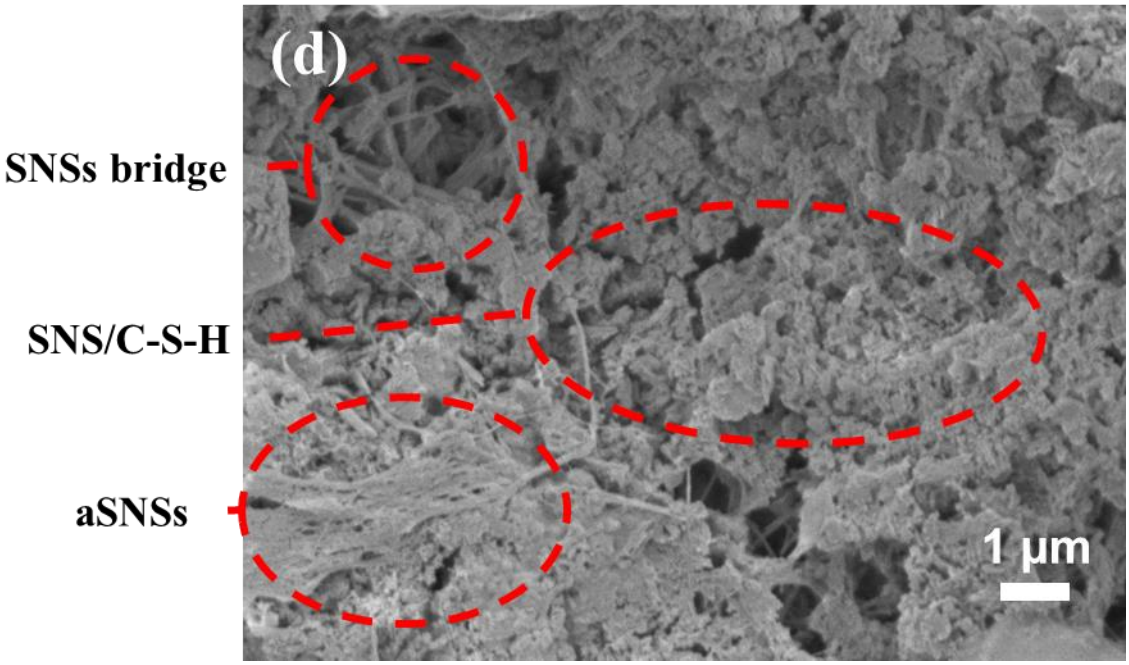

Figure 6.5 7 days SEM images of cement pastes at SNS-wt% of (a) 0, (b) 0.1, (c) 0.2 and (d) 0.3

Figure 6.6 shows the morphology of the different SNS-cementitious composites crystallisation and hydration products at 14 days. Figure 6.6(a) demonstrates the SEM images of the ordinary cement pastes at 14 days, which contains the unhydrated cement particles, a small amount of calcium hydroxide (CH) and different sizes of microcracks. Figure 6.6 (b) shows the SEM images of cementitious composites with the addition of 0.1-wt% SNS. Compared to 7 days, the production of CH cube bulk and C-S-H stacks increased significantly. Compared to the control group, the SNS/C-S-H combination structure is stacked on the matrix surface, which filled the cracks on the hydration product.

As is shown in Figure 6.6 (c), when the SNS concentration reaches 0.2-wt% SNS, the surface of the cementitious matrix becomes denser. The SNS/C-S-H layer is generated onto the hydrate matrix surface, effectively filling and covering the visible cracks and the large-sized pores of the hydration products. Therefore, some hydrate products, such

as ettringite, are hidden under the thick CH products making them difficult to distinguish. Figure 6.6 (d) shows that at 28 days, 0.3-wt% SNS addition causes the SNS to become embedded in the stacked fabric-like C-S-H gel, which appear more compact surface. The SNS sheet interacts with cement particles and, under the influence of its -OH and -OH-CH_2 functional groups, tightly attaches to C3S and C2S. The fibre sheets overlap with the hydration products, forming a more stable microstructure. The large specific surface area of the SNS/C-S-H structure provides a series of growth reaction sites for the hydration process.

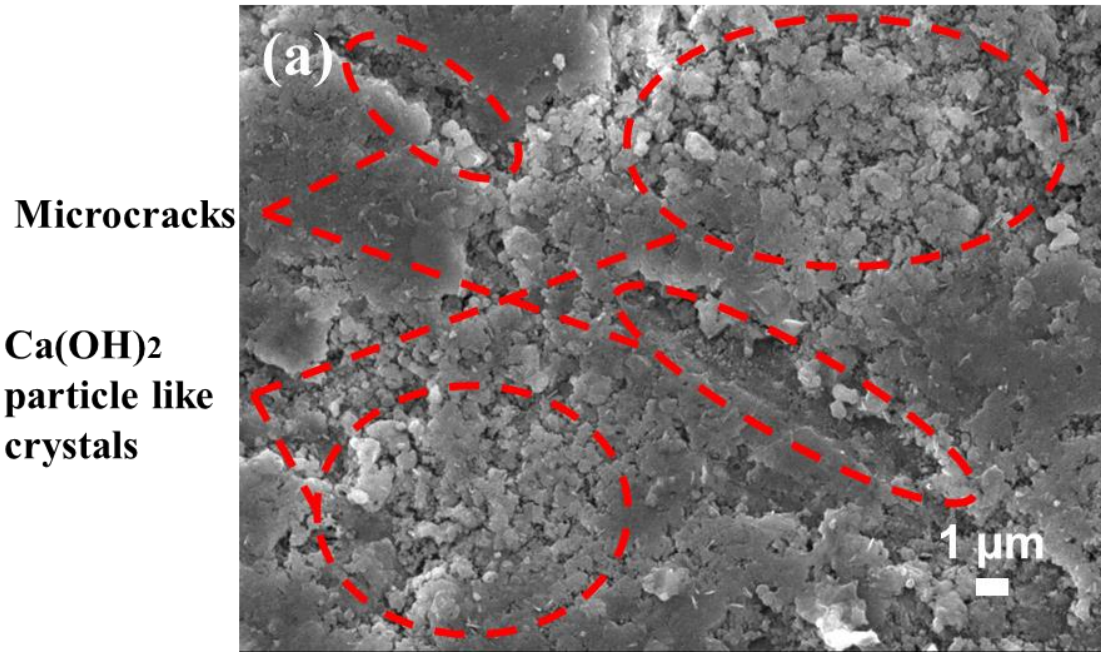

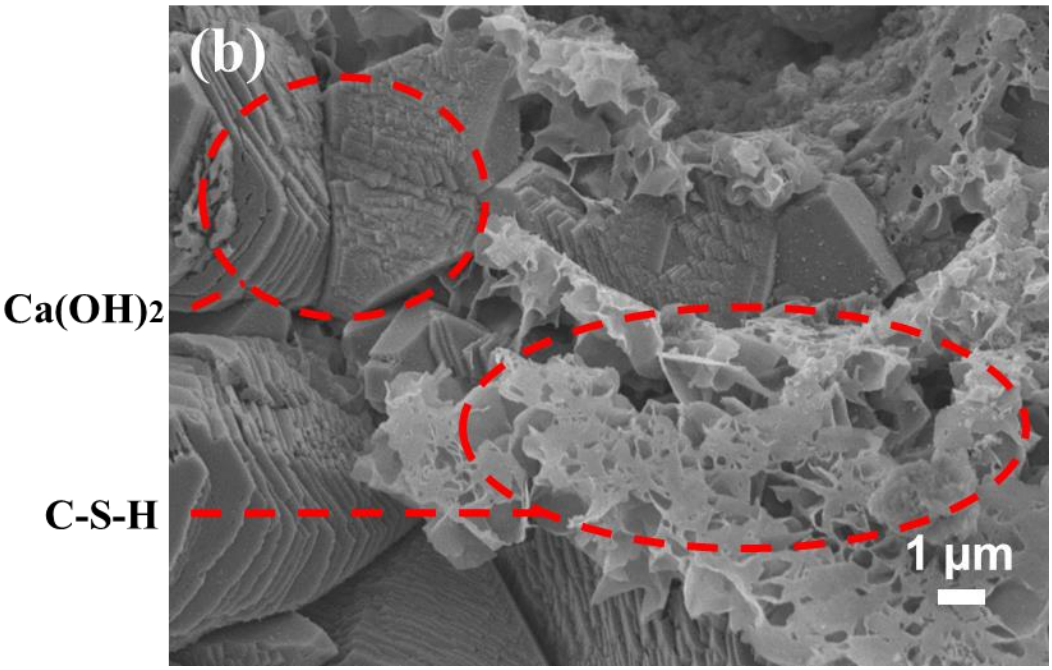
(b)
Ca(OH)2
C-S-H
1 μm

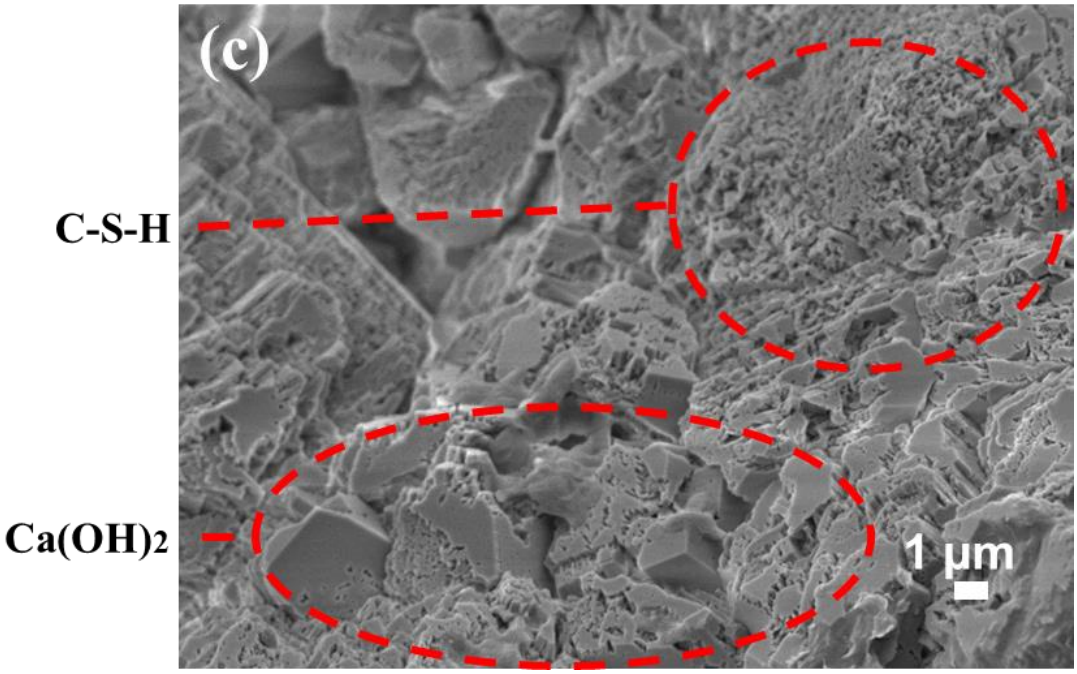
(c)
C-S-H
Ca(OH)2
1 μm

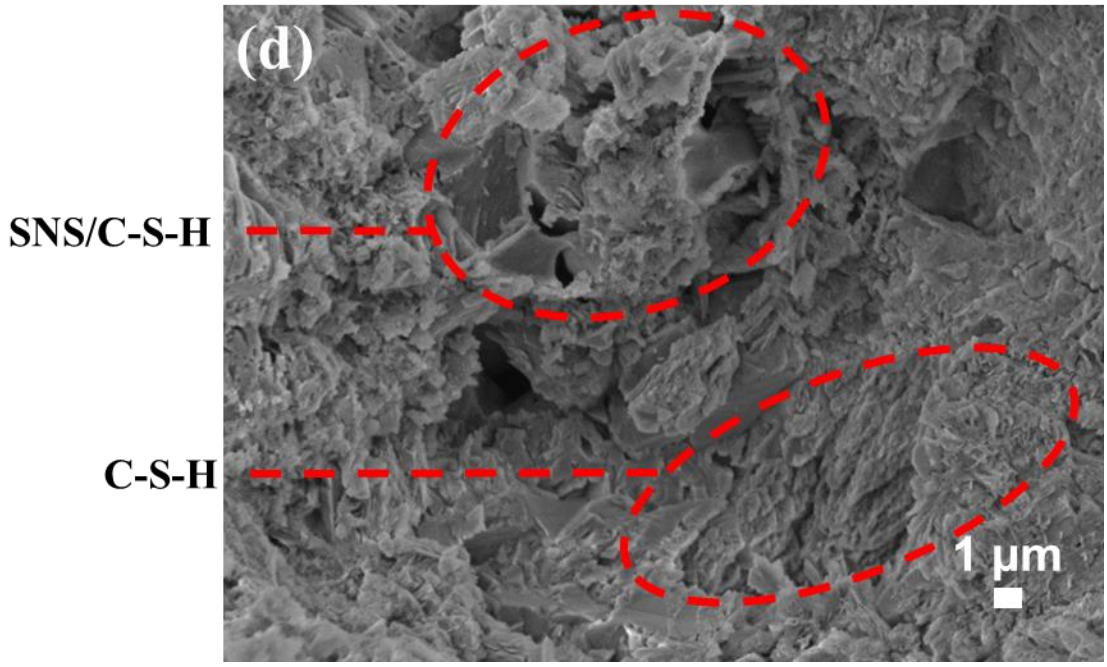

Figure 6.6 14 days SEM images of cement pastes at SNS-wt% of (a) 0, (b) 0.1, (c) 0.2 and (d) 0.3

Figure 6.7 shows at the 28 days microstructure morphology SEM of 0.0, 0.1, 0.2 and 0.3-wt% SNS cement pastes. Figure 6.7(a) shows the hydration product of the ordinary cementitious composites. The hydration is relatively complete, the irregular hexagonal granular $Ca(OH)_2$ products are generated and attached to the surface of C-S-H gel. Figure 6.7(b) shows the SNSs accumulation layer on the surface of the cement composite, at 0.1-wt% of SNS addition. The SNS hydration product formed a large quantity of $Ca(OH)_2$ cubes. The SNSs exist in the core of the hydration product, completely encapsulated whilst the $Ca(OH)_2$ cubes were growing on the SNS surface.

Figure 6.7(c) shows that the cementitious composites with 0.2-wt% SNS have promoted the CH hexagonal crystal formation. Compared to Figure 6.6(c), during the hydration different sized hexagonal SNS/CH crystal layers have generated on the surface of C-S-H gels. The uniformly distributed hexagonal SNS/CH crystals have positive implications for enhancing the cementitious composites' mechanical

performance. Figure 6.7(d) shows the dense C-S-H/SNS gel layer on the surface of the cementitious hydration products at 0.3-wt% SNS additions. This formation gel layer is due to the functional group interface of SNS during the hydration process. The SNS participate in the reaction of C3S and C2S, the format jelly-like C-S-H attached to the substrate maintains the cement particle moisture and protects the matrix against the crack. The gel layer of the hydration products SNS/C-S-H also promotes the compactness and the density of the ordinary hydration layer without obvious microcracks.

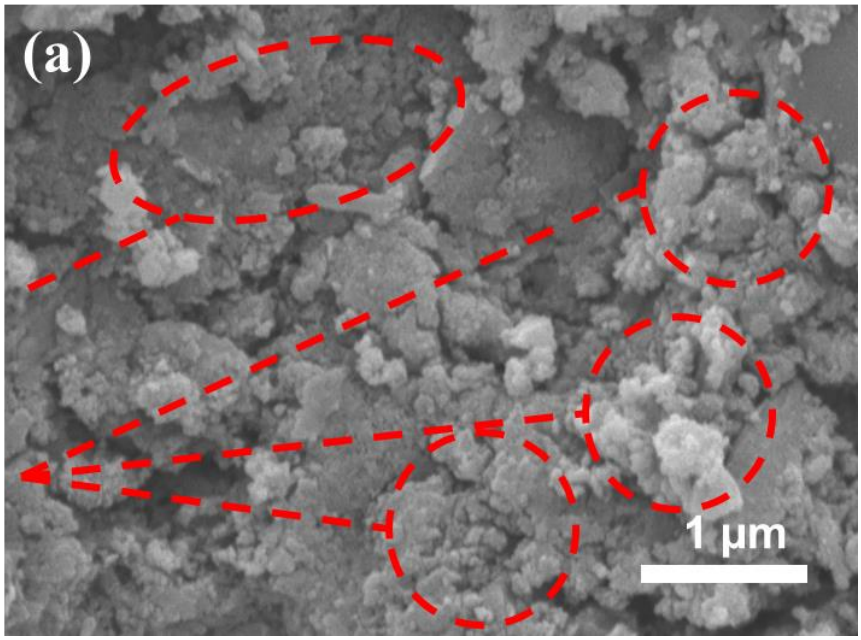

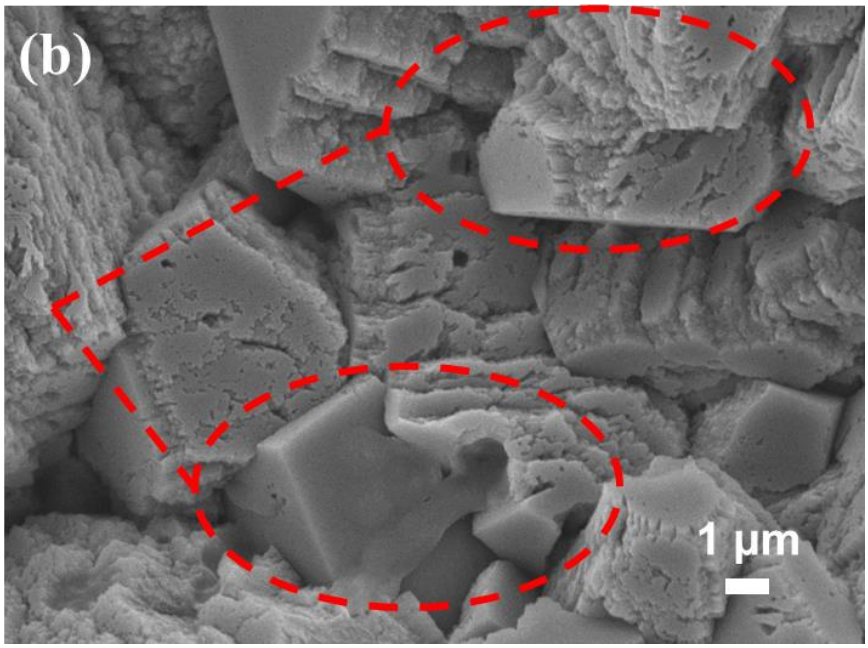

$Ca(OH)_2$ cube-shaped crystals

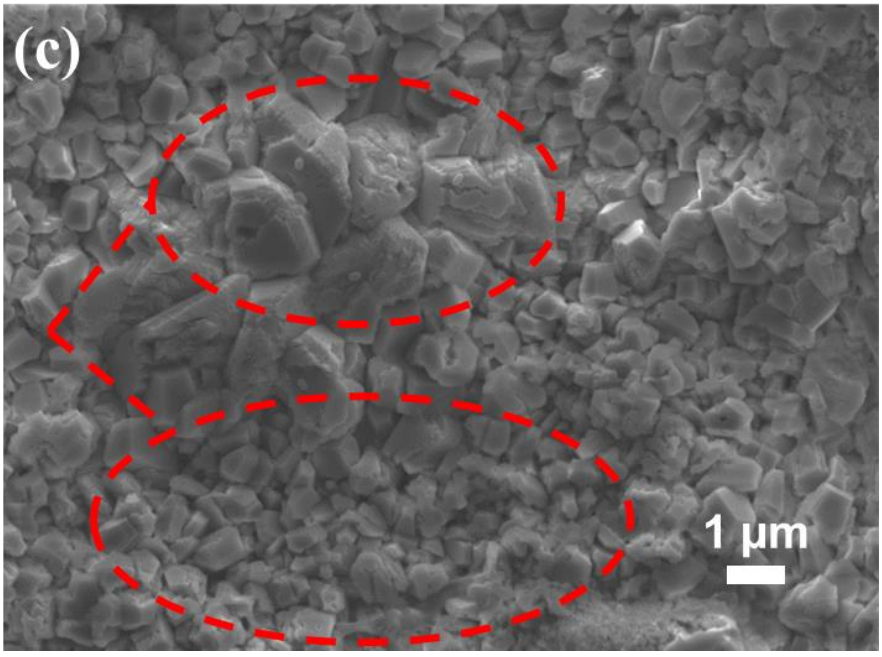

$Ca(OH)_2$ cube-shaped crystals

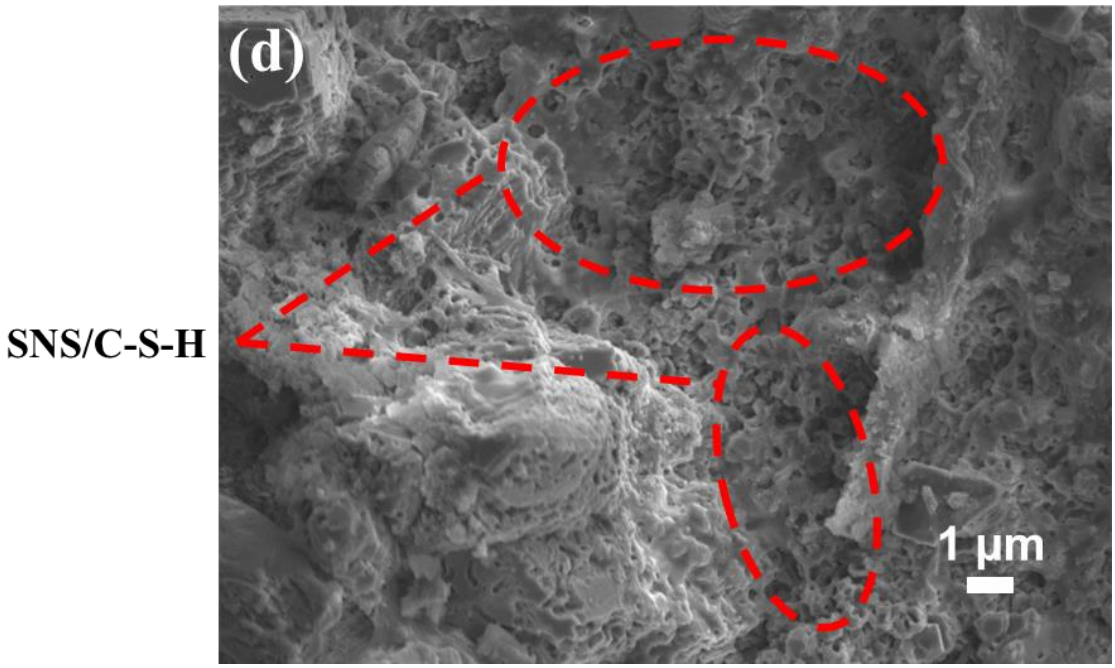

Figure 6.7 28 days SEM images of cement pastes at SNS-wt% of (a) 0, (b) 0.1, (c) 0.2 and (d) 0.3

When comparing the SEM image from Figure 6.5 to Figure 6.7, the SNS addition significantly affects the cementitious composites' hydration process. The SNS change the crystallisation and morphology of the cementitious composites' hydration products. As the SNS have strong permeability and surface adsorption properties, it can additionally attract the water molecules to the unhydrated cement. Furthermore, the surface adsorption of SNS promotes their coating on cement particles, forming denser bulk hydration products. The encapsulated SNS uniformly dispersed into the matrix, working as a highly active carrier promoting C-S-H gels and CH hydration productions.

6.3.2.2 Effect of SNS on the cement pastes interfacial transition zone

To further investigate the effect of raw and soni SNS on the cementitious mix, the SEM images were used to determine the features of SNS matrix surface. Figure 6.8 shows a comparison of the SEM images for 0 and 0.3-wt% raw and soni SNS additions (w/c=0.35) at 7 days. Figure 6.8(a) shows the distribution of Portland cement pastes

composites hydration products at an early age, including unhydrated cement particles and the irregular cracks on the surface of the plain matrix. Figure 6.8(b-c) shows the raw and soni SNS existing on the specimen surface, the morphology is clearly different from the control group. As discussed in Chapter 4, the SNS three-dimensional steric stabilisation mechanism provides the stable support between the cementitious composite particles.

Figure 6.8(b-c) shows the SEM images of SNS morphology and the fibre filament bridging mechanism contributing to reinforcing performance. With the crack bridging mechanism of SNS, the fibres reduce the size effect of the interface transition zone. These hydrated products tightly warp the SNS and result in DOH increase. The SNS effectively promote the formation of the interface between the C-S-H gel and cement pastes, which is beneficial to mechanical strength and ductility. In practical applications, the fibre is perpendicular to the direction of cracking and is subjected to tensile stress, which can continuously provide the pull-out resistance until it is broken into two fragments.

Furthermore, the SEM images of Figure 6.8(b) show raw SNSs have no significant agglomerate on the surface, and the a-SNS effect of the filling bridges is evident along the crack. There are more a-SNS existing in Figure 6.8(b) than in Figure 6.8(c), which is consistent with the centrifugation experiment results. The early hydration age of 7 days is the particular age where the fibres attached to the cement composite can be observed. Afterwards, the SEM images show that it can be challenging to locate a-SNS within the cement pastes. The hydration development on the SNS surface leads to the formation of hydration products for the SNS/C-S-H and SNS/CH structures. The SNS can be difficult to identify with the hydration products continually growing and accumulating on the SNS surface.

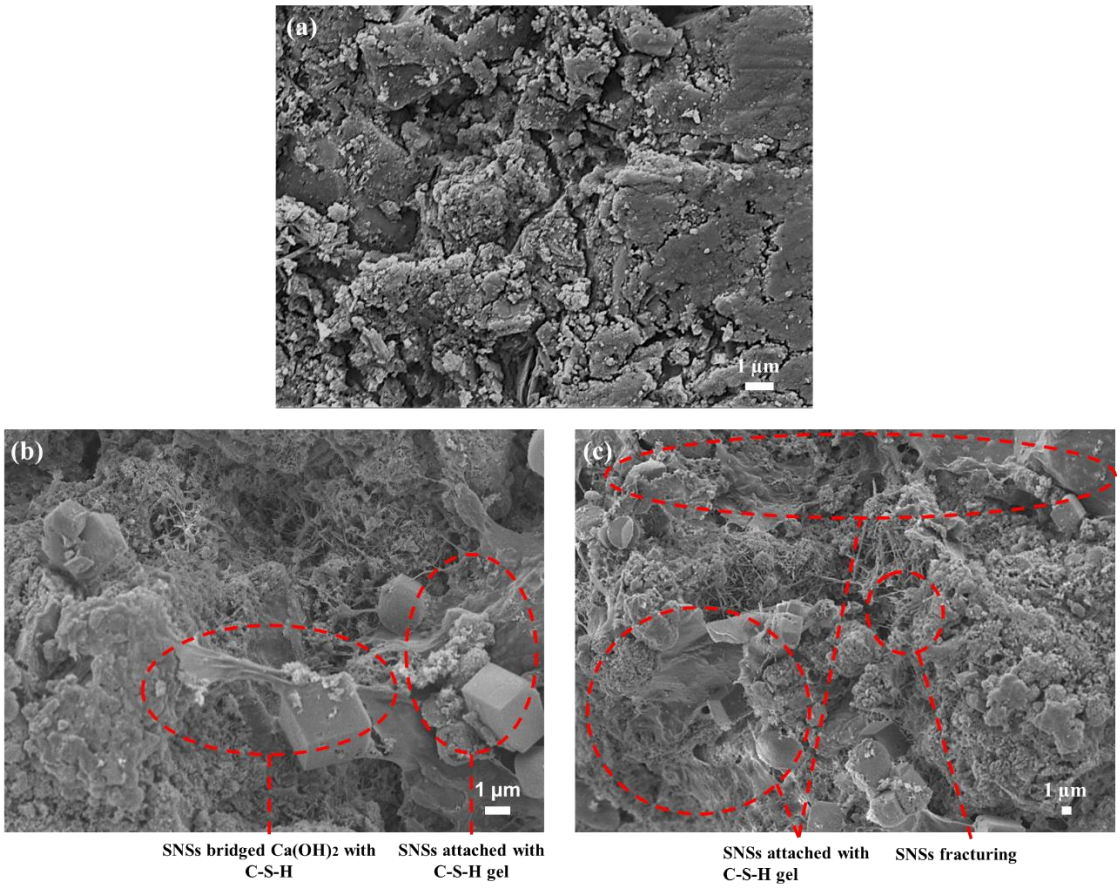

Figure 6.8 7 days SEM images of cement pastes at the w/c=0.35, SNS-wt% of (a) 0, (b) 0.3 Raw and (c) 0.3 Soni

6.3.3 The XRD of SNS-cementitious composites

Figure 6.9 shows the XRD patterns of cementitious composites with 0, 0.1, 0.2 and 0.3-wt% SNS additions at 7, 14 and 28 days, all the diffraction patterns of SNS cementitious composites hydration product detected the similar phase types. The pattern analysis reveals that the cementitious mix mainly contains un-hydrated C3S, AFt, CH and $CaCO_3$. The SNS addition does not change the cementitious composites hydration product types of crystal, but the amount of SNS addition does affect the crystal diffraction peak intensity. As the SNSs dissolve and interact with the cement pastes, the XRD patterns characteristic peaks of SNS can not detect.

Figure 6.9(a-b) shows the crystals of ettringite, calcium hydroxide and calcium carbonate peaks intensity improved by increased SNS concentration at the cementitious composites at 7 and 14 days. However, the un-hydrated phase tricalcium silicate were decreased (e.g., the peak intensities of the C3S phase decreased). It is noted that at 7 and 14 days, the portlandite content of 0.3-wt% SNS-cementitious showed a decreasing trend compared to the 0.2-wt% SNS addition, the 'less calcium' phenomenon results in a less stable microstructure of the cement pastes.

Figure 6.9 (c) shows the XRD pattern of the SNS cement pastes hydrated for 28 days. The results show that in the SNS cement matrix CH and ettringite crystal intensity is higher than in the control group. The improvement in crystalline pattern intensity indicates that the SNS sheets enhance the formation of hydration products, and further increases in the CH intensity confirms the results of the TGA and DSC findings in Chapter 4. For the C-S-H gel, as it has various compounds and includes amorphous phases, under normal curing conditions, it is difficult to identify the C-S-H through XRD diffractograms (Rendell, Jauberthie and Grantham, 2002). Therefore, the amount of the C-S-H gel in the XRD is estimated by evaluating the changes in the relative content of the other crystalline intensity peaks.

At 28 days of the SNS cement matrix composite, the addition of SNS had insignificant effects on the calcium carbonate peak intensity. Since the consumption of C3S can promote the C-S-H product, the amount of C3S is used as an index to estimate the C-S-H content. With the amount of SNS increase, the C3S content gradually decreases. The decrease in C3S peak intensity may attribute to the interaction between the C3S and the SNS surface hydroxyl/hydroxymethyl groups. The change of the crystal phase intensity peak was used to understand the mechanism of SNS reinforced cement pastes hydration process. This phenomenon is similar to the GO-reinforced cementitious

composites principle, the free water attracts into the specimen surface promote the reaction with C3S and generate the hydration products (Wang *et al.*, 2017).

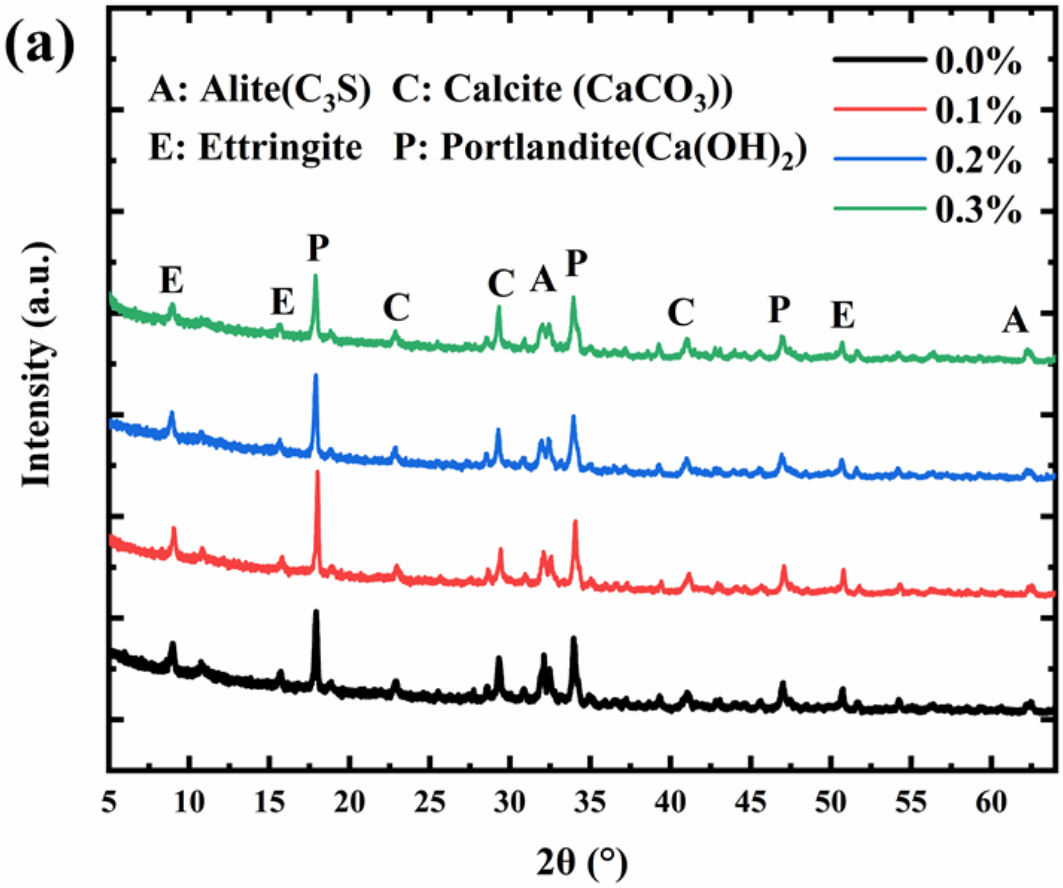

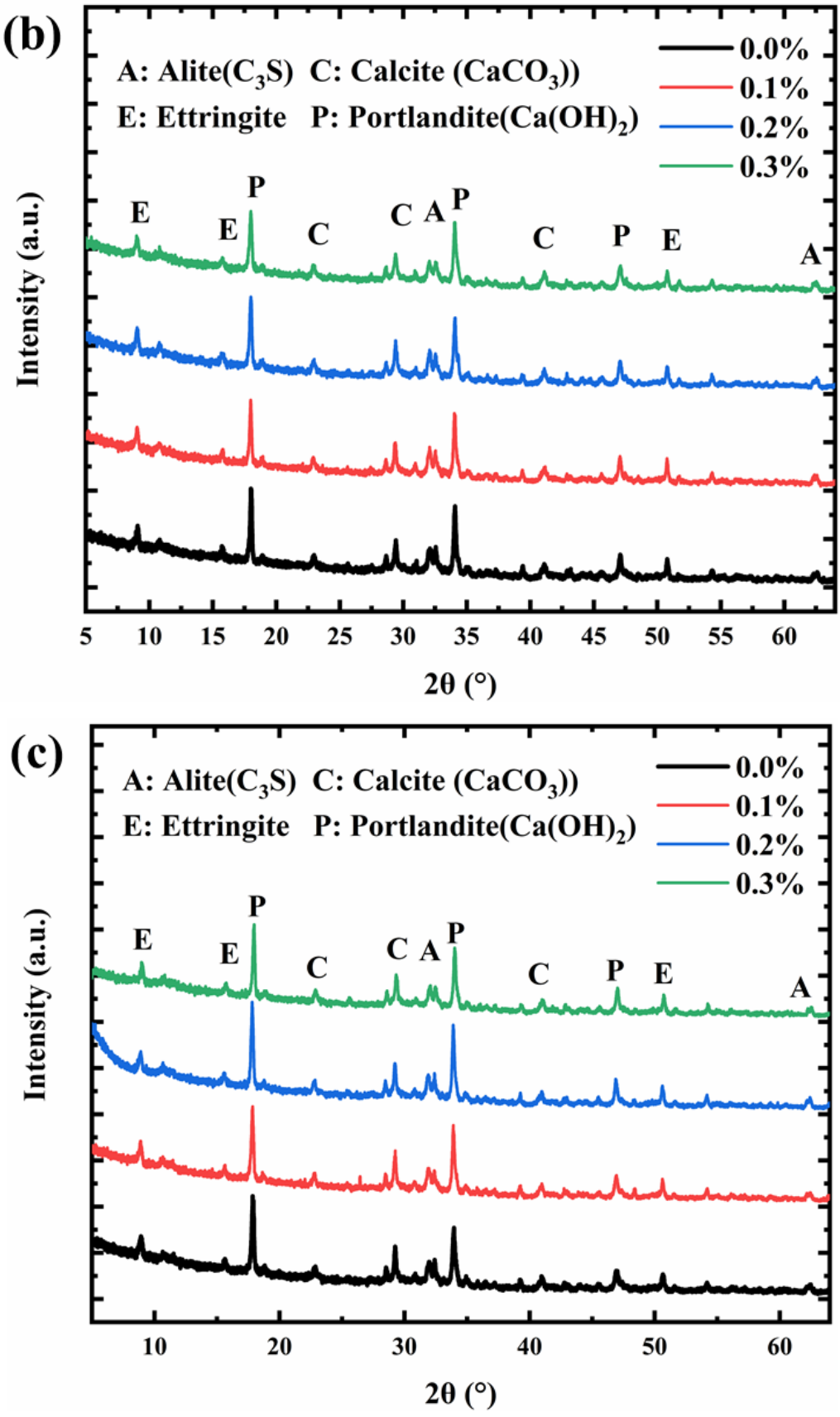

Figure 6.9 XRD analysis of cement pastes with 0%, 0.1, 0.2 and 0.3-wt% amount of SNS at days of (a) 7, (b)14 and (c) 28 (2θ=5-65°)

Figure 6.10 shows the XRD pattern of 0%, 0.3-wt% raw and 0.3-wt% soni SNS added cementitious composites at 28 days. In the Figure 6.10, the XRD pattern results show that the cementitious hydration product phase types are not affected by raw and soni SNS. All the SNS-cementitious composites hydration products include the ettringite, CH, un-hydrated tricalcium silicate (C3S) and $CaCO_3$. However, by comparing the raw and soni SNS-cementitious XRD patterns, the intensities of the diffraction peaks are slightly different.

Figure 6.10 shows that in the raw and soni SNS cement-based hydration products both show higher portlandite and calcite pattern peak intensities to the control group. The amount of calcite is insignificantly changed and the Alite intensity peak has become lower. These results show that both raw and soni SNS can noticeably affect the cementitious hydration products. The SNS suspensions with higher dispersions result in better ettringite hydration and Alite consumption. This phenomenon indicates that both raw and soni SNS can effectively promote the increase of the cementitious composites DOH. The mechanism of SNS promoting the hydration is similar to the CNCs, previous research on the CNCs show a similar reinforced cement pastes mechanism (Cao *et al.*, 2015).

Furthermore, EDS and BET characterisation will be utilised to analyse and discuss the presence of C-S-H gel.

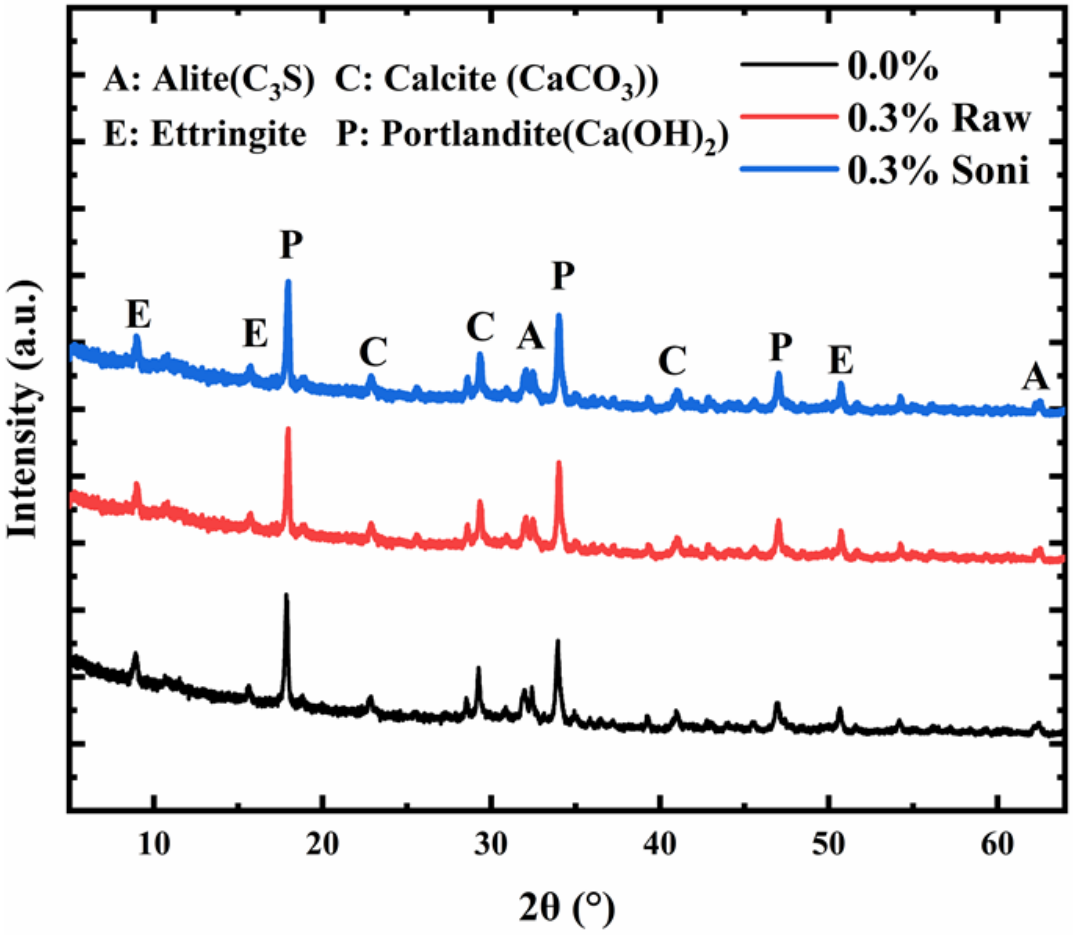

Figure 6.10 Powder XRD patterns of 28 days cement pastes with and without 0.3-wt% raw SNS and soni SNS

6.3.4 The energy dispersive spectroscopy of SNS-cementitious composites

EDS is an electron-induced X-ray spectrochemical technique, where the spectroscopy characterises the surface of the solid-phase SNS-cementitious composite's chemical composition and element distribution. The distribution of SNS in cement composites is the main microstructural parameter that affects the DOH, mechanical properties and the elemental distribution. According to the SNS characterisation in Chapter 3, the SNS chemical composition includes mainly C, H and O elements. Theoretically, by tracking these chemical elements the distribution of SNS in the cement matrix can be determined,

since cement does not contain C element and the carbon element is an important component of SNS. The tracking of the carbon element is an effective way of locating the SNS in cement paste. However, the previous EDS experiment results show that the cementitious mix is susceptible to carbonation (Sarott *et al.*, 1992; Cao, Tian, *et al.*, 2016). Therefore, in the present research, the distribution measurement of carbon element was not legitimate. Furthermore, the scanning of element H is not within the scope of this test. Therefore, this work will discuss the distribution of SNS in the cementitious mix through oxygen spectrogram concentration variation.

Figure 6.11, Figure 6.12, Figure 6.13 and Figure 6.14 show the results of EDS spectra and the different elemental profiles of the cementitious composites with 0, 0.1-wt%, 0.2-wt% and 0.3-wt% SNS at ages of 28, respectively. Figure 6.11 is the EDS result analysis chart that shows the hydration products of the OPC cement pastes are composed of Ca, O, C, Si elements, with small amounts of Al, Mg, Fe and S elements. It can be inferred that the matrix surface is composed of Al phase hydration products (calcium-aluminate-hydrate (C-A-H), calcium-alumino-silicate-hydrate (C-A-S-H) etc.) and AFt/AFm hydration products.

According to Figure 6.11, Figure 6.12, Figure 6.13, and Figure 6.14, the SNS oxygen spectrograms indicate that the distribution of the oxygen diagram is related to the SNS addition. The SNS have strong natural dispersibility at suspensions, which results in the uniform distribution in the cement pastes. The increase in SNS amount makes the oxygen elements of the cement-based composites denser and more uniformly dispersed. In addition, the surface distributions of Ca and Si are shown between Figure 6.11 from Figure 6.14 (c) and (d), respectively. With the increase of SNS addition, the distribution of the Ca and Si elements in the hydration products are not uniform, and the variability gradually increases. Compared to the control group, Figure 6.13 has a larger

calcium/silicon ratio, indicating that there are more C-H microcrystals generated. Figure 6.14 shows lower Ca/Si ratios than other groups, while the C-S-H gel is more likely to emerge in areas with a lower calcium/silica ratio. The EDS result is the evidence that uniformly distributed SNS promotes the hydration products.

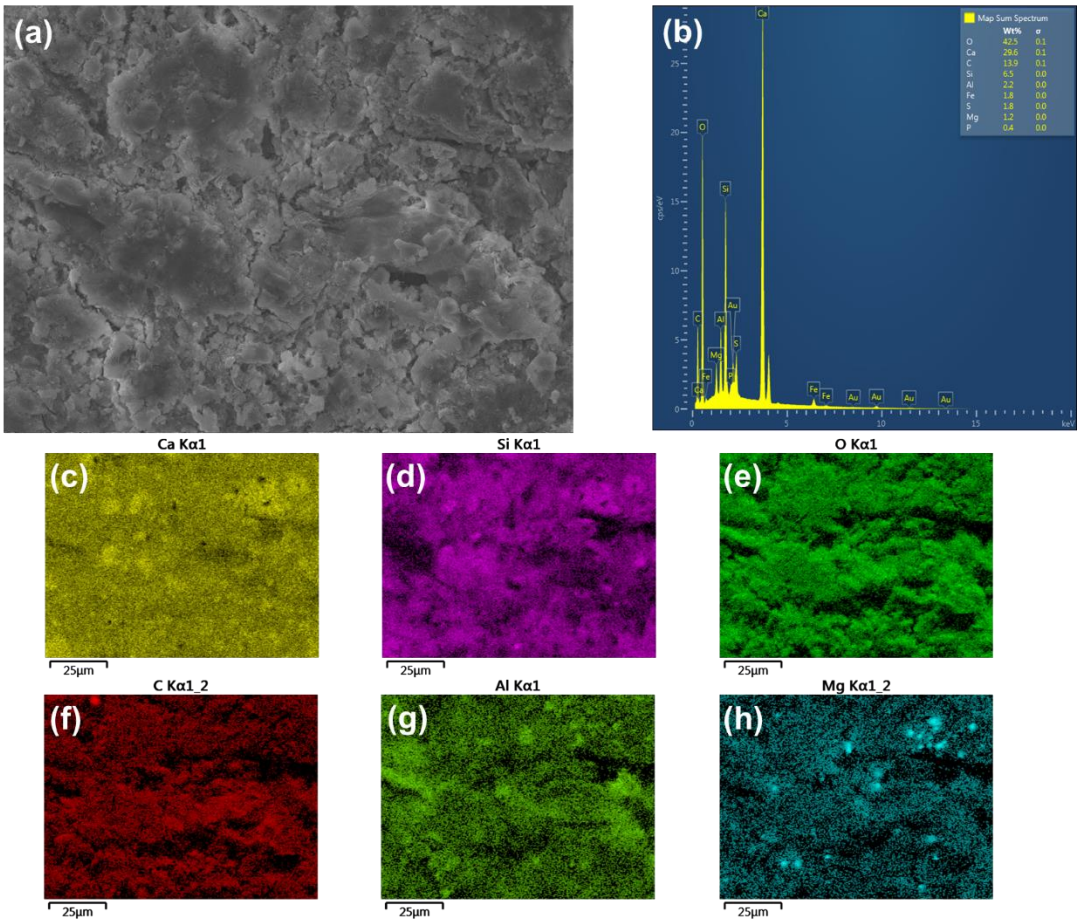

Figure 6.11 28 days 0-wt% soni SNS cement pastes (a) SEM image, (b) EDS spectrum of the specimen, (c) distribution of calcium element, (d) distribution of silicon element, (e) distribution of oxygen element, (f) distribution of carbon element, (g) distribution of aluminum element and (h) distribution of magnesium element

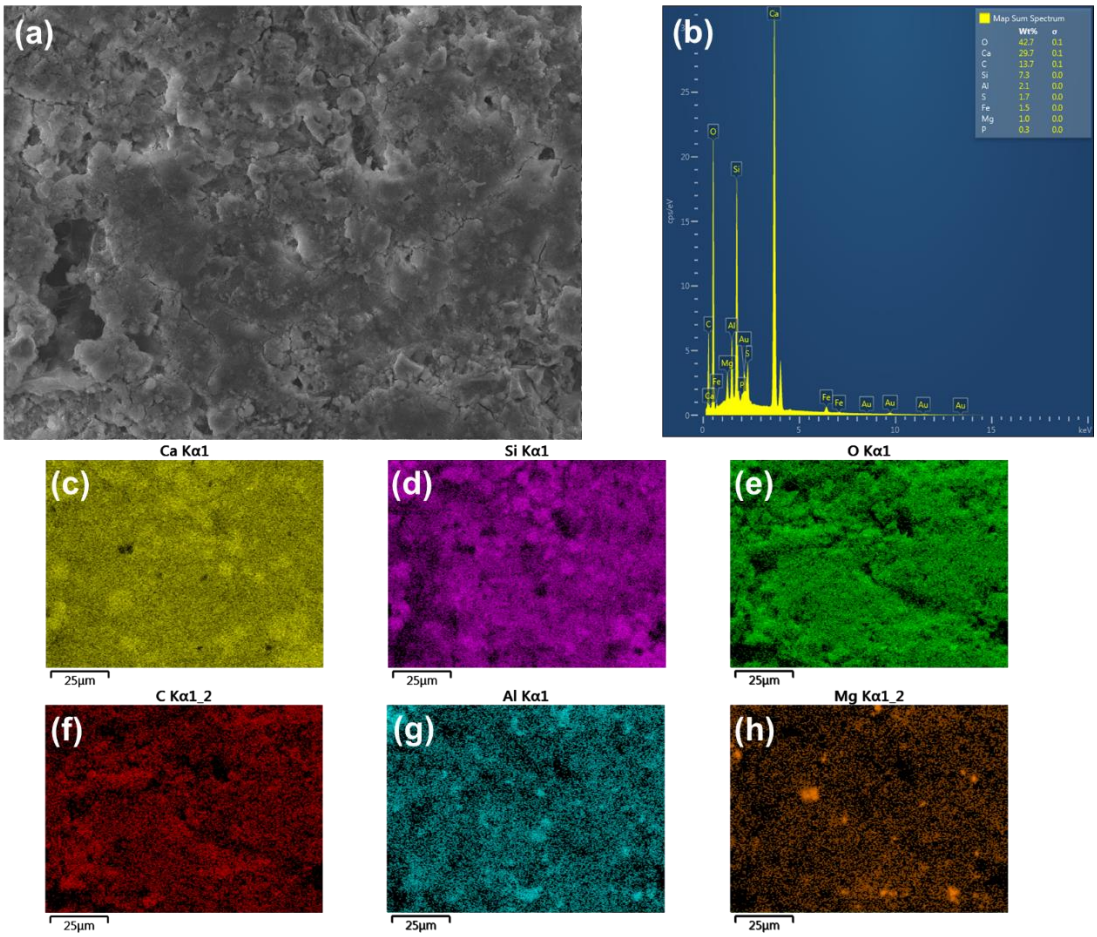

Figure 6.12 28 days 0.1-wt% soni SNS cement pastes (a) SEM image, (b) EDS spectrum of the specimen, (c) distribution of calcium element, (d) distribution of silicon element, (e) distribution of oxygen element, (f) distribution of carbon element, (g) distribution of aluminum element and (h) distribution of magnesium element

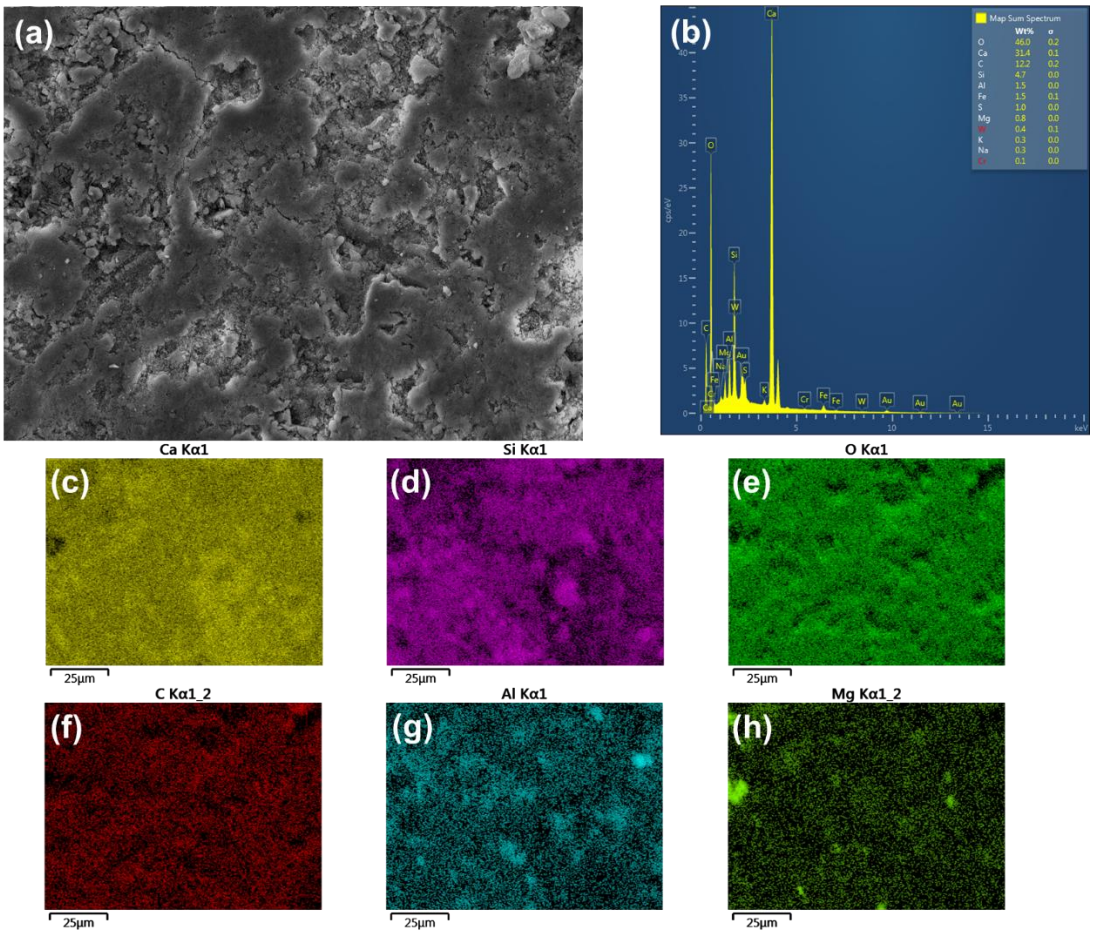

Figure 6.13 28 days 0.2-wt% soni SNS cement pastes (a) SEM image, (b) EDS spectrum of the specimen, (c) distribution of calcium element, (d) distribution of silicon element, (e) distribution of oxygen element, (f) distribution of carbon element, (g) distribution of aluminum element and (h) distribution of magnesium element

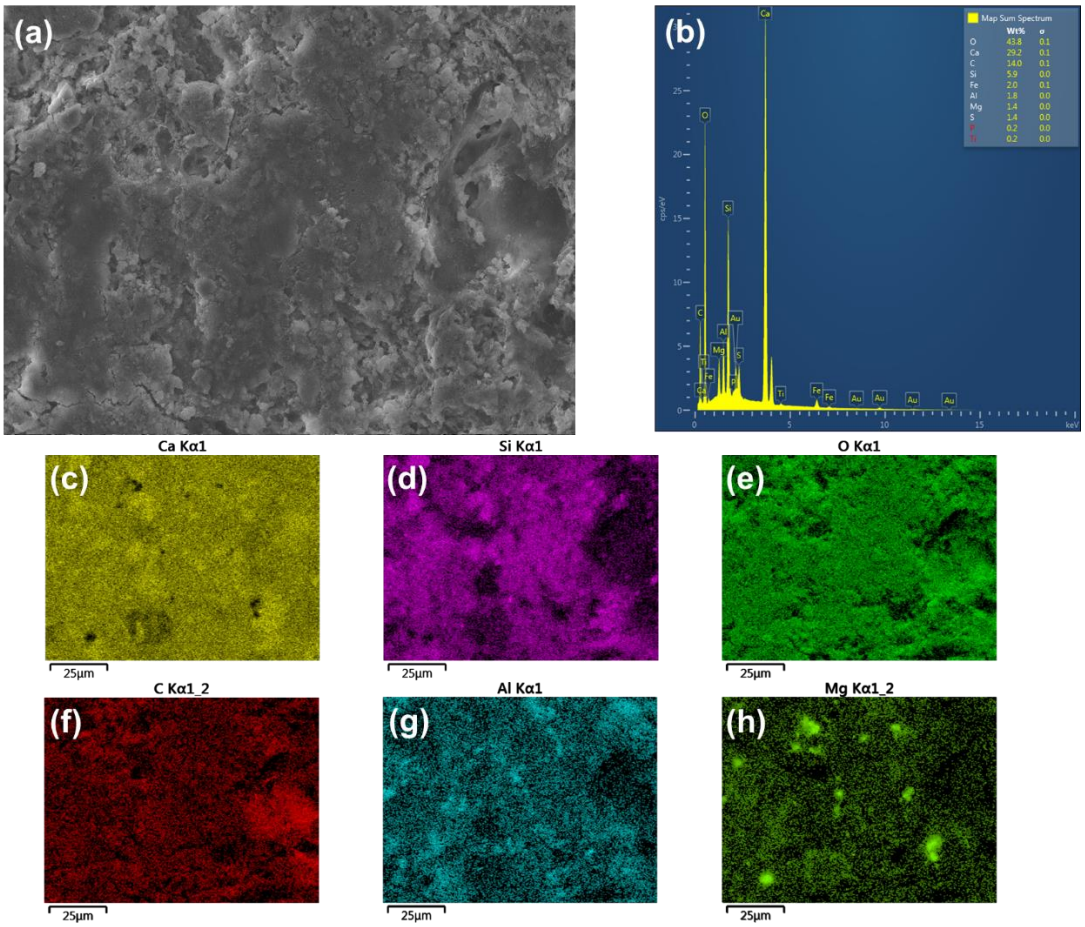

Figure 6.14 28 days 0.3-wt% soni SNS cement pastes (a) SEM image, (b) EDS spectrum of the specimen, (c) distribution of calcium element, (d) distribution of silicon element, (e) distribution of oxygen element, (f) distribution of carbon element, (g) distribution of aluminum element and (h) distribution of magnesium element

In order to characterise the raw and soni SNS dispersion effect on the cementitious mixes, the EDS compared the plain cementitious composites, with 0.3-wt% raw SNS and 0.3-wt% soni SNS. Figure 6.15 shows the EDS of the OPC cementitious composite at 7 days. EDS results show that O, Ca, C and Si are the main elements of hydration products in the early hydration age, and a small amount of Al and Mg elements are also present. Based on the elements presented, it can be inferred that C-S-H and calcium alumina hydration products were produced in the OPC cement matrix at ages of 7.

Figure 6.16 and Figure 6.17 show the SEM micrographs and the EDS spectra of the cementitious composites of SNS at 0.3-wt% in raw and soni at 7 days, respectively. Under the same SNS addition amount, the oxygen map shows the raw SNS appear more accumulated and uniformly distributed on the surface of the hydration products, SNS had also adsorbed on the high-density C-S-H. The soni SNS oxygen peak tends to be more homogeneous and randomly distributed in the matrix hydration phase. Furthermore, in Figure 6.16 and Figure 6.17, the distribution of Ca and Si elements are uneven compared to the control group, indicating higher hydration products of CH and C-S-H are generated. The EDS analysis results show that SNS promotes the growth of C-S-H and CH, takes part in the nucleation effect and promotes the cement hydration process. This can be attributed to the uniformly distributed SNS effect in the cementitious composites.

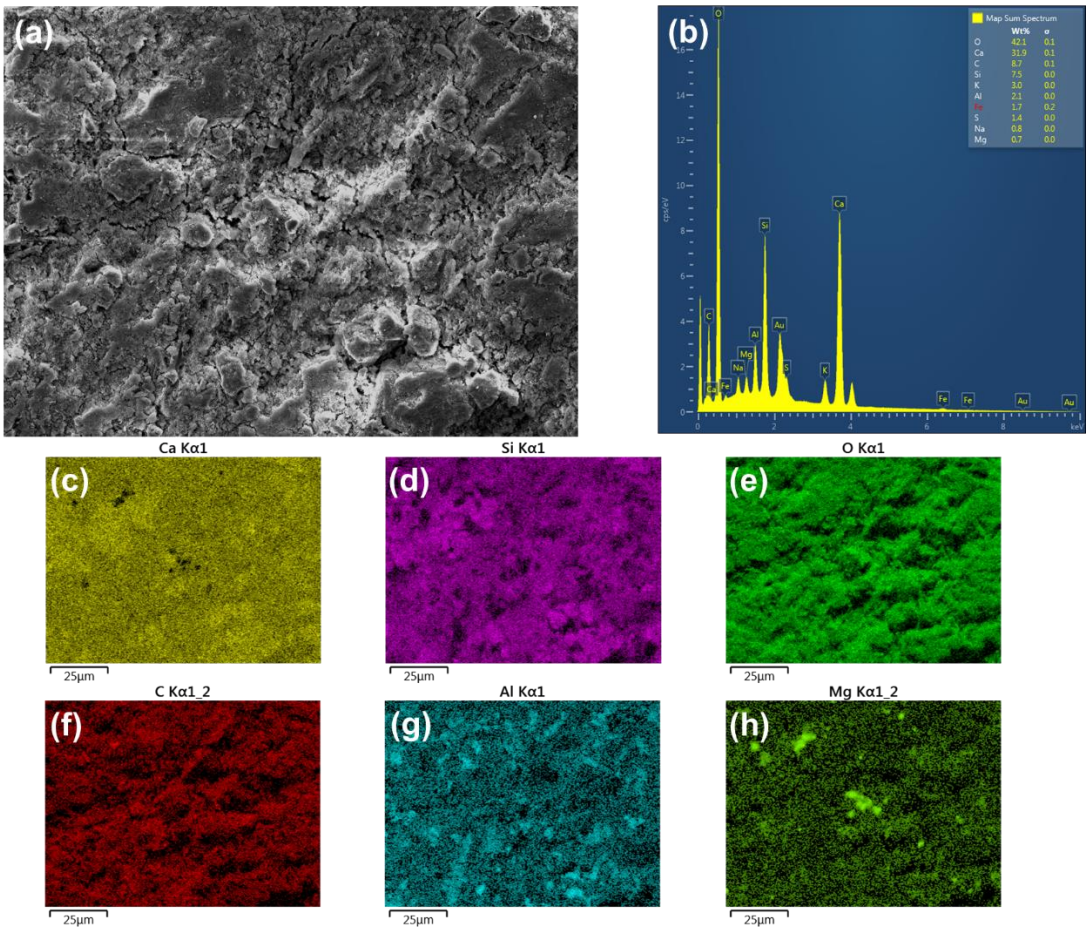

Figure 6.15 7 days plain cement pastes (a) SEM image, (b) EDS spectrum of the specimen, (c) distribution of calcium element, (d) distribution of silicon element, (e) distribution of oxygen element, (f) distribution of carbon element, (g) distribution of aluminum element and (h) distribution of magnesium element

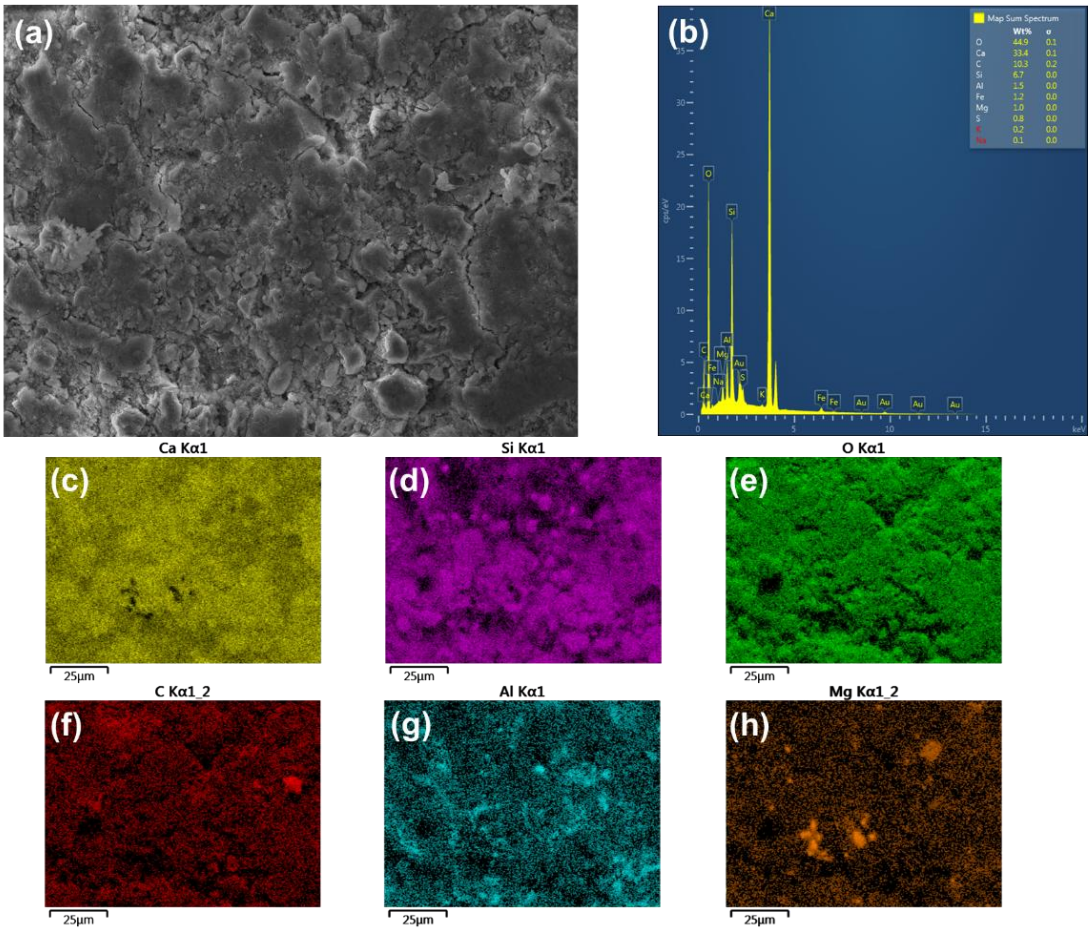

Figure 6.16 7 days 0.3-wt% raw SNS cement (a) SEM image, (b) EDS spectrum of the specimen, (c) distribution of calcium element, (d) distribution of silicon element, (e) distribution of oxygen element, (f) distribution of carbon element, (g) distribution of aluminum element and (h) distribution of magnesium element

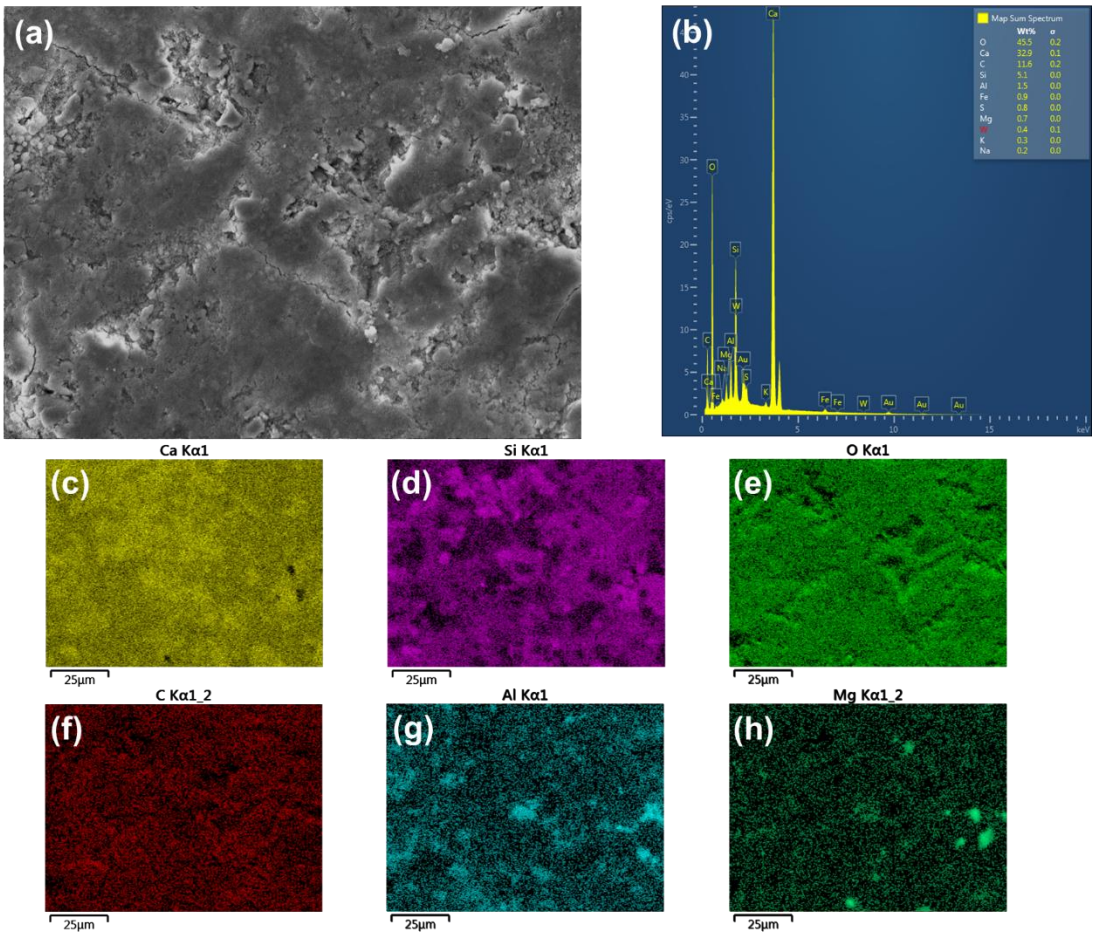

Figure 6.17 7 days 0.3-wt% soni SNS cement pastes (a) SEM image, (b) EDS spectrum of the specimen, (c) distribution of calcium element, (d) distribution of silicon element, (e) distribution of oxygen element, (f) distribution of carbon element, (g) distribution of aluminum element and (h) distribution of magnesium element

6.3.5 Nitrogen adsorption/desorption isotherms determined for the cement pastes

Figure 6.18 shows the cementitious composites nitrogen adsorption-desorption isotherms at 28 days. Both the nitrogen adsorption capacity and SSA increase as the SNS content increases. Following to the classification standards of the International Union of Pure and Applied Chemistry System (IUPAC) nitrogen adsorption isotherms (Sing, 1985), the isotherms curve is type IV with a hysteresis loop, and the hysteresis loop is H3 type. As the high P/P_o is not restricted by adsorption, the aggregates of plate-like particles are observed to produce slit-shaped pores. The cementitious composites SSA is calculated through the BET theory. The cementitious composites SNS additions of 0, 0.1, 0.2, and 0.3-wt% SSA were 28.02, 32.20, 32.33, and 43.82 m^2/g, respectively.

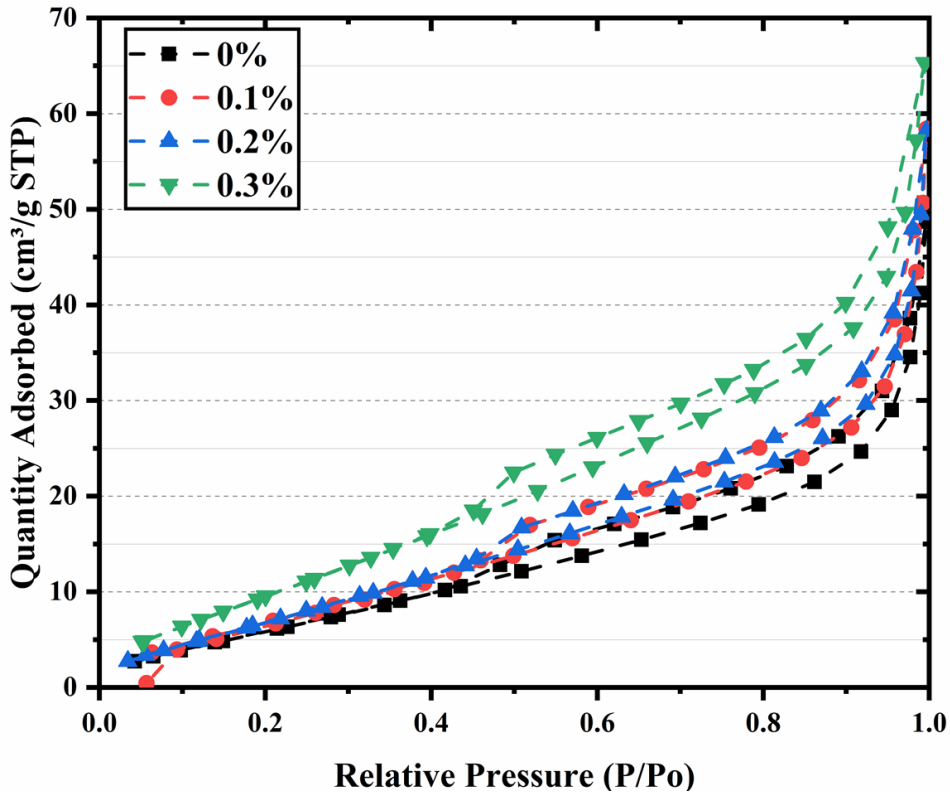

Figure 6.18 SNS-cementitious composite Nitrogen sorption isotherm curves at ages of 28

Figure 6.19 shows the cumulative pore volume of the SNS-cementitious composites at 28 days. These curves indicate that by increasing the SNS content, the cumulative pore volume of the cementitious composite shows an increasing trend. For the SNS addition amounts of 0, 0.1, 0.2 and 0.3-wt%, the specimen pore volume is 0.063, 0.071, 0.076 and 0.091 cm^3/g respectively. The cementitious composites pore volume is mainly concentrated from the 2 to10 nm region, the accumulated pore content increases sharply as the amount of SNS increases. However, the pore volume increasing trend slows down within the pore diameters ranging from 40 to 80 nm.

The cumulative pore volume and SSA both show an increasing trend by increasing the SNS content, which is attributed to the SNS helping to generate more C-S-H gels in the cement matrix. Furthermore, the SNS/C-S-H gel has a finer pore network compared to the CH, which contributes to a larger SSA and pore volume in cement pastes. Like GO, the SNS sheets trap ions (such as Ca^{2+}) on their surfaces during the hydration, which act as nucleating agents for the C-S-H or calcium hydroxide. The GO reinforced cement composite also increases the SSA from 27.3m^2/g to 64.9m^2/g and the total pore volume from 0.049 to 0.101 ml/g (Pan *et al.*, 2015).

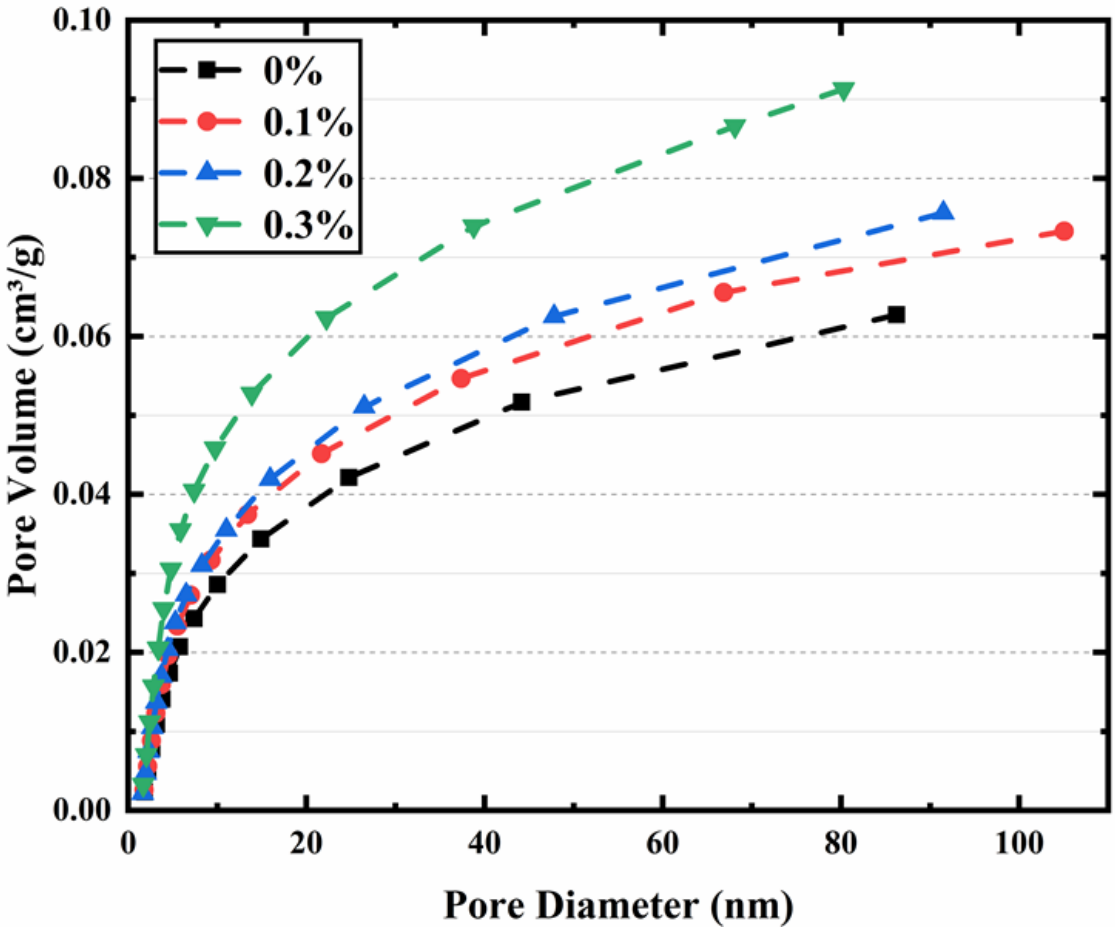

Figure 6.19 Cumulative pore volume for SNS-cementitious pastes at 28 days

Figure 6.20 shows the pore size distribution diagram of the SNS-cementitious specimens. The experiment result shows that the SNS-cementitious composite pore size increases significantly in the range of 2 nm to 10 nm, especially at the pore size of 5 nm. In the C-S-H phase surface, fine pores are concentrated from 0.5 to 10 nm (Ismail *et al.*, 2013). With the increase of SNS addition, there was an improvement in the pore size distribution of the cementitious composites hydrated products, which matched the C-S-H gel pore size distribution. The SNS-cementitious fine pores are related to the amount of C-S-H and the high SSA.

In addition, SNS results a slight increase in the pore content of the cementitious matrix in the diameter range of 45 nm to 80 nm, which relates to the pore size distribution of

the SNS material itself and influences the fluidity of the cement pastes. The experimental results confirmed that the SNS optimised the pore size distribution of the cement matrix and significantly enhanced the C-S-H gel content. The enhancement mechanism are similar to GO and CNT modified cementitious matrix (Makar and Chan, 2009; Kang *et al.*, 2019).

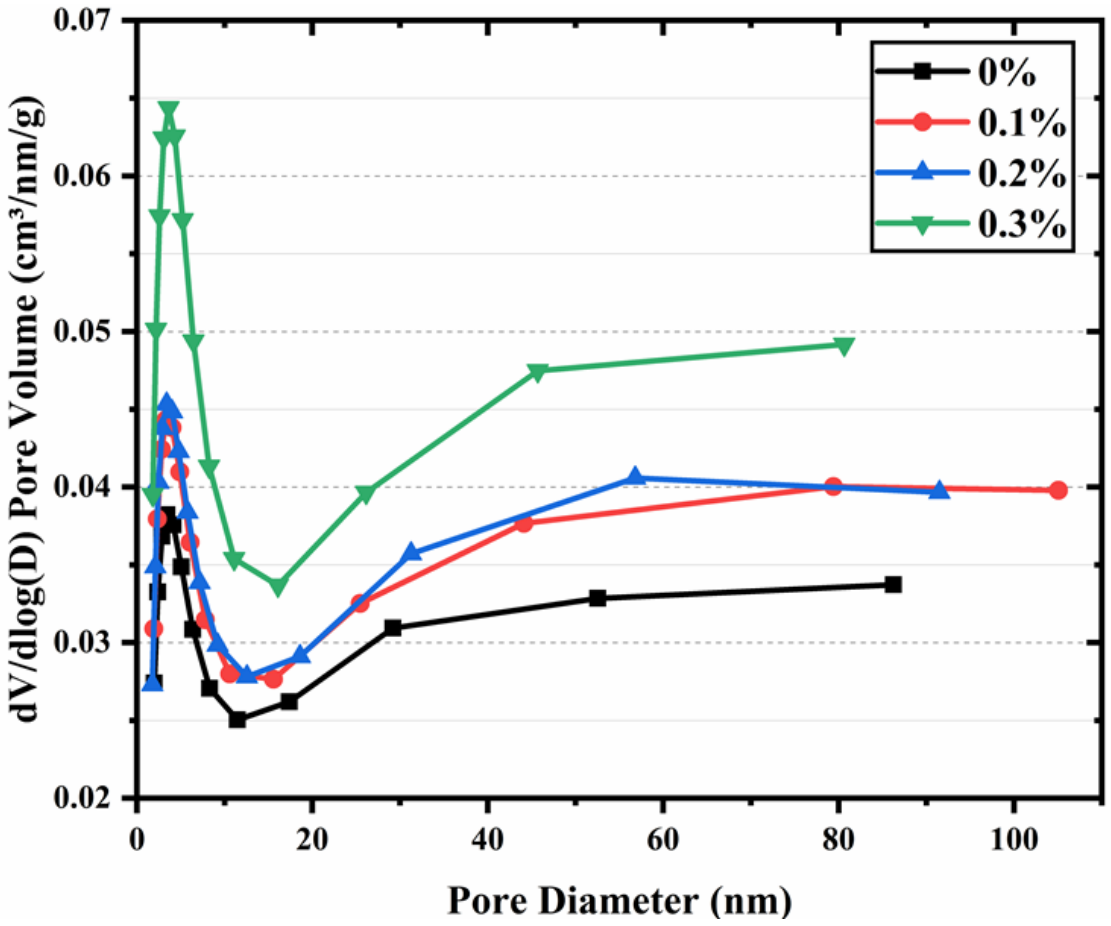

Figure 6.20 Pore size distribution of SNS-cementitious composite

To analyse the SNS dispersal influence of the pore structure on the cement pastes hydration products, Figure 6.21 shows the nitrogen adsorption-desorption isotherms of 0.0-wt%, 0.3-wt% raw and 0.3-wt% soni SNS added cementitious composites hydration products at 28 days. The raw and soni SNS-cementitious composites nitrogen adsorption-desorption isotherms plot are similar. According to the BET theory, the SSA of the control, 0.3-wt% raw and 0.3-wt% soni SNS cement matrix composites are

28.02, 44.80 and 43.82 m^2/g, respectively. The SSA results show that the dispersion states of raw and soni SNS suspension have limited effect. Both dispersion states show a similar reinforcement degree of cementitious composites hydration products.

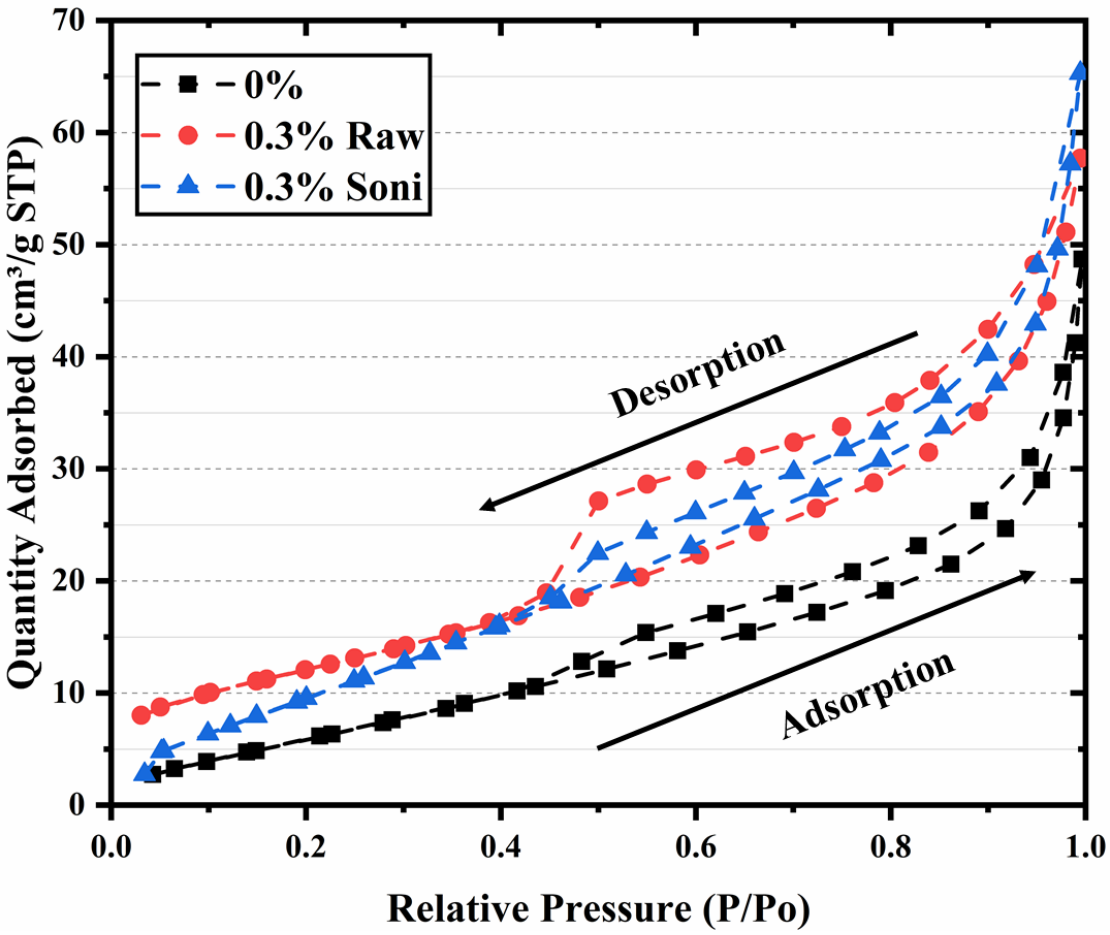

Figure 6.21 Nitrogen adsorption-desorption isotherm curves of plain, 0.3-wt% raw SNS and 0.3-wt% soni SNS-cementitious composite at ages of 28.

Figure 6.22 show the cumulative pore volume and the pore size change of the cementitious composites with 0 0.3raw and 0.3soni -wt% SNS at ages of 28. The 0.3-wt% of SNS under different conditions increases the cumulative porosity of the cement matrix by a similar range. According to Figure 6.23, the plots determined that both raw and soni SNS significantly increase the cementitious composites pore size distribution in the range of 2-10nm. The fully diffused SNS-cementitious composites pore size distribution in the range of 2-10 nm is higher than the raw SNS matrix, while the plain

cement has the minimal amount. It is worth noting that the distribution of mesoporous (2 nm to 50 nm) of raw SNS is higher than that of the soni state. The content of macropores (above 50nm) in the raw SNS matrix is lower than that of soni SNS and the plain cement. This phenomenon corresponds to the centrifugation results, where the raw SNS-cementitious contain more a-SNS that are attached to the surface of cement particles reducing the content of macroporous.

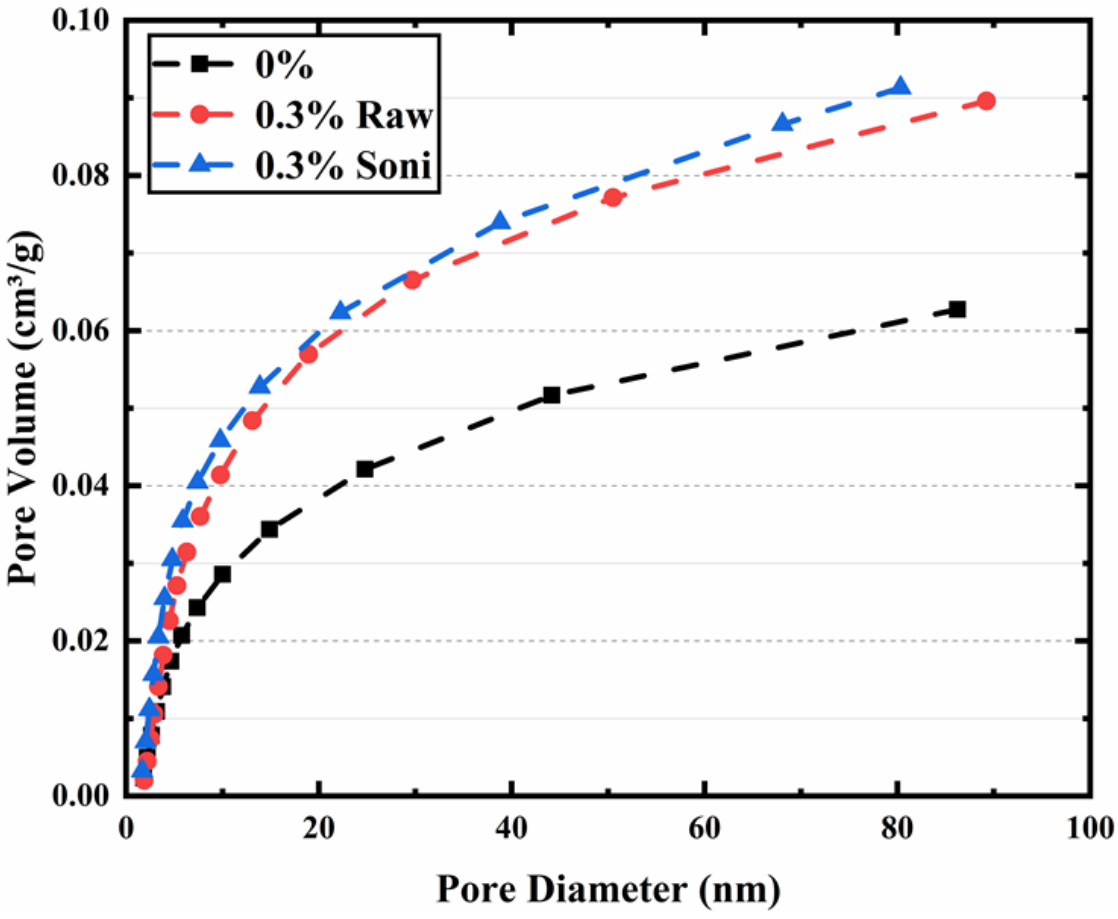

Figure 6.22 Cumulative pore volume for Plain, 0.3-wt% raw SNS and 0.3-wt% soni SNS cementitious pastes at 28 days.

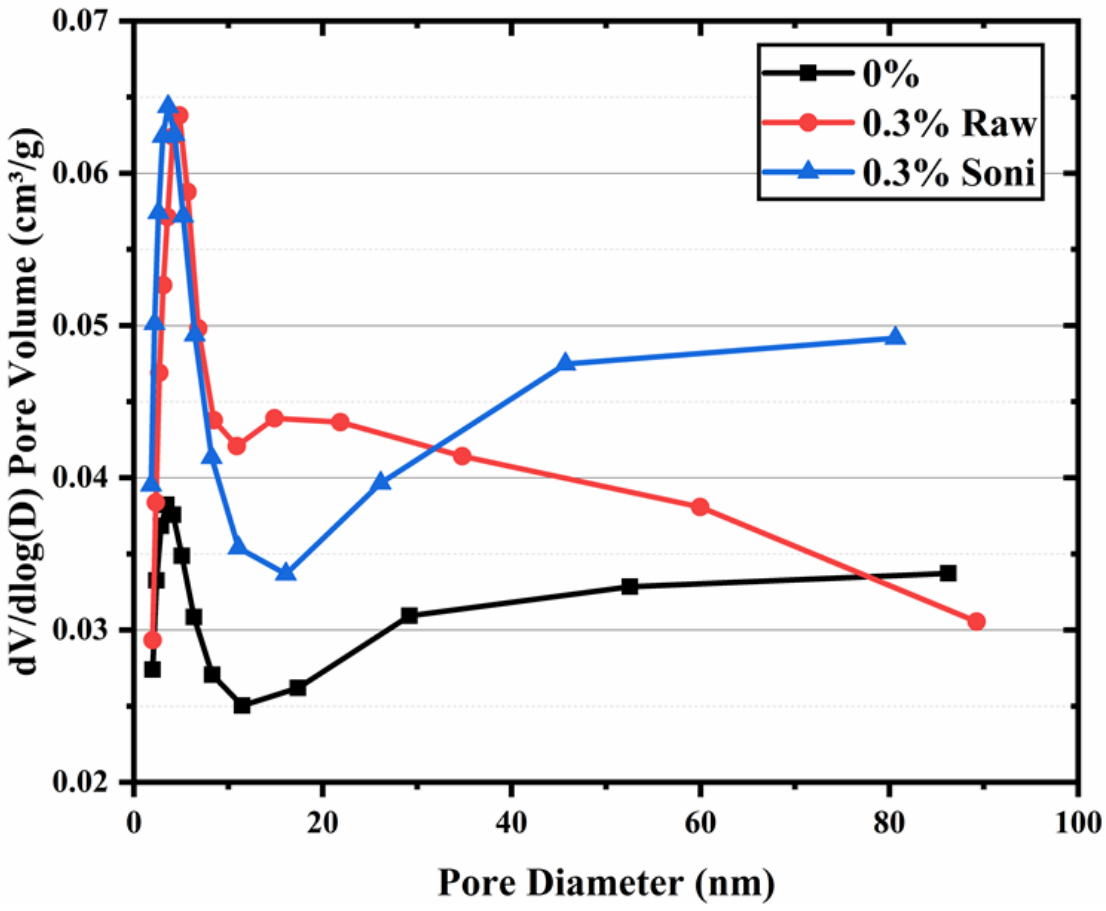

Figure 6.23 Pore size distribution for 0-wt%, 0.3-wt% raw SNS and 0.3-wt% soni SNS cementitious composite

6.3.6 TEM microtopography of SNS cementitious composites

In order to characterise the SNS promoted cementitious matrix microstructure, the TEM images were taken to compare the cement control group and the 0.3-wt% raw and 0.3-wt% soni SNS of the composite material specimens at ages of 28. Figure 6.24 shows the TEM images of the ordinary cement pastes microstructure at 28 days. It can be observed that the microstructure of the plain specimen is mainly composed of the lower contents of $Ca(OH)_2$ crystals and the C-S-H gel, of which $Ca(OH)_2$ is unevenly distributed on the surface of C-S-H gel, and moreover, shows the existing pores in the C-S-H gel.

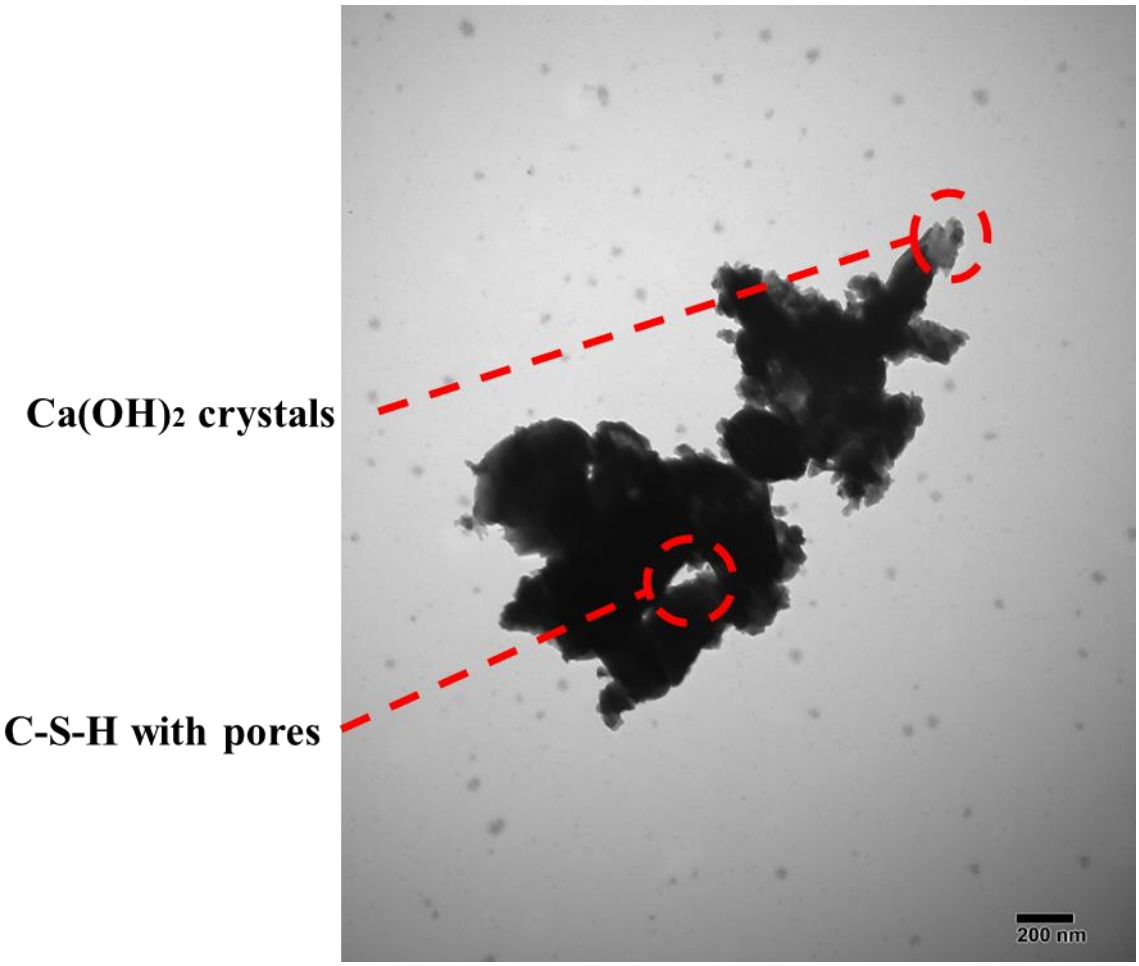

Figure 6.24 TEM images of plain cementitious pastes

Figure 6.25 shows the 0.3-wt% raw SNS added cementitious composites TEM microstructure at 28 days, where the SNS combined with the matrix significantly improved the C-S-H gel and the hydrated product of $Ca(OH)_2$ crystals. The C-S-H formed a semi-embedded structure with filled pores, resulting in a better and denser microstructure. Figure 6.26 shows the TEM microstructure morphology of the 0.3-wt% soni SNS cementitious pastes at 28 days. It can be noted that the soni SNS-cementitious accumulation of hydration products appear more laminated than the raw SNS, and it is not as compact as the raw SNS-cementitious composites. Compared to Figure 6.25, the microstructure of the soni SNS cement pastes has a more homogeneous distribution of $Ca(OH)_2$ crystal content, in small clumps embedded on the surface of the C-S-H gel.

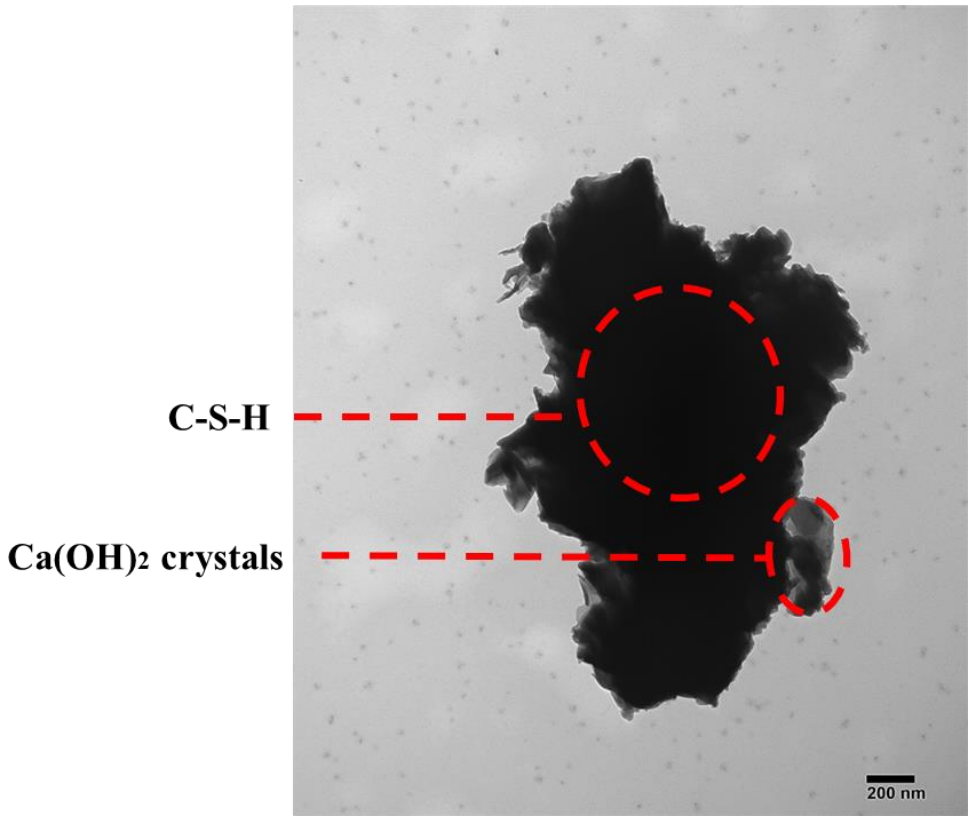

Figure 6.25 TEM images of 0.3-wt% raw SNS-cementitious pastes

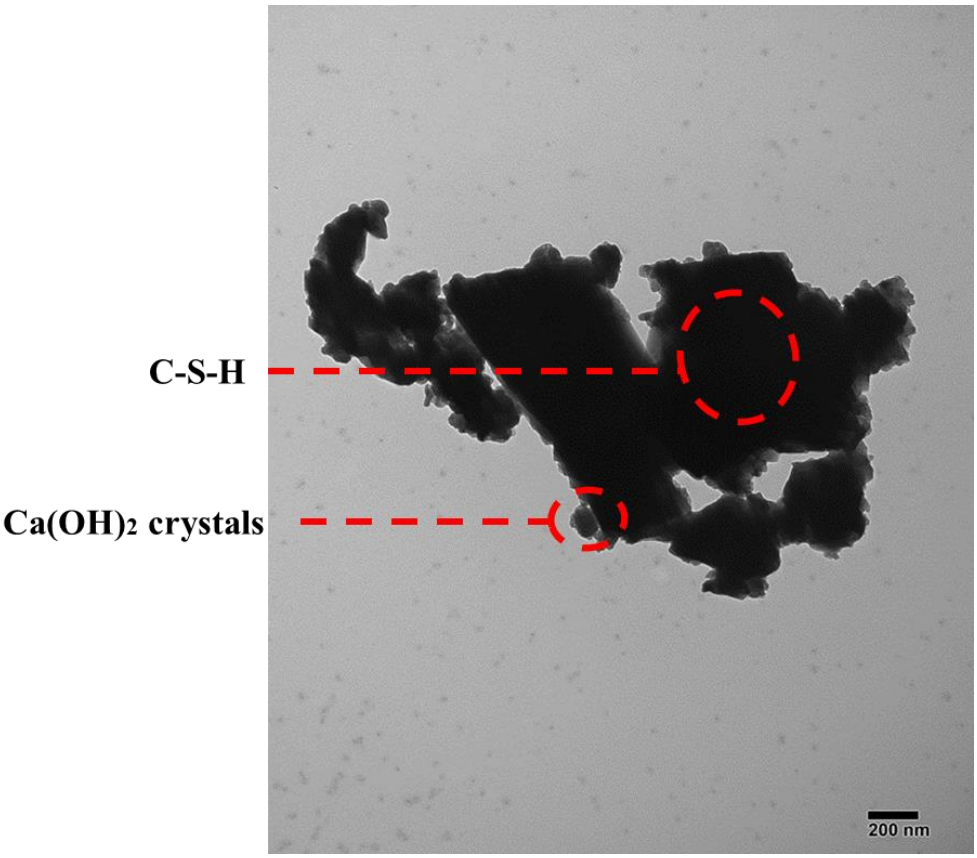

Figure 6.26 TEM images of 0.3-wt% soni SNS-cementitious pastes

The TEM image from Figure 6.24 to Figure 6.26 shows that the C-S-H gel and calcium hydroxide were observed in all the cementitious composites. Both raw and soni SNS addition made the microstructure of plain cement hydration products denser. In the later stage of the hydration, the SNS were hardly visible in SEM and TEM images. This is because most of the materials are dissolved or embedded in the matrix during the interaction with the C-S-H gel and calcium hydroxide.

Figure 6.27 shows the TEM morphology of the SNS-cementitious composites at 7 days. The SNS on the surface of the C-S-H gel helps the extension of the cement matrix. With the progress of hydration, SNSs work as bridges to develop the hydration products and fill the pores. The bridging effect appears when the highly transparent SNS are adsorbed on the C-S-H gel surface. The interfacial adhesion of the SNS reduces the microcracks and macropores in the cementitious composites and improves the mechanical properties. The TEM results validated the inferences of the SEM, EDS, XRD and BET results. These results explained the SNS having excellent correlations to the C-S-H and CH content and to promoting the hydration.

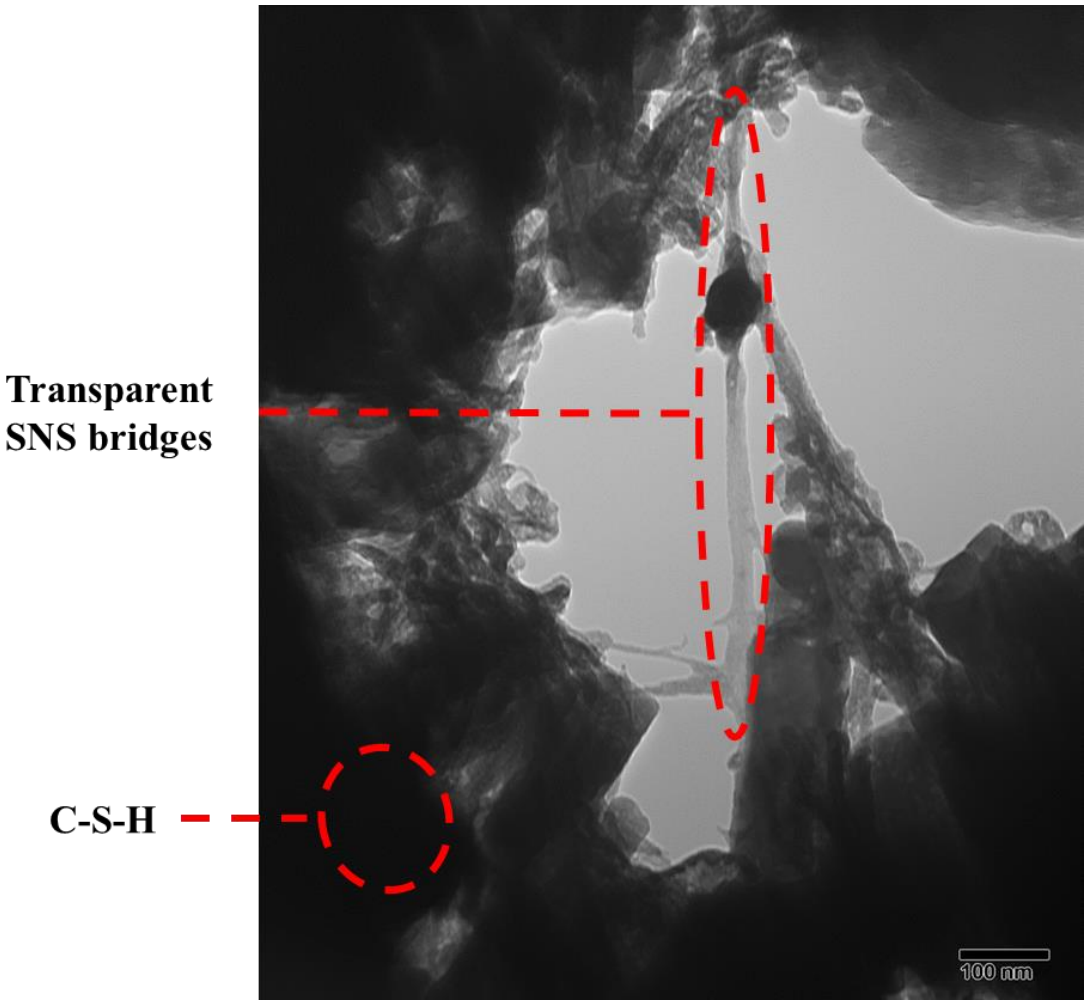

Figure 6.27 TEM images of the SNS bridge cementitious composite phase

6.4 SNS-cementitious composites bonding and reinforcing mechanism

The influence on the cement matrix macroscopic scale mechanical strength corresponds to the microstructural changes. The microscopic characterisation verified the SNS strengthening mechanism on the internal structure of the cement matrix composites.

Firstly, the SNS strengthened cementitious matrix mechanism is the new structure combination of the hydration products (SNS/C-S-H and SNS/$Ca(OH)_2$). Based on the characterisation of SNS in chapter 3, the SNS contain oxygenated functional groups with H bonds. The Ca-O in the cement particles interface interacts with the H-bond of SNS during the hydration process. Under the highly alkaline environment of the cementitious mix (pH=11.7) rich in Ca^{2+} ions, the acidic hydroxyl (-OH) and hydroxymethyl (-CH2-OH) functional groups on the surface of SNS attached to the matrix interface, were mitigated or partially dissolved. The SNS dissolution has promoted the reaction of the surface calcium atoms and oxygen atoms. As the interfacial Ca-O coordination number increases, the covalent bonding between the SNSs and C-S-H gels. The C-S-H/SNS hybrid structure's stress transfer and interfacial performance is improved. These phenomena are similar to the chemical reaction between GO and the hydrated phase C-S-H. The GO hydrophilic functional groups are effectively adsorbed on the surface of cement particles under the water reaction.

Secondly, SNS serve as the intermolecular reinforcement and microstructure filling for internal defects. The raw and soni SNS both contribute to the defect filling and packing effect of the cement matrix. During the hydration process, the hydration products are deposited on the SNS surface and the SNS grows into the nucleus aggregation. The a-

SNS located at the interlayer of the C-S-H and CH structures act as the 'centre', the functional groups of SNS are distributed in the cement matrix as a root network.

Furthermore, the SNS with significant large surface energy are linked to the adjacent calcium silicate layer to fill the internal defects emerged during the curing. The SNS are distributed in the transition region of the cement pastes hydration as the ‘secondary centres’ and the a-SNS attracts the water molecules from the surface to the interior of the cementitious particles. The water migration to the SNS retained more water molecules in the layered structure. As the surrounding hydration area was tightly combined with cement particles, it further enhanced the hydrodynamic force at the silicate nano-channels and improved the cohesion of the C-S-H gel.

Considering the homogeneous dispersion of SNS in the cement matrix, the synergy of these two reinforcement mechanisms enhances the performance of the matrix to withstand the structural deformations and damages. These mechanism results reveal the SNS enhanced the nanoscale mechanical properties, and resulted in the structural and interfacial properties stability.

6.5 Conclusion

This chapter investigates the evolution of SNS-cementitious materials on the microscopic level, the composition and microstructure characterised by centrifugation, XRD, SEM, EDS, BET and TEM methods. The results elucidate the mechanism of SNS-cementitious composites intermolecular bonding, and the SNS internal defect filling effect. The main conclusions are as follows:

The SNS-cementitious centrifuge experiment results show that SNS additions in the range of 0 to 0.5-wt%, consistently exhibit a great level of adsorption and compatibility. The SNS adsorption properties were slightly decreased after the ultrasonic treatment as

the sonication reduced the agglomeration of SNS on the cement surface. However, under any design condition, the SNS adsorption rate of the cement matrix remains above 91.8%. The SEM and TEM experiment results show that SNSs are well distributed in the cement hydration products. The integration between a-SNS and the cementitious surface can transfer more water molecules during the hydration process, densifying the C-S-H microstructure and generating more hydration products. As the concentration of SNS increases, the crystal morphology and interfacial properties of the hydrated product are improved. SNS optimises and bonds the hydration products, strengthening the microstructure by filling and bridging the microcracks in the matrix. The defect size of the structure decreases with increasing the quantity of SNS, thereby achieving an efficient load transfer.

The EDS results confirmed that the SNS contribute to a more uniform distribution of the hydration products. Compared to the control group, the oxygen spectrum shows that in the SNS specimens, the concentration of the hydration products is denser and partly concentrated in the interface area. The XRD results indicate that while the SNSs do not change the type of the cementitious composites hydration phases, the SNS addition affected the phase peak intensity. Incorporating SNS amplified the production of $Ca(OH)_2$, which is consistent with the previous TGA experimental analysis. Since the total amount of Ca in the hydration products is constant, and SNS sheets do not change the type of hydration products in the cementitious composites. In cementitious composites, a higher generation of $Ca(OH)_2$ hydration products leads to lower Ca/Si ratios in the C-S-H gels. Nitrogen adsorption-desorption isotherm curves and BET analysis indicate that SNS enhanced the specific surface area of the cement matrix. The SNS optimised and modified the matrix pore size distribution which is beneficial to the ion exchange. The change of the mesoporous distribution can be attributed to the

increase of C-S-H gel content, making the matrix form a more stable and denser cross-growth of C-S-H and SNS.

The series of characterisation experiments showed that incorporating SNS modified the cement hydration products' microstructure, the level of the hydration products' DOH, and filled and enhanced the C-S-H gels and calcium hydroxide. When comparing the cement pastes' microstructure to its macro-mechanical properties, the mechanical properties of the cement pastes continually improve with the SNS additions. The overall cementitious composites hydration reinforcement comparison is soni SNS > raw SNS > no addition.

Chapter 7 Conclusion and recommendations

7.1 Introduction

Driven by the need to curb the construction industry CO_2 emissions, the new approaches to improve the efficiency and reduce the carbon footprint of infrastructure materials have been developed using expensive and incompatible exotic nanomaterials. Because of this, their applications in the construction industry have been limited.

This PhD thesis investigates a new generation of low carbon footprint cementitious composites using 2D bio nanomaterials derived from the sugar industry waste. The 2D bio nanomaterial (SNS) improves the hydration of cement and at the same time strengthens the hydration products.

The incorporation of SNSs increases the mechanical properties of cementitious materials due to their combined strengthening and hydration effects. Thus, less OPC is needed to carry out the same function. As a result, this will create more sustainable construction materials as the carbon footprint associated with their manufacture will be lower. A comprehensive experimental programme was carried out to examine the behaviour of the cementitious composites incorporating SNSs. To understand their hydration mechanisms and determine their optimum processing-microstructure-mechanical properties relationships, the SEM, FTIR, XRD, TEM, TGA, DSC, BET, EIS, CV and mechanical testing studies have been carried out.

This chapter summarises the conclusions, the theoretical and practical implications of this study and makes recommendations for future research given the experiment limitations.

7.2 Conclusion

This research contributed to the development of new sustainable high-performance construction materials using a renewable and environmental 2D nanomaterial. The concluding statements for this study can be summarised as follows.

Chapter 2 reviews different one and two-dimensional nanomaterials and nanocelluloses reinforced cement matrix. This contains CNTs, NS, G, GO, CNC and CNF. The CNTs, G and GO dramatically improve the mechanical performance of the composites due to the nano bridging and the chemical bonding between the nano-cracks. These nanomaterials display the nano pull-out function, providing denser cementitious composites nanostructures, especially while the cementitious composites were cracking. Furthermore, the NS promote the pozzolanic reaction and increase the compressive strength of the cementitious composites. The NCs short circuit diffusion accelerates the water transportation into the cement cores to promote the cementitious composites DOH.

In the last two decades, researching the nanomaterials modified cementitious composites has made considerable progress. However, the large-scale nanoparticles utilised in the construction materials still face application difficulties caused by the dispersion and high cost. Compared to the traditional nanomaterials, cellulose fibre-based nanomaterials are relatively cheap (SNS paste cost £5/kg), and their hydroxyl properties can effectively reduce the nanomaterials agglomeration within the cementitious materials suitable for large scale construction. However, the existing research lacks a comprehensive investigation on how the 2D SNS reinforces the cementitious composites. This research bridges this gap by focusing on the sustainable infrastructure materials with a low carbon footprint. The well-dispersed SNS can

promote the fibres bridging effect and accelerate the cement degree of hydration, thus improving the mechanical and fracture properties.

To characterise the SNSs materials and to understand its properties, chemical composition, and morphology. Chapter 3 describes the SNS preparation and characterisation. Compared to the other 2D cementitious composites additive materials (e.g. graphene), SNS is a renewable sugar beetroot waste produced by the industry, and has advantages in terms of cost, safety risk, renewability and carbon neutrality. The material was manufactured into nanoplatelets with 50 μm widths and length, and 250 *nm* in thickness. SEM and TEM further indicates that the SNS were wrinkle and stack intertwined clusters in nature, due to their high aspect ratios and Van der Waals forces. The XRD pattern shows that there are crystalline and amorphous regions in the SNS, the SNS *CI* of 75.65% indicates that the fibre has great molecular chain arrangement and mechanical properties. The SNS filling in the microcracks and pores within the cementitious mixes enhances the mechanical properties of the cementitious composites.

TGA and DSC results showed that SNS have excellent thermal stability up to 100℃ and heat endurance from 100 to 300℃, which conforms to the temperature range of cementitious materials utilised in the environment. The significant thermal stability allows the SNS to participate in the interaction during the hydration process. The nitrogen adsorption and desorption results (BET) show that SNS materials have the advantages of high SSA, concentrated pore size, fast adsorption and desorption rates. SNS have many nano-sized pores (0~10 nm), which the cementitious additives can use to promote ion exchange and accelerate the hydration process.

The SNS FTIR spectrum comprises of two main types of absorptions, hydroxyl groups (OH) and the C-H stretching vibration. The existence of hydroxyl groups indicates that

SNS have a hydrophilic nature. Furthermore, the sonicated dispersion SNS aqueous suspensions were prepared and characterised, and the sonication dispersion time effect of SNS solution agglomerate behaviour and stability was studied. The UV-Vis result shows that SNS aqueous solutions pre-treated with the surfactant, have great water dispersion properties, homogeneous distribution, and stability, and after ultrasonication (30 minutes) were non-agglomerated for a prolonged storage.

To investigate the effect of SNS on the hydration behaviour of the cementitious composites, EIS, CV and the equivalent circuit being used to elucidate the interaction mechanism between SNS and cement particles. Chapter 4 discusses the SNS reinforced cementitious composites DOH mechanism. To evaluate the rheology of the interaction between SNS and cement particles, Marsh cone and mini-slump tests reveal that 2D SNS are evenly dispersed within the cementitious environment. During the hydration, SNS provide spatial steric support that can steadily disperse the cement particles' interfacial adhesion.

The CV curve shows the cementitious composites current and voltage curve area, which can effectively be improved by the increase of SNS addition. The CV area (related to the capacitance) increase can be attributed to the partially unattached SNS decomposition under the alkaline environment. The SNS decomposition generates some organic chemical compounds and contributes to a series of proton exchanges and a high diffusion rate of C3S. The chemical compounds break down the water film effect on the SNS/C3S interface, and elevated OH^- concentration to promote the Ca^{2+} reaction. The Nyquist plot shows SNS additive decreases the impedance of the cementitious composites. Changes in the equivalent circuit (EC) $R_s(R_eC_e)(R_{ct}(C_{dl}W))$ characteristic parameters reveal the evolutionary mechanism of SNS-reinforced cement composites. The increase of the pore solution resistance (R_s)

implies an intensified DOH and denser microstructure of the cementitious composite. The decrease in the charge transfer resistance (R_{ct}) is because a-SNS is attached to the cement matrix pores combining with the capillary water, which formed more efficient conductive paths and f-SNS dissolution, promoting the ionic concentration. Furthermore, the CV, EIS and EC techniques are easily used as Non-destructive testing (NDT) and to monitor the hydration process of the cementitious matrix structure.

The TGA reveal the additional SNS are effective in enhancing the cementitious composites DOH. The DOH increases with the increase of SNS concentration at the same age. During mixing, appropriate concentrations of SNS amplify the hydration of cement particles' dispersion and promote the reaction (e.g. 0.3-wt% of SNS at 28 days promotes the cementitious DOH from 72% to 78%). The DTG shows that both SNS and plain cementitious composites decomposition peak exists in the same temperature range. The thermal peaks at specific temperature bands confirmed that increased amounts of SNS are correlated with increasing the content of hydration products, and without altering the types of the hydration phases. Short-circuit diffusion (SCD) is the dominant mechanism that can contribute to the improvement of DOH. The newly generated integrated crystal structures SNS with C-S-H and calcium hydroxide provide greater hydration reaction sites to accelerate the cementitious hydration. The new nanocomposite interconnected layer acts as a water reservoir, the surface of the hydration product diffuses water molecules along with the SNS network. The SNS network integration with the hydration product continuously transports water into the unhydrated cement core, thus driving more C-S-H formation.

To investigate the effect of SNS on the mechanical properties of the cementitious materials and establish the SNS strength mechanism (fibre crack bridge), the effect of different variables such as water to cement ratios, curing ages and SNS concentrations

on the compressive, flexural strength, fracture energy, fracture toughness and splitting tensile strength is studied. Chapter 5 aims to explore the SNS cementitious composites' mechanical properties. No matter whether the ultrasonic disperse treatment is applied, both the raw and soni SNS suspensions significantly enhance the mechanical properties of cementitious materials. The SNS optimum concentrations were 0.2-wt%, the compressive strength of the raw and soni SNS cementitious matrix compared to the plain specimen was increased by 8.33 and 12.15%, the flexural strength increased by 28.73 and 39.91%, the splitting strength increased by 31.25 and 36.87%, the fracture energy increased by 38.69 and 69.01%, and the fracture toughness increased by 17.41 and 41.66% at ages of 28, respectively. It is indicated that the SNS/C-S-H cementitious composites significantly improve the strength and load transfer because SNS fills the internal microcracks and optimises the crack bridging transition zone. The SNS enhances the transition zone cohesion on the interface and their fibrous dominant microstructural transfer, inhibiting the deflection effects and development of cracks.

The SNS addition content determines its effect on the mechanical strength of the matrix. The SNS concentration going above the critical concentration (0.2-wt%) can easily trigger agglomeration. The agglomeration of SNS in the cementitious matrix leads to stress concentrations and affects the denseness matrix, which might cause defects and reduction in the macroscopic mechanical properties. The 0.35 and 0.40 water to cement ratios do not affect the optimal addition percentage of SNSs. However, the improvement of w/c ratio increases the water molecules to synergise the hydration, and promote the DOH while reducing the agglomeration. Sonication dispersion modifies the SNS suspension distribution into the cementitious composites and reduces the stress concentrations, which results in better macroscopic mechanical properties. The

mechanical strength of the ultrasonically treated SNS samples improves by 10% compared to the raw SNS samples on average.

The microstructural properties of SNS incorporated cementitious materials is studied, and the effects of the SNS dispersion and its content on the microstructure of cementitious materials is analysed. The mechanism of SNS micro-modification cementitious materials is reveal. Chapter 6 characterises the SNS cementitious composites' microstructure. The centrifugation experiment shows that incorporating SNS in the fresh cementitious pastes surface has excellent adsorption results and compatibility. The SNS adsorption properties slightly decrease after the ultrasound dispersion. The ultrasonic dispersion reduces the agglomeration of SNS attached to the cement particles' surfaces. Under all the circumstances, SNS adsorption rate on the cementitious was consistently over 91.8%.

The XRD analysis revealed that the cementitious composites hydration product types do not change with the SNS addition. The incorporation of SNS promotes the ettringite and $Ca(OH)_2$ crystals generation and decreases the unhydrated phase of tricalcium silicate and calcium carbonate. Nitrogen adsorption-desorption isotherm curves and BET analysis showed that SNS modified the cement matrix pore size distribution. The C-S-H gels pore size distribution within the matrix improved significantly with the modified SNS, and the increases in SNS specific surface area facilitated the samples ionic exchange.

SEM showed that the SNS were well dispersed in the cement matrix. During the hydration, the SNS sheets build crack bridging where cracks occurred and showed stress transfer effect. SNS significantly improves and densifies the internal stability of the cement matrix. Through the SEM and TEM the crystalline morphology and the

interfacial properties were further investigated showing that the hydrated products are denser as the SNS concentration increases. The incorporation of SNS actively fills and repairs the C-S-H microstructural defects, facilitates the water molecules transferring into the adjacent calcium silicate layer, and generates denser C-S-H hydration products compared to the plain cement pastes. To track the distribution of SNS on the cement hardened matrix, the EDS results show SNS contributes to a more uniformly distributed hydration products. The distribution of oxygen spectrum concentration has a significant increase on the interface region of the SNS hydration products.

7.3 Research limitations and future directions

This experimental PhD research is based on experimental laboratory results showing that the industry waste 2D SNS effectively improves the cementitious composites DOH, macro-mechanical properties and microstructure. Due to some limitations in the experiments, this section provides a list of recommendations for future research.

7.3.1 Molecular dynamic modelling intermolecular interactions between SNS and cement particles

Molecular-scale modelling studies could be carried out on SNS and the cement particles to examine the molecular dynamic interaction mechanism between the SNS and cementitious mix. The experiments showed that SNS have a significant enhancing effect, the relevant simulation could consolidate the understanding of the hydration process and the interactions between the SNS and C-S-H.

7.3.2 The durability of SNS cement paste, mortar and concrete

Another intriguing research area lies in examining the durability performance of SNS cement paste, mortar and concrete working in harsh and severe environments. For example, in freeze-thaw environments, chloride penetration (seawater erosion) and

corrosion (acid or alkaline) stabilisation experiments could be carried out in different pH conditions.

7.3.3 Nanomechanical behaviour of SNS reinforced cement pastes

Research could be conducted on the SNS hardened pastes' nanomechanical behaviour by employing the nanoindentation mechanics technique. In particular, the link between the microscopic mechanical properties of SNS/C-S-H and SNS/$Ca(OH)_2$ could be established statistically, thus enhancing the importance of examining the relationship between nano pressure test sites and their chemical compositions.

7.3.4 Orientation and distribution of SNS in cement pastes

Since the distribution and orientation of SNS in the cementitious matrix can significantly influence the cementitious composites' tensile strength errors, they have an impact on the result when fibres agglomerate and arrange perpendicularly to the force direction. Future research could control the optimal SNS dispersion and stability improvement, by further quantitative characterisation and computational methods.

7.3.5 Investigation of SNS mortars and concrete

The mechanical and microscopic behaviour of SNS mortar and concrete could be investigated. The extensively investigated SNS in cementitious composites cannot predict how SNS will behave in cement mortar and concrete. Further experiments are necessary to validate and promote the application in practice.

7.3.6 The amount of cement could be reduced

Further research could be undertaken to develop the relationship between SNS and cement usage, providing an insight into the cost of construction. The relationship between SNS reinforced cement mixes and cost effectiveness could be explored via

quantitative and statistical investigations which could provide further information in support of potential widespread industrial use.

Reference

Abderrahim, B. *et al.* (2015) ‘Kinetic thermal degradation of cellulose, polybutylene succinate and a green composite: comparative study’, *World J. Environ. Eng*, 3, pp. 95–110.

Abitbol, T. *et al.* (2016) ‘Nanocellulose, a tiny fiber with huge applications’, *Current opinion in biotechnology*. Elsevier, 39, pp. 76–88.

Abjameh, R., Moradi, O. and Amani, J. (2014) ‘The study of synthesis and functionalized single-walled carbon nanotubes with amide group’, *International Nano Letters*. Springer, 4(2), p. 97.

Abu Al-Rub, R. K., Ashour, A. I. and Tyson, B. M. (2012) ‘On the aspect ratio effect of multi-walled carbon nanotube reinforcements on the mechanical properties of cementitious nanocomposites’, *Construction and Building Materials*. Elsevier Ltd, 35, pp. 647–655. doi: 10.1016/j.conbuildmat.2012.04.086.

Afridi, M. U. K. *et al.* (1989) ‘Behaviour of Ca (OH) 2 in polymer modified mortars’, *International Journal of Cement Composites and Lightweight Concrete*. Elsevier, 11(4), pp. 235–244.

Aïtcin, P.-C. (2000) ‘Cements of yesterday and today: concrete of tomorrow’, *Cement and Concrete research*. Elsevier, 30(9), pp. 1349–1359.

Ajayan, P. M. (1999) ‘Nanotubes from Carbon’, *Chemical Reviews*, 99(7), pp. 1787–1799. doi: 10.1021/cr970102g.

Alemdar, A. and Sain, M. (2008) ‘Isolation and characterization of nanofibers from agricultural residues–Wheat straw and soy hulls’, *Bioresource technology*. Elsevier, 99(6), pp. 1664–1671.

Alkaya, E. and Demirer, G. N. (2011) ‘Anaerobic mesophilic co-digestion of sugar-beet processing wastewater and beet-pulp in batch reactors’, *Renewable Energy*. Elsevier, 36(3), pp. 971–975.

Allen, A. J., Thomas, J. J. and Jennings, H. M. (2007) ‘Composition and density of nanoscale calcium–silicate–hydrate in cement’, *Nature materials*. Nature Publishing Group, 6(4), pp. 311–316.

Alshaghel, A. *et al.* (2018) ‘Effect of multiscale reinforcement on the mechanical properties and microstructure of microcrystalline cellulose-carbon nanotube reinforced cementitious composites’, *Composites Part B: Engineering*. Elsevier, 149, pp. 122–134.

Anju, T. R., Ramamurthy, K. and Dhamodharan, R. (2016) ‘Surface modified microcrystalline cellulose from cotton as a potential mineral admixture in cement mortar composite’, *Cement and Concrete Composites*. Elsevier, 74, pp. 147–153.

Ardanuy, M., Claramunt, J. and Toledo Filho, R. D. (2015) ‘Cellulosic fiber reinforced cement-based composites: A review of recent research’, *Construction and building materials*. Elsevier, 79, pp. 115–128.

Arya, A. and Sharma, A. L. (2018) ‘Structural, electrical properties and dielectric relaxations in Na+-ion-conducting solid polymer electrolyte’, *Journal of Physics: Condensed Matter*. IOP Publishing, 30(16), p. 165402.

ASTM, A. (2013) ‘Standard test method for compressive strength of hydraulic cement mortars (using 2-in. or [50-mm] cube specimens)’, *Annual Book of ASTM StandardsAnnual Book of ASTM Standards*, 4(1), pp. 1–9.

ASTM, C. (2010) ‘Standard test method for flexural strength of concrete (using simple

beam with third-point loading)', in *American Society for Testing and Materials*, pp. 12959–19428.

ASTM, C. (2014) 'Standard practice for mechanical mixing of hydraulic cement pastes and mortars of plastic consistency', *ASTM West Conshohocken, PA*.

Awan, M. M. S. *et al.* (2017) 'High-performance cementitious matrix using carbon nanofibers', *Indonesian Journal of Science and Technology*, 2(1), pp. 57–75.

Balandin, A. A. *et al.* (2008) 'Superior thermal conductivity of single-layer graphene', *Nano letters*. ACS Publications, 8(3), pp. 902–907.

Balasubramaniam, B., Mondal, K., Ramasamy, K., Palani, Gadyam S, *et al.* (2017) 'Hydration phenomena of functionalized carbon nanotubes (CNT)/cement composites', *Fibers*. Multidisciplinary Digital Publishing Institute, 5(4), p. 39.

Balasubramaniam, B., Mondal, K., Ramasamy, K., Palani, Gadyam S., *et al.* (2017) 'Hydration phenomena of functionalized carbon nanotubes (CNT)/cement composites', *Fibers*, 5(4), pp. 1–13. doi: 10.3390/fib5040039.

Baldwin, C. J. (2011) *Sustainability in the food industry*. John Wiley & Sons.

Balea, A., Blanco, A. and Negro, C. (2019) 'Nanocelluloses: natural-based materials for fiber-reinforced cement composites. A critical review', *Polymers*. Multidisciplinary Digital Publishing Institute, 11(3), p. 518.

Baomin, W. and Shuang, D. (2019) 'Effect and mechanism of graphene nanoplatelets on hydration reaction, mechanical properties and microstructure of cement composites', *Construction and Building Materials*. Elsevier, 228, p. 116720.

Barrett, E. P., Joyner, L. G. and Halenda, P. P. (1951) 'The Determination of Pore Volume and Area Distributions in Porous Substances. I. Computations from Nitrogen

Isotherms', *Journal of the American Chemical Society*, 73(1), pp. 373–380. doi: 10.1021/ja01145a126.

Belli, A. *et al.* (2020) 'Commercial and recycled carbon/steel fibers for fiber-reinforced cement mortars with high electrical conductivity', *Cement and Concrete Composites*. Elsevier, 109, p. 103569.

Bencardino, F. *et al.* (2010) 'Experimental evaluation of fiber reinforced concrete fracture properties', *Composites Part B: Engineering*. Elsevier, 41(1), pp. 17–24.

Benhelal, E. *et al.* (2013) 'Global strategies and potentials to curb CO2 emissions in cement industry', *Journal of Cleaner Production*. Elsevier Ltd, 51, pp. 142–161. doi: 10.1016/j.jclepro.2012.10.049.

Bentur, A. and Mindess, S. (2006) *Fibre reinforced cementitious composites*. Crc Press.

Bentur, A. and Mindess, S. (2007) 'Fibre Reinforced Cementitious Composites', *Civil Engineering*, p. 625.

Bolotin, K. I. *et al.* (2008) 'Ultrahigh electron mobility in suspended graphene', *Solid state communications*. Elsevier, 146(9–10), pp. 351–355.

Brinchi, L. *et al.* (2013) 'Production of nanocrystalline cellulose from lignocellulosic biomass: technology and applications', *Carbohydrate polymers*. Elsevier, 94(1), pp. 154–169.

Brunauer, S., Emmett, Paul Hugh and Teller, E. (1938) 'Adsorption of gases in multimolecular layers', *Journal of the American chemical society*. ACS Publications, 60(2), pp. 309–319.

Brunauer, S., Emmett, P. H. and Teller, E. (1938) 'Adsorption of Gases in Multimolecular Layers', *Journal of the American Chemical Society*, 60(2), pp. 309–

319. doi: 10.1021/ja01269a023.

Bs Iso 9277 (2010) ‘BSI Standards Publication Determination of the specific surface area of solids by gas adsorption — BET method’.

Bullard, J. W. *et al.* (2011) ‘Mechanisms of cement hydration’, *Cement and concrete research*. Elsevier, 41(12), pp. 1208–1223.

Buzea, C., Pacheco, I. I. and Robbie, K. (2007) ‘Nanomaterials and nanoparticles: sources and toxicity’, *Biointerphases*. American Vacuum Society, 2(4), pp. MR17–MR71.

Cao, Y. *et al.* (2015) ‘The influence of cellulose nanocrystal additions on the performance of cement paste’, *Cement and Concrete Composites*. Elsevier, 56, pp. 73–83.

Cao, Y., Tian, N., *et al.* (2016) ‘The influence of cellulose nanocrystals on the microstructure of cement paste’, *Cement and Concrete Composites*. Elsevier, 74, pp. 164–173.

Cao, Y., Zavattieri, P., *et al.* (2016) ‘The relationship between cellulose nanocrystal dispersion and strength’, *Construction and Building Materials*. Elsevier, 119, pp. 71–79.

Cárdenas-Fernández, M. *et al.* (2017) ‘An integrated biorefinery concept for conversion of sugar beet pulp into value-added chemicals and pharmaceutical intermediates’, *Faraday Discussions*. The Royal Society of Chemistry, 202, pp. 415–431.

CelluComp Ltd (2020) *Revolutionary Technology: Vegetables used for high-performance materials*. Available at: https://www.cellucomp.com/products/curran

(Accessed: 8 July 2020).

Chaipanich, A. *et al.* (2010) 'Compressive strength and microstructure of carbon nanotubes-fly ash cement composites', *Materials Science and Engineering A*, 527(4–5), pp. 1063–1067. doi: 10.1016/j.msea.2009.09.039.

Chen, W. *et al.* (2018) 'Thermo-responsive cellulose-based material with switchable wettability for controllable oil/water separation', *Polymers*. Multidisciplinary Digital Publishing Institute, 10(6), p. 592.

Chen, Z. *et al.* (2018) 'Mechanical behavior of multilayer GO carbon-fiber cement composites', *Construction and Building Materials*. Elsevier, 159, pp. 205–212.

Chi, Y. *et al.* (2020) 'Carrot-based covalently bonded saccharides as a new 2D material for healing defective calcium-silicate-hydrate in cement: Integrating atomistic computational simulation with experimental studies', *Composites Part B: Engineering*. Elsevier, 199, p. 108235.

Chirayil, C. J., Mathew, L. and Thomas, S. (2014) 'REVIEW OF RECENT RESEARCH IN NANO CELLULOSE PREPARATION FROM DIFFERENT LIGNOCELLULOSIC FIBERS.', *Reviews on advanced materials science*, 37.

Chung, D. D. L. (2010) *Functional Materials: Electrical, Dielectric, Electromagnetic, Optical and Magnetic Applications:(with Companion Solution Manual)*. World scientific.

Ciolacu, D., Ciolacu, F. and Popa, V. I. (2011) 'Amorphous cellulose - Structure and characterization', *Cellulose Chemistry and Technology*, 45(1–2), pp. 13–21.

Cohen, J. (1983) 'The cost of dichotomization', *Applied psychological measurement*. Sage Publications Sage CA: Thousand Oaks, CA, 7(3), pp. 249–253.

Collepardi, M. *et al.* (1978) ‘Tricalcium aluminate hydration in the presence of lime, gypsum or sodium sulfate’, *Cement and Concrete Research*. Elsevier, 8(5), pp. 571–580.

Collins, F., Lambert, J. and Duan, W. H. (2012) ‘The influences of admixtures on the dispersion, workability, and strength of carbon nanotube-OPC paste mixtures’, *Cement and Concrete Composites*. Elsevier Ltd, 34(2), pp. 201–207. doi: 10.1016/j.cemconcomp.2011.09.013.

Contreras, A. M. *et al.* (2009) ‘Comparative Life Cycle Assessment of four alternatives for using by-products of cane sugar production’, *Journal of Cleaner Production*, 17(8), pp. 772–779. doi: 10.1016/j.jclepro.2008.12.001.

da Costa Correia, V. *et al.* (2018) ‘Nanofibrillated cellulose and cellulosic pulp for reinforcement of the extruded cement based materials’, *Construction and Building Materials*. Elsevier, 160, pp. 376–384.

Crawford, R. L. (1981) *Lignin biodegradation and transformation.* John Wiley and Sons.

Dalmay, P. *et al.* (2010) ‘Properties of cellulosic fibre reinforced plaster: influence of hemp or flax fibres on the properties of set gypsum’, *Journal of materials science*. Springer, 45(3), pp. 793–803.

Dassios, K. G. *et al.* (2015) ‘Optimization of sonication parameters for homogeneous surfactant assisted dispersion of multiwalled carbon nanotubes in aqueous solutions’, *Journal of Physical Chemistry C*, 119(13), pp. 7506–7516. doi: 10.1021/acs.jpcc.5b01349.

Deng, S. and Berry, V. (2016) ‘Wrinkled, rippled and crumpled graphene: an overview

of formation mechanism, electronic properties, and applications', *Materials Today*. Elsevier, 19(4), pp. 197–212.

Du, H. and Dai Pang, S. (2018) 'Dispersion and stability of graphene nanoplatelet in water and its influence on cement composites', *Construction and Building Materials*. Elsevier, 167, pp. 403–413.

Dubey, R. and Kumar, P. (2013) 'Effect of Fly Ash on Water/Powder Ratio and Superplasticizer Dosage in Self-Compacting Mortars', *International Journal of Architecture, Engineering and Construction*. International Association for Sustainable Development and Management, pp. 55–62. doi: 10.7492/ijaec.2013.006.

Eatemadi, A. *et al.* (2014) 'Carbon nanotubes: properties, synthesis, purification, and medical applications', *Nanoscale research letters*. SpringerOpen, 9(1), pp. 1–13.

Emran, K. M. and Hanaa, A. R. (2017) 'Electrochemical and surface investigation of Ni-Cr glassy alloys in nitric acid solution', *Int. J. Electrochem. Sci*, 12, pp. 6404–6416.

EN, B. S. (2002) '1008 (2002)', *Mixing water for concrete-Specification for sampling, testing and assessing the suitability of water, including water recovered from processes in the concrete industry, as mixing water for concrete*, 389.

EN, B. S. (2005) '196-1.(2005)', *Methods of testing cement-Part*, 1.

EN, B. S. (2011) '197-1: 2011 Cement', *Composition, specifications and conformity criteria for common cements*.

EN, B. S. 12390-2-2009 (2009) 'Testing hardened concrete–Part 6: tensile splitting strength of test specimens', *London: British Standard Institution*.

European Commission (2019) *Agriculture and rural development – sugar*. Available at: https://ec.europa.eu/info/food-farming-fisheries/plants-and-plant-products/plant-

products/sugar_en.

Fan, Z. *et al.* (2006) 'Preparation and characterization of manganese oxide/CNT composites as supercapacitive materials', *Diamond and related materials*. Elsevier, 15(9), pp. 1478–1483.

FAO (2018) *Food and Agricultural Organization, FAOSTAT*. Available at: http://www.fao.org/faostat/en/#home (Accessed: 19 December 2020).

Feng, J. *et al.* (2014) 'Mechanical analyses of hooked fiber pullout performance in ultra-high-performance concrete', *Construction and Building Materials*. Elsevier, 69, pp. 403–410.

Fu, T. *et al.* (2017) 'The influence of cellulose nanocrystals on the hydration and flexural strength of Portland cement pastes', *Polymers*. Multidisciplinary Digital Publishing Institute, 9(9), p. 424.

Fukuhara, M. *et al.* (1981) 'Mechanisms and kinetics of C4AF hydration with gypsum', *Cement and Concrete Research*. Elsevier, 11(3), pp. 407–414.

Ghahari, S. *et al.* (2020) 'Fracture properties evaluation of cellulose nanocrystals cement paste', *Materials*. Multidisciplinary Digital Publishing Institute, 13(11), p. 2507.

Giustozzi, F. (2016) 'Polymer-modified pervious concrete for durable and sustainable transportation infrastructures', *Construction and Building Materials*. Elsevier Ltd, 111, pp. 502–512. doi: 10.1016/j.conbuildmat.2016.02.136.

Gong, J. *et al.* (2017) 'Research on cellulose nanocrystals produced from cellulose sources with various polymorphs', *RSC Advances*. Royal Society of Chemistry, 7(53), pp. 33486–33493. doi: 10.1039/c7ra06222b.

Grinter, H. C. and Threlfall, T. L. (1992) ‘UV-Vis Spectroscopy and its applications’. Springer-Verlag Berlin Heidelberg. Germany.

Guerrero-Fajardo, C. A., Giraldo, L. and Moreno-Piraján, J. C. (2020) ‘Preparation and characterization of graphene oxide for Pb (II) and Zn (II) ions adsorption from aqueous solution: experimental, thermodynamic and kinetic study’, *Nanomaterials*. Multidisciplinary Digital Publishing Institute, 10(6), p. 1022.

Habibi, Y., Goffin, A. L., *et al.* (2008) ‘Bionanocomposites based on poly(ε-caprolactone)-grafted cellulose nanocrystals by ring-opening polymerization’, *Journal of Materials Chemistry*, 18(41), pp. 5002–5010. doi: 10.1039/b809212e.

Habibi, Y., Goffin, A.-L., *et al.* (2008) ‘Bionanocomposites based on poly (ε-caprolactone)-grafted cellulose nanocrystals by ring-opening polymerization’, *Journal of Materials Chemistry*. Royal Society of Chemistry, 18(41), pp. 5002–5010.

Han, B. *et al.* (2017) ‘Nano-core effect in nano-engineered cementitious composites’, *Composites Part A: Applied Science and Manufacturing*. Elsevier, 95, pp. 100–109.

Han, B. *et al.* (2019) *Nano-engineered cementitious composites: principles and practices*. Springer.

Harrington, R. F. (2003) *Introduction to electromagnetic engineering*. Courier Corporation.

Haruehansapong, S., Pulngern, T. and Chucheepsakul, S. (2014) ‘Effect of the particle size of nanosilica on the compressive strength and the optimum replacement content of cement mortar containing nano-SiO2’, *Construction and Building Materials*. Elsevier, 50, pp. 471–477.

Hasan, H. *et al.* (2019) ‘Novel engineered high performance sugar beetroot 2D

nanoplatelet-cementitious composites', *Construction and Building Materials*. Elsevier Ltd, 202, pp. 546–562. doi: 10.1016/j.conbuildmat.2019.01.019.

Hassan, A., Elkady, H. and Shaaban, I. G. (2019) 'Effect of adding carbon nanotubes on corrosion rates and steel-concrete bond', *Scientific reports*. Nature Publishing Group, 9(1), pp. 1–12.

Hepworth, D. and Whale, E. (2017) 'Cellulose platelet compositions, methods of preparing cellulose platelet compositions and products comprising same'. US Patents 9,834,664 B2.

Hisseine, O. A., Omran, A. F. and Tagnit-Hamou, A. (2018) 'Influence of cellulose filaments on cement paste and concrete', *Journal of materials in civil engineering*. American Society of Civil Engineers, 30(6), p. 4018109.

Horszczaruk, E., Łukowski, P. and Seul, C. (2020) 'Influence of Dispersing Method on the Quality of Nano-Admixtures Homogenization in Cement Matrix', *Materials*. Multidisciplinary Digital Publishing Institute, 13(21), p. 4865.

Hsu, W. K. *et al.* (2004) 'Circuit elements in carbon nanotube-polymer composites', *Carbon*. Elsevier, 42(8–9), pp. 1707–1712.

Hu, Y. *et al.* (2014) 'Fracture toughness enhancement of cement paste with multi-walled carbon nanotubes', *Construction and Building Materials*. Elsevier, 70, pp. 332–338.

Hughes, B. P. and Ash, J. E. (1970) 'Anisotropy and failure criteria for concrete', *Matériaux et Construction*. Springer, 3(6), pp. 371–374.

Iijima, S. (1991) 'Helical microtubules of graphitic carbon', *nature*. Nature Publishing Group, 354(6348), pp. 56–58.

Isfahani, F. T., Li, W. and Redaelli, E. (2016) ‘Dispersion of multi-walled carbon nanotubes and its effects on the properties of cement composites’, *Cement and Concrete Composites*. Elsevier, 74, pp. 154–163.

Ismail, I. *et al.* (2013) ‘Drying-induced changes in the structure of alkali-activated pastes’, *Journal of Materials Science*, 48(9), pp. 3566–3577. doi: 10.1007/s10853-013-7152-9.

Iwan, A. and Chuchmała, A. (2012) ‘Perspectives of applied graphene: Polymer solar cells’, *Progress in Polymer Science*. Elsevier, 37(12), pp. 1805–1828.

Jing, G. *et al.* (2017) ‘Effect of graphene nanoplatelets on hydration behaviour of Portland cement by thermal analysis’, *Advances in Cement Research*. Thomas Telford Ltd, 29(2), pp. 63–70.

Jo, B.-W. *et al.* (2007) ‘Characteristics of cement mortar with nano-SiO2 particles’, *Construction and building materials*. Elsevier, 21(6), pp. 1351–1355.

Jo, B. W. *et al.* (2007) ‘Characteristics of cement mortar with nano-SiO2 particles’, *Construction and Building Materials*, 21(6), pp. 1351–1355. doi: 10.1016/j.conbuildmat.2005.12.020.

Jonoobi, M. *et al.* (2015) ‘Different preparation methods and properties of nanostructured cellulose from various natural resources and residues: a review’, *Cellulose*. Springer, 22(2), pp. 935–969.

Juenger, M. C. G. and Jennings, H. M. (2001) ‘The use of nitrogen adsorption to assess the microstructure of cement paste’, *Cement and Concrete Research*. Elsevier, 31(6), pp. 883–892.

Kakooei, S. *et al.* (2012) ‘The corrosion investigation of rebar embedded in the fibers

reinforced concrete', *Construction and Building Materials*. Elsevier, 35, pp. 564–570.

Kang, X. *et al.* (2019) 'Effect of graphene oxide (GO) on hydration of tricalcium silicate (C 3 S)', *Construction and Building Materials*. Elsevier Ltd, 203, pp. 514–524. doi: 10.1016/j.conbuildmat.2019.01.117.

Kantro, D. L. and WEISE, C. H. (1979) 'Hydration of Various Beta-Dicalcium Silicate Preparations', *Journal of the American Ceramic Society*. Wiley Online Library, 62(11-12), pp. 621–626.

Kaushik, A. and Singh, M. (2011) 'Isolation and characterization of cellulose nanofibrils from wheat straw using steam explosion coupled with high shear homogenization', *Carbohydrate research*. Elsevier, 346(1), pp. 76–85.

Kim, S. *et al.* (2016) 'Effect of chlorides on conductivity and dielectric constant in hardened cement mortar: NDT for durability evaluation', *Advances in Materials Science and Engineering*. Hindawi, 2016.

Klemm, D. *et al.* (2018) 'Nanocellulose as a natural source for groundbreaking applications in materials science: Today's state', *Materials Today*. Elsevier Ltd, 21(7), pp. 720–748. doi: 10.1016/j.mattod.2018.02.001.

Konsta-Gdoutos, M. S., Metaxa, Z. S. and Shah, S. P. (2010) 'Multi-scale mechanical and fracture characteristics and early-age strain capacity of high performance carbon nanotube/cement nanocomposites', *Cement and Concrete Composites*. Elsevier, 32(2), pp. 110–115.

Kontoleontos, F. *et al.* (2012) 'Influence of colloidal nanosilica on ultrafine cement hydration: Physicochemical and microstructural characterization', *Construction and building materials*. Elsevier, 35, pp. 347–360.

Kumar, A. *et al.* (2012) ‘Synthesis and characterization of methylcellulose/PVA based porous composite’, *Carbohydrate Polymers*. Elsevier, 88(4), pp. 1364–1372.

Lai, G.-C., Nojiri, T. and Nakano, K. (1992) ‘Studies of the stability of β-Ca2SiO4 doped by minor ions’, *Cement and Concrete Research*. Elsevier, 22(5), pp. 743–754.

Lawrence, M. (2015) ‘Reducing the environmental impact of construction by using renewable materials’, *Journal of renewable materials*. Tech Science Press, 3(3), pp. 163–174.

Lee, C. *et al.* (2008) ‘Measurement of the elastic properties and intrinsic strength of monolayer graphene’, *science*. American Association for the Advancement of Science, 321(5887), pp. 385–388.

Li, G. Y., Wang, P. M. and Zhao, X. (2005) ‘Mechanical behavior and microstructure of cement composites incorporating surface-treated multi-walled carbon nanotubes’, *Carbon*. Elsevier, 43(6), pp. 1239–1245.

Li, H. *et al.* (2004) ‘Microstructure of cement mortar with nano-particles’, *Composites Part B: Engineering*, 35(2), pp. 185–189. doi: 10.1016/S1359-8368(03)00052-0.

Li, H. *et al.* (2009) ‘Theoretical and experimental specific capacitance of polyaniline in sulfuric acid’, *Journal of Power Sources*. Elsevier, 190(2), pp. 578–586.

Li, M. *et al.* (2014) ‘Preparation and characterization of cellulose nanofibers from de-pectinated sugar beet pulp’, *Carbohydrate Polymers*. Elsevier Ltd., 102(1), pp. 136–143. doi: 10.1016/j.carbpol.2013.11.021.

Li, W. *et al.* (2016) ‘Electrochemical impedance interpretation for the fracture toughness of carbon nanotube/cement composites’, *Construction and Building Materials*. Elsevier, 114, pp. 499–505.

Luo, J., Duan, Z. and Li, H. (2009) ‘The influence of surfactants on the processing of multi-walled carbon nanotubes in reinforced cement matrix composites’, *Physica Status Solidi (A) Applications and Materials Science*, 206(12), pp. 2783–2790. doi: 10.1002/pssa.200824310.

Lv, C. *et al.* (2013) ‘Optimization of production yield and functional properties of pectin extracted from sugar beet pulp’, *Carbohydrate Polymers*. Elsevier, 95(1), pp. 233–240.

Lv, S. *et al.* (2013) ‘Effect of graphene oxide nanosheets of microstructure and mechanical properties of cement composites’, *Construction and Building Materials*. Elsevier Ltd, 49, pp. 121–127. doi: 10.1016/j.conbuildmat.2013.08.022.

Ma, B. *et al.* (2019) ‘Effect of Nano Silica on Hydration and Microstructure Characteristics of Cement High Volume Fly Ash System Under Steam Curing’, *Journal of Wuhan University of Technology-Mater. Sci. Ed.* Springer, 34(3), pp. 604–613.

Ma, P.-C. *et al.* (2010) ‘Dispersion and functionalization of carbon nanotubes for polymer-based nanocomposites: a review’, *Composites Part A: Applied Science and Manufacturing*. Elsevier, 41(10), pp. 1345–1367.

Ma, Q. and Zhu, Y. (2017) ‘Experimental research on the microstructure and compressive and tensile properties of nano-SiO2 concrete containing basalt fibers’, *Underground Space*. Elsevier, 2(3), pp. 175–181.

Makar, J. M. and Chan, G. W. (2009) ‘Growth of cement hydration products on single-walled carbon nanotubes’, *Journal of the American Ceramic Society*, 92(6), pp. 1303–1310. doi: 10.1111/j.1551-2916.2009.03055.x.

Makar, J M, Margeson, J. C. and Luh, J. (2005) ‘Carbon nanotube/cement composites-early results and potential applications’.

Makar, J.M., Margeson, J. and Luh, J. (2005) ‘Carbon nanotube/cement composites - early results and potential applications’, *NRC Publication Records*, pp. 1–10. doi: 10.1039/B910216G.

Malhotra, V. M. and Mehta, P. K. (1996) *Pozzolanic and cementitious materials*. Taylor & Francis.

Manzur, T., Yazdani, N. and Emon, M. A. B. (2014) ‘Effect of carbon nanotube size on compressive strengths of nanotube reinforced cementitious composites’, *Journal of Materials*. Hindawi, 2014, pp. 1–8.

Mármol, G. *et al.* (2013) ‘Mechanical and physical performance of low alkalinity cementitious composites reinforced with recycled cellulosic fibres pulp from cement kraft bags’, *Industrial Crops and Products*. Elsevier, 49, pp. 422–427.

Mata, Y. N. *et al.* (2009) ‘Sugar-beet pulp pectin gels as biosorbent for heavy metals: preparation and determination of biosorption and desorption characteristics’, *Chemical Engineering Journal*. Elsevier, 150(2–3), pp. 289–301.

Mathesh, M. *et al.* (2015) ‘Surface chemistry of two-dimensional layered nanosheets’, *Nanotubes and nanosheets functionalization and applications of boron nitride and other nanomaterials. CRC, Boca Raton*, pp. 333–366.

Mazlan, D., Din, M., *et al.* (2016) ‘Cellulose nanocrystals addition effects on cement mortar matrix properties’, *Int. J. Adv. Mech. Civ. Eng*, 3, pp. 44–48.

Mazlan, D., Md Din, M. F., *et al.* (2016) ‘Cellulose Nanocrystals Addition Effects on Cement Mortar Matrix Properties’, *International Journal of Advances in Mechanical*

and Civil Engineering, 3(1), pp. 44–48.

McCarter, W. J. and Brousseau, R. (1990) 'The AC response of hardened cement paste', *Cement and Concrete Research*. Elsevier, 20(6), pp. 891–900.

Mejdoub, R. *et al.* (2017) 'Nanofibrillated cellulose as nanoreinforcement in Portland cement: Thermal, mechanical and microstructural properties', *Journal of Composite Materials*. SAGE Publications Ltd, 51(17), pp. 2491–2503. doi: 10.1177/0021998316672090.

Minard, H. *et al.* (2007) 'Mechanisms and parameters controlling the tricalcium aluminate reactivity in the presence of gypsum', *Cement and Concrete Research*. Elsevier, 37(10), pp. 1418–1426.

Mindess, S., Young, J. F. and Darwin, D. (1981) 'Concrete Prentice-Hall', *Englewood Cliffs, NJ*, 481.

Mokhtar, M M *et al.* (2017) 'Mechanical performance, pore structure and micro-structural characteristics of graphene oxide nano platelets reinforced cement', *Construction and Building Materials*. Elsevier, 138, pp. 333–339.

Mokhtar, M. M. *et al.* (2017) 'Mechanical performance, pore structure and micro-structural characteristics of graphene oxide nano platelets reinforced cement', *Construction and Building Materials*. Elsevier Ltd, 138, pp. 333–339. doi: 10.1016/j.conbuildmat.2017.02.021.

Mondal, S. (2017) 'Preparation, properties and applications of nanocellulosic materials', *Carbohydrate polymers*. Elsevier, 163, pp. 301–316.

Monteiro, P. (2006) *Concrete: microstructure, properties, and materials*. McGraw-Hill Publishing.

Monteiro, P. J. M., Miller, S. A. and Horvath, A. (2017) 'Towards sustainable concrete', *Nature Materials*. Nature Publishing Group, 16(7), pp. 698–699.

Moon, R. J. *et al.* (2011) 'Cellulose nanomaterials review: structure, properties and nanocomposites', *Chemical Society Reviews*. Royal Society of Chemistry, 40(7), pp. 3941–3994.

Mounet, N. *et al.* (2018) 'Two-dimensional materials from high-throughput computational exfoliation of experimentally known compounds', *Nature nanotechnology*. Nature Publishing Group, 13(3), pp. 246–252.

Naderi, N. *et al.* (2013) 'Enhanced optical performance of electrochemically etched porous silicon carbide', *Semiconductor Science and Technology*. IOP Publishing, 28(2), p. 25011.

Nair, R. R. *et al.* (2012) 'Unimpeded permeation of water through helium-leak–tight graphene-based membranes', *Science*. American Association for the Advancement of Science, 335(6067), pp. 442–444.

Najigivi, A. *et al.* (2013) 'Investigating the effects of using different types of SiO2 nanoparticles on the mechanical properties of binary blended concrete', *Composites Part B: Engineering*. Elsevier Ltd, 54(1), pp. 52–58. doi: 10.1016/j.compositesb.2013.04.035.

Najigivi, A., Khaloo, A. and Rashid, S. A. (2013) 'Investigating the effects of using different types of SiO2 nanoparticles on the mechanical properties of binary blended concrete', *Composites Part B: Engineering*. Elsevier, 54, pp. 52–58.

Neville, A. M. (1995) *Properties of concrete*. Longman London.

Neville, A. M. (2013) *Properities of Concrete*.

Nishiyama, Y. *et al.* (2003) ‘Crystal Structure and Hydrogen Bonding System in Cellulose Iα from Synchrotron X-ray and Neutron Fiber Diffraction’, *Journal of the American Chemical Society*, 125(47), pp. 14300–14306. doi: 10.1021/ja037055w.

Njuguna, J., Vanli, O. A. and Liang, R. (2015) ‘A Review of Spectral Methods for Dispersion Characterization of Carbon Nanotubes in Aqueous Suspensions’, *Journal of Spectroscopy*, 2015. doi: 10.1155/2015/463156.

Norizan, M. N. *et al.* (2020) ‘Carbon nanotubes: functionalisation and their application in chemical sensors’, *RSC Advances*. Royal Society of Chemistry, 10(71), pp. 43704–43732.

Novoselov, K. S. *et al.* (2004) ‘Electric field effect in atomically thin carbon films’, *science*. American Association for the Advancement of Science, 306(5696), pp. 666–669.

Novoselov, K. S. and Geim, A. K. (2007) ‘The rise of graphene’, *Nat. Mater*, 6(3), pp. 183–191.

Odler, I. (1998) ‘Hydration, setting and hardening of Portland cement’, *Lea’s Chemistry of cement and concrete*. Butterworth-Hinemann.

Oliveira, R. L. *et al.* (2015) ‘Synthesis and characterization of methylcellulose produced from bacterial cellulose under heterogeneous condition’, *Journal of the Brazilian Chemical Society*. SciELO Brasil, 26(9), pp. 1861–1870.

Olmos, J. C. and Hansen, M. E. Z. (2012) ‘Enzymatic depolymerization of sugar beet pulp: Production and characterization of pectin and pectic-oligosaccharides as a potential source for functional carbohydrates’, *Chemical Engineering Journal*. Elsevier, 192, pp. 29–36.

Onuaguluchi, O. and Banthia, N. (2016) ‘Plant-based natural fibre reinforced cement composites: A review’, *Cement and Concrete Composites*. Elsevier, 68, pp. 96–108.

Onuaguluchi, O., Panesar, D. K. and Sain, M. (2014) ‘Properties of nanofibre reinforced cement composites’, *Construction and Building Materials*. Elsevier Ltd, 63, pp. 119–124. doi: 10.1016/j.conbuildmat.2014.04.072.

Osong, S. H., Norgren, S. and Engstrand, P. (2016) ‘Processing of wood-based microfibrillated cellulose and nanofibrillated cellulose, and applications relating to papermaking: a review’, *Cellulose*. Springer, 23(1), pp. 93–123.

Pacheco-Torgal, F. and Jalali, S. (2011) ‘Cementitious building materials reinforced with vegetable fibres: A review’, *Construction and Building Materials*. Elsevier, 25(2), pp. 575–581.

Pan, Z. *et al.* (2015) ‘Mechanical properties and microstructure of a graphene oxide–cement composite’, *Cement and Concrete Composites*. Elsevier, 58, pp. 140–147.

Pane, I. and Hansen, W. (2005) ‘Investigation of blended cement hydration by isothermal calorimetry and thermal analysis’, *Cement and concrete research*. Elsevier, 35(6), pp. 1155–1164.

Parawira, W. *et al.* (2004) ‘Anaerobic batch digestion of solid potato waste alone and in combination with sugar beet leaves’, *Renewable Energy*. Elsevier, 29(11), pp. 1811–1823.

Parveen, S., Rana, S. and Fangueiro, R. (2013) ‘A Review on Nanomaterial Dispersion, Microstructure, and Mechanical Properties of Carbon Nanotube and Nanofiber Reinforced Cementitious Composites’, *Journal of Nanomaterials*. Hindawi Limited, 2013, pp. 1–19. doi: 10.1155/2013/710175.

Payakaniti, P. *et al.* (2017) 'Electrical conductivity and compressive strength of carbon fiber reinforced fly ash geopolymeric composites', *Construction and Building Materials*. Elsevier, 135, pp. 164–176.

Pereira, V. M., Neto, A. H. C. and Peres, N. M. R. (2009) 'Tight-binding approach to uniaxial strain in graphene', *Physical Review B*. APS, 80(4), p. 45401.

Peters, Sarah J *et al.* (2010) 'Nanocellulose and microcellulose fibers for concrete', *Transportation Research Record*. SAGE Publications Sage CA: Los Angeles, CA, 2142(1), pp. 25–28.

Peters, Sarah J. *et al.* (2010) 'Nanocellulose and Microcellulose Fibers for Concrete', *Transportation Research Record: Journal of the Transportation Research Board*, 2142(1), pp. 25–28. doi: 10.3141/2142-04.

Powers, T. C. and Brownyard, T. L. (1948) 'Studies of the physical properties of hardened cement paste. Portland Cem. Ass', *Bull*, 22, pp. 53–66.

Psarras, G. C., Manolakaki, E. and Tsangaris, G. M. (2003) 'Dielectric dispersion and ac conductivity in—Iron particles loaded—polymer composites', *Composites Part A: Applied Science and Manufacturing*. Elsevier, 34(12), pp. 1187–1198.

Rafiee, M. A. *et al.* (2013) 'Hexagonal boron nitride and graphite oxide reinforced multifunctional porous cement composites', *Advanced Functional Materials*. Wiley Online Library, 23(45), pp. 5624–5630.

Rafique, I. *et al.* (2016) 'Exploration of epoxy resins, hardening systems, and epoxy/carbon nanotube composite designed for high performance materials: A review', *Polymer-Plastics Technology and Engineering*. Taylor & Francis, 55(3), pp. 312–333.

Rajabipour, F. *et al.* (2005) 'Procedure to interpret electrical conductivity

measurements in cover concrete during rewetting', *Journal of materials in civil engineering*. American Society of Civil Engineers, 17(5), pp. 586–594.

Rajabipour, F., Sant, G. and Weiss, J. (2008) 'Interactions between shrinkage reducing admixtures (SRA) and cement paste's pore solution', *Cement and Concrete Research*. Elsevier, 38(5), pp. 606–615.

Rashid, K. *et al.* (2015) 'Experimental and analytical investigations on the behavior of interface between concrete and polymer cement mortar under hygrothermal conditions', *Construction and Building Materials*. Elsevier Ltd, 94, pp. 414–425. doi: 10.1016/j.conbuildmat.2015.07.035.

Rendell, F., Jauberthie, R. and Grantham, M. (2002) *Deteriorated concrete: Inspection and physicochemical analysis*. Thomas Telford.

Renouf, M. A., Wegener, M. K. and Nielsen, L. K. (2008) 'An environmental life cycle assessment comparing Australian sugarcane with US corn and UK sugar beet as producers of sugars for fermentation', *Biomass and Bioenergy*. Elsevier, 32(12), pp. 1144–1155.

Richardson, I. G. (2000) 'The nature of the hydration products in hardened cement pastes', *Cement and Concrete Composites*. Elsevier, 22(2), pp. 97–113.

RILEM, D. R. (1985) 'Determination of the fracture energy of mortar and concrete by means of three-point bend tests on notched beams', *Materials and structures*, 18(106), pp. 285–290.

Saafi, M. *et al.* (2015) 'Enhanced properties of graphene/fly ash geopolymeric composite cement', *Cement and Concrete Research*. Elsevier Ltd, 67, pp. 292–299. doi: 10.1016/j.cemconres.2014.08.011.

Saifuddin, N., Raziah, A. Z. and Junizah, A. R. (2013) ‘Carbon nanotubes: a review on structure and their interaction with proteins’, *Journal of Chemistry*. Hindawi, 2013.

Sain, M. and Panthapulakkal, S. (2006) ‘Bioprocess preparation of wheat straw fibers and their characterization’, *Industrial Crops and Products*. Elsevier, 23(1), pp. 1–8.

Saito, T. *et al.* (2007) ‘Cellulose nanofibers prepared by TEMPO-mediated oxidation of native cellulose’, *Biomacromolecules*. ACS Publications, 8(8), pp. 2485–2491.

Saito, T. *et al.* (2013) ‘An ultrastrong nanofibrillar biomaterial: the strength of single cellulose nanofibrils revealed via sonication-induced fragmentation’, *Biomacromolecules*. ACS Publications, 14(1), pp. 248–253.

Salazar-Ordóñez, M., Pérez-Hernández, P. P. and Martín-Lozano, J. M. (2013) ‘Sugar beet for bioethanol production: An approach based on environmental agricultural outputs’, *Energy Policy*. Elsevier, 55, pp. 662–668.

Salvetat, J.-P. *et al.* (1999) ‘Mechanical properties of carbon nanotubes’, *Applied Physics A*. Springer, 69(3), pp. 255–260.

Şanal, İ., Zihnioğlu, N. Ö. and Hosseini, A. (2015) ‘Particle image velocimetry (PIV) to evaluate fresh and hardened state properties of self compacting fiber-reinforced cementitious composites (SC-FRCCs)’, *Construction and Building Materials*. Elsevier, 78, pp. 450–463.

Sanchez, F. and Sobolev, K. (2010) ‘Nanotechnology in concrete–a review’, *Construction and building materials*. Elsevier, 24(11), pp. 2060–2071.

Sarott, F. A. *et al.* (1992) ‘Diffusion and adsorption studies on hardened cement paste and the effect of carbonation on diffusion rates’, *Cement and Concrete Research*, 22(2–3), pp. 439–444. doi: 10.1016/0008-8846(92)90086-B.

Scrivener, K. *et al.* (2019) ‘Advances in understanding cement hydration mechanisms’, *Cement and Concrete Research*. Elsevier, 124, p. 105823.

Scrivener, K. L., Juilland, P. and Monteiro, P. J. M. (2015) ‘Advances in understanding hydration of Portland cement’, *Cement and Concrete Research*. Elsevier, 78, pp. 38–56.

Scrivener, K. L. and Nonat, A. (2011) ‘Hydration of cementitious materials, present and future’, *Cement and concrete research*. Elsevier, 41(7), pp. 651–665.

Segal, L. *et al.* (1959) ‘An Empirical Method for Estimating the Degree of Crystallinity of Native Cellulose Using the X-Ray Diffractometer’, *Textile Research Journal*, 29(10), pp. 786–794. doi: 10.1177/004051755902901003.

Sharon Fisher (2017) *A positive future for the UK beet sugar industry*. Available at: https://www.britishsugar.co.uk/media/news/2017-02-20-a-positive-future-for-the-uk-beet-sugar-industry (Accessed: 8 July 2020).

Shen, W. *et al.* (2019) ‘The microstructure formation of C-S-H in the HPC paste from nano-scale feature’, *Journal of Sustainable Cement-Based Materials*. Taylor & Francis, 8(4), pp. 199–213. doi: 10.1080/21650373.2018.1564397.

Siddique, R. and Cachim, P. (2018) *Waste and Supplementary Cementitious Materials in Concrete: Characterisation, Properties and Applications*. Woodhead Publishing.

Sing, K. S. W. (1985) ‘Reporting physisorption data for gas/solid systems with special reference to the determination of surface area and porosity (Recommendations 1984)’, *Pure and applied chemistry*. De Gruyter, 57(4), pp. 603–619.

Srinivasan, R. and Fasmin, F. (2021) *An Introduction to Electrochemical Impedance Spectroscopy*. CRC Press.

St John, D. A., Poole, A. B. and Sims, I. (1998) *Concrete petrography: a handbook of investigative techniques*.

Statista (2020) *Sugar production worldwide in 2019/2020*. Available at: https://www.statista.com/statistics/495973/sugar-production-worldwide/.

Statista (2021) *Cement production in the United States and worldwide from 2010 to 2020*. Available at: https://www.statista.com/statistics/219343/cement-production-worldwide/#statisticContainer (Accessed: 28 May 2021).

Stoller, M. D. *et al.* (2008) 'Graphene-based ultracapacitors', *Nano letters*. ACS Publications, 8(10), pp. 3498–3502.

Sun, X. *et al.* (2016) 'Cellulose Nanofibers as a Modifier for Rheology, Curing and Mechanical Performance of Oil Well Cement', *Scientific Reports*. Nature Publishing Group, 6. doi: 10.1038/srep31654.

Sun, Z. and Xu, Q. (2009) 'Microscopic, physical and mechanical analysis of polypropylene fiber reinforced concrete', *Materials Science and Engineering: A*. Elsevier, 527(1–2), pp. 198–204.

Tang, C. *et al.* (2008) 'Synthetic routes and formation mechanisms of spherical boron nitride nanoparticles', *Advanced Functional Materials*. Wiley Online Library, 18(22), pp. 3653–3661.

Tao, J. *et al.* (2014) 'Hierarchical nanostructures of polypyrrole@ MnO 2 composite electrodes for high performance solid-state asymmetric supercapacitors', *Nanoscale*. Royal Society of Chemistry, 6(5), pp. 2922–2928.

Taylor, H. F. W. (1993) 'Nanostructure of C-S-H: Current status', *Advanced cement based materials*. Elsevier, 1(1), pp. 38–46.

Taylor, H. F. W. (1997) *Cement chemistry*. Thomas Telford.

Thomas, J. J., Jennings, H. M. and Allen, A. J. (1999) 'The surface area of hardened cement paste as measured by various techniques', *Concrete Science and Engineering*. Citeseer, 1(1), pp. 45–64.

Tonoli, G. H. D. *et al.* (2009) 'Cellulose modified fibres in cement based composites', *Composites Part A: Applied Science and Manufacturing*. Elsevier, 40(12), pp. 2046–2053.

Torgovnikov, G. I. (1993) 'Dielectric properties of wood-based materials', in *Dielectric properties of wood and wood-based materials*. Springer, pp. 135–159.

United States Department of Agriculture (2020) 'Sugar: World Markets and Trade'. Available at: https://apps.fas.usda.gov/psdonline/circulars/sugar.pdf.

Vinayan, B. P. (2016) 'Heteroatom-doped graphene-based hybrid materials for hydrogen energy conversion, recent advances in graphene research', *InTech*, pp. 177–194.

Voisin, H. *et al.* (2017) 'Nanocellulose-based materials for water purification', *Nanomaterials*. Multidisciplinary Digital Publishing Institute, 7(3), p. 57.

Wafa, F. F. (1990) 'Properties & applications of fiber reinforced concrete', *Engineering Sciences*. Scientific Publishing Center, 2(1).

Wang, B., Jiang, R. and Wu, Z. (2016) 'Investigation of the mechanical properties and microstructure of graphene nanoplatelet-cement composite', *Nanomaterials*. Multidisciplinary Digital Publishing Institute, 6(11), p. 200.

Wang, L. *et al.* (2017) 'Effect of graphene oxide (GO) on the morphology and microstructure of cement hydration products', *Nanomaterials*. Multidisciplinary

Digital Publishing Institute, 7(12), p. 429.

Wang, L., Han, G. and Zhang, Y. (2007) ‘Comparative study of composition, structure and properties of Apocynum venetum fibers under different pretreatments’, *Carbohydrate Polymers*, 69(2), pp. 391–397. doi: 10.1016/j.carbpol.2006.12.028.

Wang, M. *et al.* (2016) ‘The dispersion and aggregation of graphene oxide in aqueous media’, *Nanoscale*. Royal Society of Chemistry, 8(30), pp. 14587–14592.

Xie, X. *et al.* (2015) ‘Cellulosic fibers from rice straw and bamboo used as reinforcement of cement-based composites for remarkably improving mechanical properties’, *Composites Part B: Engineering*. Elsevier Ltd, 78, pp. 153–161. doi: 10.1016/j.compositesb.2015.03.086.

Yao, W., Li, J. and Wu, K. (2003) ‘Mechanical properties of hybrid fiber-reinforced concrete at low fiber volume fraction’, *Cement and concrete research*. Elsevier, 33(1), pp. 27–30.

Yuan, X.-Z. *et al.* (2010) ‘Electrochemical impedance spectroscopy in PEM fuel cells: fundamentals and applications’. Springer.

van Zanten, H. H. E. *et al.* (2014) ‘Assessing environmental consequences of using co-products in animal feed’, *The International Journal of Life Cycle Assessment*. Springer, 19(1), pp. 79–88.

Zhang, J. *et al.* (2014) ‘Analysis of CO2 emission for the cement manufacturing with alternative raw materials: a LCA-based framework’, *Energy Procedia*. Elsevier, 61, pp. 2541–2545.

Zhang, X. *et al.* (1996) ‘Dielectric and electrical properties of ordinary Portland cement and slag cement in the early hydration period’, *Journal of materials science*. Springer,

31(5), pp. 1345–1352.

Zheng, Y. *et al.* (2012) 'Integrating sugar beet pulp storage, hydrolysis and fermentation for fuel ethanol production', *Applied Energy*. Elsevier, 93, pp. 168–175.

Zhou, C. *et al.* (2017) 'Enhanced mechanical properties of cement paste by hybrid graphene oxide/carbon nanotubes', *Construction and Building Materials*. Elsevier, 134, pp. 336–345.

Zhu, Y. *et al.* (2010) 'Graphene and graphene oxide: synthesis, properties, and applications', *Advanced materials*. Wiley Online Library, 22(35), pp. 3906–3924.

Zihlif, A. M., Ayish, I. O. and Elimat, Z. M. (2013) 'The AC electrical behavior of cement–polymer composite', *Journal of Thermoplastic Composite Materials*. SAGE Publications Sage UK: London, England, 26(9), pp. 1168–1179.